FINAL REPORT

to the

NATIONAL AERONAUTICS AND SPACE ADMINISTRATION

Contract NAS9-12334

APOLLO PASSIVE SEISMIC EXPERIMENT PARTICIPATION

1 January 1972 - 30 September 1978

M. Nafi Toksöz

Principal Investigator

Department of Earth and Planetary Sciences
Massachusetts Institute of Technology
Cambridge, Massachusetts   02139

LUNAR SEISMOLOGY:

THE INTERNAL STRUCTURE OF THE MOON

by

Neal Rodney Goins

Submitted to the Department of Earth and Planetary Sciences

on May 24, 1978, in partial fulfillment of the requirements

for the degree of Doctor of Philosophy.

ABSTRACT

A primary goal of the Apollo missions was the exploration
and scientific study of the moon. The nature of the lunar
interior is of particular interest for comparison with the
earth and in studying comparative planetology. The principal
experiment designed to study the lunar interior was the
passive seismic experiment (PSE) included as part of the
science package on missions 12, 14, 15, and 16. Thus seis-
mologists were provided with a unique opportunity to study
the seismicity and seismic characteristics of a second
planetary body and ascertain if analysis methods developed on
earth could illuminate the structure of the lunar interior.

The lunar seismic data differ from terrestrial data in
three major respects. First, the seismic sources are much
smaller than on earth, so that no significant information has
been yet obtained for the very deep lunar interior. Second,
a strong, high Q scattering layer exists on the surface of
the moon, resulting in very emergent seismic arrivals, long
ringing codas that obscure secondary (later arriving) phases,
and the destruction of coherent dispersed surface wave trains.
Third, the lunar seismic network consists of only four sta-
tions, so that after locating the natural seismic events,
only a small amount of data is left for structural analyses.
Thus the analysis methods used are designed to overcome
these difficulties and extract as much information as
possible concerning the structure of the lunar interior.

The direct P and S wave arrival times are the primary
data set that can be measured on the seismograms of natural
lunar seismic events (meteorite impacts, shallow moonquakes,
and deep moonquakes). These are inverted using linearized
matrix inversion and parameter search methods to determine
event locations, origin times, and various structural

parameters simultaneously. Polarization filtering techniques allow the enhancement of secondary body wave arrivals and record section plots are correlated with theoretical travel time curves to identify the secondary phases and deduce structural information. Finally, shear wave amplitude vs. distance curves yield information on the location and magnitude of seismic velocity gradients in the interior.

The results of these analyses show that the moon appears to have a two-layer crust at all four seismic stations: a 20 km upper crust that seems to be constant at all sites and a lower crust that is 40 km thick at stations 12 and 14 (mare), 55 ±10 km at station 16 (highland), and tentatively either 40 km or 70 km at station 15. (These values are dependent on various assumptions used in identifying secondary wave arrivals, and so should be regarded with suitable caution.) Seismic quality factors Q_S and Q_p are about 5000 and 3000, respectively. Between 400 km and 480 km depth there is a transition zone with a sharply decreasing shear wave velocity and an accompanying possible small decrease in V_p. The dominant velocity drop may occur at a 480 km interface. The lower mantle extends from 480 km to at least 1100 km depth which is the maximum depth of penetration of all but a few seismic waves used as data. The average velocities are $V_p = 7.6$ km/sec and $V_S = 4.2$ km/sec, and a small negative gradient may again be present. Attenuation is increased, with $Q_p \sim 1500$ and $Q_S \sim 1000$. Below 1100 km there is tentative indication that the attenuation may increase still further for shear waves, with Q_S dropping to a few hundreds. The velocity structure is not known although further velocity decrease is possible, and no definitive evidence for or against a lunar core exists.

The above model is the result of analyzing nearly all of the seismic data from the Apollo phase of lunar exploration that is useful in determining interior structure. Thus the structure above 1100 km depth is well-constrained and uncertainties on the above values are given explicitly by the analysis methods. The seismic model of the moon given above therefore serves as a strong constraint on the present-day lunar compositional and thermal structure and on various models of lunar evolution.

ORIGINAL PAGE IS
OF POOR QUALITY

ACKNOWLEDGEMENTS

I owe a great debt to my advisor, M. Nafi Toksöz, for providing me with the unique opportunity to work on the lunar seismology project, thus combining my research field with an interest in the planets that I have had since childhood. His patience in listening to my complaints about the lunar data and his unfailing ability to point me in the proper direction during crises were indispensible. Finally, I would like to express my appreciation for the many opportunities that he made available to me to broaden my experience in research, speaking, and science.

Dr. Anton Dainty also devoted many an hour to answering questions and puzzling with me over the vagaries of the seismic data and the computer center. Without his clear thinking in the midst of confusion all would have been lost. His insight and knowledge were invaluable throughout the entire project.

During the course of this work several undergraduates made significant contributions. Loren Shure did a prodigious amount of work in stacking the moonquake data; Ted Anderson created masterpieces of data handling programs; David Band wrote an incredible number of special-purpose ray tracing programs, many of which were quaranteed to be the last one; Bill Baker struggled with a recalcitrant maximum entropy spectral analyzer.

Dorothy Frank typed the bulk of the thesis and deserves special credit for the large number of tables she produced. Ann Harlow rescued Chapter 3 from desperate straits and produced a beautifully proof-read final copy. Finally, Sara Brydges monitored the entire process, typed many last minute corrections, numbered most of the figures, stayed late to spare me a sleepless night, and generally kept me sane and organized in the last few weeks of effort.

My fellow graduate students deserve special credit for making the entire grad student experience more worthwhile than it would otherwise have been, not only in terms of late-night research discussions, but also because of the many fine sporting opportunities.

None of this would have been possible without the continuing support and encouragement provided by my parents. Their continued devotion in enabling me to obtain an excellent education and their unfailing confidence in my efforts have been responsible for the successful completion of my educational experience.

Finally, it is impossible to adequately acknowledge Ms. Sheila Newton for willingly giving up many weekends of free time to help in putting together this thesis. Her continuing assistance and encouragement throughout my years in graduate school and her insistence that there were other aspects to life are deeply appreciated.

TABLE OF CONTENTS

INTRODUCTION.

0.1 Statement of Problem and Context

Traditionally, seismology and seismic methods have provided the most detailed and well-constrained information concerning the structure and state of the earth's interior. Beginning in 1969, a series of seismometers were landed on the moon by the Apollo missions, providing the first opportunity to attempt similar studies on another planetary body. As will be discussed below, the lunar seismic data set is in many ways different from the data that is obtained terrestrially, presenting a variety of analysis difficulties and challenges, although perhaps surprisingly there are many basic similarities. The primary distinction, of course, is that the lunar data are far more limited than is the case on earth, and since the ALSEP stations were turned off in October 1977, no more seismic data will be obtained until the next phase of lunar exploration.

The object of this thesis is to determine the seismic structure of the lunar interior. The analysis of the lunar data has been approached in a systematic fashion using applicable terrestrial techniques so as to minimize the number of necessary assumptions, extract the maximum amount of structural information, determine its

reliability, and thus highlight the real conclusions
that one can draw. The allowable uncertainties in the
final model are no less important than the model itself.
This seismic model can then be interpreted in conjunction
with other geophysical data, such as magnetic sounding
(Parkin et al., 1973; Duba and Ringwood, 1973; Olhoeft
et al., 1974; Dyal et al., 1974, 1975, 1976; Piwinskii and
Duba, 1975; Vanyan and Egorov, 1977; Schwerer et al., 1974;
Wiskerchen and Sonett, 1977), gravity and topographic
figure analyses (Kaula, 1971, 1975b; Kaula et al., 1974;
Runcorn, 1975; Bills and Ferrari, 1977; Ananda, 1977;
Ferrari, 1977; Thurber and Solomon, 1978; Vermillion, 1976)
and average density and moment of inertia values (Blackshear
and Gapcynski, 1977; Solomon, 1974; Solomon and Toksöz,
1973; Michael and Blackshear, 1972; Gast and Giuli, 1972)
so that the final structural model is compatible with all
information.

The direct implications of the seismic model will be
on the temperature and compositional distribution within
the moon. This is essentially an inverse-type of problem,
and is assuredly non-unique. The objective is to find
temperature and composition profiles that will produce the
observed seismic velocity, attenuation, and required
density constraints (average density and moment of inertia).
While this can be readily accomplished in a qualitative

sense (e.g. high attenuation suggests high temperature)
quantitative models depend critically on laboratory
measurements of velocity attenuation, and density as a
function of pressure, temperature, physical structure
and volatile content in rocks of candidate lunar
compositions. Much work has been accomplished in this
area (Tittman et al., 1976, 1977, 1978; Schreiber, 1977;
Kanamori et al., 1972; Mizutani et al., 1977; Talwani
et al., 1974; Todd et al., 1972, 1973; Warren et al.,
1973; Chung, 1970, 1971; Frisillo and Barsch, 1972), but
there are still many pressing questions. Given this
situation, the most reasonable approach is to examine
specific compositional and temperature models, use what
rock physics data is available and determine if the seismic
results can be satisfied within the allowable uncertainties.
Through this process unsatisfactory models can be eliminated
and families of allowable structures can be generated.

These present-day models in turn are coupled in a
variety of ways to the initial composition and thermal
state of the moon. There has been a great deal of research
on the allowable parent rocks and magmas of the lunar
samples taken from both highland and mare regions (Binder,
1976b,c; Binder and Lange, 1978; Drake, 1976; Drake and
Consolmagno, 1976; Herbert et al., 1977a, 1978; Herzburg,
1978; Irving, 1975; Hubbard and Minear, 1975, 1976;

Kesson and Ringwood, 1977; Krähenbühl et al., 1973; Longhi,
1977, 1978; Papike et al., 1976; Ringwood and Kesson,
1977a,b; Ringwood, 1976, 1977; Shih and Schonfeld, 1976;
Taylor and Bence, 1975; Taylor and Jakes, 1974, 1977;
Taylor, 1978; Walker et al., 1975; Wood, 1975; many others),
and although there are many assumptions involved in this
work models of initial compositions which can produce the
observed samples, and the resulting present-day compositions,
have emerged.   Interacting with this is the initial
temperature distribution required to provide appropriate
regions of melting at appropriate times, the present-day
temperatures and heat flow, the absence of large-scale
extensional and compressional tectonic features, and the
material strength required to support observed density
variations.   These aspects are treated with thermal
evolution modeling (Arkani-Hamed, 1973a,b; Binder and
Lange, 1977; Butt and Bastin, 1977; Cassen and Young, 1975;
Head, 1976; Herbert et al., 1977b; Kaula, 1975a; Keihm
and Langseth, 1977; Meissner and Lange, 1977; Minear and
Fletcher, 1978; Oberli et al., 1977; Palme and Wänke, 1975;
Solomon, 1975, 1977; Solomon and Chaiken, 1976; Solomon
and Longhi, 1977; Solomon and Toksöz, 1973; Strangway and
Sharpe, 1975; Toksöz and Solomon, 1973; Toksöz et al., 1972d,
1978; Turcotte et al., 1972; Wood, 1975) and, although again
a number of assumptions are involved, families of possible

initial temperature models have emerged.

This inductive process leads finally to the question of the origin of the moon, in particular the locus of formation, and its relation to initial terrestrial conditions, meteorite formation, and the characteristics of the primitive solar nebula, including questions of initial energy sources and the presence or absence of a lunar dynamo are also involved (Alfven and Arrhenius, 1972; Anderson, 1973a,b, 1975; Binder, 1974, 1976a; Cameron, 1973; Dolginov, 1975; Fuller, 1974; Ganapathy et al., 1970; Ganapathy and Anders, 1974; Goswami, 1976; Hanks and Anderson, 1972; Head, 1977; Herbert et al., 1977b; Hovedt, 1976; Kaula, 1977; Kaula and Harris, 1975; Lewis, 1974; Mitler, 1975; O'Keefe, 1974; Ringwood, 1978; Singer, 1972; Smith, 1977; Sonett and Runcorn, 1973; Turner, 1977).

In sum, the detailed seismic structure of the moon provides the most focussed view of the present-day lunar interior and is a major and critical constraint that affects more or less strongly nearly all aspects of lunar science and planetology. The object of this thesis is to determine that structure and the allowable uncertainties, and briefly discuss possible preliminary implications of the final model.

0.2   Review of Previous Work

There has been a great deal of research done on lunar seismology, and many papers have been published. A fair amount of duplicate reporting has occurred because the research field essentially began in 1969 and there has been a need to present the early results simultaneously to a variety of forums. In this section the research will be reviewed only briefly; detailed discussions of various papers are included in the appropriate chapters. Nearly all published papers will be referenced here in order to present the scope of the research done to date.

Lunar seismology began in 1969 with the description of the Passive Seismic Experiment (Latham et al., 1969a) that was to be landed on the moon later that year by the Apollo 11 mission. For the ensuing three or four years, all reports on the seismic results were published jointly by the Apollo Seismology Team, summarizing the on-going research on seismicity and internal structure as the seismic network was built up and the data base and analysis ideas increased rapidly. The preliminary science reports (Latham et al., 1969b, 1970d, 1971b, 1972b, 1972d, 1973c) published by NASA were accompanied by a series of Science articles (Latham et al., 1970a, 1970b, 1971a; Toksöz et al., 1972b; Nakamura et al., 1973) reporting progressively more

complete analyses on all aspects of the seismic data.
Simultaneously reports appeared in the Lunar Science
Conference Proceedings (Latham et al., 1970c, 1972c,
Toksöz et al., 1972c), and as the seismic network was
completed in 1972, summary papers were published (Latham
et al., 1972a, 1973b; Toksöz et al., 1972a).

With the end of the Apollo mission program, the
data flow became steady and the research reports dealt
with specific topics in more depth. At the same time,
the seismic team separated into two main groups located
at M.I.T. and the University of Texas at Galveston, both
of which continued to contribute steadily, while several
other researchers published reports more or less
occasionally. In reviewing this work, it is best to
discuss specific research areas insofar as possible.

The natural seismicity of the moon is divided into
four categories. Thermal moonquakes (Duennebier and
Sutton, 1974a; Cooper and Kovach, 1975; Duennebier, 1976)
are small events caused by thermal stresses and slumping,
and are detectable only near the seismic stations. High fre-
quency teleseisms (Nakamura et al., 1974a; Nakamura, 1977a;
Lammlein, 1977; Goins et al., 1978b) are probably shallow
seismic events. The most studied of lunar seismic events
have been the deep-focus moonquakes (Meissner et al.,

1973; Runcorn, 1974, 1977; Lammlein et al., 1974; Goins et al., 1976a, 1978b; Lammlein, 1977; Toksöz et al., 1977; Cheng and Toksöz, 1978; Nakamura, 1978; Smith et al., 1977). Finally, meteorite impacts, while not considered a seismic source on earth, account for some of the largest seismic sources on the moon (Duennebier and Sutton, 1974b; Duennebier et al., 1975b, 1976; Dorman et al., 1978; Dainty et al., 1975b). Some of this research (Toksöz et al., 1977; Goins et al., 1976a,b, 1978b) was conducted in conjunction with the work reported in this thesis, but only those aspects directly pertinent to the thesis problem will be discussed in detail.

Another research area has concerned the apparent existence of a strong scattering layer on the lunar surface (Strohback, 1970; Gold and Soter, 1970; Berckhemer, 1970; Steg and Klemens, 1970; Dainty et al., 1974a; Dainty and Toksöz, 1977; Nakamura, 1976, 1977b). This feature has profound effects on the character of lunar seismograms, as discussed below.

The very near-surface seismic structure of the moon, defined as being within a few kilometers of the surface and possibly within the zone of scatterers, has been treated in several papers (Warren, 1972; Kovach and Watkins, 1973a,b,c; Mark and Sutton, 1975; Nakamura et al., 1975; Watkins and Kovach, 1973), and summarized in Cooper et al. (1974). Their

results will be used in this work.

Perhaps the most research effort has been devoted to the problem of lunar seismic structure below the surficial layer, which is the subject of this thesis. In a series of papers, the Galveston group presented their developing lunar model (Nakamura et al., 1974b, 1976a,b, 1977; Latham et al., 1978). Concurrently, the M.I.T. researchers published their lunar modeling results (Toksöz et al., 1973; 1974a,b; Dainty et al., 1974b, 1975a, 1976; Goins et al., 1974, 1976b, 1977a,b,c, 1978a); ranging from crustal structure (earlier papers) to the deep interior. (Much of the work in the later M.I.T. papers forms sections of this thesis.) These two seismic models differ substantially in several ways, and an attempt to delineate the source of the differences and reconcile the two models will be made in Chapter 3, analyzing the latest results from each group. A few other researchers have made contributions to the structural models (Simmons et al., 1973; Burkhard and Jackson, 1975; Nyland and Roebrock, 1975; Voss et al., 1976; Jarosch, 1977). They will be discussed in later sections.

Finally, there are several review papers which summarize sections of the above research. Latham et al. (1973a; 1974) discuss the Galveston group's seismic conclusions. Toksöz.

(1974, 1975) presents a somewhat broader view of the geophysics and geochemistry of planetary interiors. The former paper is especially valuable in supplying extensive early references (pre-1974) on all aspects of lunar science in addition to those included herein.

0.3 Thesis Summary

The objective of this thesis is to use the most efficient analysis methods possible to determine the structure of the lunar interior from the available seismic data. The lunar seismograms, however, are markedly different from terrestrial records as a result of the intense surficial scattering layer and extremely high Q. As will be discussed below, this produces long codas after the direct P and S wave arrivals, effectively obscuring secondary phases. In addition, surface wave propagation is effectively a diffusion process, and no coherent, dispersed wave trains are observable. Therefore, only the direct P and S wave arrival times are directly measurable on the lunar seismograms, and these arrivals constitute the primary, most complete, and most reliable data set available from the lunar records. Given that there are only four stations, and that the natural seismic

events must be located, both parameter search and matrix-inversion (or stochastic) methods are used in this thesis to extract structural information from the arrival time data. These techniques complement each other, and allow exploration of the parameter space, determination of stability, and calculation of formal uncertainties in the model parameters. As a result, it is possible to determine the maximum amount of structural information obtainable from the data.

Once this has been accomplished and event locations and origin times calculated, further processing can produce secondary data sets. First, the three-component seismograms are rotated to radial, transverse, and vertical directions relative to the event epicenters and passed through a polarization filter that enhances rectilinear particle motion relative to ellipsoidal particle motion. The rationale for this is that secondary seismic waves will initially arrive with rectilinear particle motion while the obscuring direct wave scattered coda will in general contain ellipsoidal particle paths, and so the secondary phases should be relatively amplified. True secondary arrivals can then be recognized by arranging the filtered seismograms in record sections so that the secondary phases follow predicted travel time curves across many records.

This procedure hopefully prevents misidentification since noise pulses, which may also have rectilinear particle motion, will not in general line up consistently across several seismograms.

Finally, amplitudes of the direct waves and their codas as a function of source-receiver separation can be used to further infer the structural properties of the lunar interior. This has been done in three ways. First, spectral amplitude ratios from the short-period records have been used to deduce effective Q values at various depths. Second, there is a pronounced shear wave shadow zone at about 90° distance. Lastly, the amplitude-distance curve can be fit quantitatively to constrain seismic velocity gradients in the moon. This last aspect has numerous uncertainties due to the assumptions needed to construct the observational curve, as discussed in Chapter 3.

These various research efforts are described in this thesis. Chapter 1, along with Appendix 1, is concerned with the lunar seismic data. Its characteristics, their causes, and the consequences are discussed in light of previous work. The data used herein are presented, along with some preliminary processing results. Chapter 2 deals with the lunar crustal structure. Previous work is discussed, and then the present results obtained from

secondary phases on filtered record sections are described.
In Appendix 2, the necessary ray tracers are discussed,
including the calculation of theoretical amplitudes.
Appendix 3 contains the theoretical basis for the
polarization filter and the necessary considerations for
application to the lunar data. In Chapter 3 the structure
of the lunar mantle is presented. Again, previous work is
reviewed, followed by the results from various analyses.
First, the direct wave arrival time data set is inverted
in various ways, and the results are tested and examined.
Appendix 4 describes the theoretical background for each
inversion method, and along with Appendix 2, discusses the
specific techniques applicable to the lunar case. The
latter part of Chapter 3 considers the secondary data sets,
notably additional seismic wave arrivals and amplitude-
distance curves. Finally, Chapter 4 discusses the deeper
structure, below about 1100 km depth. The data here is
scarce, and only tentative conclusions are drawn.

The last chapter summarizes the results, describing
a consistent model of lunar seismic structure. This model
is considered in conjunction with other geophysical data,
and some tentative implications for compositional, thermal,
and evolutionary lunar models are discussed.

CHAPTER 1

SEISMIC DATA

1.1 Seismogram Characteristics

The completed lunar seismic network consists of four stations located within a few hundred meters of the landing sites of Apollo missions 12, 14, 15, and 16. The station locations, separations, and installation dates are listed in Table 1-1 and plotted in Fig. 1-1. All instruments were shut down in October, 1977. The array is roughly in the shape of an equilateral triangle, 1000 km on a side, with 181 km between stations 12 and 14. As a result, although in theory any three stations will suffice in locating a natural seismic event, in practice it is necessary to observe the event at all three corners of the triangle to obtain a stable location. Thus observations at stations 15, 16, and at least one of 12 and 14 are required.

Each seismic station is a part of the ALSEP (Apollo Lunar Scientific Experiments Package), connected by cable to a central station that telemeters the seismic and other data back to earth. The stations each contain four seismometers, three matched long-period instruments (two horizontal and one vertical) and one short-period vertical instrument. The orientations of the LP horizontal components are given in Table 1-2. In addition heaters and automatic leveling devices are provided at each station. Technical descriptions

are given in Latham et al. (1969a) and Sutton and Latham (1964).

The frequency response of the instruments is shown in Fig. 1-2. The overall sensitivity is about 3 orders of magnitude greater than WWSSN stations due to the extremely low lunar noise level. The SP instrument has a fixed response centered at 8 Hz, while the LP seismometers are switchable, with a broadband mode (essentially flat gain from 1 to 10 sec period) and a more sensitive but narrower peaked mode (maximum magnification at 2.2 sec). This latter response mode acts as a narrow bandpass filter and the resulting records are very sinusoidal in character. The SP seismometer at station 12 failed to operate, and the vertical LP instrument at station 14 has operated only intermittently. As a result, three-component processing is generally not feasible at ALSEP 14. In addition, the broadband response mode, obtained via a feedback loop, was initially unstable in several of the LP sensors, and only in the latter part of the seismic array operation was any broadband mode data obtained. Table 1-3 lists the periods of broadband mode operation for each seismometer. Thus, only limited long-period data is available, and the vast majority of seismograms used in this thesis were received in peaked response mode. All seismograms shown are so recorded unless stated otherwise.

The stations are located in a variety of tectonic settings. ALSEPs 12 and 15 are essentially on mare material,

12 between Mare Cognitum and Oceanus Procellarum and 15 on a
basalt embayment next to the lunar Appenines. ALSEP 14 is in
a transitional region (Fra Mauro complex) between mare and
highland, and ALSEP 16 is in the central highland area. This
last is the only true highland site. The seismometer-ground
coupling is different at each station. ALSEPs 12 and 15 are
the least sensitive, with nearly equal amplitudes on all three
LP sensors. Station 14 is a factor of 2-3 more sensitive, and
the recorded y-component of ground motion is typically 50%
larger than the x-component. This is probably due to the
effect of the central station connecting cable which runs
along the y-direction and acts as an extra moment arm (Dainty,
personal communication). ALSEP 14 is also unique in that the
dominant period on the LP seismograms is about 1 Hz, rather
than the 0.5 Hz peak response frequency that dominates at
other stations. This is possibly the result of a resonance
in the near-surface structure that acts as a strong filter.
Station 16 is the most sensitive, by a factor of 3-4 over
ALSEP 12, and again the y-axis predominates. In addition,
the ALSEP 16 records have the most "ringing" character of all
the lunar stations. The relative gains of the components at
each station are quantified in Table A3-1 and discussed in
Appendix 3, and Lammlein (1977) presents estimates of overall
relative station sensitivity.

As the passive seismic experiment proceeded, it rapidly
became apparent that lunar seismograms and seismic wave

propagation in general differed substantially from that ob-
served terrestrially. The ambient noise level is far lower
than on earth, generally around one du on the LP instruments,
or about 10^{-8} cm of ground displacement. All observed signals
are emergent with extended rise times ($\sim$10 minutes) and long,
ringing codas; a large event typically produces records with
an hour or more of observable seismic energy. In addition,
there are no coherent dispersed surface wave trains and only
little coherence between different components of ground
motion. Essentially no impulsive arrivals are observed.
These features can be observed on typical compressed-time
seismograms as shown in Figs. 1-3 to 1-5. Figure 1-3 contains
the records produced by the SIVB booster from Apollo 14 when
it was crashed into the moon, as recorded by the ALSEP 12 LP
seismometers. Figs. 1-4 and 1-5 are natural seismic events,
recorded by the three-component LP sensors and the SP ver-
tical seismometer, respectively. Expanded time playouts are
included in Appendix 1.

These characteristics of the lunar seismograms were
attributed to the combination of strong scattering and high
Q values (cf. Latham et al., 1971b; Strobach, 1970;
Berckhemer, 1970). This conclusion has been confirmed by
later research (Dainty et al., 1974a; Dainty and Toksöz,
1977; Nakamura, 1976, 1977b; Pines, 1973). The following
review is based on these papers; research on scattering
effects in terrestrial seismograms has also been done (Aki,

1969, 1973; Aki and Chouet, 1975; Wesley, 1965; Knopoff and Hudson, 1964).

The fundamental proposition is that strong scattering can be treated as the diffusion of seismic energy along an energy gradient. Energy is conserved, and by using the anisotropic diffusion equation, different horizontal and vertical diffusivities are allowed. A term corresponding to anelastic attenuation is included. Assuming an impulsive source, this equation can be solved to obtain the energy envelope (rise time and decay) as a function of the diffusivities and the quality factor Q. Such a treatment ignores the differences between body and surface, and shear and compressional waves, but this is in accordance with the observed three component seismograms in which the three traces are quite similar except for overall scaling factors. (See Figs. 1-3 through 1-5.) Physically this implies that in the scattering zone the different types of energy propagation reach a steady-state balance.

The applicability of this formalism to lunar seismograms has been tested by model seismology experiments (Pines, 1973; Dainty et al., 1974a). Briefly, the experimental apparatus consists of a metal plate (either rectangular or circular) with various configurations of holes drilled in it to represent scatterers. Transducers are attached on opposite edges, one acting as an impulsive source, and clay is molded around all edges to inhibit reflections. An example of the

resulting records as the scatterers increase in number and
size are shown in Fig. 1-6, and they bear close resemblance to
lunar seismograms. Additional experiments have shown that a
surficial zone of scatterers one skin depth (one wavelength)
thick suffices to destroy any coherent dispersed surface wave
trains. Quantitative solution of the diffusion equation for
the rectangular plate situation yields good agreement with the
observed energy envelopes in Fig. 1-6.

To transfer this theory to lunar seismograms, it is
necessary to have a model for the scattering situation. Such
a model is shown in Fig. 1-7, where a surficial layer of
intense scattering overlies a homogeneous, isotropic interior.
There are then three possible types of seismic wave propaga-
tion. "Near" surface sources, shown by 1, produce energy
that travels only through the scattering layer. As the
source-receiver separation increases, the rise time of the
signals should increase as the square of the distance.
Beyond a critical distance determined by the characteristics
of the scattering layer, the bulk of the seismic energy
arriving at the receiver will have bottomed in the non-
scattering interior, and the rise time should cease to
increase. These are "far" surface sources (2) and the energy
traverses the scattering zone twice. Interior sources, or
moonquakes (3) produce energy which only crosses one thick-
ness of scattering layer, and in fact by the principle of
reciprocity there should be a convolutional relationship

between far surface event and moonquake envelopes.

To test this model of lunar scattering, the energy envelopes of signals produced by impacting spacecraft sections (Saturn IVB booster and Lander Module) were calculated in a narrow frequency band. Theoretical envelope curves were computed using diffusion theory: as shown in Fig. 1-8, the agreement is quite good out to about 150 km. Beyond this distance, the observed rise time ceases to increase, indicating that the transition to "far" surface events has occurred, and producing a mismatch with theory. At greater distances, of course, the S and P wave envelopes separate due to different propagational velocities in the half-space, as seen in Fig. 1-5. A range of 150 km is equivalent to a bottoming depth of about 20 km, using the velocity structure given in Chapter 2, suggesting that (for 0.45 Hz seismic energy) the maximum effective scattering layer thickness is $\sim$20 km. The actual thickness cannot be determined uniquely, only its ratio with the vertical diffusivity. Finally, the predicted relationship between "far" surface event and moonquake energy envelopes does in fact hold.

The same sort of diffusion analysis has been applied to the seismic signals generated by the Lunar Rovers on various traverses, extending to a distance of 4 km from the respective ALSEP (Nakamura et al., 1976). The application was again successful, and the results implied that the scatterer size distribution is similar to the observed crater diameter

distribution, suggesting that for very close seismic sources,
the heterogeneities associated with surface topography are the
main scattering agent.

Thus a surficial strong scattering zone can account for
the observed features of lunar seismograms. The long decay
time is a consequence of the extremely high seismic Q: on the
close order of 5000. This value was used in making the fits
in Fig. 1-8. The lack of surface waves, lack of coherency
between components of ground motion, and emergent arrivals are
all the result of the diffusional process every lunar seismic
signal must undergo to reach the ALSEP receivers. The re-
maining questions concern primarily the exact size and depth
distribution of the scatterers, and thus their physical iden-
tification. The depth range of significant scatterer density
(for the seismic frequencies studied) appears to be between
1 and 20 km. The deeper bound comes from the "near" to "far"
surface event transition, while the shallower bound derives
from the fact that Hadley Rille does not noticeably modify
the envelope of seismic energy that crosses it (Toksöz et al.,
1974a). Various suggestions have been made concerning the
scatterers themselves, including cracks due to cratering,
surface and related subsurface heterogeneities, and irregular
powder layers (Strobach, 1970; Steg and Klemens, 1970; Warren,
1972; Gold and Soter, 1970; Berckhemer, 1970). The favored
hypothesis at this point is that cratering effects have
produced a complex series of cracks and fissures in a layer

of extremely dry, volatile-poor, outgassed rock. Below a

certain depth, 1 to 20 km, either no cracks were formed

because meteorite impact disruption did not extend that far

into the moon, or pressure and subsequent processes have

annealed or replaced most of the cracked material (Simmons

et al., 1973).

The actual mechanism producing the surficial scattering

zone is not crucial to this thesis, but the effects of the

diffusion process on the various seismic signals are. In

particular, they constrain which analysis methods are appli-

cable in attempting to determine lunar interior structure.

Since there are no observable surface wave trains, the many

methods available to interpret dispersion and amplitude rela-

tionships are of no use. The long, ringing codas from the

direct P and S wave arrivals effectively mask secondary

arrivals, eliminating a great deal of information. Finally,

the emergent character makes even simple P and S wave arrival

time measurements difficult.

Nevertheless, the direct wave arrival times are the

primary data set that can be extracted from the lunar seis-

mograms. As discussed in Chapter 3, the arrival times can be

inverted to obtain structural information and determine the

event locations. Using these locations, the seismograms can

be further processed by polarization filtering and record

section plotting (Appendix 3) in an attempt to observe secon-

dary phases. The rest of this chapter and Appendix 1 are

devoted to the process of obtaining the direct P and S wave
arrival times despite the scattering layer effects.

1.2   Selection of Events

There are five classes of seismic events that have been
recorded by the ALSEP seismometers. Thermal moonquakes are
very local sources around each station, and provide no struc-
tural information. Artificial impacts, caused by crashing
spacecraft sections into the moon, generate only enough energy
to illuminate crustal structure and the very top of the upper
mantle. Rays from these events that penetrate deeper are not
observable. Furthermore, the impacts occurred at known places
and times, so that travel times can be measured directly
instead of only arrival times. The analysis and resulting
crustal structure will be reviewed in Chapter 2. The last
three categories are natural lunar seismic events: meteorite
impacts, near-surface moonquakes (HFT's), and deep moonquakes.
It is with these events that this work is concerned.

Hundreds of meteorite impacts have been recorded by the
ALSEP network, including some of the largest seismic signals
yet observed. The apparent mass and time distributions of the
impacting bodies have been studied by Duennebier and Sutton
(1974b), Duennebier et al. (1975b, 1976), Dorman et al. (1978)
and Dainty et al. (1975b). Characteristically, the impacts
produce little shear wave energy since the source is theore-
tically purely compressional. What shear energy is seen

usually arrives gradually, and is probably the result of near-source conversions. P wave arrivals are similar to those observed from artificial impacts, indicating that the signals traverse the scattering layer at both source and receiver, and so the impacts apparently do not penetrate below the scattering zone. The SP seismometers generally record some energy from impact events, but especially the more distant ones are best observed on the LP seismograms; the SP records often just show an apparent increase in background level. Thus, typical meteorite impact seismograms show good P arrivals, weak and emergent S arrivals, and small signals on the SP instrument. These features can be observed in Figs. Al-1 through Al-5.

HFT's (high-frequency teleseisms) are much rarer events; less than 30 have been detected between 1971 and 1976 (Nakamura et al., 1974a; Nakamura, 1977a; Lammlein, 1977). They appear to be near-surface moonquakes. Their focal depths are shallow, between 0 and about 100 km. Several of the events are quite large, producing records comparable to the largest impacts. The time and space distribution of the HFT's is nearly random although Lammlein (1977) proposes that they occur in "belts" and are related to tidal stresses. As discussed in Chapter 3, the evidence for this is slim, and the HFT's probably release frozen-in stresses in the lunar crust or upper mantle.

Records from these events differ from impact seismograms in three significant ways. First, the P wave arrivals are

somewhat more impulsive, comparable to those from deep-focus
moonquakes. This implies that the HFT sources occur at least
below the bulk of the scattering zone, say at five to ten km
depth. Second, there are well-developed shear wave arrivals,
suggesting that the source is indeed a shear-dislocation type.
Finally, the SP records contain a great deal of high-frequency
energy, especially in the shear envelope, possibly implying
small fault areas. In sum, the HFT seismograms show distinc-
tive P and S wave arrivals and substantial high-frequency
energy. See Figs. A1-6 through A1-10 for examples.

The last and possibly most interesting natural lunar
seismic events are the deep-focus moonquakes, hereinafter
referred to simply as moonquakes. The numerous references
cited in the introduction will not all be repeated since many
of the results reported here on moonquake sources were ob-
tained in conjunction with this thesis. The moonquakes are
different from nearly all terrestrial events in that the
signals form groups of matching records. Each group contains
seismograms from events occurring months and years apart that
are nearly identical. A striking example is shown in Fig. 1-9
using events separated by nearly two years. As discussed in
section 1-3, several groups have signals that are of reverse
polarity relative to other signals in the same group; Fig. 1-9
shows two such records, and the top trace has been inverted
to match the lower. Phases correspond along the entire length
of the records, although some amplitude variations do occur.

The only feasible explanation for this phenomenon is that the events from a particular group are occurring at the same location. In particular, in order to produce nearly identical scattered wave trains the ray paths must be very nearly the same. Correlation measurements along the seismograms suggest that the source region for a matching group of events must be confined to well within a wavelength (5-10 km), and recent work (Nakamura, 1978) seems to imply that the sources are contained within one kilometer.

The time history of the events provide further clues concerning moonquake sources (Toksöz et al., 1977; Cheng and Toksöz, 1977; Lammlein et al., 1977). Fig. 1-10 shows the time history of the A1 focus or group of events, each bar representing the amplitude of an A1 moonquake. Some bars represent cumulative amplitudes of two or three events which occurred within a few days of each other. Negative amplitudes indicate events whose signals were of predominantly reversed polarity with respect to traces from the 1970-71 period. Three distinct periodicities, 27 day, 206 day, and 6 year, are apparent in Fig. 1-10. These correspond closely to various cycles and beat periods in the moon's orbital and librational motion, strongly suggesting that moonquakes are at least triggered by the tidal stresses caused by the earth's gravitational field. These periodicities are manifested at all other foci, and the tidal stresses probably provide a dominant part

of the energy released by the moonquakes. This conclusion is
further strengthened by the close coincidence of the moonquake
foci depth range (Chapter 3) with the zone of maximum tidal
stress within the moon.

The reverse polarity signals are an interesting puzzle.
These have been observed at two moonquake foci, the only two
that have remained active for more than three years at a time.
(Several foci have "turned off" for two to three year periods
and then become active again.) Cross-correlation analysis,
discussed below, has indicated that if a reverse-polarity
signal is observed at one station, the other stations receive
reverse-polarity signals also. However, the substantial pro-
portion of noisy records and the near-sinusoidal character of
the lunar seismograms prevent this from being a definitive
conclusion. As a result it is possible that total source
motion reversal is not required, and that slip vector and thus
radiation pattern rotation would be sufficient. The actual
source mechanisms of the moonquake foci have been studied by
comparing occurrence histories with calculated tidal stresses,
and by examining S/P amplitude ratios. The moonquakes do seem
to occur in "belts" which may imply some sort of common fault
plane orientation. It has also been suggested (Runcorn, 1977)
that the moonquakes cluster around mascon edges and so are
related to surface subsidence effects, but the great depth of
the moonquakes and the actually weak correlation between

mascons and epicenters argue against the idea.

In sum, the source characteristics of the moonquakes seem
to result from periodic tidal stresses acting upon a passive
system of weaknesses or release points in the lunar interior.
Indeed, except for HFT events and a possible small ambient
stress field contributing to the deep moonquakes, the moon is
a passive seismic system acted upon by impacting bodies, tidal
stresses, and thermal stresses, all of which provide the
energy for seismic sources. Both deep moonquakes and thermal
moonquakes (Duennebier and Sutton, 1974a) occur in repeating
groups, the former cycling with tides and the latter with
temperature. While such influences do occasionally occur in
terrestrial seismology (Cheng et al., 1978; Heaton, 1975;
Klein, 1976), the earth is clearly an active seismic environ-
ment, releasing 8 to 10 orders of magnitude more seismic
energy than the moon.

Returning to the main theme of this chapter, the deep
moonquake seismic sources and resulting seismograms are much
weaker than those from either HFT's or impacts. This is in
agreement with the small values of calculated tidal stress
components (less than one bar) and the extremely slow evolu-
tion of the repeating foci. In fact, six years of observation
has revealed almost no documented secular evolution of the
seismic sources. As a result of the small signal amplitudes,
the initial onset of P waves is often not well-observed. In

contrast, clear shear wave arrivals are common, in agreement with a shear dislocation type source which should produce about five times as much shear wave displacement as compressional. One of the largest moonquake signals as recorded on a horizontal LP seismometer at ALSEP 16 is shown in Fig. 1-11, and the S/P amplitude is roughly 5. (Stacked LP moonquake records plotted on an expanded time scale can be seen in Figs. A1-12 through A1-14, as discussed below and in Appendix 1.) The moonquakes are not well observed on the SP instruments, probably as a result of the low source stresses which would tend not to produce much high-frequency energy, combined with increased anelastic attenuation in the regions through which all deep moonquake signals must travel (Chapter 3).

The criterion by which seismic sources were chosen for the structural analyses were determined by the above characteristics and by the nature of the ALSEP array. Specifically, as mentioned before, an event must produce measurable arrival times at each of the three corners of the array. Stations 12 and 14 occupy one corner of this network 180 km apart, and although three stations, e.g. 12, 14, and 15, are theoretically sufficient to locate an event, in practice data from the above three stations would only weakly constrain the location along a particular path determined by the relative times at 15 and the 12, 14 station pair. Thus, arrival time measurements from ALSEPs 16, 15, and 14 or 12 are required.

In addition to a triangulation network, to locate a seismic event in space and time the number of arrivals (data points) must at least equal the number of unknown parameters in the location, and a seismic velocity structure must be assumed. Additional data points are required to extract any structural information, as is the purpose of this thesis. For events known to be on the surface, such as meteorite impacts, three space-time location parameters are needed (e.g. latitude, longitude, and origin time) and so only events with four or more measurable arrival times are useful in this work. Interior seismic sources, such as moonquakes, must also be located in depth, so five or more observable arrival times are required.

These considerations were applied to the lunar seismic data set to select from the large number of recorded events those which would be useful in determining the lunar structure. Both the primary event log (Duennebier et al., 1975a) and the selected seismic event catalogue (Latham, 1975) were used; they list all observed events up through the beginning of 1975, and identify them as meteorites, HFT's, or moonquakes. In addition, special listings and tapes of the major seismic events in late 1975, 1976, and 1977 were kindly supplied by Dr. Nakamura of the Galveston group. Since in general only the larger events were of use in this study, essentially all of the seismic data collected by the ALSEP

network that can provide significant structural information are used.

The initial selection of events from the catalogues was made using the amplitudes listed for each event at each station in order to reduce the number of candidate events to a reasonable size. (The amplitudes listed in the Galveston catalogues are measured on velocity seismograms, which are time-differentiated compressed versions of the original data. Empirical comparison shows that one Galveston mm equals roughly 2 du on the original displacement seismograms for the dominant frequency of 0.5 Hz on the LP records. Displacement du will be used herein, except when noted otherwise.) The seismograms of these candidate events were then examined individually to see how many measurable arrivals were in fact present, and final events were chosen on the basis of the criteria discussed above. In all cases it was found that the final number of useful events was far smaller than the number of candidate events, so it is unlikely that any useful events were overlooked in the initial culling by amplitude.

Meteorite impacts: Most impacts do not generate ob-servable shear waves, and the few S arrivals that are seen are generally too emergent to allow accurate arrival time measurement. Since at least four arrival times are needed for the structural analyses, it was initially required that a candidate event produce at least 10 du of signal amplitude at

each of the four stations. Thus potentially all four P wave

arrivals could be measured. Thirty-three events meet that

criterion out of the six-year operation of the full ALSEP net,

excluding those noted in the catalogues as containing timing

errors. Most of these thirty-three events are on microfilm

supplied by NSSDC, and so each was scanned visually to see if

the records actually contained at least measurable P arrivals.

The remaining few were transferred from magnetic tape to disc,

and then plotted (see Appendix 1). The primary requirement

for further consideration of the event was that a good-

quality, relatively unambiguous P pick be present at at least

a triangle of stations, in addition to at least one other pick

to make the necessary total of four. Only eight events passed

this selection process, indicating that the initial criterion

of 10 du of amplitude did not overlook any possibly useful

events. The eight events are listed in Table 1-4.

HFT's: In most of this work HFT events are assumed to

be surface events, and so only three space-time location

parameters are needed. As mentioned before, the HFT's appear

to be shallower than a few hundred km depth, and unfortunate-

ly most of them are far outside of the array. As a result,

it is nearly impossible to accurately constrain the depth of

an HFT, and so the depth was fixed at the surface. In

Chapter 3 this assumption is re-investigated, and the HFT

arrival time data suggest that the best average source

location is in fact at the surface. (Lammlein (1977) actually
attempted to determine the depths of individual HFT's from the
arrival times, and often obtained negative depths.)

Nevertheless, as discussed above, the HFT's do seem to be
beneath the bulk of the scattering zone, and this, combined
with their good shear wave generation, means that quite often
shear arrival times are measurable. Thus, although only 27
HFT events have been observed on the moon, all 22 that were re-
corded at a triangle of stations were considered as candidate
events. Again, the microfilm records supplemented by computer
plots were examined to identify measurable phases. Eight
events met the criteria for locatability and structural
usefulness, as listed in Table 1-5. As a result, there are a
total of 16 "surface" events used in this work.

Moonquakes: Roughly 1000 individual moonquake events
representing 68 repeating moonquake sources are listed in the
available catalogues. Recent reports (Latham et al., 1978)
have indicated that about 12 new moonquake sources have since
been identified. This data is not presently available, but
the additional foci are in all likelihood less active and
smaller than the original 68, since they were the last to be
successfully identified. As shown below, only 24 of the
original 68 are sufficiently well-observed for the purposes
of this work, and so again it is unlikely that any signifi-
cant information was missed.

The initial step was to punch all the moonquakes listed in the catalogue on cards, including the year and date of occurrence. A computer program sorted the events by focus and listed them in chronological order for each focus, as shown in Table A1-12. Then, for each focus, the catalogued amplitudes at each station for each event were listed along-side the year and day, providing a complete picture of the activity at each focus. Thirty-nine foci were immediately eliminated because no measurable amplitudes were recorded from any event at those foci at one or more of the triangle corners, usually ALSEPs 15 or 16.

The events from the remaining 29 foci were then plotted and examined. As discussed in Appendix 1, the individual moonquake event amplitudes are generally too small to allow direct arrival time measurement. However, since the events occurring at a particular focus produce essentially identical records except for random noise, they can be stacked together to enhance the signal-to-noise ratio (by a factor of about $\sqrt{n}$) producing one stacked record (three LP component traces) at each station for each moonquake focus. This effectively creates an artificially large event that represents and summarizes all the available data from a given moonquake focus; thus each moonquake source is treated as a single seismic event.

These stacked records were then examined for measurable arrival times, and an additional five foci were eliminated

because less than four picks were available. Two of the re-
maining 24 foci only had four measurable arrival times, which
as discussed before is sufficient for event location but does
not provide any redundant data from which to extract struc-
tural information. Nevertheless, they were retained in the
final data set because the stacking effort had already been
invested and the distribution of moonquake locations is
interesting in itself, in terms of both moonquake sources and
lunar structure. Table 1-6 lists the 24 foci, along with the
reference time of the single event to which all events at a
given focus were stacked (see Appendix 1).

The final data set thus contains 8 meteorite impacts, 8
HFT events, and 24 deep moonquake foci, for a grand total of
40 seismic sources, listed in Tables 1-4 through 1-6. The
seismograms are discussed and presented in Appendix 1. These
represent all the seismic data presently available to the
M.I.T. group that can provide significant structural infor-
mation, excluding the artificial impacts to be discussed in
Chapter 2. Some data remains to be processed at Galveston,
but all major events have already been sent to M.I.T.
(Nakamura, personal communication).

1.3 Arrival Time Measurements

As a result of the scattering layer effects, the primary
data set that must be used to locate the seismic events and

determine interior structure consists of the direct P and S wave arrival times. At this point it is appropriate to justify the assumption that the two distinct envelopes present on most lunar seismograms do in fact represent direct P and S. First, the artificial impacts are seismic sources with known locations and origin times, and so travel times for the two envelopes can be measured. The times are in agreement with "reasonable" compressional and shear wave seismic velocities, and any other assumption would entail a more complicated crustal structure. Second, the natural events produce envelopes that are consistent with this assumption at a wide range of distances. Third, when redundant arrivals are available over the minimum number required for focal location, they appear at times appropriate for P and S. Finally, the S phase is generally strongest on the horizontal components, and the P arrival is often, but by no means always, best observed on the vertical traces. This is appropriate for waves arriving nearly vertically, which is the case on the moon due to the very low velocity surface layers. Of course, due to the uncertainties of a limited network, unknown natural event locations, and unknown interior structure, it is not possible to state unequivocally that the appropriate interpretation of the dominant phases has been made. Nevertheless, all evidence to date, including that developed in this thesis, is consistent with and provides reasonable results from this assumption.

The effect of the scattering layer is to receive a relatively impulsive seismic phase and spread it out into a long wave train. Signals from surface sources go through this process twice. The resulting signal at the seismometer theoretically has a small but finite onset, as the packet of energy that traversed or "diffused" through the scattering layer without colliding with a scatterer arrives first. This initial amplitude depends on the length of the travel path of the arriving ray through, and the "mean free path" (or equivalently, the diffusivity) of the scattering zone. As time proceeds, more and more energy packets arrive that have been scattered a few times, many times, and so on. As a result, the initial arrival as the signal emerges out of the background noise or the P wave coda is often quite difficult to measure.

To partially remedy this situation, the raw seismograms have been supplemented with polarization-filtered versions of the same records, as described in Appendix 3. This filter enhances the rectilinear particle motion expected to be present in the initial relatively unscattered arrival relative to the later scattered energy which in general will have ellipsoidal particle motion. Picks are made from both the raw and filtered records, but since the filter is non-linear and susceptible to noise, the original seismograms are always checked to confirm any measurements made on the filtered

records.

It is clear from the above discussions that the arrival time picks on lunar seismograms often require judgement. Published arrival times for the same events measured on the same seismograms often differ by as much as minutes. Every effort has been made in this thesis to remove as much of the arbitrary judgement as possible, and to make it clear when and how judgement is involved. First, uncertain and ambiguous arrival time measurements are discarded completely, and from the final data set a group of "most confident" arrival times are used as a second data set to confirm structural results that are obtained from the original data. Second, strict procedures as described below are followed in picking and measuring arrival times, using previously developed criteria. The rest of this section will outline the general methodology used in making the picks, discuss the considerations specific to each class of natural events, show some typical seismograms, and present the final arrival time data set. Appendix 1 describes the lunar seismograms themselves, the individual picks, and the process culminating in the final data set. Thus, although judgement is involved, the points where it enters the process are made explicit and so the data and results herein are readily reproducible.

In the following discussion, three different plotting scales are referred to. Expanded plots are drawn at 2-5

inches per minute, allowing accurate arrival time measurement to within 0.1-0.3 seconds. In addition, only three traces are plotted per 10 inch width, so that the amplitude scales are large enough to see 1 du of ground motion, ensuring that no small arrivals are missed. Compressed scale playouts are plotted at 5 inches per minute; they are mostly useful for observing energy envelopes. Finally, reduced scale plots are intermediate, either 0.6, 1.1, or 1.2 inches per minute. These contain records from all four stations plotted on a single page and lined up temporally. Thus they are useful in confirming arrival time measurements made on other records and in examining the relationship between arrivals at different stations. Examples of the first two plot types for the various classes of events are shown with this chapter; a complete set of reduced scale plots are shown for all events in Appendix 1.

The emergent nature of both P and S arrivals is the primary difficulty that must be overcome in making arrival time measurements. As the phases emerge from either the background noise or the P wave coda (often quite large on surface event records), commonly several (between one and three) possible "onsets" of the arrival can be seen. (This is shown in Figs. 1-12; they are described below.) It is usually clear that the arrival begins at one of these points rather than just anywhere in between; otherwise the pick is

not used. In other words, the arrival time possibilities are nearly always distinct, rather than continuous which would make accurate arrival time measurement difficult. These possible onsets may be separated by as much as 30 or 40 seconds, and are often measured on different traces at the same station, i.e. the three LP and SP records. All reasonable onsets are measured and considered, and every attempt is made to observe the earliest possible onset on each trace in order to avoid missing the small first arrival. There is of course the possibility that all first arrivals are missed as their true beginnings may well be below the ambient noise level. Three observations argue against this. First, larger events often produce first arrivals that jump abruptly over the ambient noise level. Second, redundant phases often arrive within a cycle (two seconds) or less of expected. Finally, as shown in Fig. 2-6, theoretical seismograms reproduce the first several cycles of the arrival onsets quite well (apart from a uniform scale factor), indicating that at least the initial few energy packets are free from significant scattering effects. In addition, if all arrivals from a parti- cular event were missed by a roughly constant amount of time, then the primary effect would only be to make the derived origin time late by that much time. This would have no effect on the location or structural results, and so with care in looking for the earliest onsets, there should be no serious effects.

Once the best options for the P and S arrivals at all
four stations from a particular event have been measured and
listed, they are then compared for consistency. The primary
criterion is for rough agreement of relative S and P times at
different stations, especially 12 and 14. For instance, if
the S arrivals are 100 and 120 sec at stations 12 and 14
respectively, then the 14 P pick should be reasonably close
to 12 seconds later than the P arrival at station 12. Now
several assumptions are involved in this test. First, it is
assumed that the P and S waves travel identical paths. This
will be true only if the Vp/Vs ratio, or equivalently
Poisson's ratio, stays constant over the entire ray path.
Second, an average Vp/Vs ratio of 1.73, corresponding to a
Poisson's ratio of 0.25, has been used. Finally, this value
must be the same for all source-station ray paths, which is a
weak requirement of lateral homogeneity. Based on previous
structural studies, all of these assumptions are probably
reasonable in an approximate sense, but the key to using them
is not to inadvertently discard valid data which one needs in
order to properly find average structural properties. In
addition, later work may be able to detect systematic lateral
variations from such "inconsistent" data.

Therefore this criterion was applied in the following
way. If, 1) the suspected pick (say S) differed from the
expected time by at least 30 seconds, 2) the other three

picks involved were well observed and constrained, and 3) some
evidence for the true arrival being in the expected place
could be seen, then the possible pick was rejected and another
option, if any, was considered. A careful watch was kept to
insure that no trend of discarded picks emerged, which might
represent a plug of differing material beneath one station, or
a particular region of anomalous velocity deeper in the moon.
No such pattern was observed, and ultimately the primary use-
fulness of this criterion was in an instructive sense, illus-
trating the various manifestations of P and S wave envelopes
at the different stations from different classes of events.
In sum, this criterion was useful in eliminating some pick
alternatives, and care was taken not to discard valid data.

The remaining picks were then arranged into groups of
arrival times for each focus. Typically, each focus would
have between one and about ten different sets of up to eight
(four P and S) arrival times representing possible combina-
tions of picks that had been made. For instance, two possible
12 P times might be considered, and arrival time sets with
and without a weak 16 S pick would be tried. The different
options for each focus and the details of selecting the "best"
set of arrival times are listed and described in Appendix 1.
Overall, the method consisted of using each set in turn for a
particular focus to locate that focus. (The location method
is described in Appendix 4.) A reasonable velocity model was

used, and for each set of picks a best location in a least-squares sense was found, along with the associated least-square error. The velocity model was then changed, typically increasing and decreasing mantle Vp and Vs systematically so that a total of nine velocity models were considered (e.g. Vp = 7.0, 7.5, 7.8 and Vs = 4.0, 4.4, 4.8). For each model new best locations and errors were found, and put into a 3 x 3 array for each arrival time set.

The purpose of using a wide range of velocity models was to insure that arrival time sets requiring different average velocities from those of the selected model were not eliminated. Both two-layer and single-layer mantle models were used, with an assumed crustal structure (Chapter 2), and the velocity ranges for P and S waves were designed to cover all reasonable average velocity values, based on previous work and the measured seismic velocities in rocks of model lunar composition. As the work progressed, it became apparent that the residuals for a particular arrival time set would all follow a similar pattern; if one value was overly large relative to those from other arrival time sets, then all the residuals from that set, regardless of the velocity model, would be overly large. Thus each residual set, or grid, could be characterized as a whole relative to other sets, making it unnecessary to use a specific model to compare the arrival time data sets. Indeed, this would have produced a

very biased data set. The type of model used, i.e. one or two
constant-velocity mantle layers, is consistent with previous
work and sufficient for data selection purposes (see Chapter
3). The effects of including velocity gradients or transition
zones are negligible in the gross comparisons discussed below.

The arrays for the possible pick groups for each focus
were thus compared, with reference to the seismograms as
needed, in an effort to identify the "best" arrival time set.
Again, a specific procedure was followed. First, sets that
required locations outside the moon were rejected. Second,
groups of picks that produced overly large residual arrival
time errors were rejected on the grounds that at least one
arrival time was grossly inconsistent with any location. This
may seem to be an arbitrary criterion, but in practice it is
not. "Large" residuals were considered to be greater than
about 100 seconds^2 or so (standard deviation of the arrival
time data) which would imply an average arrival time misfit
of about 10 seconds. Invariably there were other pick groups
for the same focus that could be located with much smaller
errors, and in a sense there was a definite bi-modal distri-
bution in error magnitudes. It could be argued that the
groups with large residuals in fact were the correct values
and represented lateral and local heterogeneities and radi-
cally different velocity models, but since other possibilities
from each focus were always available which produced smaller

residuals and were therefore apparently in agreement with
lateral homogeneity and the wide range of velocities allowed
in the grid, it did not appear to be justified to assume the
greatly increased structural complexity that would be required
to satisfy each group of inconsistent arrival times. Further-
more, the entire structural problem would then have far too
many degrees of freedom and a reasonable analysis procedure
based on only four stations would be impossible. It must be
emphasized that at this point in the arrival time selection
procedure all the alternative sets are equally well-defined
on the seismograms, and the idea is to choose among equal but
distinct possibilities.

Finally, the few remaining alternative sets are elimina-
ted in a variety of ways. In general pick groups with smaller
residual errors are favored; sets that appear to prefer less
likely velocity structures, such as very high or low Vp, are
eliminated if other sets favor more reasonable velocity
values. Often, two arrival time sets will differ only in one
pick which varies by less than four or five seconds; and thus
the locations and residuals are nearly identical. In this
case the two possible picks are simply averaged, giving a
reasonable compromise between the two possibilities. Occa-
sionally the same phenomenon will occur when two picks are
more significantly different, so that the choice will not
dramatically affect any structural solutions, and after

looking again at the seismograms, one is simply chosen ad hoc. In the end, a unique set of arrival time measurements for each seismic source is obtained.

This elaborate selection procedure is made necessary by the unique nature of the lunar seismic data and the paucity of stations. Every effort has been made to follow a clear-cut selection procedure established a priori and laid out explicitly, following the most advantageous aspects of the seismograms. Appendix 1 describes its systematic application to the lunar data. Unfortunately, it is always possible that erroneous data has been retained at the expense of correct data, and no amount of effort on the present data set can totally rule out that possibility. Nevertheless, the method outlined above minimizes the probability of including incorrect arrival times, and hopefully any remaining errors will be averaged away in the full structural solution. Based on visual estimates, the a priori error in each arrival time measurement is considered to be about $\pm$ 2 cycles, or $\pm$ 4 seconds, on average for each pick. The following paragraphs outline the specific procedure followed for each set of the lunar data, tailored from the general procedure above to accommodate the special characteristics of each type of natural seismic event; examples of expanded records are shown to illustrate the arrival time features described above.

Meteorite impacts: Since these sources are on the sur-
face, the signals must traverse the scattering layer twice and
the resulting arrivals are the most emergent of any lunar
seismic waves. This, combined with the poor shear wave gener-
ation, make impact seismograms the most difficult to analyze.
The P wave arrivals are measured primarily on the expanded-
scale raw and filtered three-component LP seismograms, with
reference to the expanded SP records for consistency whenever
the impacts are close enough and large enough to yield sub-
stantial SP energy at the seismic stations. Fig. 1-12a shows
an example of expanded scale LP filtered records for a
meteorite impact; the P wave arrival was measured as marked.
The general time of S is first obtained by extrapolating
backwards to zero amplitude the shear wave envelope, if any,
developed on the expanded SP record or the LP compressed
playout seismograms. The SP envelopes when available are more
useful even though only the vertical component of ground
motion is recorded because of the shorter rise time relative
to LP records (this feature is not entirely understood in
terms of the scattering layer, although some work is in
progress (Malin, 1977). As mentioned before, this is probably
due to a decreasing scatterer thickness with depth, making the
effective scattering layer thinner for high-frequency energy.
After polarization filtering the LP seismograms, both filtered
expanded-plot and raw reduced-scale LP records are searched

for candidate S arrivals in the region indicated by the enve-
lopes. Without the SP or LP envelope studies, most of the S
arrivals would be nearly impossible to locate on the expanded
seismograms. Even with this procedure, only a few reliable S
wave arrival times are obtainable. One such is exemplified in
Fig. 1-12a. The selection of the best impact source arrival
time sets is detailed in Appendix 4, and the resulting data
set is presented in Table 1-4.

HFT's: These events have relatively more impulsive
arrivals than impacts, and produce a large amount of shear and
SP energy. Accordingly, P picks are made on expanded SP, LP
raw, and LP filtered plots simultaneously, producing P arrival
times that are often well-constrained. In order to minimize
the effects of the obscuring P wave coda, the S picks are made
on LP expanded scale filtered records, and the SP shear enve-
lope and reduced scale LP raw records are checked for con-
sistency. In all, the large HFT seismograms are the easiest
on which to make arrival time measurements. Of course, as
seen in Figs. A1-6 through A1-10, some of the HFT's used in
this study are quite small, and the picks are more difficult.
Fig. 1-12b shows a raw ALSEP 14 LP record; only the x compo-
nent (horizontal) is operating properly in this time period.
As can be seen, several possibilities for the S arrival are
marked. Ultimately, none were used due to the ambiguity of
the initial onset. The final best arrival time sets are shown
in Table 1-5.

Moonquakes: The first step in analyzing the deep moon-
quakes is to stack all the events from a particular focus
together so as to enhance the signal-to-noise ratio. Only
the three-component LP records are stacked; little SP energy
is recorded from the moonquakes. The individual moonquake
events are nearly all so small that only the S arrival is
clearly observable; the P wave only rises above the ambient
noise and station sensitivity level in later portions of the
P coda. The purpose of the stacking is primarily to recover
the initial P arrival, although the S wave is also enhanced.
Without the advantage of multiple events, most of the moon-
quakes could not provide any redundant phases for structural
information. The stacked records are passed through the
polarization filter; picks are made primarily on the raw
expanded scale stacked records and then confirmed on reduced-
scale filtered records. Fig. 1-12c shows a typical stacked
LP record from a moonquake focus, and two alternative P
arrivals are marked; the earlier one was ultimately chosen.
The relatively impulsive nature of the moonquake arrivals,
however, makes the filtered records mostly useful in searching
for secondary phases. The final best arrival time sets are
listed in Tables 1-6 and 1-6a, and the relative scarcity of
measurable P picks is clear. (The reference times in Table
1-6a are those of an arbitrary event from each focus chosen
to be the time basis for all events from that focus.)

Thus the complete list of events and direct P and S wave arrival times are as shown in Tables 1-4 through 1-6. As mentioned before, this constitutes the primary data set. The SP seismograms and LP filtered records will also be used to search for secondary phases, shadow zones, and amplitude systematics. Details pertaining to the data are included in Appendix 1, along with reduced plots of all records.

Table 1-1

Locations, separation, and installation date of ALSEP seismometers.

Station	Location	Separation (km) 12	14	15	16	Installation Date
12	3.04°S,23.42°W	--	181	1188	1187	19 November 1969
14	3.65°S,17.48°W	181	--	1095	1007	5 February 1971
15	26.08°N,3.66°E	1188	1095	--	1119	31 July 1971
16	8.97°S,15.51°E	1187	1007	1119	--	21 April 1972

Table 1-2   61

Orientation of long-period horizontal seismometers.

Station	Azimuth of horizontal instruments	
	x	y
12	180°	-90°
14	0°	90°
15	0°	90°
16	334.5°	64.5°

Note: Upward ground motion is positive vertical, and the above azimuths are positive x and y. The coordinate system is left-handed.

Table 1-3

Broadband response mode operation period.

Station	Period in broadband response mode
12	10/16/74-4/9/75; 6/28/75-3/27/77
14	none
15	6/28/75-3/27/77
16	6/28/75-3/27/77

Table 1-4

P and S wave arrival times at all four stations for
meteorite impact events.

Reference		Time		Arrival Times (sec relative to reference time)							
Yr	Day	Hr	Min	12P	14P	15P	16P	12S	14S	15S	16S
72	134	8	47	25.2	12.5	114.3	120.6	62.7	36.8	217.0	--
72	99	21	57	55.0	63.8	-13.7	16.7	--	--	--	--
72	213	18	9	136.4	118.1	-8.7	139.5	285.5	--	35.5	--
72	324	18	24	87.6	94.3	21.3	131.3	284.2	--	--	--
75	102	18	15	111.8	95.8	40.4	-15.5	292.0	--	--	70.5
75	124	10	5	1.3	15.5	77.5	53.6	--	--	410.0	--
76	25	16	10	-8.9	--	94.5	110.7	133.5	--	312.2	--
77	107	23	35	6.9	18.3	127.9	126.5	--	--	--	--

Table 1-5

P and S wave arrival times at all four stations for HFT events.

Reference		Time		Arrival Times (sec relative to reference time)							
Yr	Day	Hr	Min	12P	14P	15P	16P	12S	14S	15S	16S
73	72	8	1	34.1	35.9	99.7	27.8	272.0	--	--	259.4
73	171	20	25	-5.0	6.5	85.7	138.5	125.3	--	--	352.5
74	192	0	51	78.5	65.3	-3.5	-9.7	--	--	--	--
75	3	1	46	33.6	51.3	60.5	127.5	269.0	--	--	453.0
75	44	22	5	--	-1.8	129.5	89.6	--	47.8	265.0	197.0
76	4	11	21	--	--	-4.9	87.7	--	293.8	82.0	252.0
76	66	10	15	50.8	53.3	-20.8	--	202.0	208.7	75.8	286.0
76	68	14	43	--	24.2	141.5	74.9	98.8	70.3	272.1	--

Table 1-6

P and S wave arrival times at all four stations for moonquake events.

Focus	Reference Time				Arrival Times (sec relative to reference time)							
A	Yr	Day	Hour	Min	12P	14P	15P	16P	12S	14S	15S	16S
1	75	86	18	47.5	8.1	10.2	73.0	58.3	99.8	103.0	212.9	193.3
15	72	190	18	12	--	--	54.3	--	164.4	152.2	180.8	136.5
16	71	260	11	16	--	9.8	6.0	6.2	129.0	127.2	119.3	120.0
17	72	284	21	21	1.5	--	-10.8	--	102.2	100.9	85.1	172.6
18	71	298	14	33	--	75.3	31.2	45.2	231.7	215.0	135.0	161.4
20	72	136	17	21	--	-10.3	-1.8	33.3	99.3	104.1	110.7	178.2
27	71	290	14	33	--	--	34.6	--	208.5	192.8	140.1	168.5
30	73	154	1	27	--	22.8	46.0	--	114.3	123.9	162.0	207.2
31	72	161	7	52	--	--	--	3.8	--	137.0	113.0	126.2
32	72	148	5	55	--	--	18.2	34.4	--	183.1	105.4	131.5
33	72	285	19	40	--	51.2	19.5	8.7	--	--	228.0	211.7
34	72	166	18	36	--	--	40.7	--	141.1	137.7	146.0	159.8

Table 1-6 (Cont'd)

Focus A	Reference Time Yr Day Hr Min	Arrival Times (sec relative to reference time)							
		12P	14P	15P	16P	12S	14S	15S	16S
36	72 128 15 12	--	87.6	--	98.8	--	245.2	171.2	268.8
40	73 42 16 46	45.3	--	--	61.5	136.4	133.2	177.4	169.0
41	73 123 15 43	--	27.0	--	--	116.5	134.4	149.6	247.1
42	74 58 6 25	39.3	46.1	--	--	160.2	172.3	193.0	262.3
44	74 58 2 56	--	102.3	32.4	--	289.8	266.2	162.8	230.0
45	74 124 22 10	14.6	14.4	--	--	122.2	121.7	220.2	200.1
46	73 303 1 0	41.6	44.3	104.6	--	136.2	142.7	242.3	223.8
50	73 205 14 57	23.4	30.5	--	--	131.4	144.5	207.2	257.6
51	74 49 8 37	--	61.9	36.2	37.2	193.6	171.8	135.3	131.0
56	73 163 21 17	--	51.8	--	--	119.4	135.3	183.8	227.3
61	75 58 6 16	--	-3.1	--	--	--	149.0	51.0	74.0
62	75 167 11 11	--	79.4	27.3	53.4	279.5	266.6	151.4	215.7

Figure Captions

Fig. 1-1. Location map of the ALSEP seismic stations, shown
as squares and labeled A-12, etc. The triangles and
open circles represent impact points of the LM and SIVB
spacecraft sections respectively (from Toksöz et al.,
1974a).

Fig. 1-2. Seismometer reponses as a function of frequency.
Curves for the short-period vertical instrument and the
two response modes of the three-component long-period
seismometers are shown (from Toksöz et al., 1974a).

Fig. 1-3. Compressed-playout LP three-component seismograms
produced by the SIVB impact recorded at ALSEP 12.
Vertical scale is 1083 du between the trace centers.
Component orientations are given in Table 1-2 (from
Toksöz et al., 1974a).

Fig. 1-4. Moonquake LP seismograms recorded at ALSEP 12.
Vertical scale is 22 du between trace centers (from
Toksöz et al., 1974a).

Fig. 1-5. Meteorite impact (Day 25, 1972) recorded at ALSEP 15
on the SPZ seismometer. Scales as marked.

Fig. 1-6. Effects of scattering holes in a metal plate. As
shown schematically, holes increase in number and size
from top to bottom, the resulting model seismograms
shown at right (from Dainty and Toksöz, 1977).

Fig. 1-7. Schematic (not to scale) illustration of relation of
lunar seismic sources to scattering layer (from Toksöz
et al., 1974a).

Fig. 1-8. Energy envelopes of artificial impacts recorded at
ALSEP 12. Energy is calculated in a narrow spectral
window around 0.45 Hz in 51.2 sec intervals, and
plotted as a function of time on semi-log paper.
Dashed curves are theoretical fits; see text (from
Toksöz et al., 1974a)

Fig. 1-9. Comparison of Y components of groun motion recorded
at ALSEP 16 from two matching A1 moonquakes. Vertical
scale ~20 du/in.

Fig. 1-10. Time history of the A1 moonquake source. Bar
heights are event amplitudes listed for ALSEP 12; some
bars represent cumulative amplitudes listed for 2-3
events occurring within a few days of each other.
Negative amplitudes represent reverse polarity events.

Fig. 1-11. Compressed plot of an A1 moonquake recorded in the
Y component of the ALSEP 16 seismometers.

Fig. 1-12 Sample expanded-scale plots for a meteorite
impact, HFT, and stacked deep moonquake event, showing
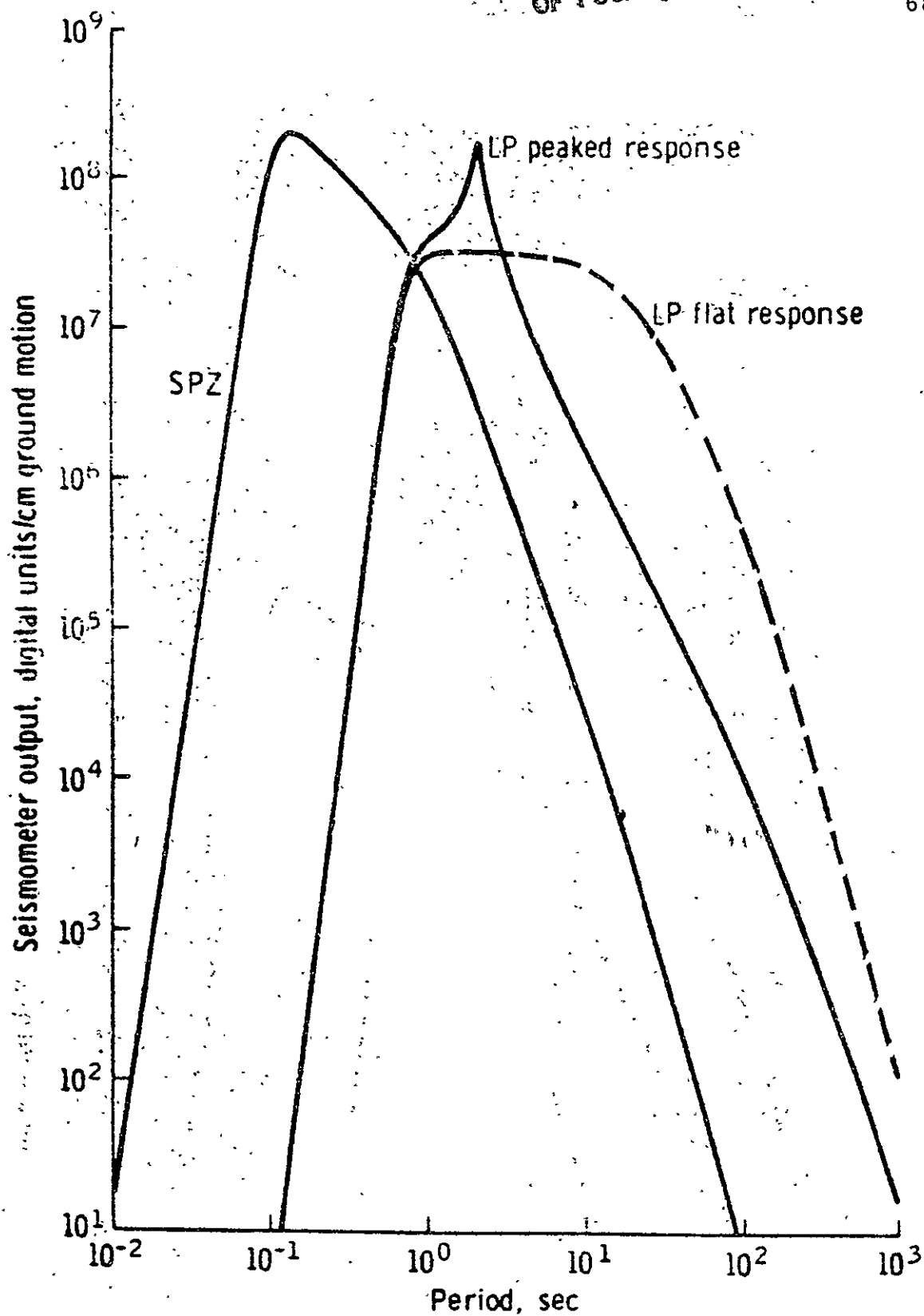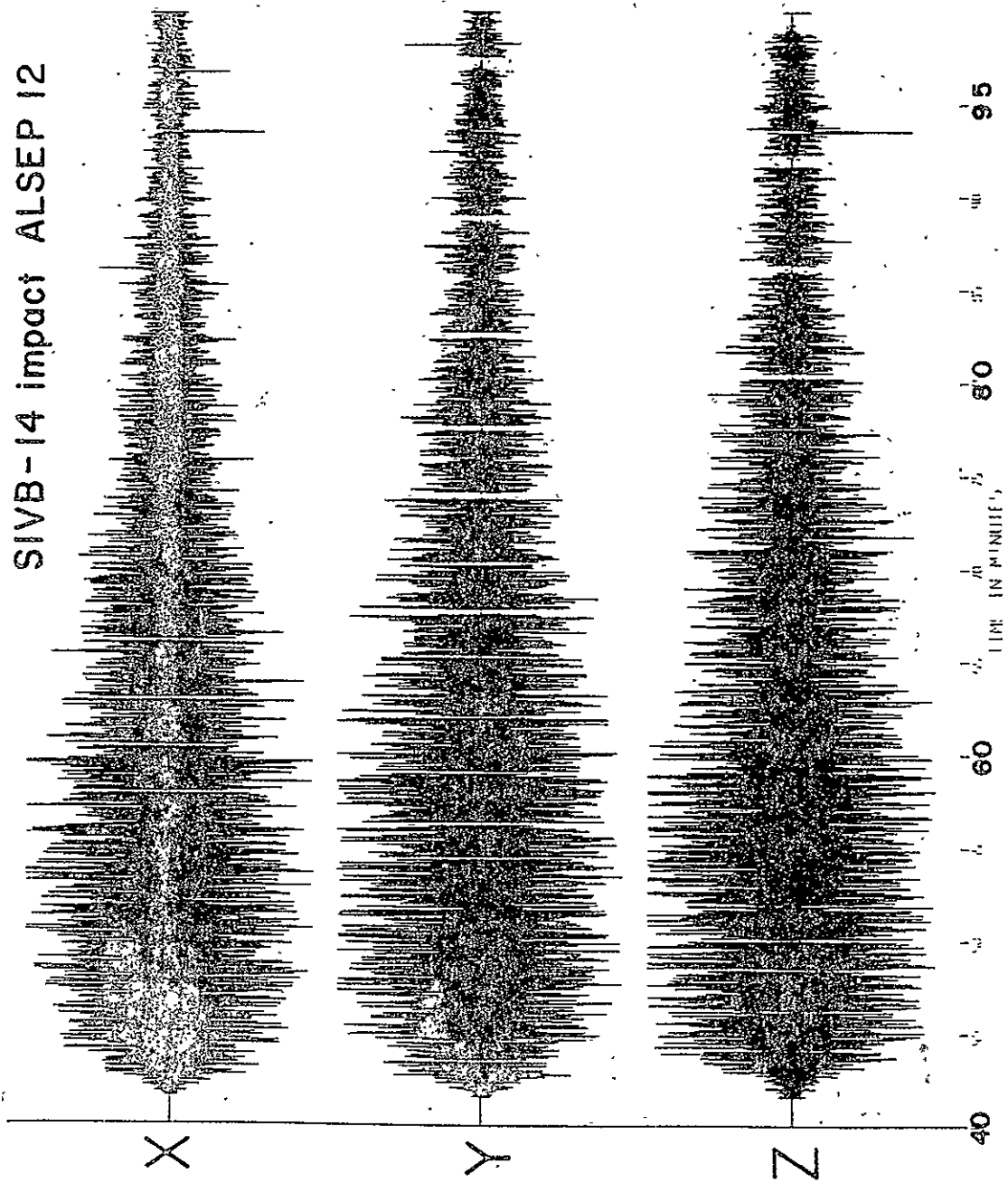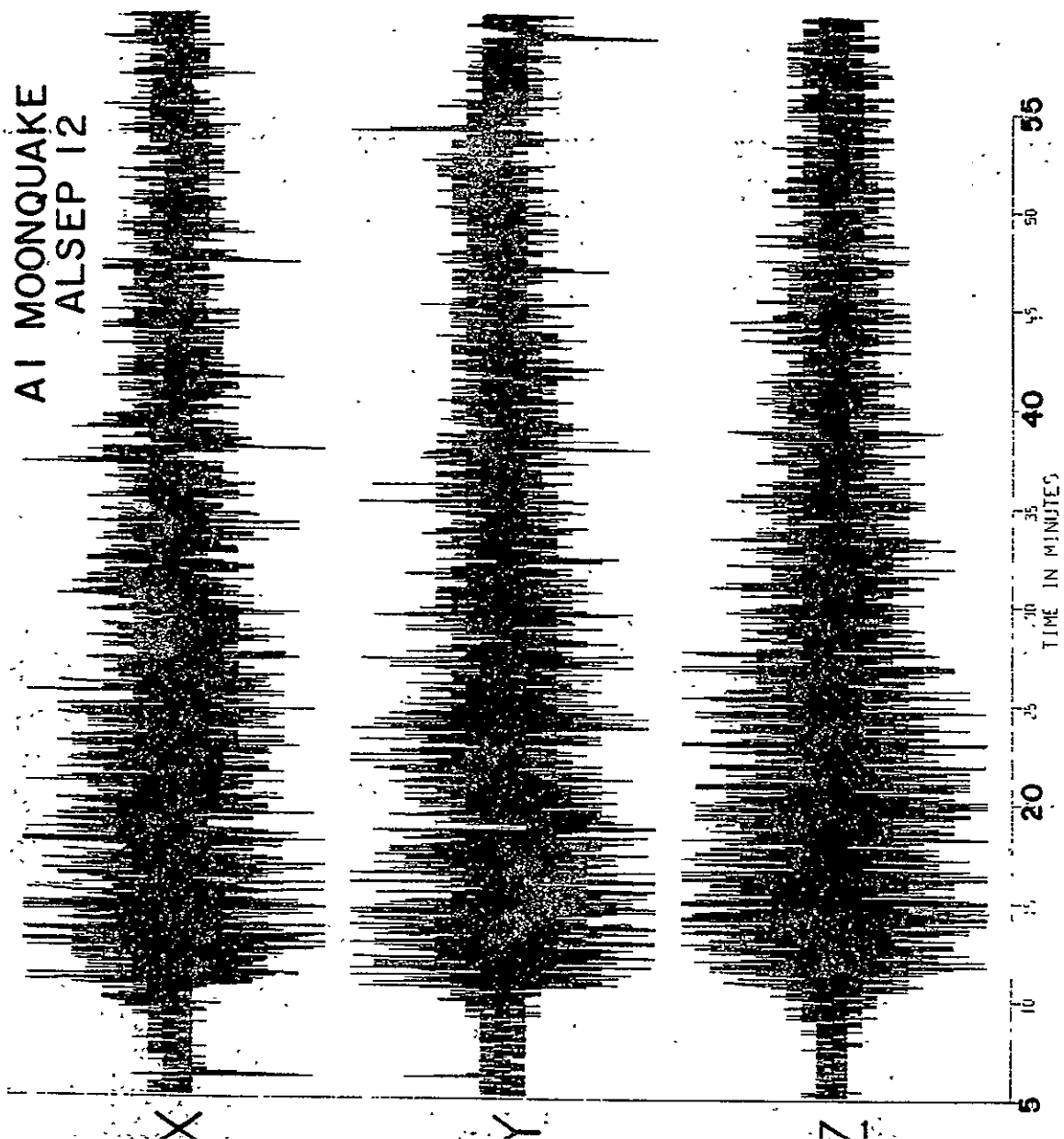alternative sets of arrival time picks.

Figure 1-1

Figure 1-2

Figure 1-3

A I MOONQUAKE
ALSEP I2

X

Y

Z

TIME IN MINUTES

Figure 1-4

METEOR IMPACT DAY 25,1972   ALSEP 15

Figure 1-5

a

b

c

d

Figure 1-6

SEISMOMETER

Figure 1-7

73

ALSEP 12
FREQ. 0.45 Hz
——— THEORY

LM 12
Δ = 73 km

10 dB

LM 14
Δ = 114 km

S4B 16
Δ = 132 km

S4B 14
Δ = 172 km

TIME (MIN)

0   20   40   60
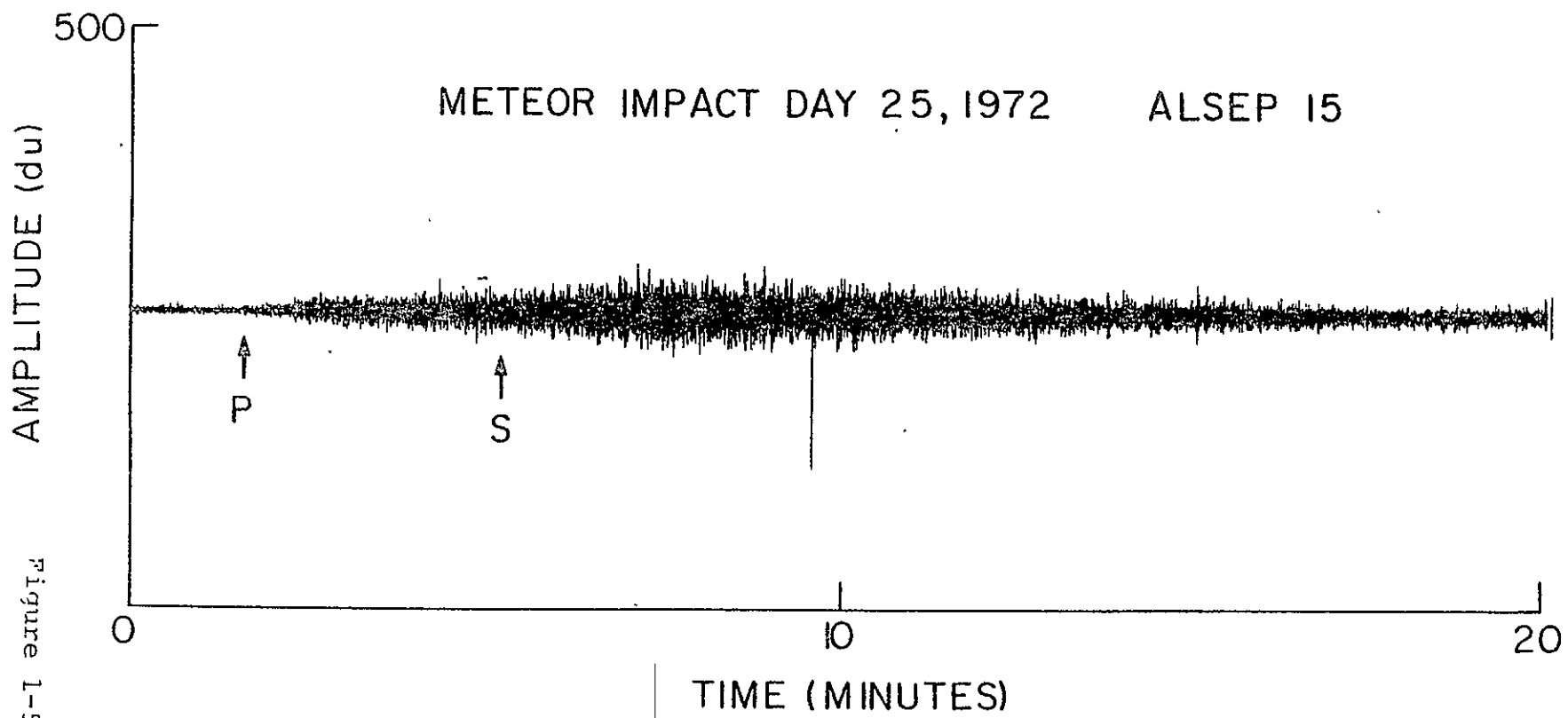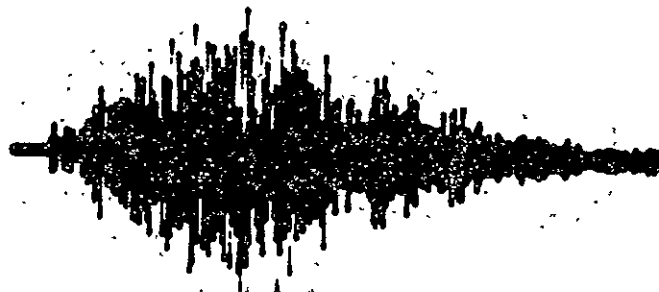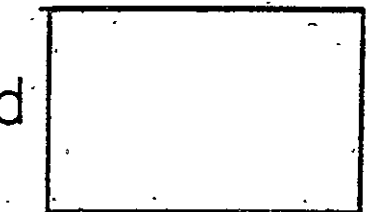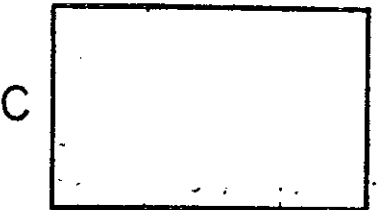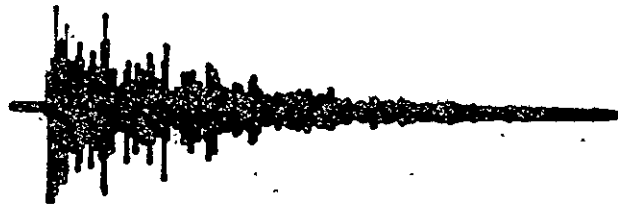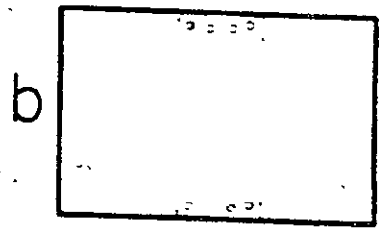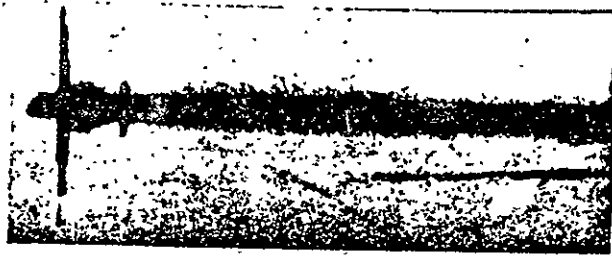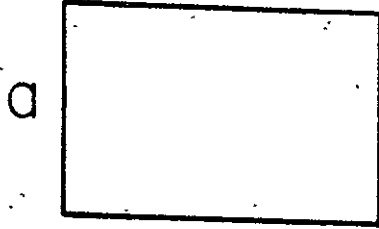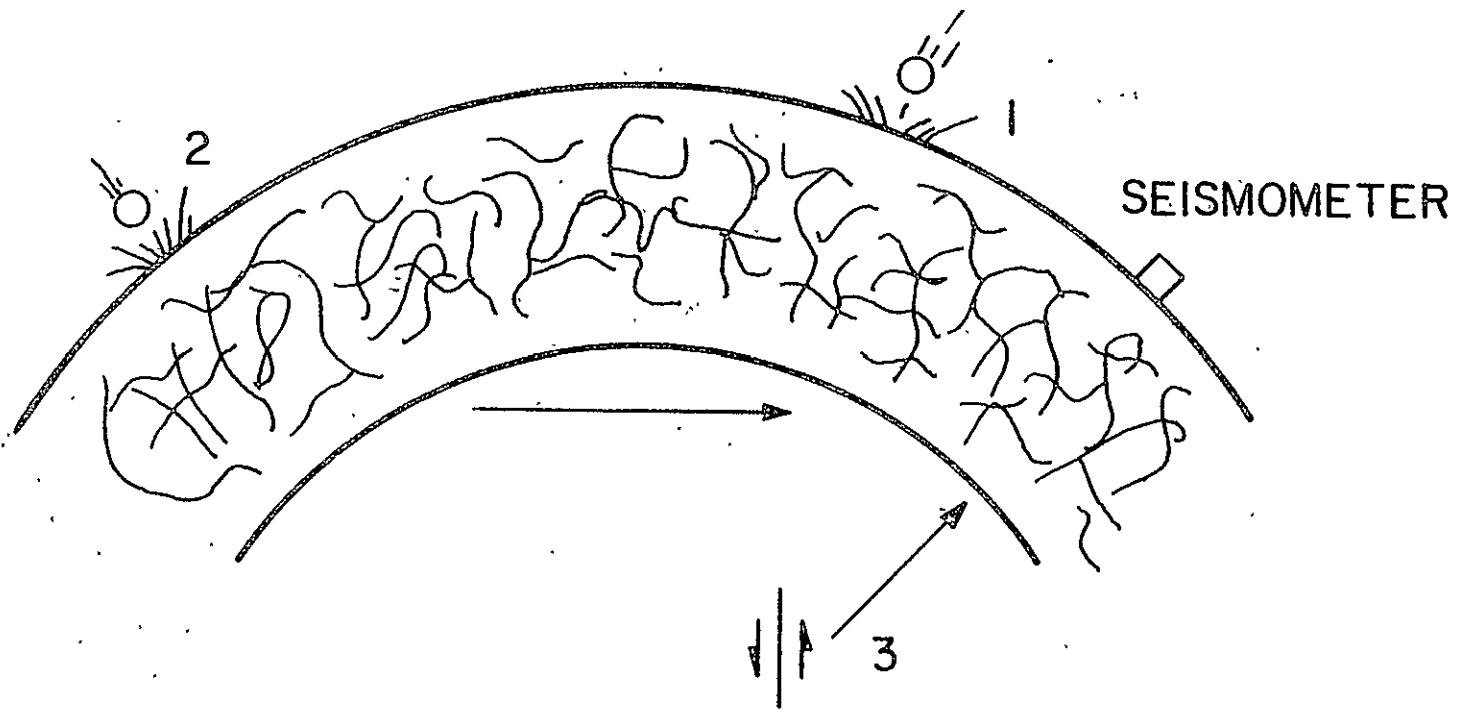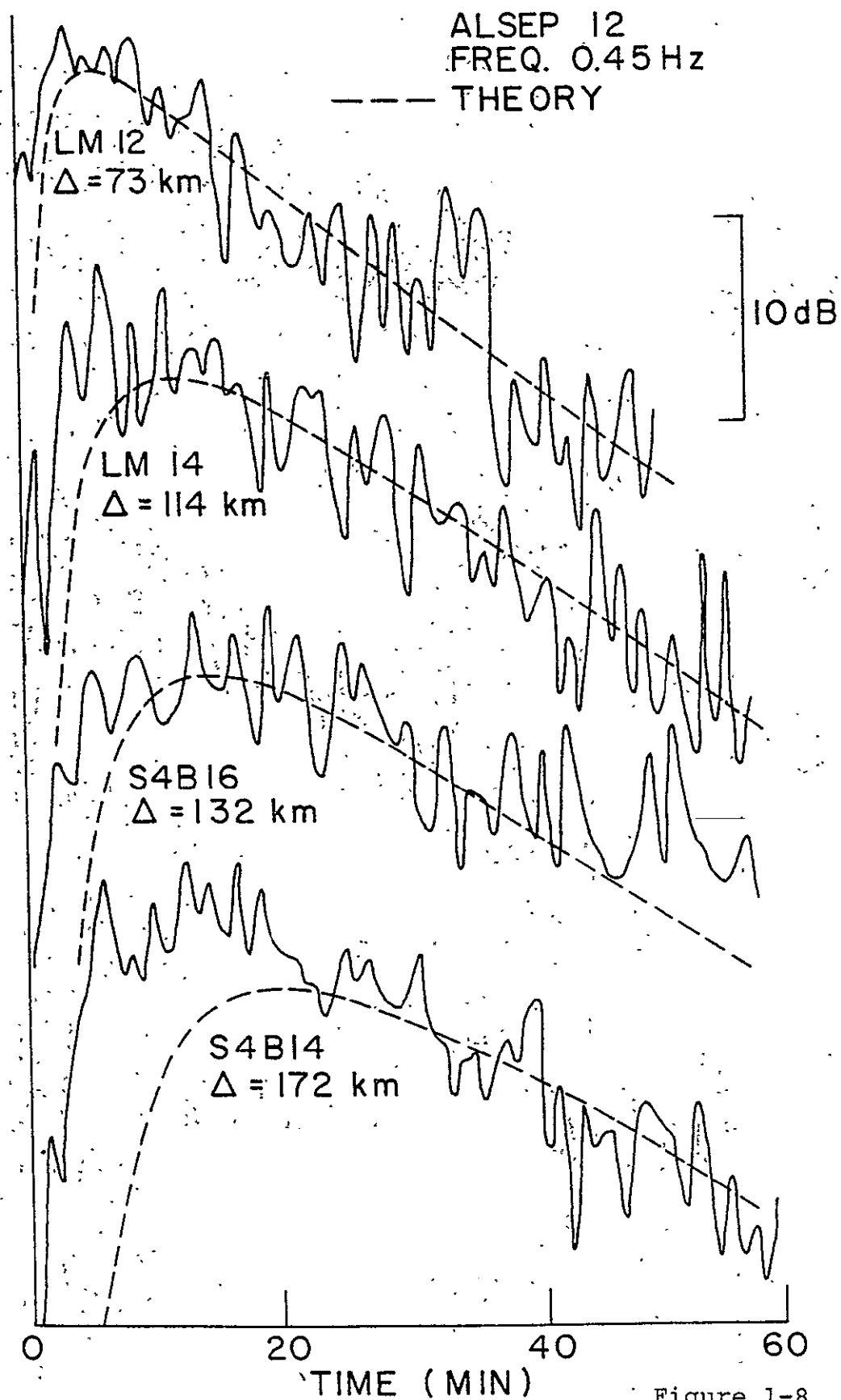
Figure 1-8

DAY 156, 1973 (reversed)

S↓

⊢ 30 SEC ⊣
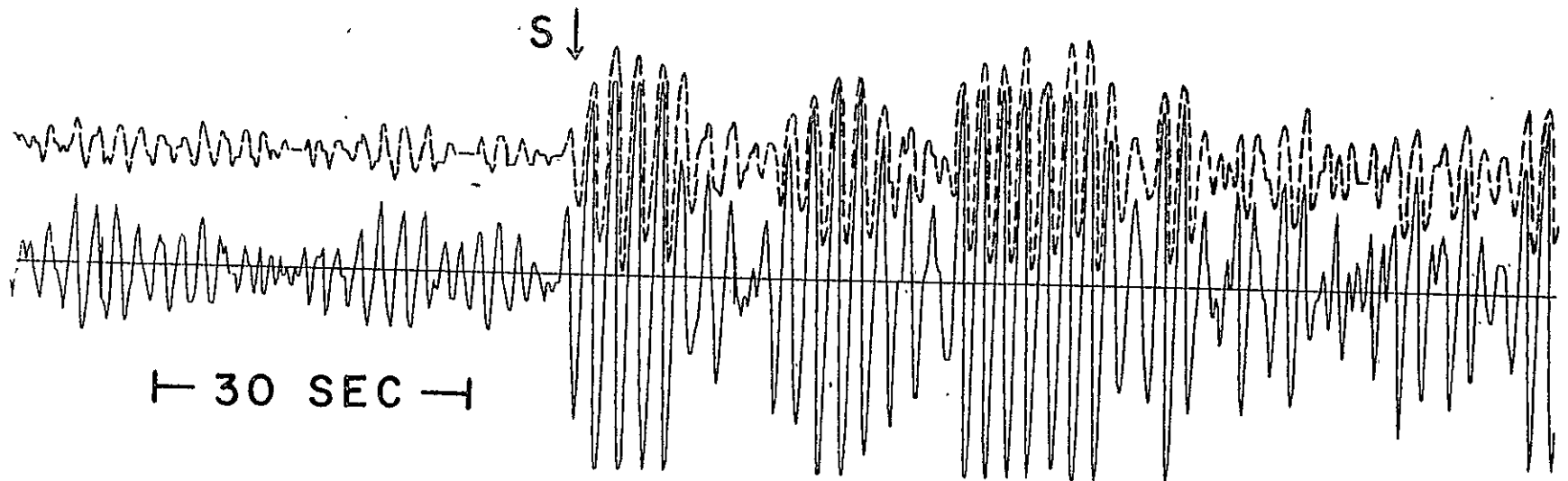
Figure 1-9

DAY 86, 1975 (normal)

Figure 1-10

A$_1$ MOONQUAKES

76
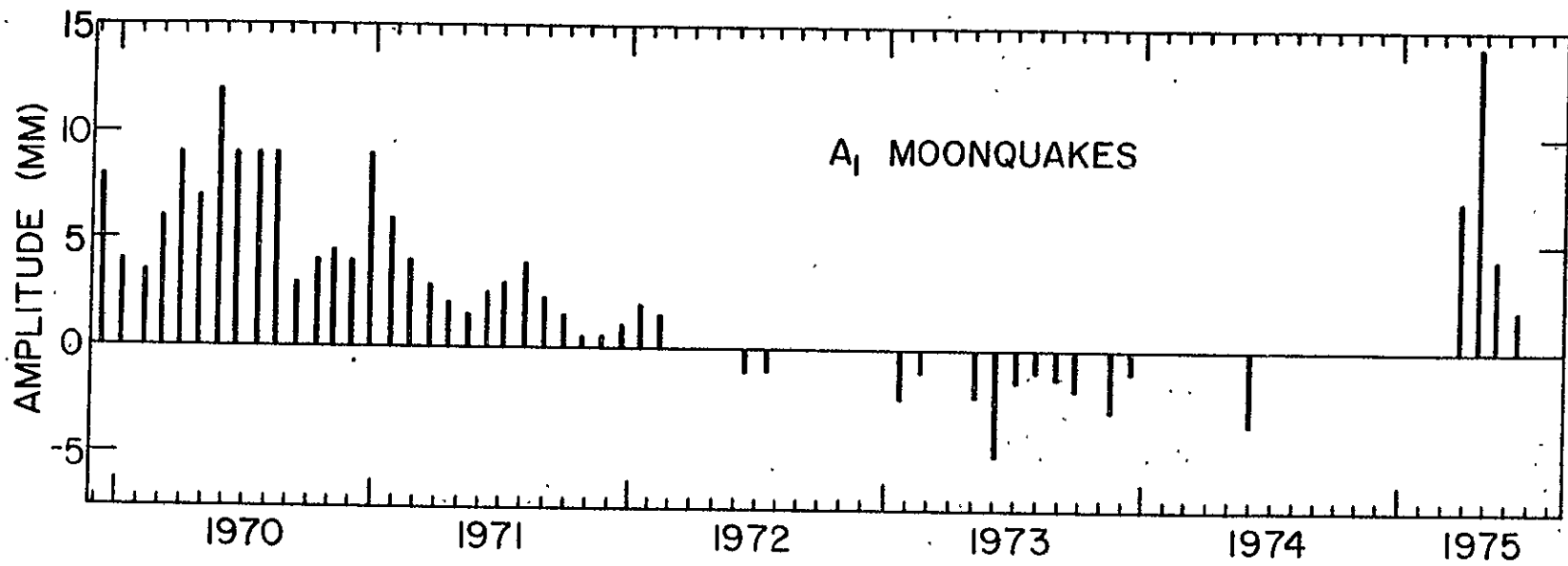
DAY 304, 1975 (normal)

P ↓

S ↑

⊢ 10 MIN ⊣

T
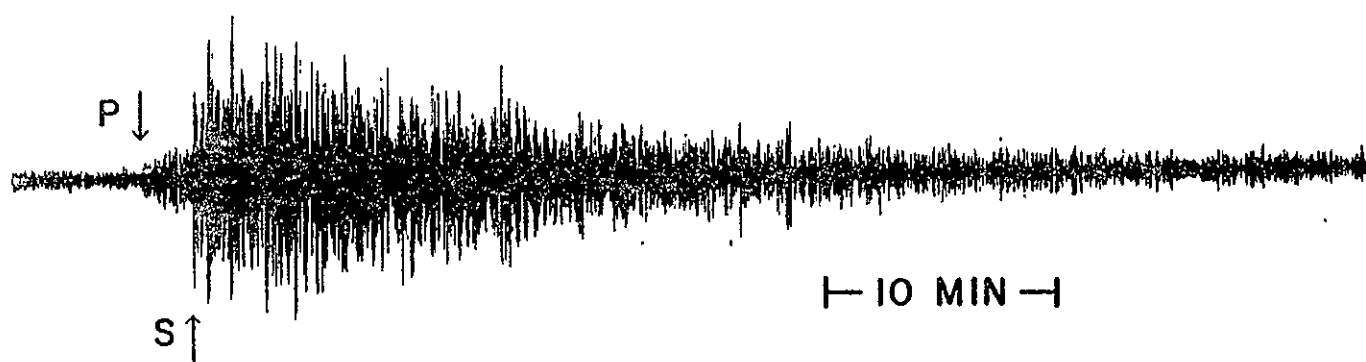
DAY 25, 1976   ALSEP 12

R

Z

P

10

13

TIME (MIN)

Figure 1-12a
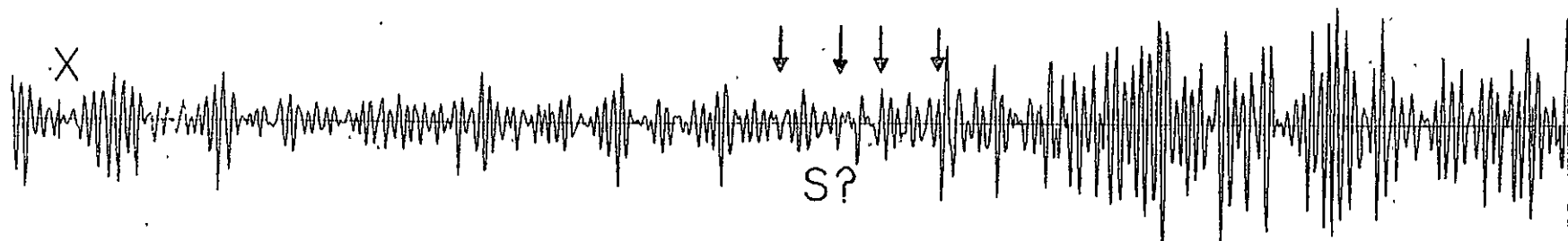
DAY 72, 1973   ALSEP 14
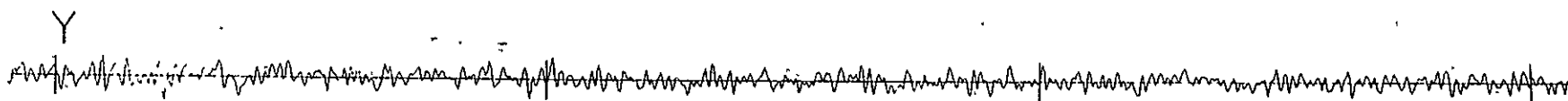
Figure 1-12b
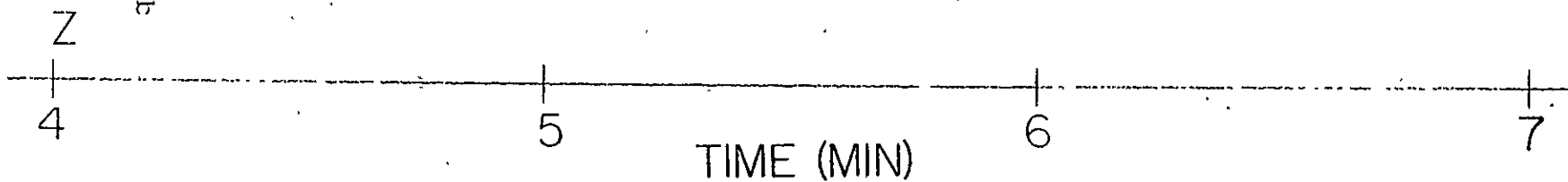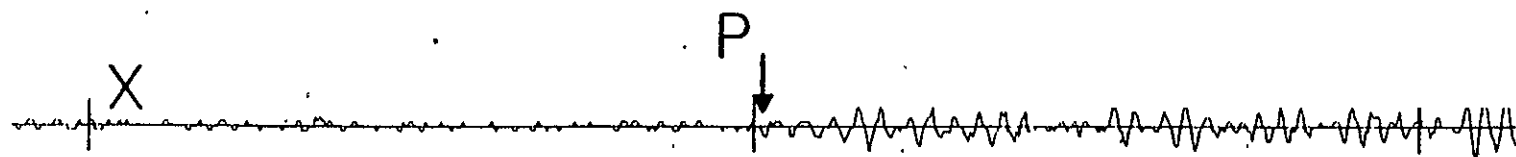
TIME (MIN)

FOCUS A33   ALSEP 16
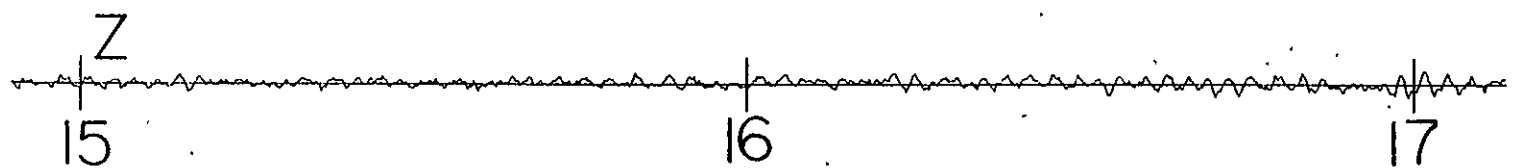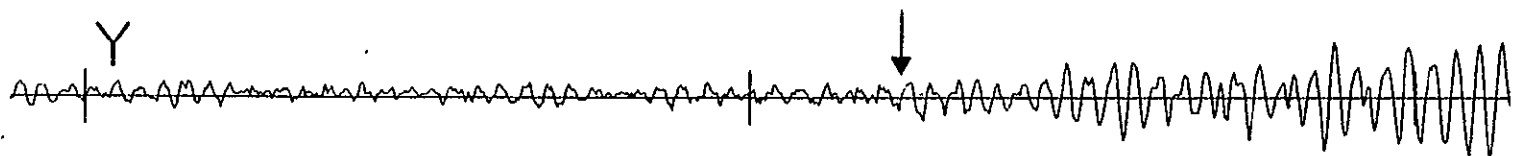
TIME (MIN)

Figure 1-12c

80

CHAPTER 2

CRUST

2.1 Introduction

The structure of the lunar crust can be divided into two
regions based on scale size. The very near-surface structure,
as studied by Cooper et al. (1974), Nakamura et al. (1975),
and Mark and Sutton (1975) covers the outer two kilometers of
the moon, while whole crustal structure studies extend to
depths of 60-100 km (Latham et al., 1973b; Toksöz et al.,
1972b, 1974a). Complete references are given in section 0.2,
and the results as they pertain to this thesis are summarized
below.

The near-surface structure of the moon has been ascer-
tained primarily from the active seismic experiment data
(Cooper et al., 1974; Kovach and Watkins, 1973a,b,c; Watkins
and Kovach, 1973). These experiments were landed on missions
14, 16, and 17, each containing a small array of geophones and
various seismic sources such as thumpers, mortar-fired
grenades, and explosive packages. The available source
energies and array dimensions were largest at ALSEP 17,
capable of illuminating the seismic structure to nearly 2 km
depth. The results at all stations are remarkably similar;
a top layer between 4 and 12 meters thick with Vp $\sim$ 100 m/sec,
underlain by faster material with Vp $\sim$ 300 m/sec. At the
ALSEP 17 site, the 300 m/sec layer was found to be about 30 m

thick, underlain successively by 500 m/sec and 960 m/sec zones
of thickness 400 m and 1 km respectively. At a depth of 1.4
km the P wave velocity jumps to 4.7 km/sec. These results are
supported by the relevant data from the passive seismic exper-
iment stations. In particular, signals from the LM take-off
yield similar seismic velocities and depths for the two
uppermost layers mentioned above (Nakamura et al., 1975;
Latham et al., 1972b). In addition, the amplification of the
horizontal components of ground motion relative to the ver-
tical components at all the PSE (Passive Seismic Experiment)
stations can be explained by the effect of a very-low-velocity
surface layer on the ellipsoidal particle motion of Rayleigh
waves. A resonance peak analysis (Nakamura et al., 1975) and
a more complete calculation of expected Rayleigh wave spectral
ratios over a frequency band 0.4 to 2.0 seconds (Mark and
Sutton, 1975) both produce results that are roughly consistent
with the active seismic conclusions.

The uppermost layer probably represents the lunar
"regolith", extending to a depth of 4-12 meters. The uniform
and very low seismic velocities at all stations are probably
controlled by the physical constitution, i.e. a rubble layer,
rather than by the particular chemical composition. The
thickness of the regolith at various stations is consistent
with other estimates from crater counting and the floor
characteristics of fresh craters (Cooper et al., 1974). The

next layer at Vp = 300 m/sec is probably more competent but
still highly fractured rock. One possibility discussed by
Cooper et al. (1974) is that this layer represents ejected
brecciated rock; the Fra Mauro formation at ALSEP 14, and the
Cayley formation at ALSEP 16. Below these layers at ALSEP 17
there appear to be two layers of higher velocity material,
possibly representing basalt-type materials of varying com-
petence. Finally the velocity jumps to 4.7 km/sec; this
region is discussed below. Note that the entire low-velocity
sequence of materials is contained within the outermost 2 km
of the moon, and thus coincides with and probably represents
at least a part of the strong scattering region.

The implications of these results for this thesis are
two-fold. First, the steep velocity gradient means that
arriving rays from teleseismic events will be bent towards the
vertical and thus will be near normal incidence at the sur-
face. This is only strictly true for waves of infinite
frequency (ray theory), but since the low-velocity layer is
about 1.5 km thick (at least at station 17) and the seismic
wavelengths are about 1.5 and 0.5 km for P and S waves res-
pectively, the bending effect will be at least partially
operative, especially for shear waves. As a reference, ray
theory predicts an incident angle of 3.5° event for surface
events at $4^{\circ}-5^{\circ}$ from a station. Thus, to a reasonable
approximation, compressional waves should be seen mostly on

the vertical components of ground motion, while shear energy
should appear on the horizontal records, independent of event
location. Second, the low velocities introduce a time lag
that must be accounted for in constructing travel-time curves.
In this work a one-way P wave transit time of 2 seconds is
used, in agreement with the model of Cooper et al., 1974.
Assuming a Poisson's ratio of 0.25 (this value may be some-
what low; see Mark and Sutton (1975)), the corresponding S
time is 3.5 seconds. Both numbers are sufficiently accurate
for our purposes.

The deeper crustal structure of the moon has been sum-
marized primarily by Toksöz et al. (1974a). Earlier papers
are referenced therein. The data base used to determine the
structure is almost exclusively the seismograms produced by
impacting sections of the spacecraft onto the moon at known
places and times. This means that travel times are measured
instead of arrival times, leaving all the data for use in
determining structure rather than having to use the bulk of it
to calculate the source parameters. Nine such impacts were
effected: five SIVB booster sections and four LM sections;
a total of about 20 compressional wave travel times were
measured from these sources. Fig. 2-1a shows the data (for
distances less than 400 km) and theoretical travel times cal-
culated from the model in Fig. 2-7. There are two triplica-
tions caused by rapid velocity increases at depths of 20 and

55-60 km; only the second one is strongly required by the travel time data. The corresponding amplitudes are shown in the middle drawing (b) along with the same theoretical fit calculated from ray theory; not the high amplitudes caused by the cusp at 160 km. The triplication due to the 20 km velocity jump is required to produce the low amplitudes seen at 100-150 km distance. Fig. 2-1c shows the ray theory travel paths for the model in Fig. 2-7. Based on analogy with earth, the major velocity increase at 55-60 km depth is termed the crust-mantle boundary.

The prograde travel time branch moving out past 400 km distance in Fig. 2-1a represents rays bottoming below the 60 km boundary in a region where the P wave velocity is about 9.0 km/sec. Figure 2-2, however, shows the three arrivals observed from more distant artificial impacts, and they appear to require a slower velocity below 60 km depth; the solid line shown is for Vp = 7.7 km/sec. This discrepancy can be explained in four possible ways. First, the arrivals marked at 900-1100 km distance could represent secondary seismic phases, indicating that the small first arrivals were missed; they could then be in agreement with the closer travel times. Second, the high-velocity region could be a relatively thin layer beneath the crust, so that the refracted waves traveling along in it are attenuated rapidly with distance and would therefore not be seen at greater source-receiver separations.

Third, the high-velocity zone may only exist in a limited area. Finally, since the apparent travel times are obtained from an unreversed refraction line, a dipping interface might partially account for the high apparent velocities. None of these possibilities can be completely ruled out. The natural seismic event data (discussed in Chapter 3) require that the average upper mantle velocities be less than 8 km/sec, thus implying that any high velocity zone is probably confined to a thin layer below the crust. In addition, compositional models for the lunar interior favor the lower values for mantle velocities. Furthermore, the velocity drop below such a layer would produce a large shadow zone for surface events if the layer were significantly larger than the seismic wave-lengths; this is in disagreement with the calculated locations and observed arrivals. In sum, the high velocity region below the crust is not likely to be representative of the lunar mantle but may exist locally, or globally as a thin layer.

The shear wave travel time data produced by the artificial impact events is shown in Fig. 2-3. The measurements are much less certain due to the relatively small amount of shear energy produced by impacts, but the times and amplitudes can be adequately fit with a velocity model proportional to the compressional wave velocity shown in Fig. 2-7. A ratio of $3^{-1/2}$, corresponding to a Poisson's ratio of 0.25, is used. Finally, the implications of the travel time data are

summarized in Fig. 2-4, showing allowable velocity bounds for the upper 100 km of the moon, using the tau method of Bessonova et al. (1974); the center line is an average model.

To further constrain the crustal velocity structure, theoretical seismograms have been calculated to fit the observed records. A suite of the observed seismograms is shown in Fig. 2-5; theoretical comparisons are given in Fig. 2-6. There are three major conclusions to be drawn that are of importance to this thesis. First, the initial 10-20 seconds of the observed seismograms evolve systematically as the source-receiver separation is increased, and the theoretical seismograms are successful in matching this time period. Further along the records, both these observations fail. The implication is that the initial part of a seismic wave arrival is well-represented as a relatively non-scattered phase, which gradually deteriorates into random scattered energy as time increases (see Chapter 1). This suggests that the polarization filter discussed in Appendix 3 is in fact an appropriate approach to take in extracting body waves with initial rectilinearly-polarized particle motion from scattered energy of random particle motion. (The results have shown that at least the direct wave arrivals (P and S) are recovered by the filter at the times expected from eyeball picks on the raw records.) Second, the large amplitude phase seen at the triplication cusp (170 km or 6 degrees) is present on the

observed records and is modeled as the sub-critical reflection
from the crust-mantle interface. The fact that this is the
largest amplitude arrival seen for both P and S (see Fig. 2-3,
bottom) at this distance is critical to the discussions in
section 3.3.3. Finally, the matching of theoretical seismo-
grams to the observed records places tighter constraints on
the velocity model than those obtained from travel times alone.
In particular, the short-period records imply that the tran-
sition region at the crust-mantle junction is 3 ± 1 km wide.

The final crustal model determined from the artificial
impact data is shown in Fig. 2-7. It must be noted that this
structure is valid only for the region near stations 12 and
14, since all but three travel time values were measured at
these stations. This is a result of the sequential station
emplacement and subsequent spacecraft impacts during the
Apollo mission series; consequently most impacts were ob-
served at the early stations. In fact the primary evidence
for assuming that a moon-wide crust exists comes from geo-
chemical, geological, and gravity considerations (cf. Kaula
et al., 1974); the seismic data from artificial impacts con-
strains its characteristics at only one location. The struc-
tural and compositional interpretations are discussed in
section 2.4 after the new results obtained in this work are
presented.

In calculating theoretical travel times and amplitudes in the remainder of this thesis, a simplified version of this crustal structure is used to reduce computation time and cost. Specifically, the crust is modeled as two constant-velocity layers; an upper crust from 0-20 km with $V_p = 5.1$ and $V_s = 2.94$, and a lower crust from 20-60 km with $V_p = 6.8$ and $V_s = 3.9$. In addition, as mentioned before, a time of 2 seconds for P waves and 3.5 seconds for S waves is added to account for the low-velocity surficial zone. The only real approximation this simplified model contains is in the upper 20 km where there is a relatively strong gradient. The constant velocity values used (5.1, 2.94) are designed to give essentially the same vertical travel time (3.9 seconds for a P wave) as the original model of the upper crust (excluding the surficial layer). The approximation will of course deteriorate for non-vertically incident waves. However, for rays that bottom below the crust, either from surface sources or (obviously) deep moonquakes, the maximum error caused by the constant velocity approximation in the upper crust is 0.2 seconds (one-way travel time for S waves) as shown by tracing rays through both structures. Thus, even for "peg-leg" phases discussed below which traverse the crust three times, the maximum error possible is about half a second, well within required accuracies both in this chapter and Chapter 3. The only rays traced which do not bottom in the mantle are the

direct P and S arrivals at stations 12 and 14 from the Day 134
meteorite impact which occurred close to these stations; the
errors in this case for the two-way S wave travel times are
still less than two seconds which is sufficient for the
inversion described in Chapter 3 (since it only applies to
these two rays).

The effect of the crustal approximation on calculated ray
theory amplitudes is slightly more complex, but still within
tolerable limits. In nearly all of the amplitude calculations
done herein the object is only to determine the approximate
relative amplitudes of various possible seismic phases (in
order to ascertain which ones might be visible on the lunar
seismograms discussed below); thus only relative, approximate
values are important. Therefore as long as the waves whose
amplitudes are being compared have traversed the upper crustal
zone the same number of times (e.g. once up, once down) the
effect of the above approximation should be roughly the same
for each wave and will therefore have little effect on the
comparison. This is particularly true since the rays from
natural seismic events used in this work are teleseismic and
therefore traverse the upper crust at a small range of angles
with respect to the vertical. The only additional complica-
tion concerns those rays which include a reflection at the
free surface, but again the effect of the crustal approxima-
tion is small, because the wave will be equally focused and

defocused on its way up and down, thus roughly canceling any effects of near-surface structure. (There is also some effect on the surface reflection coefficient calculated in the programs described below, but this calculation is only done for deep moonquakes which are far beneath the array and within 60° of its center; the incident angles of the resulting rays at the surface are within 15° of the vertical and the steepening effect of the true upper crustal velocity gradient is small.)

In sum, this simplified crustal model is sufficient for the purposes of this thesis, but its use should be noted. In section 3.7, where it is necessary to compare the amplitudes of rays over a wide range of distances with an observed data curve, the detailed crustal model is used. Even in this case, however, test runs show that the simplified crustal structure produces essentially the same results.

2.2 Natural Event Data

In order to extend our knowledge of lunar crustal structure, it is necessary to use the natural seismic event data set. Several lines of evidence imply that this approach might be effective, and point towards the proper analysis procedures. The "ringing" character of the lunar seismograms, especially after strong shear wave arrivals, may be partially the result of strong reflectors near the lunar surface in addition to the effects of scattering and high Q. This is especially true at ALSEP 16 where the reverberating nature

of the seismograms is most apparent. Thus there is the possi-
bility that secondary shear waves, reflected from crustal
interfaces, may be visible on the lunar seismograms. If so,
these would provide close constraints on the crustal thick-
ness assuming that the layer velocities are reasonably well-
known. Of course, to see such reflections (post-critical) it
is necessary that the width of the interface between different
layers be small compared to the wavelength of the seismic
wave. For shear waves at the base of the crust, the wave-
length is about 8 km at the dominant period of 2 seconds.
This is only 2-4 times larger than the crust-mantle interface
width predicted for stations 12 and 14 from theoretical seis-
mogram matching (3 ± 1 km) so the reflection coefficients may
be diminished and thus it may be difficult to observe these
phases there. Nevertheless, the analysis was carried through
in the hopes that some evidence might be visible and that
other boundaries or other stations might produce strong
reflections.

The above phases are termed "peg-leg multiples" in the
oil industry and typical ray paths are shown in Fig. 2-8a.
Primarily peg-legs from the shear wave incident at the base
of the crust will be considered; the incident P wave is
generally much smaller except for a few of the meteorite
impact events. There are then nine possible peg-leg reflec-
tions from any interface, corresponding to conversions at

either the surface or the interface. The nomenclature will be SSS-V, SSP, SPS, PSS, SPP, PSP, PPS, PPP, and SSS-H. The letters refer to the up, down, and up wave types in the crust, respectively; the incident wave is S (SV and SH) unless otherwise noted. SSS-H is the horizontally-polarized SH phase, while SSS-V refers to SV waves. There are only four distinct travel times, SSS (V and H), SSP-SPS-PSS; SPP-PSP-PPS; and PPP. In addition, if such reflected phases are observed, it is appropriate to see if refracted converted phases are also present; there is only one from each interface for an incident S (SV) wave, as shown in Fig 2-8.

In order to determine the optimal approach in searching for these phases, it is necessary to calculate theoretical travel times and amplitudes for the expected arrivals so as to ascertain their characteristics. The travel times are used in conjunction with the record sections discussed below to identify secondary phases and determine the structural implications, while the theoretical amplitudes are most useful in deciding a priori which secondary phases are likely to produce the largest amplitudes and therefore be most easily visible. (Due to the non-linear filtering necessary (see below) and the very low signal-to-noise ratio of the secondary phases, it is not feasible to quantitatively correlate observed and calculated amplitudes.) The programs used in these calculations are described in detail in Appendix 2. Briefly, the

calculations use ray theory (Bullen, 1965), and include the effects of ray-tube spreading and reflection and transmission coefficients. In the tables presented below, a unit source energy is assumed. The quantity of interest is the relative level of the secondary phase amplitudes as compared to the predicted shear wave amplitudes; by comparing this ratio to the observed direct wave amplitude we may estimate the actual secondary phase amplitude expected on the seismograms.

The mantle velocity model used in the theoretical calculations is a preliminary one derived from the methods in Chapter 4, but the exact values of the velocity structure below the crust are not critical as long as they are reasonably close (± 0.5 km/sec) to the true quantities, since the differential travel time of direct S and the peg-leg multiples are almost independent of the mantle velocities. The effects of varying crustal velocities are discussed below.

Moonquakes (interior sources): The models used are listed in Table 2.1; the depths refer to the bottom interface of constant-velocity layers. The source depth is at 1000 km (except in Table 2-2d) and reflections are calculated for interface depths of 20 km (upper crustal layer), and 60 and 75 km (crust-mantle boundary), as marked by the X's.

The theoretical results are given in Tables 2-2a, b, c, and d. As mentioned before, there are four distinct travel times, depending on the number of P and S legs. The amplitude

values are listed by the component of gound motion where they
are likely to be seen. SSS-H is the only phase expected on
the transverse component (with respect to the epicenter). The
next three, generally in order of decreasing amplitude, will
be seen on the radial component since the last leg of each is
SV. SPS and PSS arrive simultaneously. The last three are
expected on the vertical records since they all terminate as
P. Again, the first two arrive together, and they are roughly
in order of decreasing amplitude. For comparison, the direct
P and S wave amplitudes for the first model of Table 2-1 are
given in Table 2-3a. In addition, the times and amplitudes of
the refracted converted phases are listed in Tables 2-3a, b
for the three interfaces considered above.

The following conclusions can be drawn from these tables.
First, the largest of the peg-leg multiple amplitudes are
about 0.07 to 0.10 of the direct P and S wave amplitudes,
implying that there is some chance of seeing such phases which
derive from incident S waves, especially on the larger moon-
quake records. Second, the largest amplitude is consistently
seen for the SSS-H phase, which should be found on the trans-
verse component of ground motion. Depending on the distance
range and source depth, either the SPS+PSS or SSS-V phase will
dominate on the radial, and either SPP+PSP or SSP will be seen
on the vertical records. In both cases the former phase will
be the larger at greater distances; the phases PPS and PPP

will probably not be visible at all. (As mentioned above,
these results are calculated for a source depth of 1000 km;
the actual moonquake focal depths actually vary from 700 km to
1100 km with an average depth of 900-1000 km. Comparison of
Tables 2-2c and d illustrate the relative amplitude dependence
on focal depth.) Third, the refracted converted phases listed
in Tables 2-3a and b reach relative amplitudes of 0.10 to
0.15, similar to the peg-leg waves. The larger amplitudes are
obtained by the S to P conversion, and since the incident S
wave is largest for all deep moonquakes, this is the phase of
choice to look for; it is expected on the vertical records.
Naturally, the true amplitudes are dependent on the precise
structure of the velocity interface, particularly in terms of
relative amplitudes of refracted and reflected phases, and the
above results from ideal-case calculations are used as
indicators only.

Surface sources: The situation for seismic events
located on the surface turns out to be much simpler than for
interior sources. For distances greater than about 10^{0}, the
surface event rays bottom in the mantle and enter the crust in
the same way as moonquake phases; see Fig. 2-8a. However, the
incident angle is much greater (relative to the vertical) so
that for an arriving shear wave no conversions to P waves
(e.g. S-PSS, S-SPS, etc.) in the crust are possible until the
source-receiver separation is at least 110^{0} (using a

reasonable velocity structure). For a 20 km interface, the source must be at least 65° distant. As discussed in section 3.3.2, the shear waves arriving from sources beyond 85°-95° are strongly attenuated, and so no peg-leg multiples with P wave legs will exist from crustal boundaries deeper than about 40 km. Even a 20 km boundary is not likely to produce such phases with observable amplitudes due to the restricted distance range and thus limited number of records available. Of course, a full set of peg-leg multiples can be generated from the incident P wave at the base of the crust, but as discussed above, the P wave is generally weaker and we want to search for phases that are most likely to be visible.) Accordingly, only the SSS-H and SSS-V peg-leg multiples are considered.

A typical travel-time curve is shown in Fig. 2-8b for an interface depth of 75 km. The model used is given in Table 2-4, and again is the same as that used in locating the surface events and determining their origin times. Theoretical amplitudes were not calculated for these phases explicitly because they are expected to be similar to the analogous phases from deep moonquakes. The reason for this is that the reflection (without conversion) coefficients at the interface and free surface are roughly the same for all pre-critical incident angles, except for a single node. Thus, it is appropriate to search for SSS-H and SSS-V on the transverse and radial components of ground motion from surface events;

no converted (reflected or refracted) waves are likely to exist.

Now all of these secondary phases by definition arrive at the seismometer after the direct wave arrivals; the refracted converted S-P wave after P (and slightly before S), the peg-leg multiples after S. As discussed in Chapter 1, the lunar seismograms are completely dominated by the scattered codas of the direct P and S waves because of the strong surficial scattering layer, so even if present the secondary phases would be nearly impossible to observe on the raw records. However, as a result of matching theoretical seismograms to the artificial impact data, it is known that the first ten or twenty seconds of the direct wave arrivals are relatively free of scattering effects, and so the particle motion is roughly rectilinear as expected for a body wave phase. This is also indicated by the high coherence of the initial direct wave arrivals (Nakamura, 1977b). Therefore the initial arrivals of secondary body waves should also be free from scattering effects and have relatively rectilinear particle motion. This should even be true for peg-leg multiples in spite of the fact that they traverse the scattering layer an additional two times while reflecting at the surface; the initial onsets will probably be somewhat reduced in amplitude. It is also possible that the peg-leg "surface" reflection would actually occur at the base of the very-low-velocity zone rather than at the true surface,

C-2

so that the most intense part of the scattering layer would not be traversed.

The scattered energy of the P and S wave codas that overlies the secondary arrivals has been scattered several to many times, is arriving simultaneously from different directions, and therefore will have essentially random particle motion. Random particle motion is in general ellipsoidal, and so the secondary body wave arrivals, if present, can be extracted from the obscuring scattered energy by searching for rectilinear particle motion. This can be done effectively with a digital non-linear polarization filter, as described in Appendix 3. In essence, the filter discriminates against ellipsoidal particle motion and enhances rectilinear motion. This eliminates a great deal of the energy observed on the lunar seismograms, as can be seen by comparing the filtered and unfiltered records included in Appendix 4. What remains is a large number of energy pulses, not all of which can represent true body wave arrivals. Indeed the polarization filter will pass without attenuation any large noise pulse that appears on only one component of ground motion. Thus the next step in searching for secondary phases is to arrange filtered seismograms in record sections, or montage plots. Pulses which represent true body wave arrivals will then be aligned along travel-time curves, while noise pulses will not. In this way a reasonable measure of confidence can be attached

to candidate arrivals which correlate well across different
records that represent different sources.

In sum, then, the following procedure is used to search
for secondary body waves pertaining to crustal structure.
More details are included in Appendix 3. First, the raw
three-component LP seismograms are scaled so that the three
component traces are of roughly equal amplitude and the hori-
zontal records are rotated to radial and transverse directions
relative to approximate event epicenters. The former process
is to enhance the effectiveness of the polarization filter,
and the latter is to aid in the identification of phases. The
resulting traces are then passed through the polarization
filter and plotted. Second, the filtered records are arranged
in record sections one component of ground motion at a time.
The surface events and deep moonquakes are plotted separately
to reduce confusion; also, the deep moonquakes entail an addi-
tional step. A record section plot aligns the origin time of.
all events and positions the records as a function of source-
receiver separation. If, however, the event foci are not on
the surface or at a common source depth, then the actual
origin times must be corrected to simulate a common focal
depth. This correction requires knowledge of the velocity
structure through which the rays travel, the location of the
focus, and is different for each particular seismic wave.
Finally, theoretical travel time curves are fitted to the

record section plots in order to determine the identity of the secondary phase arrivals and evaluate the ensuing structural implications.

The actual velocity structure and moonquake locations used in section 2.3 to align the moonquake record sections are preliminary results obtained using the methods in Chapter 3, rather than the final values presented therein. However, this has little effect on the record section-travel time curve correlation for crustal reflections, because the locations and velocity model are determined simultaneously and are therefore consistent no matter which of the similar lunar models considered in the course of this work is used, and the same model is used to calculate the theoretical travel time curves. Furthermore, the primary quantity of interest is the time difference between the direct S phase and the peg-leg multiples, and this is almost totally independent of the mantle velocities; they contribute only a baseline origin time and travel time shift.

While it is true that the required origin time corrections for moonquake source depth variations are different for each seismic wave, the corrections for waves of the same geometry are very similar; to wit, the maximum difference between the corrections for the various peg-leg multiples is less than two seconds. Even including refracted S-P phases and varying boundary depths between 20 and 90 km, the

differences are less than three seconds. In fact, this is
true of all rays leaving the moonquake sources and traveling
upwards as long as no change in wave type (e.g. S-P) occurs
between the actual source depth and the corrected common
source depth. Therefore in the figures of section 2.3 unless
otherwise noted the origin time correction has been applied
for the S-SSS peg-leg multiple phase, with an interface depth
of 60 km. Given a dominant period of 2 seconds and a reading
accuracy of $\pm$ one cycle, this correction is adequate for all.

2.3 Results of Natural Event Studies

The analysis methods described above were applied to the
full lunar data set as listed in Chapter 1 and Appendix 1.
The individual raw and filtered records are shown for each
focus in Appendix 1. Since it is the crustal structure that
is of interest in this chapter, it is appropriate to examine
the lunar records grouped by station. Nearly all moonquake
sources are within $60°$ of the ALSEP array center, so each
group will be sampling the crust within a radius of at most
40 km from each station, providing a fairly localized struc-
tural picture. The surface events naturally traverse a wider
zone, but all record sections shown extend from $20°$ to $90°$, sc
that a region of at most 60 km radius is traversed.

On all plots that follow, both in this chapter and in
subsequent ones, there are three conventions to be noted.
First, often a few of the available traces are omitted from

a record section for one of two reasons: a) it overlaps another record, and so the stronger is chosen for presentation; b) in the moonquakes case, the A33 focus is much farther (100°) from the stations than all others, and so inclusion of the A33 records would compress the other records which are all contained within about 70°. In both cases the excluded seismograms have been examined, and invariably add little information to the primary record section. Second, the zero time point on the record sections usually represents a constant time shift from the origin times, which are always to the left of (before) the times shown. The offset is chosen only for plotting convenience to permit clearer presentation of the records. It is not explicitly given for each plot but can be readily determined by comparing the plotted travel time curves with the appropriate tabulated values. Finally, each trace is identified by a label. For moonquakes, the second character refers to the last digit of the corresponding station (e.g. 4 = 14), while the fifth and sixth digits are the focus number. Surface events contain the same station code, and then either HFT (near-surface moonquake) or C (meteorite impact) and the day the event occurred.

ALSEP 16: This station was chosen for initial examination due to the "ringing" characteristic of seismograms recorded here, perhaps suggesting sharp near-surface interfaces. The moonquake event results are discussed first

because all peg-leg multiples should be present and there are fewer additional phases that might arrive at similar times and cause misidentification. The surface event records would not contain converted phases and contamination by the SS (surface reflection) phase is possible. The transverse filtered components from all but three moonquakes are shown in Fig. 2-9a; the origin times are all 200 seconds to left of the zero time point. The travel time curves for direct S and two SSS-H peg-leg multiples, calculated from the models in Table 2-1, are as shown. These are the only phases expected on the transverse component, assuming spherical layering. The S arrival is well-observed, illustrating that the velocity model and locations fit the direct wave arrival time quite well (see Chapter 3). There is also some evidence for a 75 km and 20 km peg-leg phase, as shown, particularly in the regions between 40° and 60° and between 25° and 30°. While the correlations are by no means perfect it does seem that 20 km and 75 km reflecting interfaces may exist at the ALSEP 16 site. A more detailed view is given in Fig. 2-9b, showing an expanded version of the records between 45° and 55°; the correlation is reasonably convincing. For comparison, the unfiltered transverse components are shown in Fig. 2-9c; there is a great deal more scattered energy present and the secondary phases are much less obvious.

In order to confirm these observations it is necessary to

examine the other components of ground motion. Figs. 2-9d and 2-9e contain the radial components of ground motion. Again the theoretical S arrival time is shown, along with the SSS-V and SPS+PSS phases from both interfaces. In general the later arrival should dominate at greater distances while the former is strongest at short range. (Hence only the later curves are indicated in Fig. 2-9e.) The exact characteristics vary substantially with focal depth, as seen in Tables 2-2c and d, and so the extent of the curves in Fig. 2-9d is only approximate. Again there is a fair amount of correlation with the predicted arrival times. The amplitudes do not closely follow the predicted systematics, but as mentioned above it would be surprising if they did, because the true amplitudes are strongly affected by minor variations in interface characteristics and local velocity variations not modeled in the theoretical calculations.

The vertical records are shown in Figs. 2-9f and g. Of particular interest is the dashed line on both plots which represents the expected S arrival. It is clearly not observed, as is expected if the seismic wave is arriving vertically, and in fact is often in a quiet region flanked by energy on both sides; this suggests that there is in fact particle motion consistency on the lunar seismograms and that the polarization filter has properly discriminated between coherent and scattered energy. Three expected phases are

plotted for each interface: SPP+PSP, expected to dominate, SSP
which is usually somewhat smaller, and the refracted phase S-P.
The 20 km interface is particularly convincing, and reasonable
correlation is seen for the 75 km boundary. The S-P amplitudes
are small, although in general there is a small wave train ob-
served at the proper time. (Note that the expanded plot Fig.
2-9g is corrected for the SPP phase while Fig. 2-9f is aligned
for SSS; there is virtually no difference, as asserted above.)

Finally, the transverse and radial components of ground
motion for surface events recorded at ALSEP 16 are shown in
Figs. 2-9h and i. Only records between 20° and 90° distance
are used because a) there are few if any surface events within
20° of the ALSEP stations that produce good quality records,
and b) beyond 90° the S wave arrival is strongly attenuated
and so little energy is available for reflected phases. Theor-
etical curves are plotted for direct S and the SSS peg-leg
multiples. The correlations are actually quite good, espe-
cially on the radial section. The dashed line drawn on the
transverse section is the expected arrival time of the SS
surface bounce phase, and it unfortunately has the same general
trend as the peg-leg multiples. As discussed in Chapter 3,
the SS arrival is observable, especially on the short-period
records beyond 90° distance, and so it may appear on these
record sections. Nevertheless, the trends seen in Figs. 2-9h
and i seem to follow predominantly the peg-leg multiple

curves, confirming the phases seen on the moonquakes record sections.

Based on these figures, it is likely that there are two sharp crustal interfaces in the ALSEP 16 area, at depths of 20 and 75 km. While the individual component sections do not show perfect correlation between expected times and energy pulses, the confidence level is much increased by the fact that the analogous phases expected on the other components of ground motion, especially the vertical, appear at the appropriate times. In view of the generally small signal amplitudes and the presence of scattered codas, the observed correlations are quite good. The additional confirmation provided by the agreement of the moonquake and surface event record sections as to the boundary depth is also encouraging. Thus in sum there appear to be two sharp layer interfaces at 20 and 75 km depth; the structural interpretations are discussed below.

ALSEP 12: Here the crustal interface depths are known to be at 20 and 60 km, and so it would be encouraging if peg-leg multiples from these boundaries were visible on the record section plots. However, as mentioned before, there is evidence that on average the boundaries are too broad to produce large reflection coefficients for waves of wavelength 8 km. The data are shown in Figs. 2-10a through e in the same format as before (first the three components of the moonquake

records, and then the transverse and radial surface event sections). The theoretical curves are again as shown. Notice that for the 20 km interface the SSS-V and SSP lines on the radial and vertical components respectively are stopped at about 40° to emphasize the dominance of the other peg-leg multiples at greater distances. While the correlations are not as striking as for station 16, there is some positive evidence agreeing with 20 and 60 km interface depths. In particular, a general look at the figures shows that larger amplitudes often commence at the expected arrival time of peg-leg multiples from 60 km. The surface event record sections are shown in Fig. 2-10d and e, and again there is some agreement, particularly with the 20 km seismic phases. In sum, the record section plots are reasonably consistent with the crustal models derived from artificial impact data, thus lending confidence to the analysis technique and the results obtained at station 16.

ALSEP 14: Due to the intermittent operation of the vertical LP instrument, only a few records are amenable to polarization filtering, not nearly enough for an adequate record section. In fact, only one of the surface events (Day 107) was filtered, and although eight deep-focus moonquakes were filtered, due to the nearly non-existent signal amplitudes on the vertical component the results are of dubious value. Accordingly, the transverse unfiltered traces are plotted in

Fig. 2-11, with theoretical lines as drawn. Although some correlation is possible and expected in view of the results at station 12 and the known crustal structure, the figure serves mainly to illustrate the value of polarization filtering in identifying secondary seismic phases.

ALSEP 15: This is one of the least sensitive of the Apollo seismometer stations, and so is predictably difficult to analyze. The record sections are shown in Figs. 2-12a through 2-12h. Since six pairs of moonquake records over-lapped sufficiently to require the elimination of one from each pair, two sections are shown for each focus so as not to omit a large part of the data. The first two show the trans-verse traces, along with travel time curves drawn for 20, 60, and 90 km interface peg-legs. There is some evidence for the 20 km boundary, and also somewhat weak correlations for both 60 and 90 km reflections. It is of course possible that all three interfaces in fact exist. The next two figures contain the radial components of ground motion, along with the two phases expected from each reflector. Notice that the SSS-H (60) and the SPS+PSS (90) arrive at essentially the same time, further complicating matters. Again there is some evidence for a 20 km interface, and mixed correlations for the other two. Finally the vertical traces are given in Figs. 2-10e and f, and all three phases obtained from each interface are as drawn. Note the poor S wave amplitudes as expected and the

larger S-P amplitude train. As before, there is some evidence for all three boundary depths. The last two figures contain the horizontal components for the surface events. The dashed lines in Fig. 2-12g represent waves reflected once from boundaries at depths of 400 and 480 km, and are shown to again emphasize that there are other expected arrivals which might interfere with the expected crustal bounces. These arrivals are discussed in Chapter 3. In any case, the correlations for all three crustal interfaces are weak, and cannot resolve the uncertainties on the moonquake record sections.

The ALSEP 15 crustal structure thus remains uncertain. The 20 km interface is probably the most confident and one or both of the 60 and 90 km interfaces may exist. It is difficult to draw further conclusions.

2.4   Implications of the Seismic Results

The identification of crustal reflected phases has important consequences for lunar structure. The purpose of this section is to enumerate some of the first-order inferences that may be drawn from the above results and present some of the important issues to be considered; it is not intended to be, nor is it, a complete treatment.

The fact that these reflected waves are reasonably well-observed, at least at station 16, suggests that the interfaces responsible are at most 2 or 3 km thick, but more probably

less than a kilometer, in order to efficiently reflect and refract seismic wavelengths of 6-8 km. The ALSEP 16 boundaries at 20 and 75 km depth are almost surely analogous to the 20 and 60 km crustal layers found at ALSEP 12 by seismic refraction analysis of artificial impacts and confirmed above by observed peg-leg multiples from natural teleseismic events. This represents the first direct seismic evidence that the crust is in fact a moon-wide phenomenon, although the same inference has been made from a wealth of geochemical data. The evidence from station 15, albeit somewhat uncertain, supports this conclusion.

As discussed above, the boundary depths and velocities are well-known at station 12. Assuming the same layer velocities, the 20 and 75 km depths at ALSEP 16 are closely constrained by the travel time curve-observed pulse alignment; a depth variation of 5 km for the lower boundary would change the arrival time by 2 1/2 seconds or slightly more than one cycle, enough to significantly deteriorate the average fit of the travel time curve. The 20 km interface is even more tightly constrained. If the layer velocities are different from those observed at station 12, say by 10%, then the layer thicknesses would also change by 10%, or 2 and 5 km, respectively. Thus, assuming that the phase identification is correct, the boundary depths are controlled to at least ± 15 km, probably close to ± 10 km.

A critical assumption here of course is that the surface reflection in fact occurs at the free surface rather that at say the base of the low-velocity layer. This assumption seems to be valid at ALSEP 12, since the tentatively identified reflections arrive at times appropriate for the 20 km and 60 km interfaces (known to exist from independent data) only if the surface reflection occurs at the surface; if it occurs at the base of the low-velocity zone then the predicted arrival times would be up to seven seconds earlier than the observed pulses (the exact value depends on the wave type). Furthermore, since the relative arrival times between the various peg-leg multiples (e.g. SSS and SPS) would be different, the fit between the predicted curves and observed arrivals at ALSEP 16 would deteriorate slightly. (In addition, there would be six different arrival times for the nine peg-legs rather than four since the third (up) leg would be different from the first two.) Nevertheless, this assumption must be noted and could potentially increase the above uncertainty estimates.

If we take the ALSEP 16 results at face value, it appears that the intermediate crustal layer at 20 km is the same at both stations 12 and 16, while the lower crustal layer is significantly thicker at station 16. Perhaps coincidentally, the 15 km difference is exactly sufficient to offset by isostasy the elevation difference between the stations (16 is about 1.5 km higher than 12, King et al., 1976) assuming crust and

mantle densities of 3.0 g/cc and 3.3 g/cc, respectively. In addition, Thurber and Solomon (1978) have shown that the above crustal thicknesses are compatible with the observed gravity data, although in view of the non-uniqueness of the potential field data this is not surprising.

The geological and compositional interpretation of the set of crustal seismic results is not totally clear (compare for example Toksöz et al., 1974a, and Ryder and Wood, 1977.) The final seismic model for ALSEP 12 is shown in Fig. 2-7; for ALSEP 16 the velocities are assumed to be similar, with the base of the crust at 75 km depth instead of 60. The 20 km boundary appears to exist at both sites. The ALSEP 14 crust is by all indications similar to that at station 12, while station 15 tentatively appears to have the same 20 km interface along with possibly a 60 and/or 90 km boundary, one of which probably represents the base of the crust. This situation is summarized in Fig. 2-13.

The existence of the 20 km layer and interface at apparently all stations, particularly at the highland site, is the most interesting aspect of the above results. The rapidly increasing velocities in the layer are most likely the result of the closing of cracks and fractures by increasing pressure (Todd et al., 1973). The velocity values have been interpreted as being consistent with basaltic composition (Toksöz et al., 1974a), but other possibilities cannot be ruled out,

and in view of the great variability of elastic properties caused by the fracturing effects (Trice et al., 1974) it is not possible to uniquely constrain the composition. The nature of the interface is an interesting question. The higher velocities below 20 km and the fact that they are nearly constant with depth suggests that 20 km represents the change-over from fractured to competent rock. However, the suddenness of the velocity increase at 20 km is somewhat surprising if it is solely due to a final closing of cracks. Simmons et al. (1973) have discussed this problem in depth, and it is possible that the interface also represents a compositional change. The issue remains unresolved.

However, the fact that the interface appears to exist at both highland and mare ALSEP sites is an important datum. First, it means that the initial tentative interpretation by Toksöz et al. (1974a) identifying it as mare basalt fill at ALSEP 12 is probably not correct, especially in view of photogeologic evidence implying that the mare basalts are at most 8-10 km thick (Howard et al., 1974; Head, 1974; DeHon, 1977). Unfortunately, gravity data cannot further constrain the thickness of mare basalt fill (Thurber and Solomon, 1978) although many quantitative models have been calculated (cf. Bowin et al., 1975; Sjogren and Smith, 1976). Second, the layer appears to be at least somewhat widespread since there is some evidence for it at all ALSEP sites. This suggests.

that it is the result of some process or processes that
occurred over a substantial portion of the moon. Thus a simple
model consistent with the seismic results would have a 20 km
layer occurring extensively over the moon, overlain by a few
km of basalt in the mare basins. The bottom interface of the
basalt layer is not of course observed at ALSEP 12, but this
could be due to a variety of reasons: 1) the boundary is
shallow (2-3 km) and so is not adequately observed by the
artificial impact data or peg-leg multiples, and/or 2) it is
diffuse and the transition is obscured by the general trend of
rapidly increasing velocities attributed to the closing of
fractures and cracks under pressure (Todd et al., 1973) as
mentioned above.

Now there are significant compositional variations ob-
served on the lunar surface (cf. Metzger et al., 1974) other
than just the mare-highland contrast. This is not necessarily
inconsistent with the above model since the compositional
variations may be primarily surficial, but an important question
in this regard is the nature of the process that created
the 20 km layer and the interaction between possible chemical
layering and impact excavation processes. If for example the
interface represents in part a compositional change, then the
layer could be a feature of and result of the original crustal
formation that apparently occurred planet-wide. This would
imply that, at least at the ALSEP sites, later meteorite

impacts have not appreciably "gardened" the lunar crust at 20 km depth; this is in agreement with recent estimates of bombardment intensity since magma ocean solidification (Hörz et al., 1976) and "megaregolith" depths surmised from photogeologic studies (Head, 1976b), representing the layer of brecciated material excavated from craters.. (Of course, the largest impacts such as Imbrium would presumably have disturbed or eradicated layering at 20 km; no seismometers are located in such basins.) Nevertheless, it is possible that the 20 km interface is in fact a physical properties boundary only, and then its surmised widespread existence would have a different set of implications. In sum, the correct interpretation of the 20 km layer and its relation to crustal formation, meteorite impact processes, and present-day surface composition remains an open question.

The lower crustal layer also appears to exist at all stations, apparently representing competent rock of varying thickness with nearly constant seismic velocities. Again, the composition cannot be determined uniquely by comparing the velocities with measurements made on lunar samples, but the velocity values are compatible with a wide range of both anorthosites and basalts (Toksöz et al., 1974a). The thickness of this lower layer appears to be at least in partial isostatic equilibrium with topography. The large velocity jump at the base of the crust to the upper mantle velocities

suggests that a compositional change is responsible. The possible 60 and 90 km interfaces observed at ALSEP 15, if they indeed exist, could represent layering in the upper mantle, thus potentially implying (along with the variation in crust-mantle boundary depth observed between the other stations) lateral heterogeneity in the upper mantle. This is also discussed in Chapter 3.

In concluding this section, it is appropriate to discuss the relation between the very-low-velocity (VLV) surface layer, the surficial scattering zone, the megaregolith, and the primary crustal layers. The VLV layer probably represents the rubble and severely cracked rock (and lava flows) produced by meteorite bombardment, and constitutes a major portion of the scattering region. Below that is more competent but still highly fractured rock probably dominated by impact ejecta material for up to a few kilometers. From here to 20 km depth the velocities increase rapidly as pressure effects close the cracks; in this region varying amounts of scattering probably take place depending on the wavelength of the seismic energy. At 20 km begins truly competent and consolidated rock, producing little scattering, with constant velocities down to the major crust-mantle discontinuity.

A definitive detailed compositional and physical model for these various zones is at present non-existent, even with the accumulated geophysical, geochemical, and geological

evidence. The considerations discussed above are by no means comprehensive, and more detailed and quantitative modeling including geochemical, petrological, and cratering effect constraints is required to further analyze the problem. Nevertheless, the additional seismic constraints imposed by the observation of peg-leg multiple phases, especially at the highland ALSEP 16 site, are important to any proposed model.

Table 2-1

Velocity models used in Tables 2-2 and 2-3

Depth (km)	Vp (km/sec)	Vs (km/sec)	ρ(gm/cm^3)	Reflection
20	5.1	2.94	3.04	
60	6.8	3.9	3.06	X
520	8.0	4.6	3.4	
1738	7.5	4.1	3.5	
20	5.1	2.94	3.04	
75	6.8	3.9	3.06	X
520	8.0	4.6	3.4	
1738	7.5	4.1	3.5	
20	5.1	2.94	3.04	X
75	6.8	3.9	3.06	
520	8.0	4.6	3.4	
1738	7.5	4.1	3.5	

Table 2-2a
Travel times and amplitudes for peg-leg multiples from a 60 km interface
(source depth 1000 km)

Distance (degrees)	Travel Times (sec)				Amplitudes (x 10^3)						
	SSS	SSP	SPP	PPP	SSS-H	SPS&PSS	SSS-V	PPS	SPP&PSP	SSP	PPP
10	282.8	274.1	265.7	256.7	.117	.010	.104	.001	.026	.036	.003
20	295.5	286.5	277.6	268.7	.108	.030	.070	.003	.041	.055	.005
30	315.0	305.8	296.6	287.5	.098	.044	.037	.005	.045	.056	.005
40	339.7	330.2	320.8	311.5	.087	.046	.014	.005	.046	.046	.004
50	367.9	358.3	348.7	339.1	.078	.042	.002	.004	.050	.036	.004
60	398.4	388.6	378.8	369.1	.071	.037	.004	.004	.055	.029	.005
70	429.7	419.9	410.1	400.2	.066	.034	.005	.003	.055	.025	.005
80	460.9	451.1	441.3	431.5	.063	.033	.003	.003	.050	.025	.005
90	491.1	481.4	471.8	462.1	.060	.033	.002	.003	.041	.028	.004

Table 2-2b

75 km interface

Distance (degrees)	Travel Times (sec)				Amplitudes (x 10^3)						
	SSS	SSP	SPP	PPP	SSS-H	SPS&PSS	SSS-V	PPS	SPP&PSP	SSP	PPP
10	291.1	280.7	270.3	259.9	.115	.010	.103	.001	.025	.036	.003
20	303.6	292.9	282.3	271.7	.107	.030	.070	.003	.040	.055	.005
30	322.9	312.0	301.1	290.2	.097	.044	.037	.005	.044	.055	.005
40	347.5	336.2	325.0	313.8	.087	.046	.013	.005	.045	.046	.004
50	375.6	364.1	352.6	341.1	.078	.041	.001	.004	.049	.036	.004
60	406.0	394.3	382.6	370.9	.071	.036	.005	.004	.055	.028	.005
70	437.3	425.5	413.7	401.9	.066	.033	.006	.003	.057	.024	.005
80	468.5	456.7	445.0	433.3	.063	.032	.004	.003	.052	.025	.005
90	498.8	487.2	475.6	464.0	.060	.032	.001	.003	.043	.027	.004

Table 2-2c

20 km interface

Distance (degrees)	Travel Times (sec)				Amplitudes ($\times 10^3$)						
	SSS	SSP	SPP	PPP	SSS-H	SPS&PSS	SSS-V	PPS	SSP&PSP	SSP	PPP
10	263.0	258.8	254.4	250.1	.131	.010	.120	.001	.034	.033	.005
20	276.0	271.7	267.3	263.0	.121	.030	.087	.004	.055	.050	.008
30	296.0	291.6	287.2	282.8	.108	.045	.054	.006	.064	.051	.009
40	321.1	316.6	312.2	307.7	.096	.049	.031	.006	.065	.044	.008
50	349.7	345.2	340.6	336.1	.086	.048	.019	.006	.066	.038	.007
60	380.3	375.8	371.2	366.7	.079	.044	.013	.005	.064	.032	.007
70	411.7	407.1	402.6	398.0	.073	.041	.011	.005	.060	.030	.007
80	442.8	438.2	433.7	429.2	.069	.039	.013	.004	.055	.029	.006
90	472.8	468.3	463.8	459.3	.066	.037	.016	.004	.050	.029	.006

Table 2-2d

20 km interface; source depth 700 km

Distance (degrees)	Travel Times (sec)				Amplitudes (x 10^3)						
	SSS	SSP	SPP	PPP	SSS-H	SPS&ISS	SSS-V	PPS	SSP&PSP	SSP	PPP
10	193.9	189.6	185.2	180.9	.168	.042	.121	.005	.076	.069	.011
20	217.3	212.8	208.2	203.8	.132	.072	.033	.009	.097	.059	.011
30	250.6	245.9	241.2	236.5	.100	.048	.005	.005	.113	.025	.011
40	289.6	284.8	280.0	275.2	.077	.017	.015	.001	.162	.002	.013
50	331.9	327.0	322.1	317.2	.064	.063	.018	.003	.298	.013	.020
60	375.7	370.7	365.8	360.9	.059	.170	.023	.009	.678	.037	.042
70	419.8	414.9	410.0	405.0	.061	.101	.019	.006	.445	.022	.029
80	462.7	457.9	453.0	448.2	.059	.022	.013	.001	.181	.004	.014
90	503.3	498.6	493.9	489.1	.056	.021	.008	.001	.092	.007	.008

Table 2-3a

Travel times and amplitudes of direct P and S waves and refracted converted P and S waves from a 60 km interface for a moonquake focus at 1000 km depth.

Distance (degrees)	Travel Times (sec)				Amplitudes (x 10^3)				
	P	S	PS	SP	S-H	P	S-V	PS	SP
10	135.8	242.1	144.5	233.4	.930	.946	.929	.018	.031
20	143.1	255.2	151.9	246.3	.881	.891	.876	.032	.057
30	154.3	275.3	163.1	266.1	.815	.820	.805	.041	.075
40	168.2	300.6	177.1	291.1	.749	.748	.726	.044	.084
50	184.0	329.3	192.9	319.6	.689	.683	.677	.044	.089
60	200.8	359.9	209.8	350.1	.637	.627	.624	.042	.089
70	218.0	391.2	226.9	381.4	.593	.581	.580	.039	.084
80	234.9	422.3	243.9	412.6	.555	.541	.544	.035	.077
90	251.2	452.3	260.1	442.7	.521	.509	.513	.031	.068

Table 2-3b

Refracted converted waves from 20 km and 75 km interfaces

Distance (degrees)	Travel Times (sec)				Amplitudes ($\times 10^3$)			
	20 km		75 km		20 km		75 km	
	PS	SP	PS	SP	PS	SP	PS	SP
10	140.5	238.4	146.5	232.3	.0233	.0409	.0185	.0311
20	147.8	251.4	153.9	245.2	.0411	.0743	.0328	.0569
30	158.9	271.5	165.1	264.9	.0517	.0965	.0412	.0749
40	172.9	296.7	179.1	289.9	.0559	.1070	.0446	.0841
50	188.7	325.4	195.0	318.3	.0559	.1124	.0445	.0901
60	205.6	356.0	211.9	348.8	.0534	.1099	.0425	.0896
70	222.7	387.4	229.0	380.1	.0495	.1032	.0393	.0852
80	239.6	418.4	245.9	411.2	.0449	.0938	.0356	.0778
90	256.0	448.4	262.2	441.4	.0401	.0830	.0316	.0688

Table 2-4

Velocity model used in Fig. 2-8b.

Depth to bottom of layer (km)	Vp (km/sec)	Vs (km/sec)
20	5.1	2.94
75	6.8	3.9
520	7.8	4.47
1738	7.7	4.24

Figure Captions

Fig. 2-1.   Compressional wave travel time and amplitude
data and theoretical curves (Fig. 2-7) for artifical
impact data, including a ray path diagram (from Toksöz
et al., 1974a).

Fig. 2-2.   Compressional wave travel time data and theory
for farther distance; two possible mantle velocity
curves are shown (from Toksöz et al., 1974a).

Fig. 2-3.   Shear wave data and curves corresponding to Fig.
2-1 (from Toksöz et al., 1974a).

Fig. 2-4.   Tau method velocity bounds for the lunar crust
(from Toksöz et al., 1974a).

Fig. 2-5.   Record section plot of artificial impact
seismograms with theoretical travel time curve showing
large amplitude cusp (from Toksöz et al., 1974a).

Fig. 2-6.   Observed and theoretical seismograms calculated
for artificial impact data (from Toksöz et al., 1974a).

Fig. 2-7.   Final crustal velocity structure for the ALSEPS
12-14 region (from Toksöz et al., 1974a).

Fig. 2-8a. Ray paths of reflected and converted crustal
phases. b. Travel time curve for SSS peg-leg multiple
from a 75 km interface for a surface source. Velocity
model as given in Table 2-4.

Fig. 2-9. Record section plots for ALSEP 16 station, with theoretical travel time curves as shown. Note that in this and other record section figures the A45 and A46 records are very similar to those from A1, and so do not represent totally independent information.

Fig. 2-10. Record section plots for ALSEP 12.

Fig. 2-11. Record section plot for ALSEP 14.

Fig. 2-12. Record section plots for ALSEP 15.
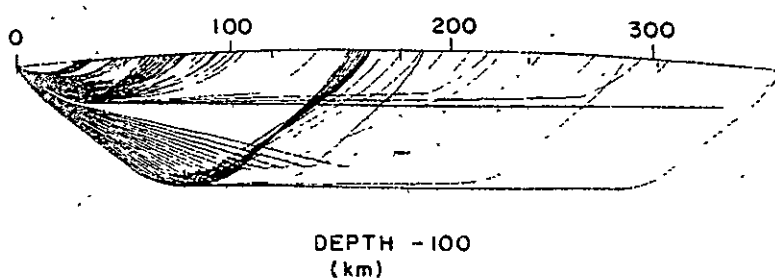
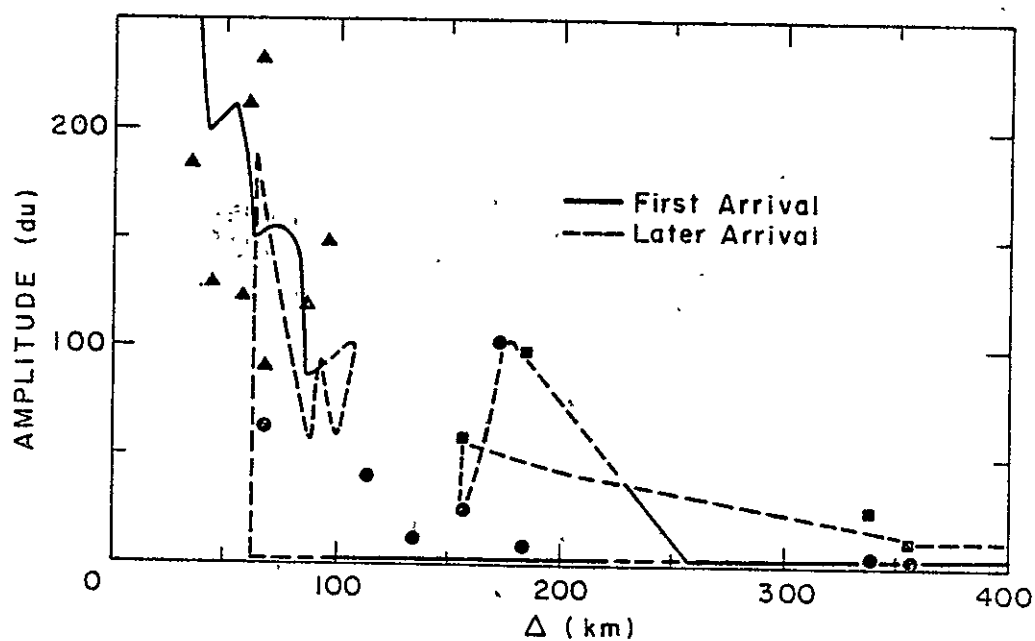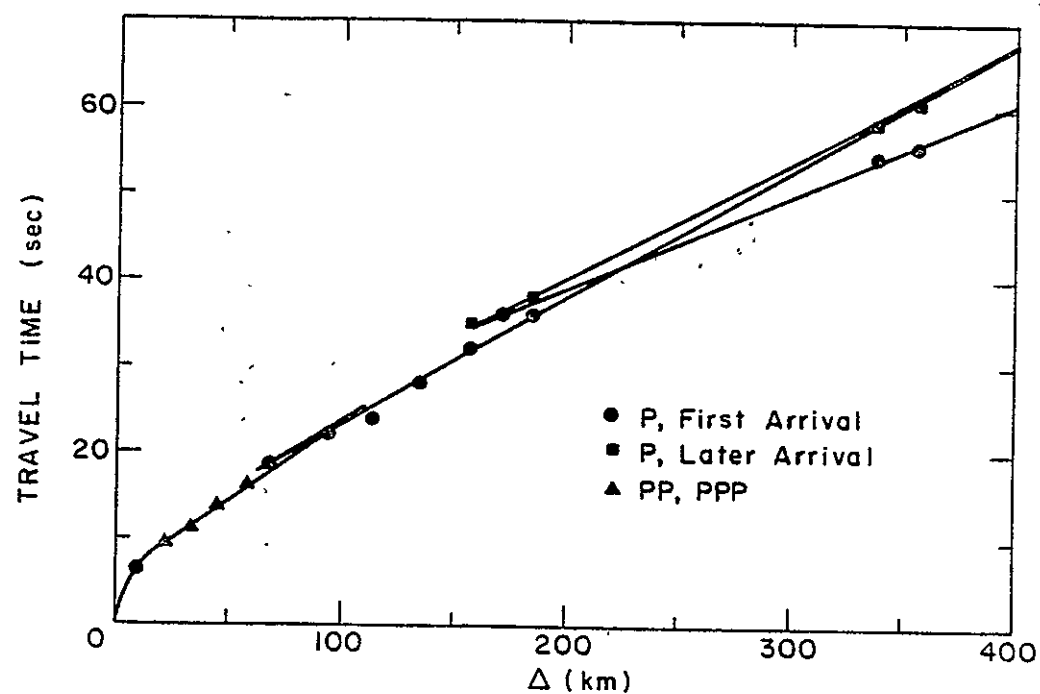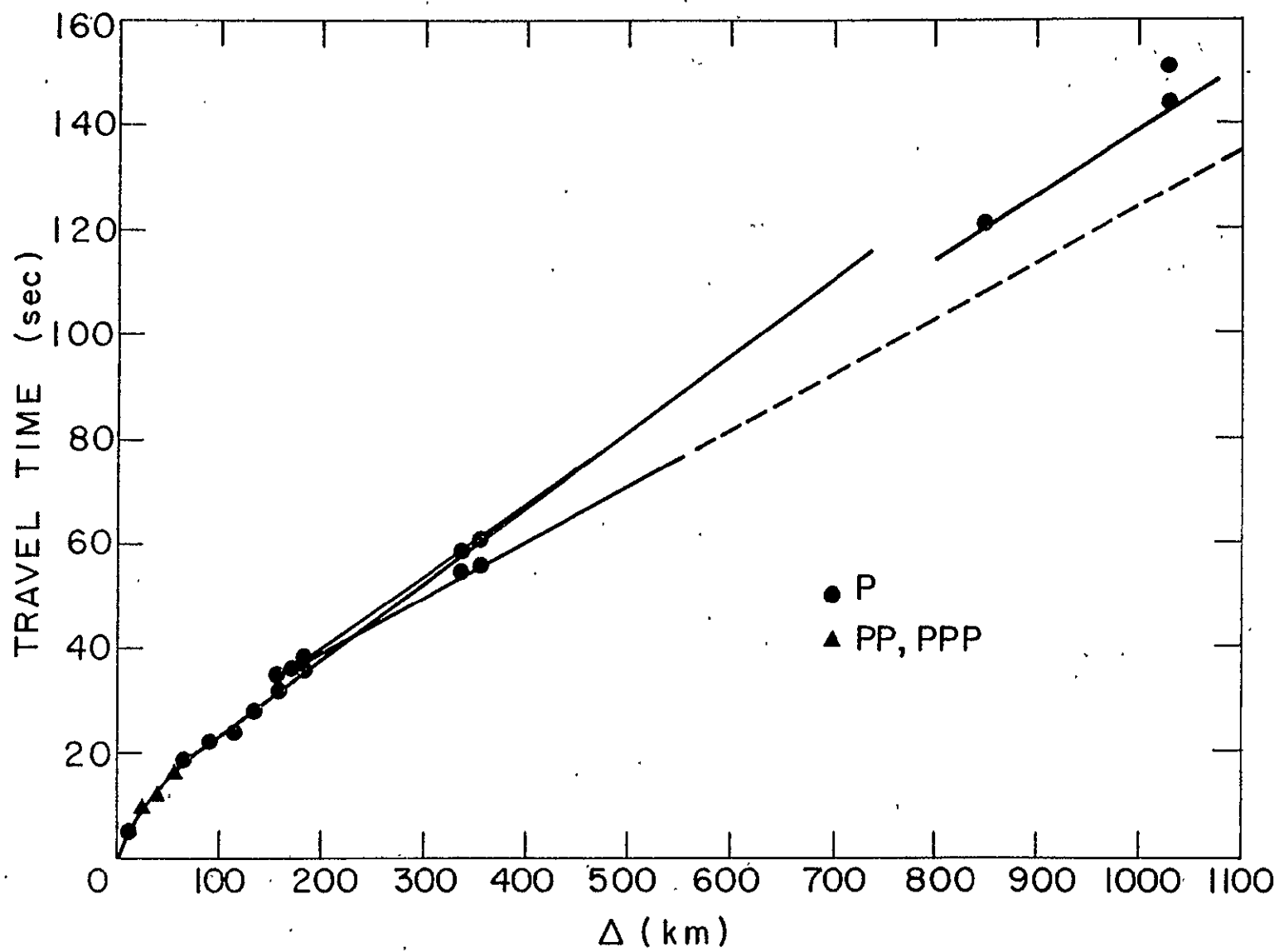Fig. 2-13. Crustal interfaces observed at each station.

Figure 2-1
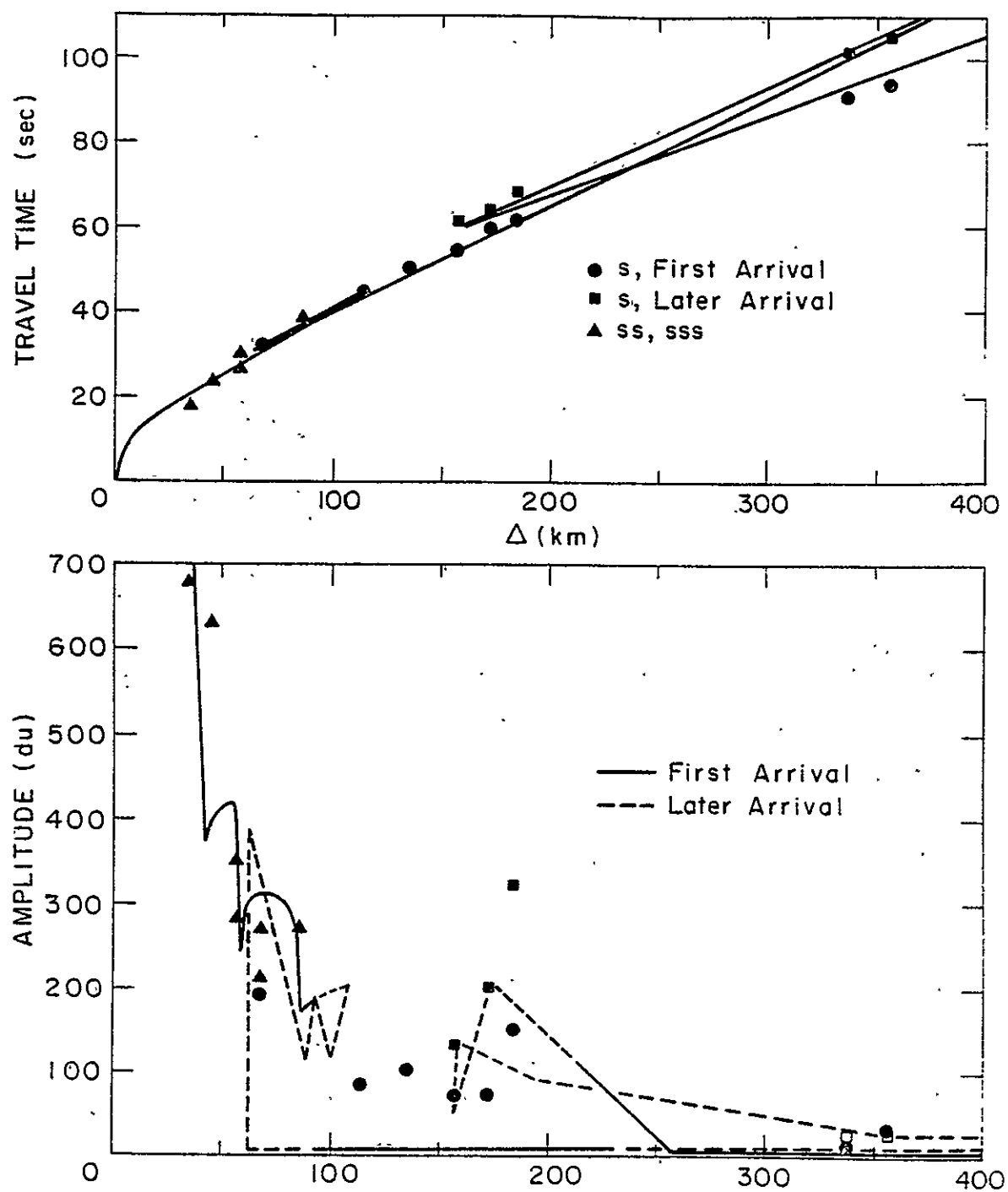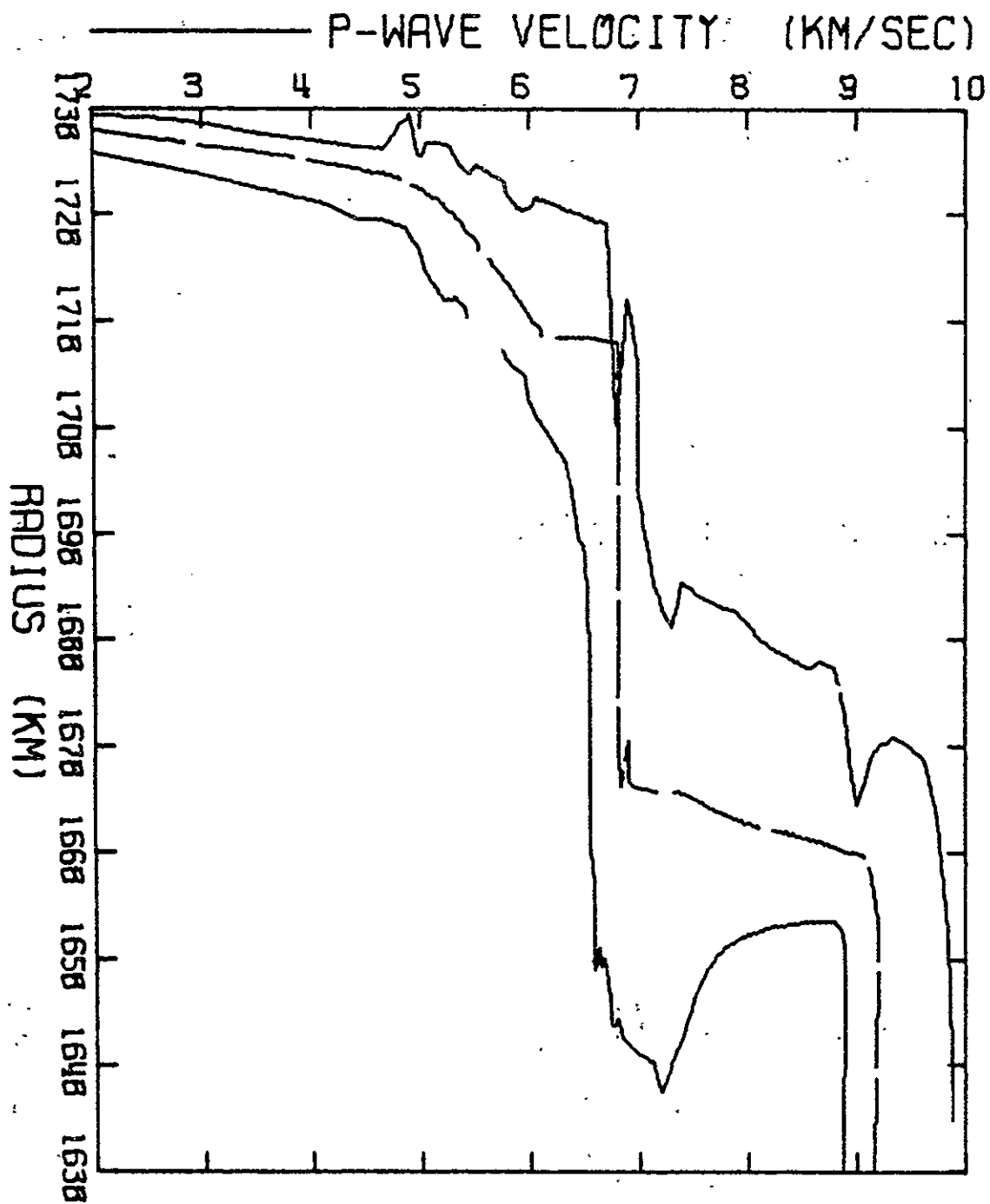
Figure 2-2

Figure 2-3

Figure 2-4

Figure 2-5

TIME (SEC)

OBSERVED   THEORY

DISTANCE (DEG)

Figure 2-6

Figure 2-7

135
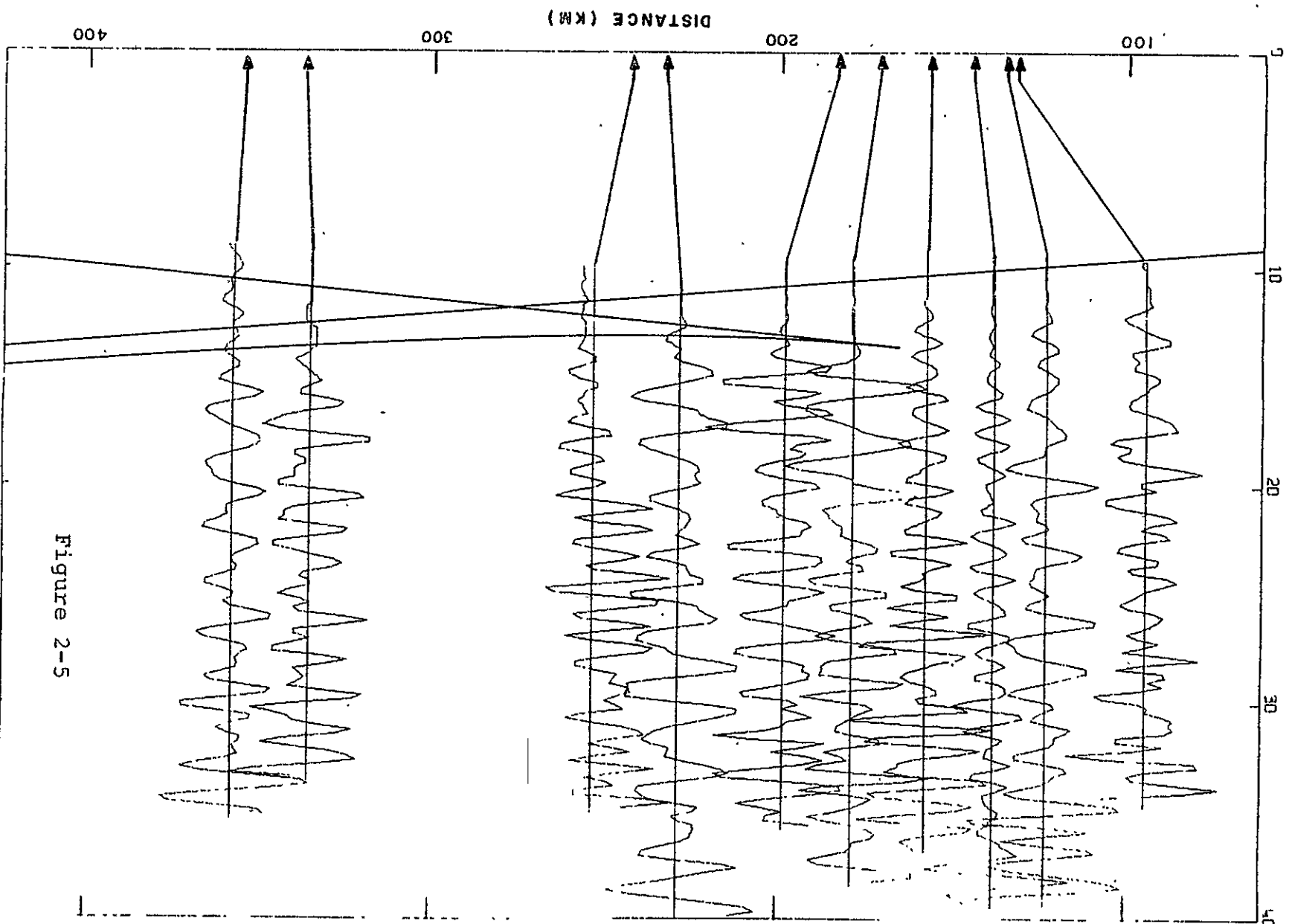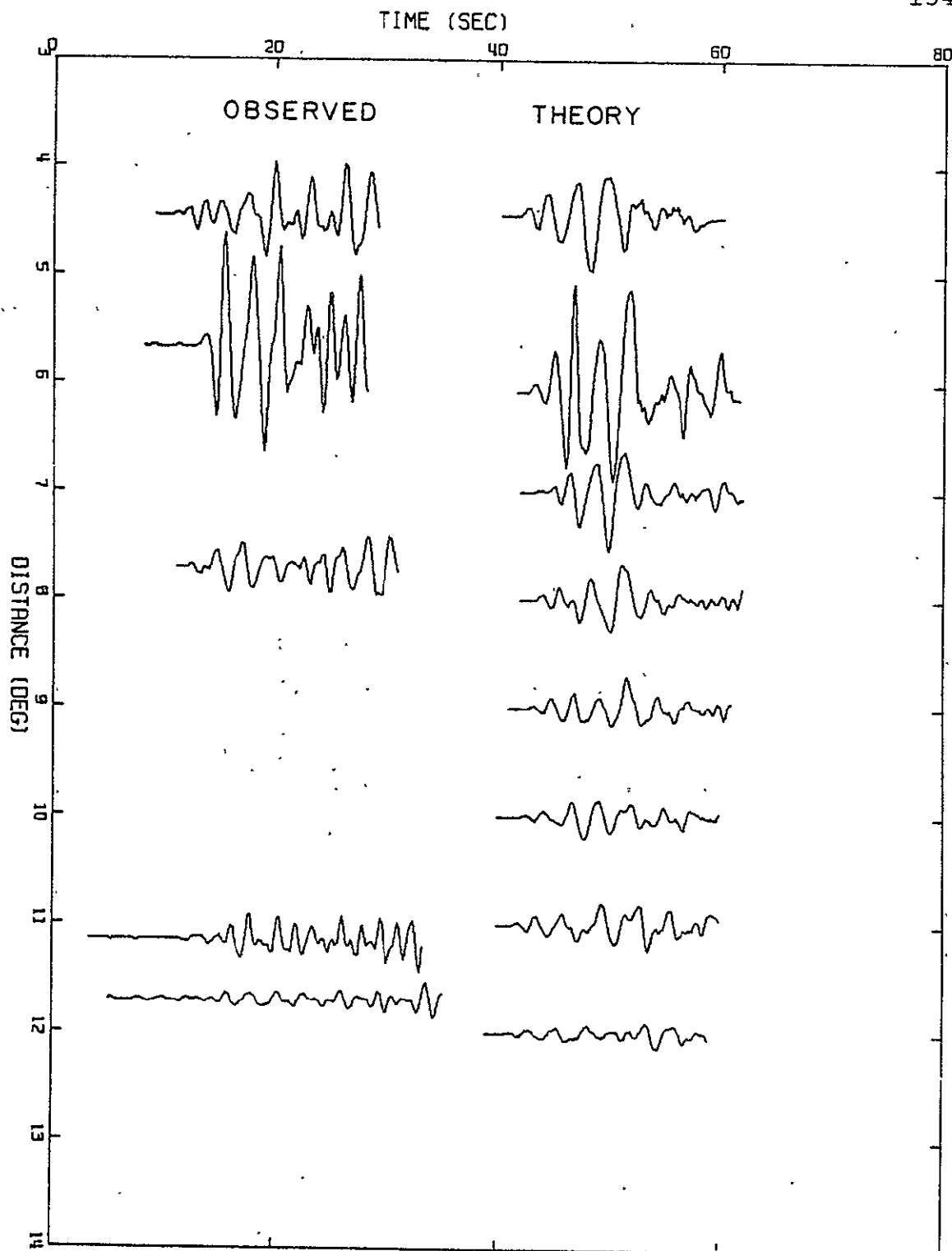
Figure 2-8a

Figure 2-8b
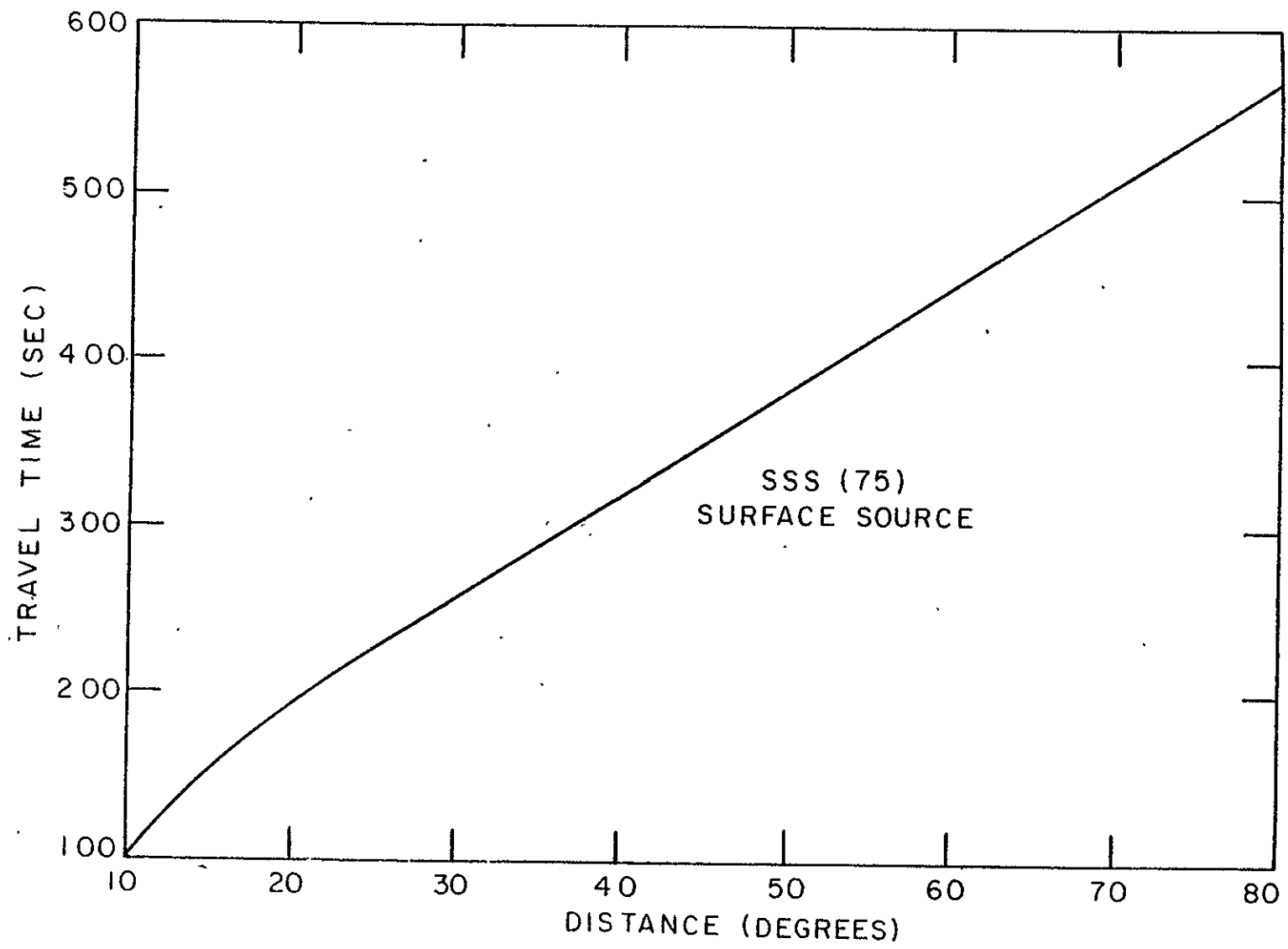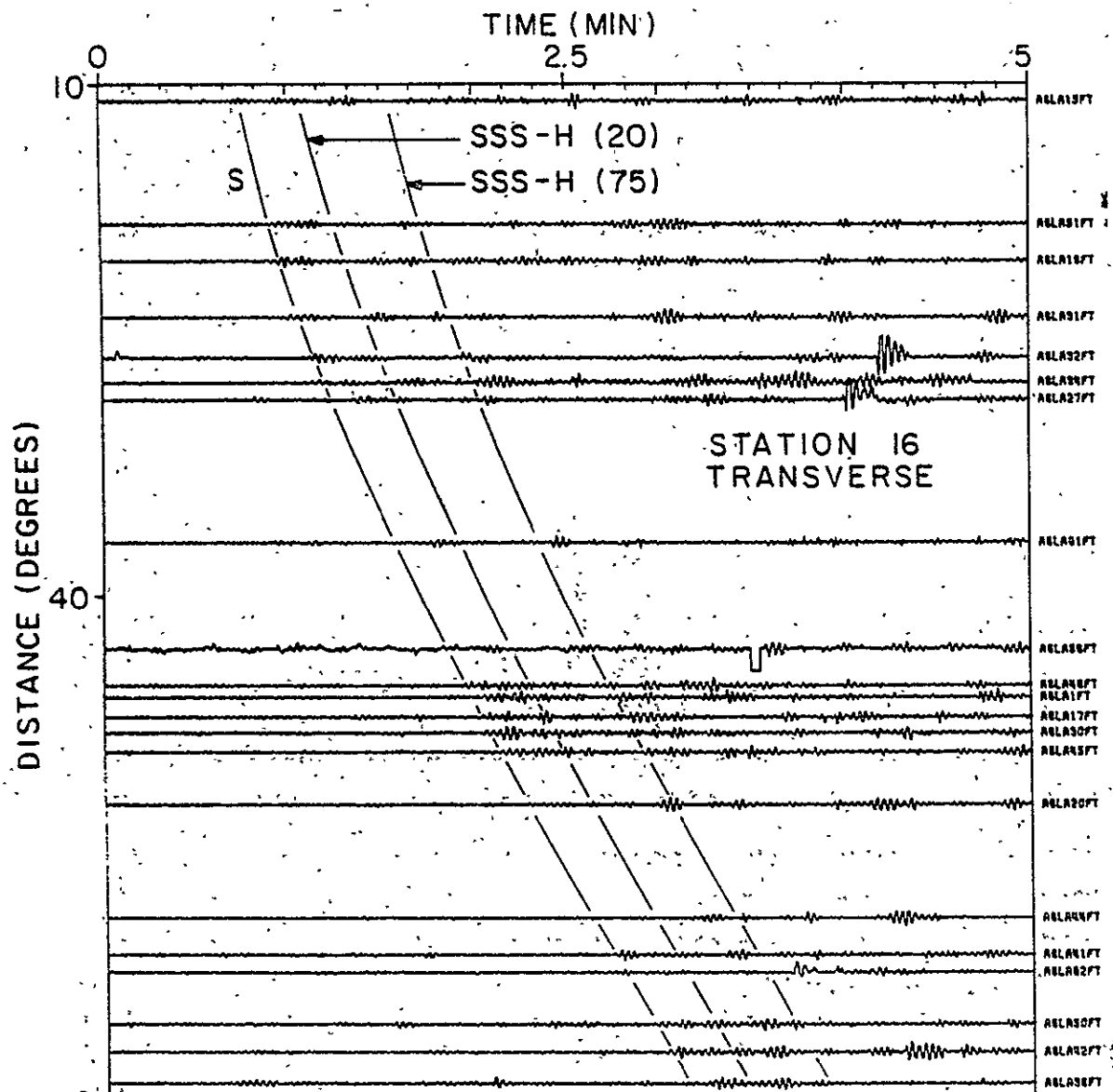
SSS (75)
SURFACE SOURCE

TRAVEL TIME (SEC)

DISTANCE (DEGREES)

137

Figure 2-9a

Figure 2-9b
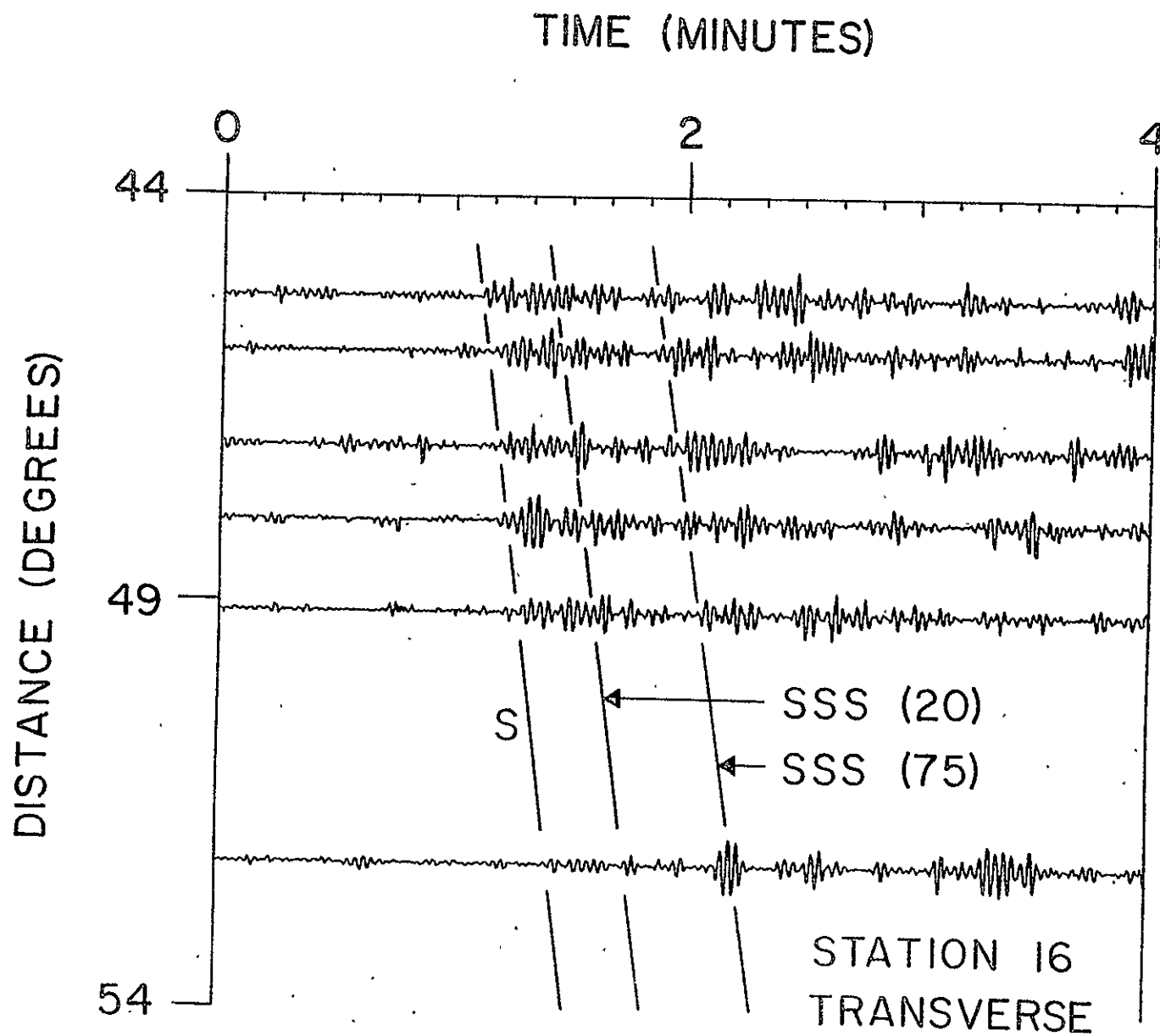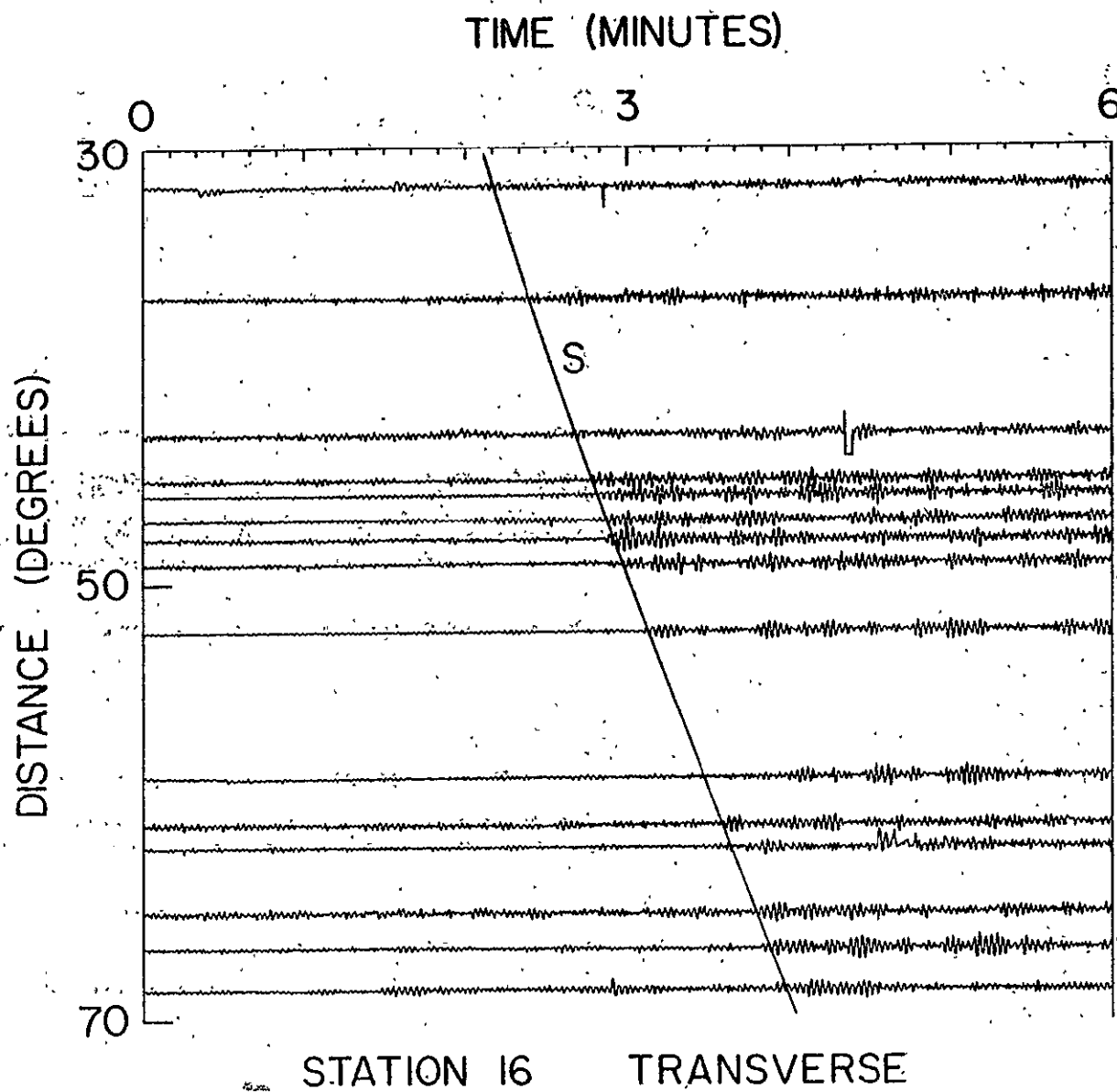
TIME (MINUTES)

DISTANCE (DEGREES)

STATION 16
TRANSVERSE

SSS (20)

SSS (75)

S

TIME (MINUTES)

DISTANCE (DEGREES)

STATION 16   TRANSVERSE

Figure 2-9c

Figure 2-9d

Figure 2-9e

TIME (MIN)

DISTANCE (DEGREES)

STATION 16
VERTICAL

SSP (75)
SPP & PSP (75)

SSP (20)
SPP & PSP (20)

S-P (20)
S-P (75)
S
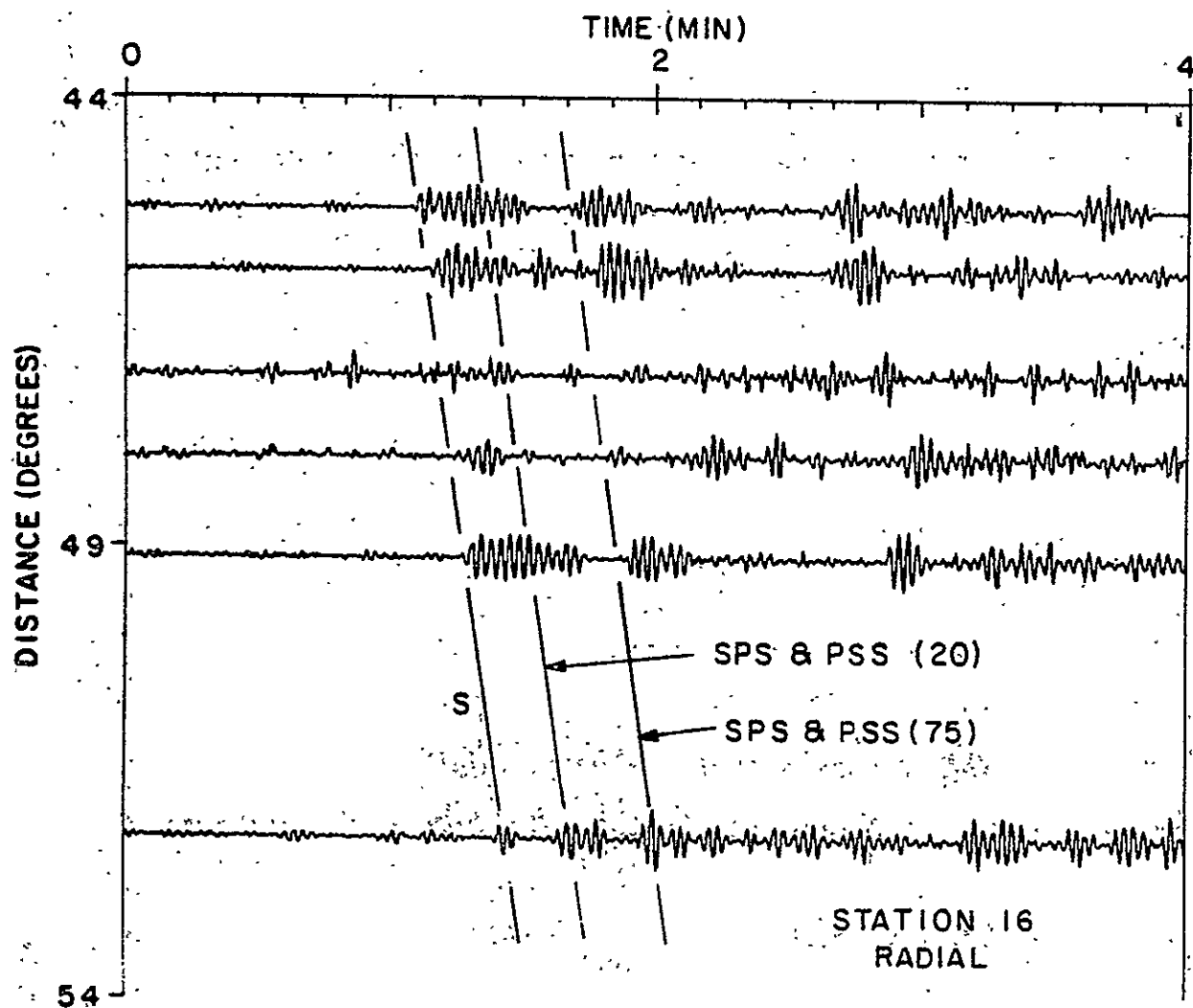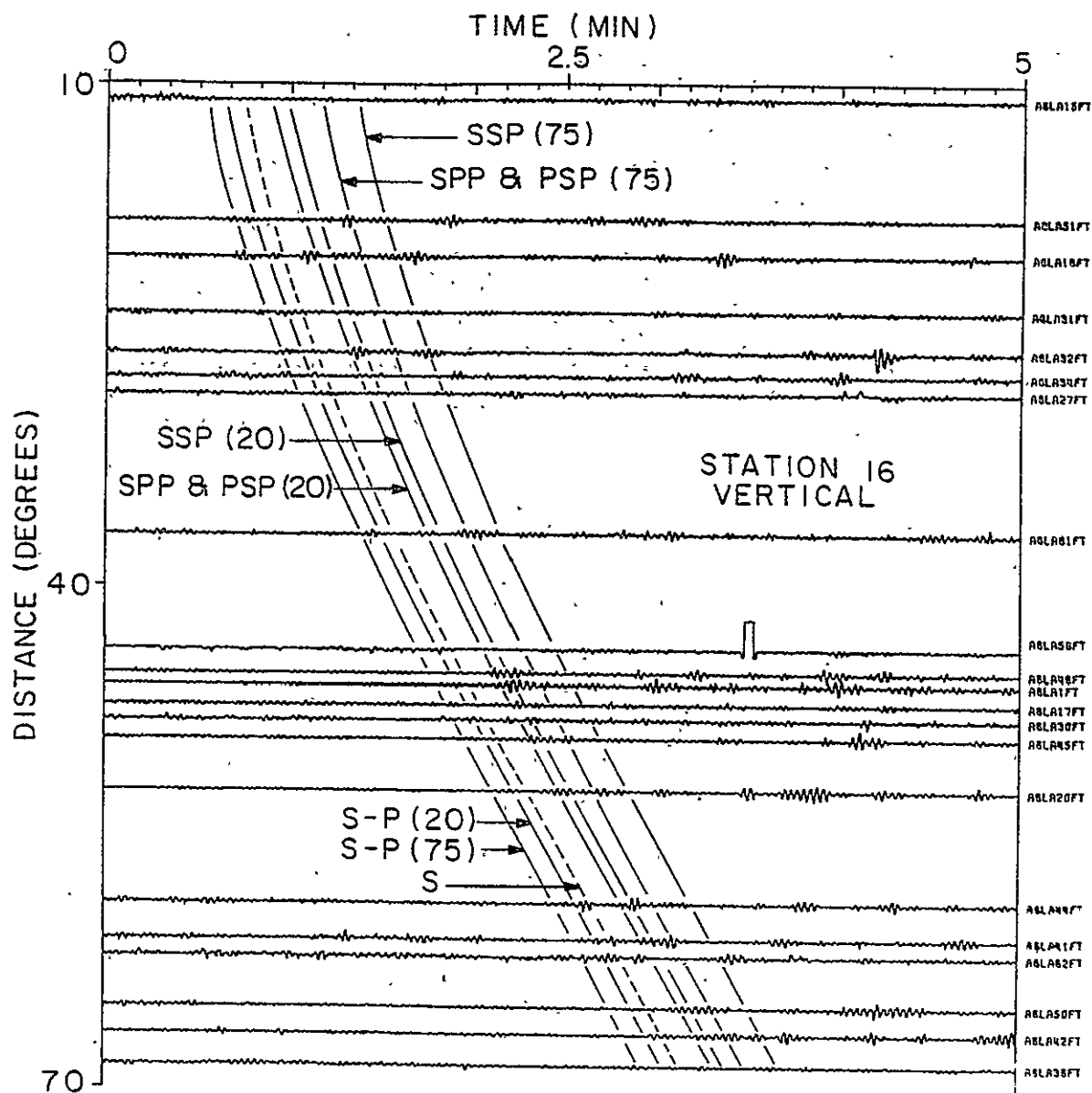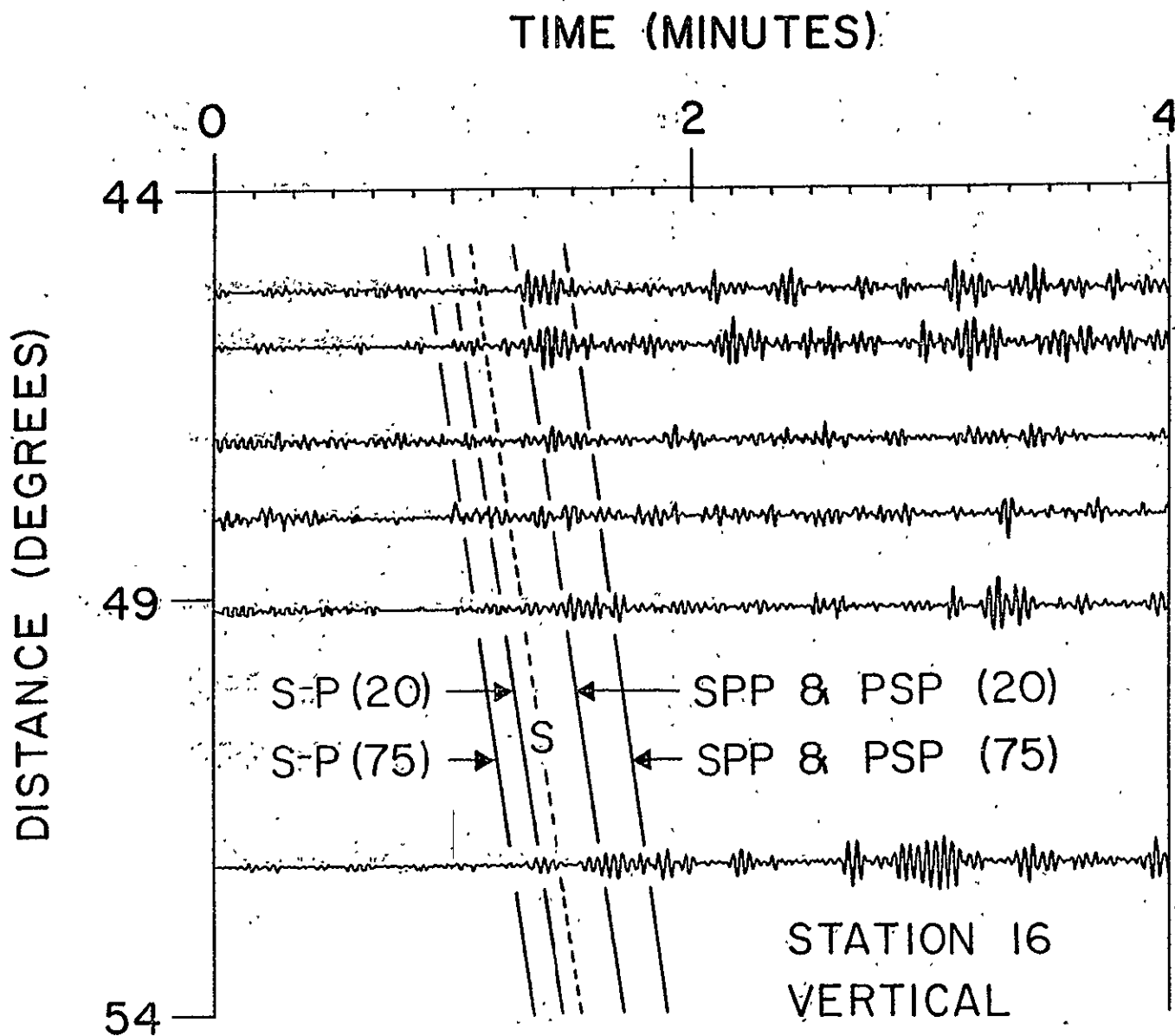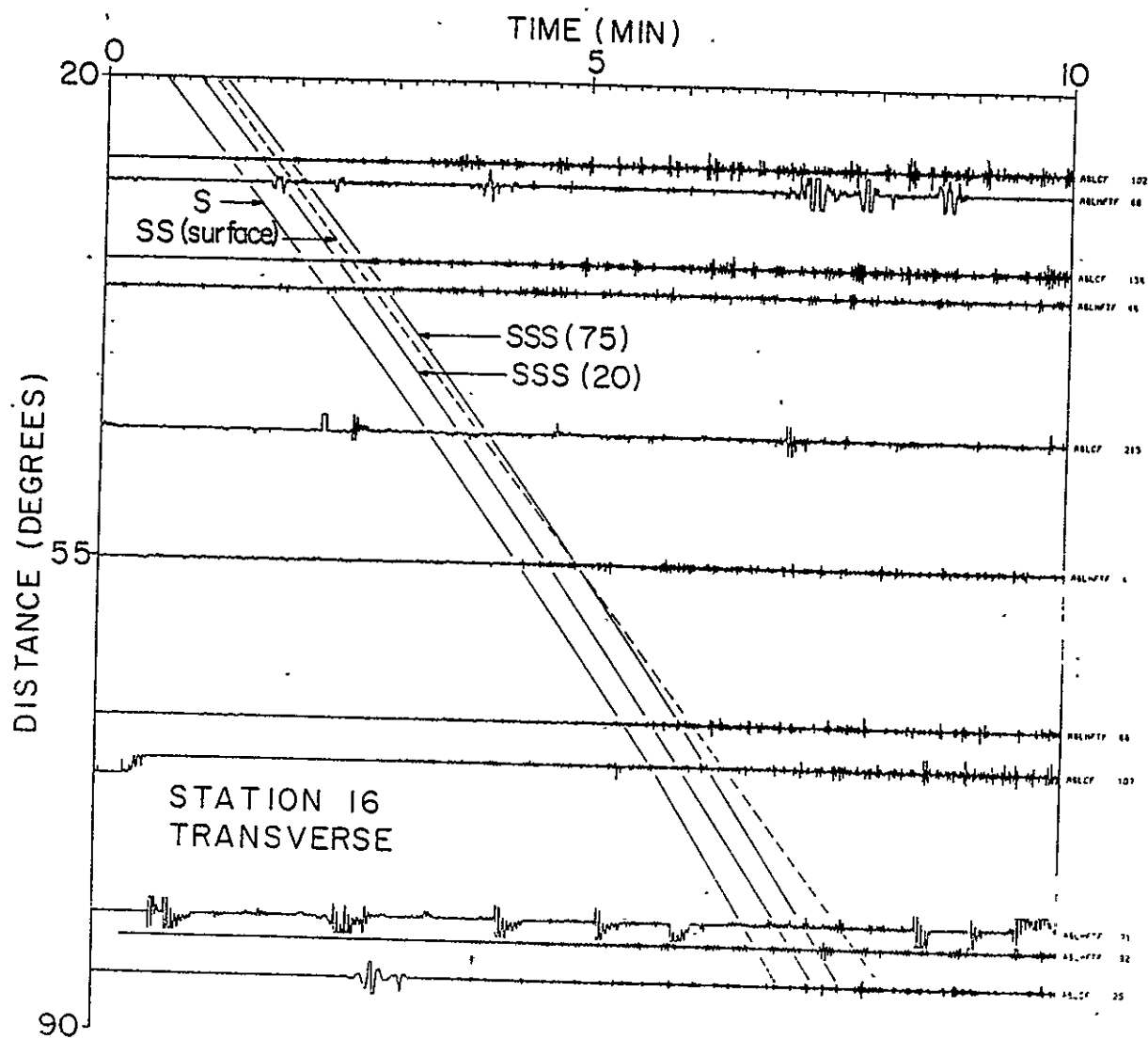
Figure 2-9f

Figure 2-9g

Figure 2-9h
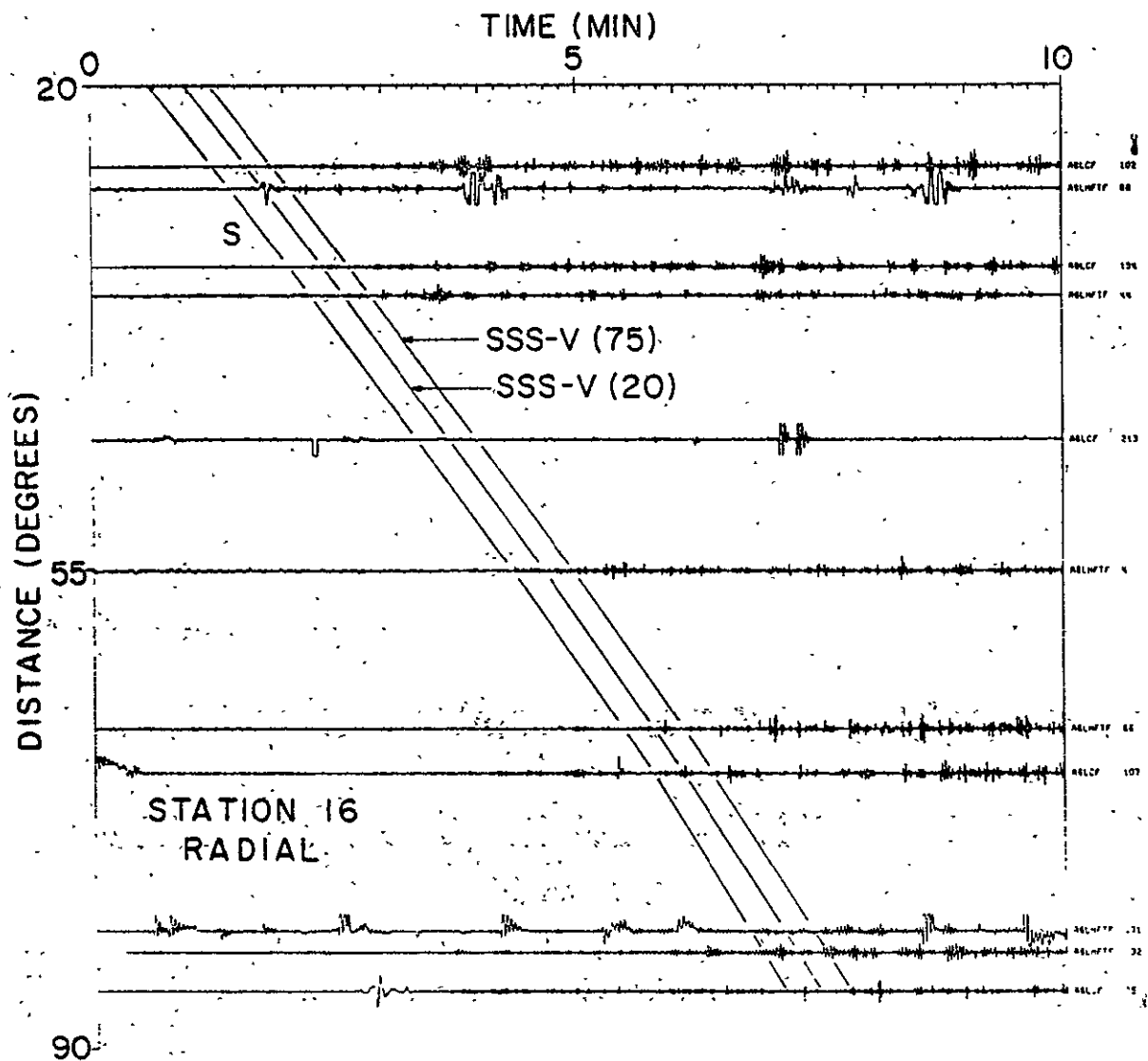
Figure 2-9i

Figure 2-10a

Figure 2-10b

Figure 2-10c
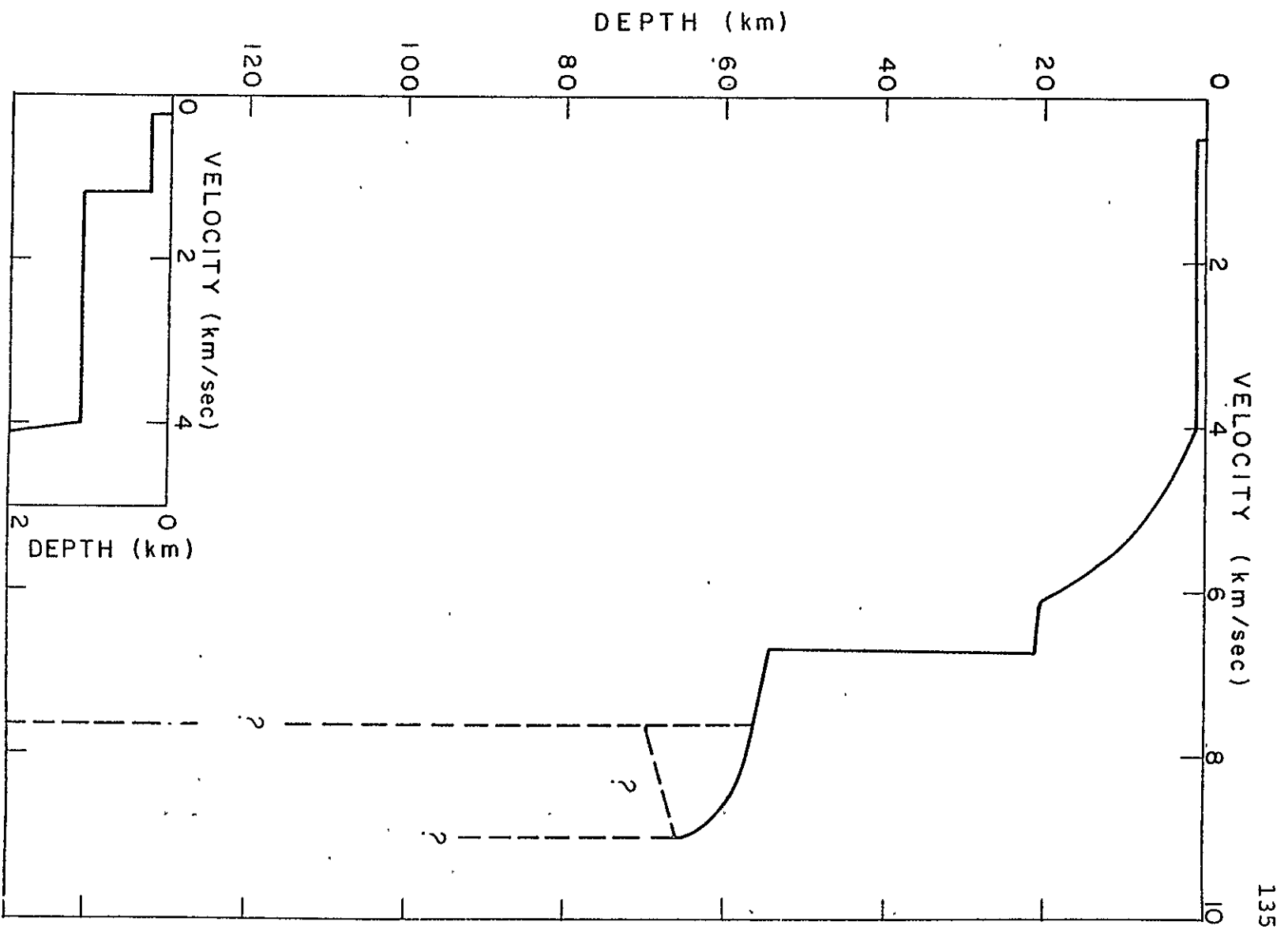
Figure 2-10d

Figure 2-10e

152

Figure 2-11

Figure 2-12a

TIME (MIN)

0   2.5   5

SSS-H (20)
SSS-H (60)
SSS-H (90)

S

STATION 15
TRANSVERSE
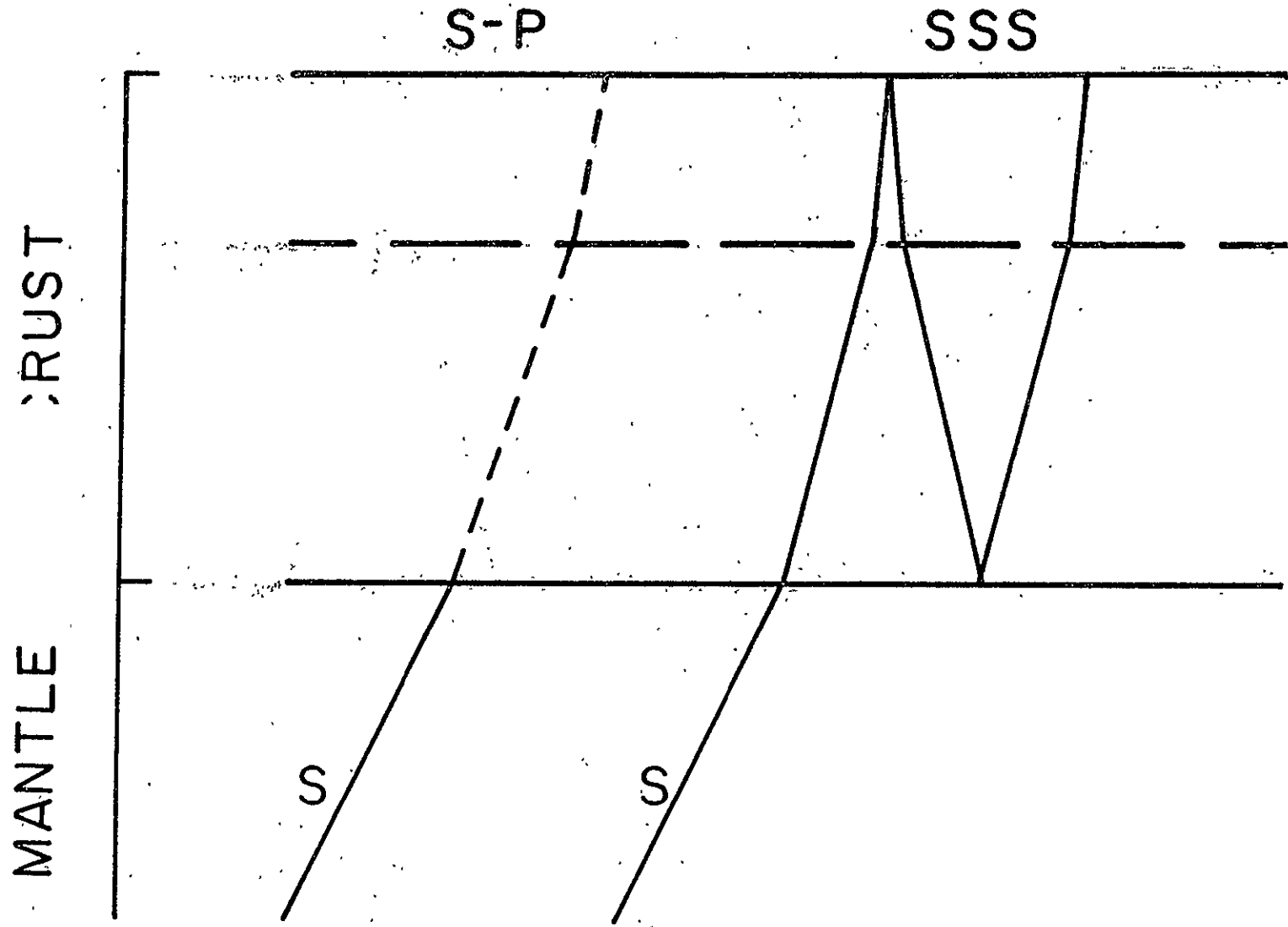
DISTANCE (DEGREES)

1.0
40
70

ASLAS1FT
ASLA17FT
ASLA81FT
ASLA90FT
ASLA96FT
ASLA50FT
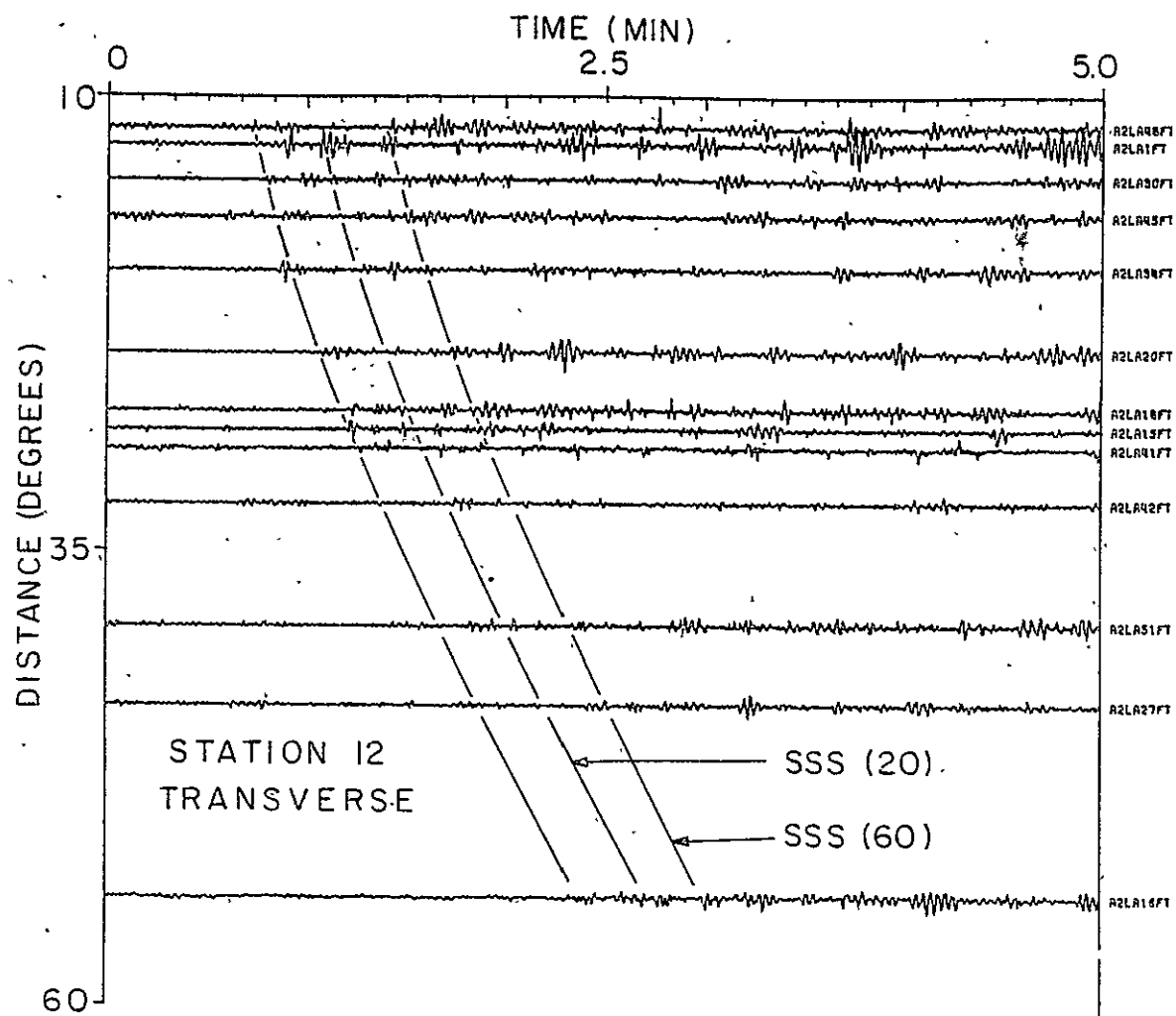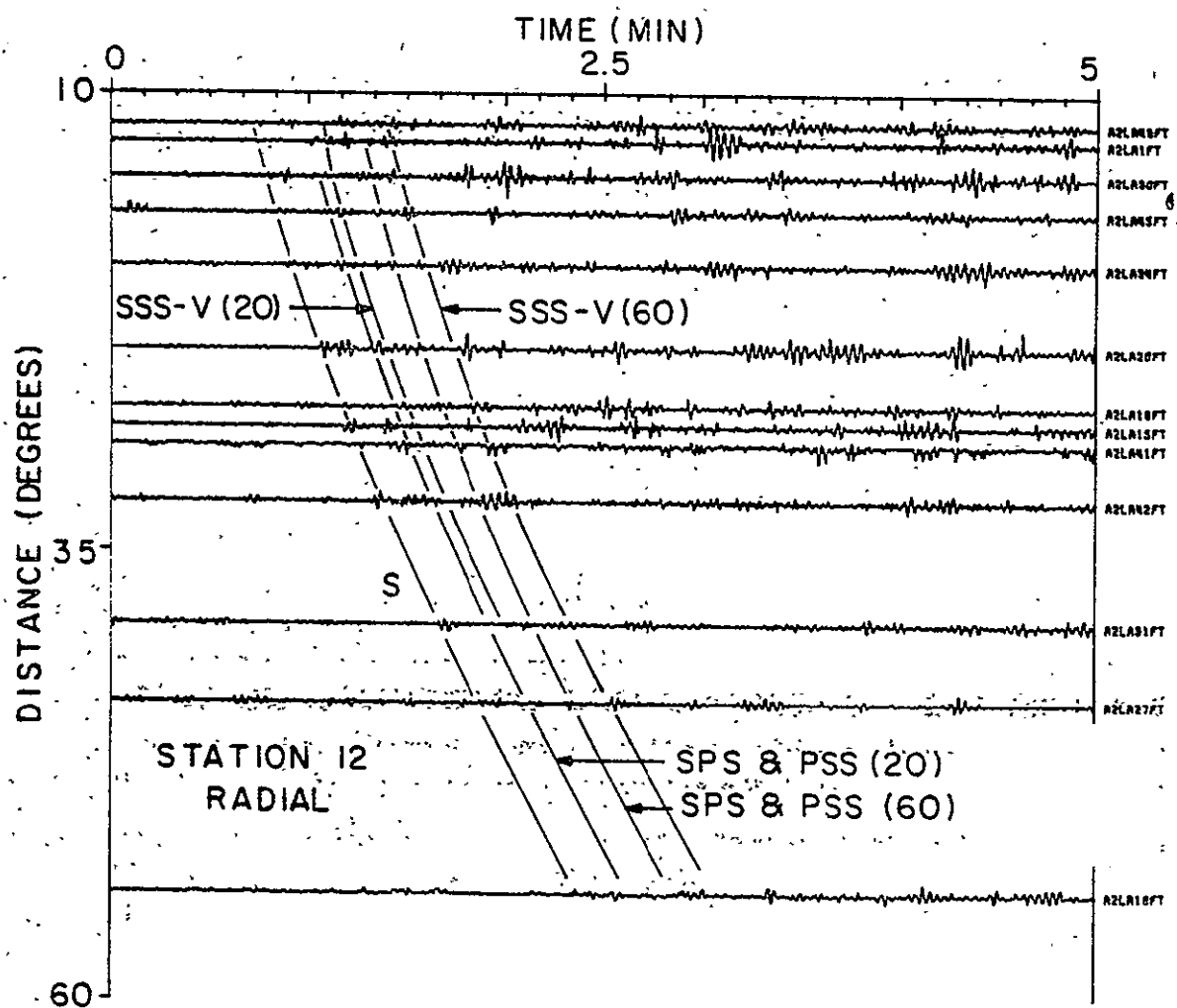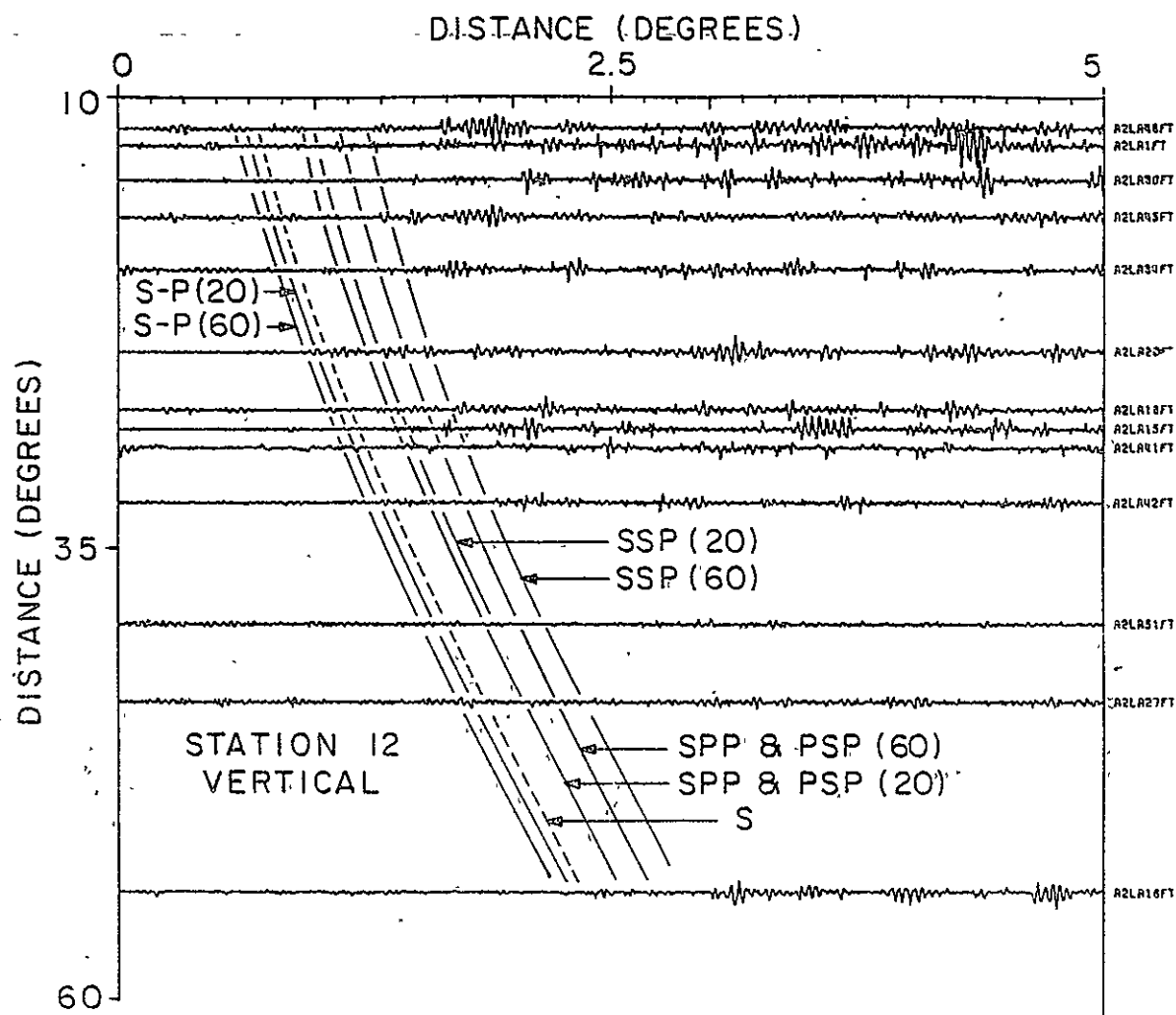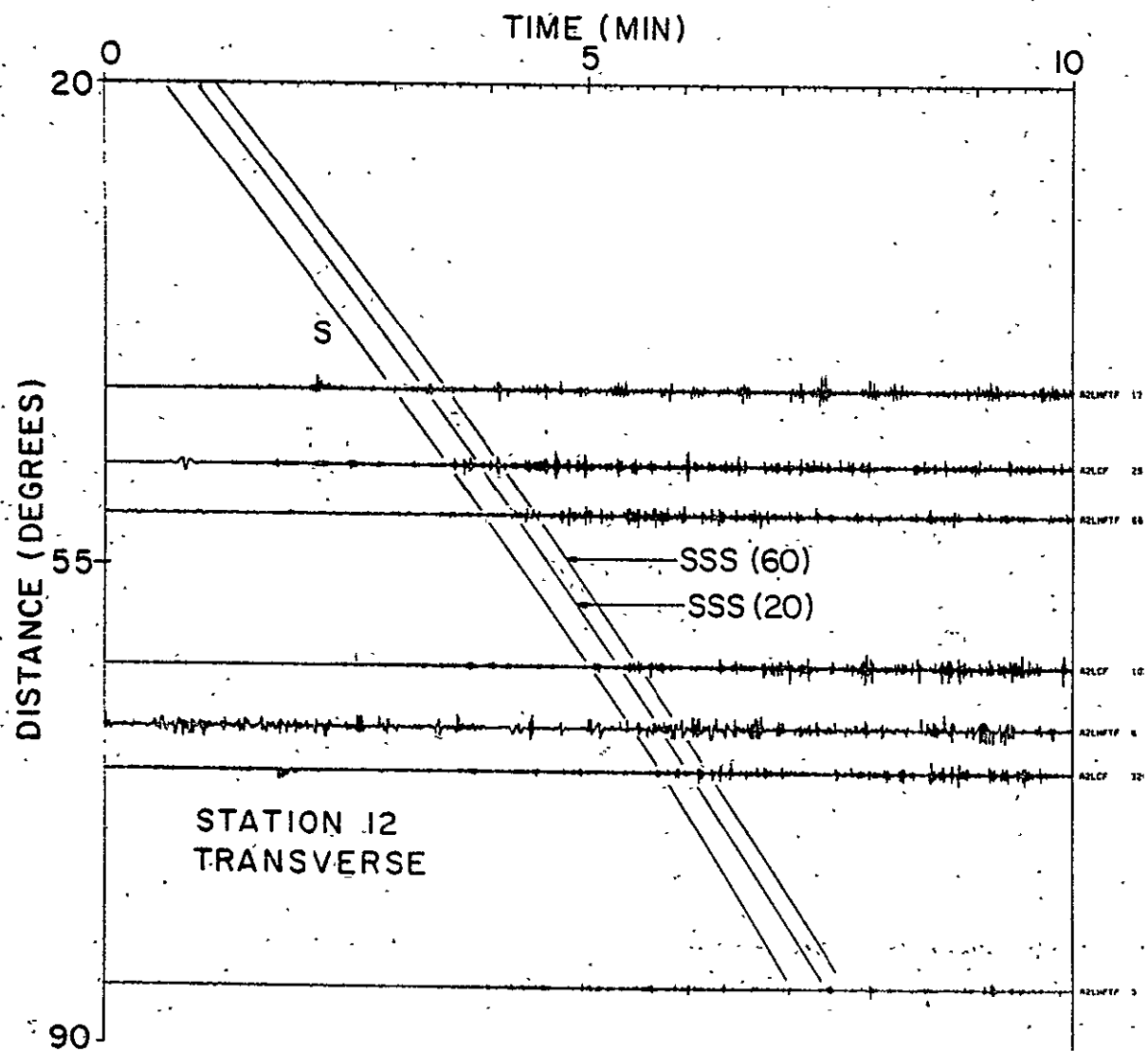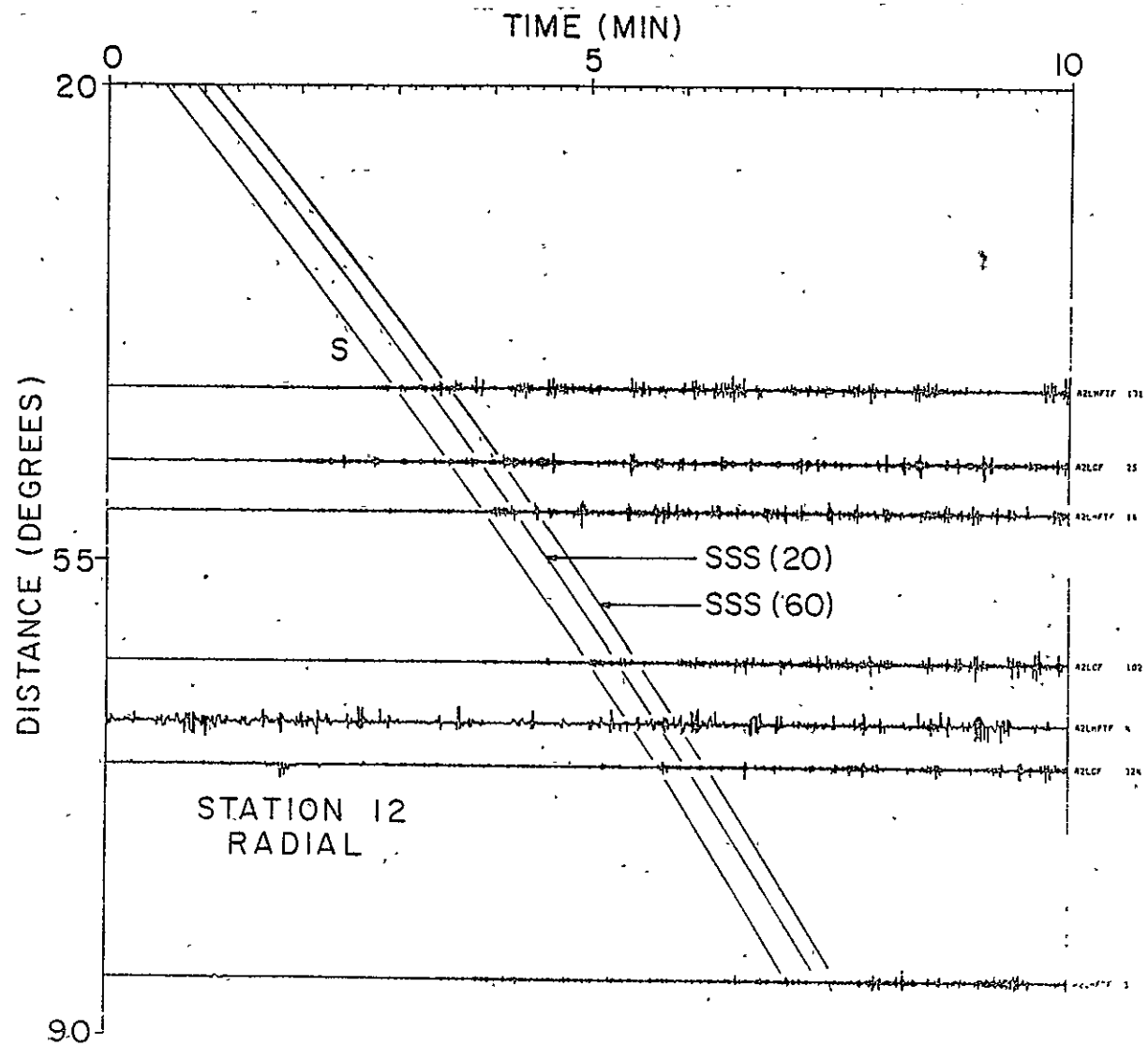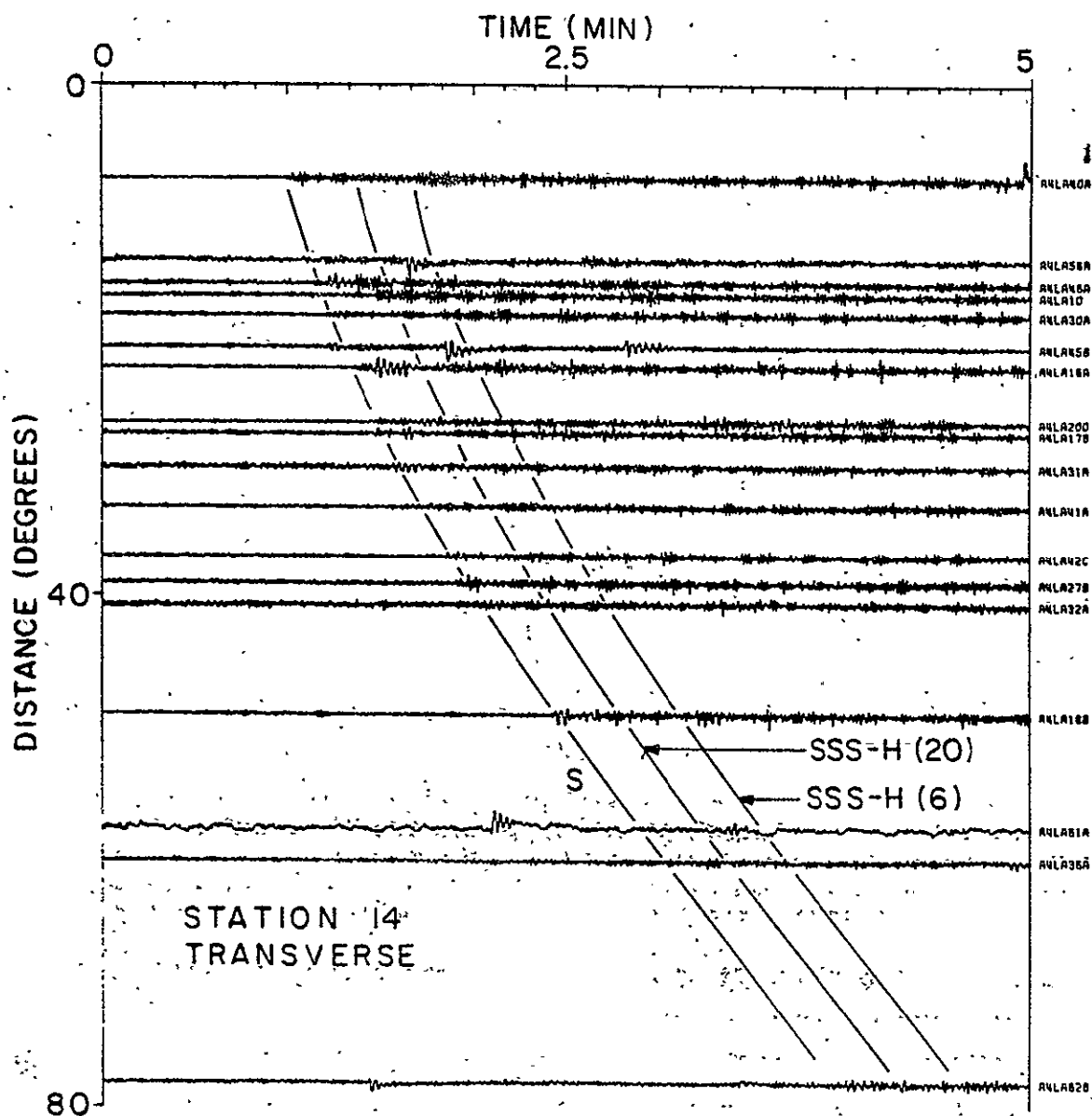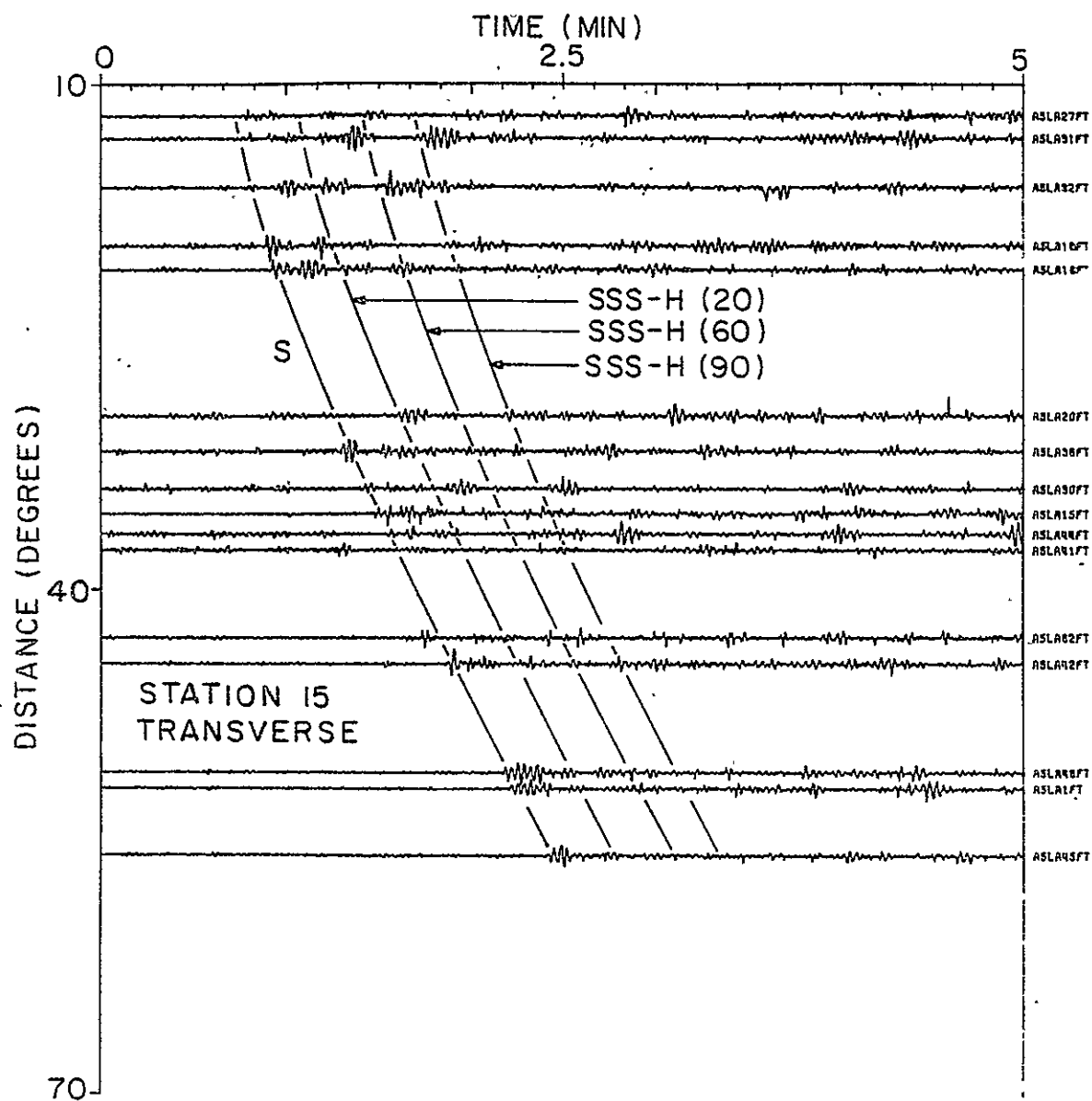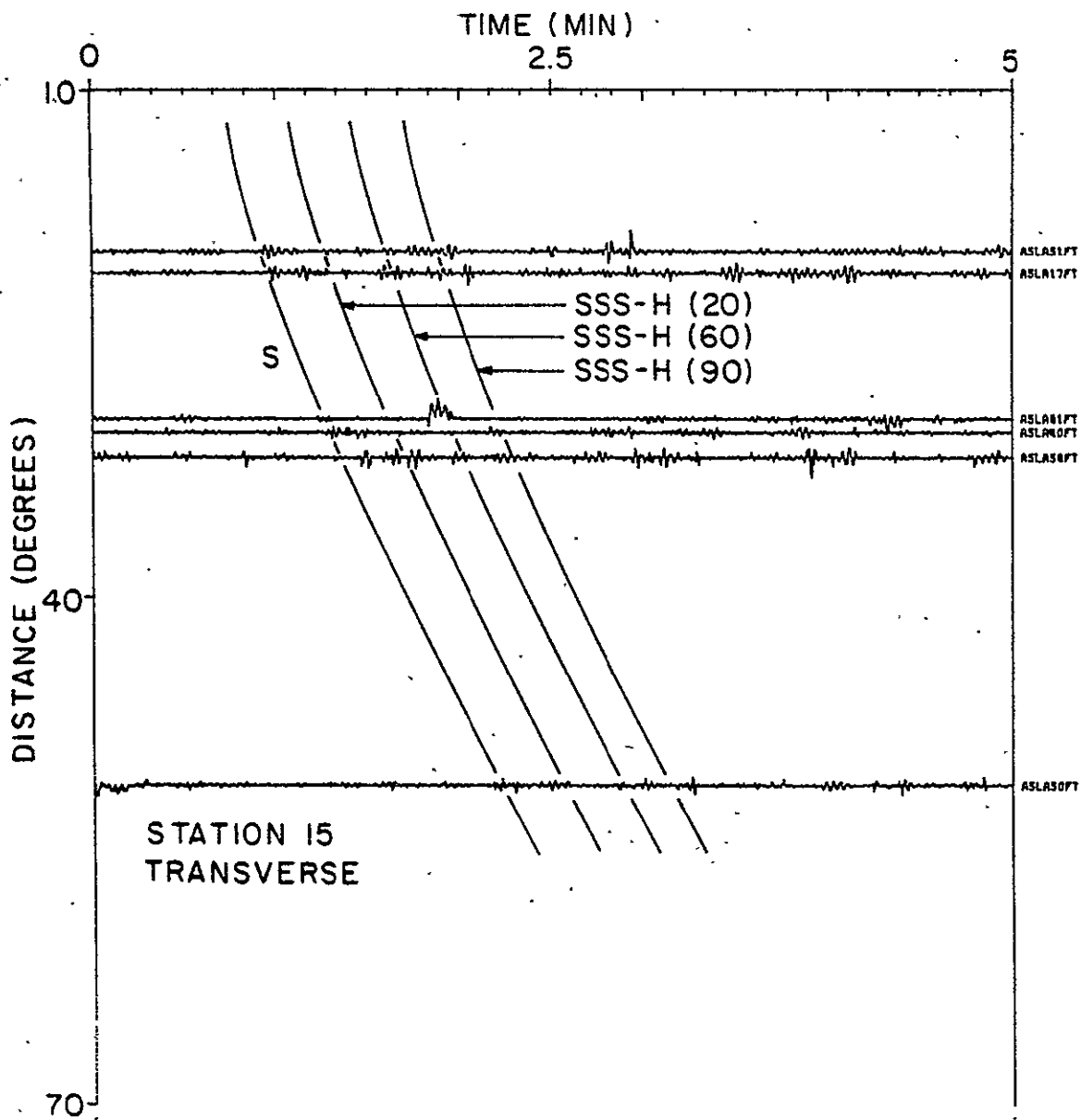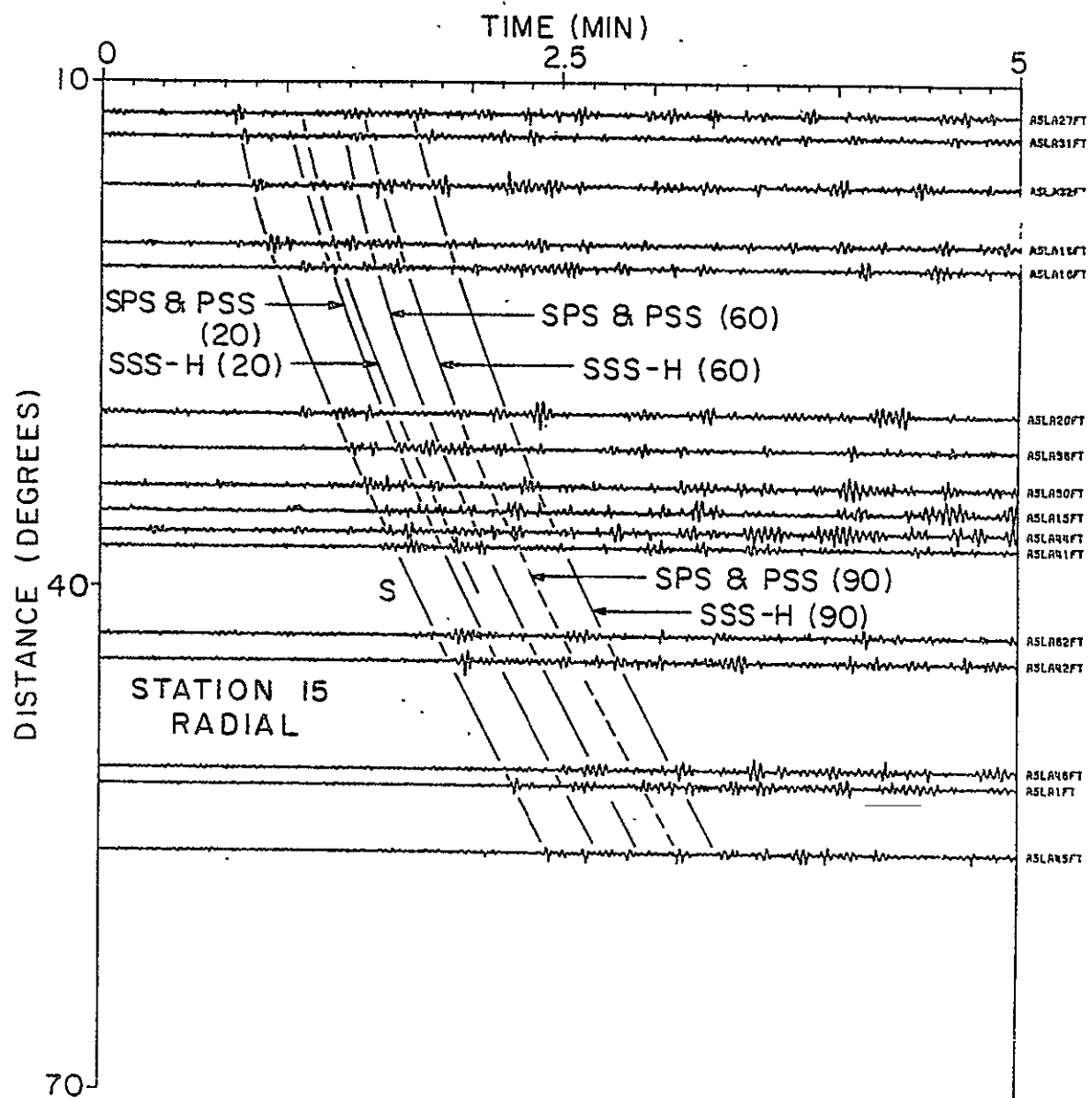
Figure 2-12b

Figure 2-12c
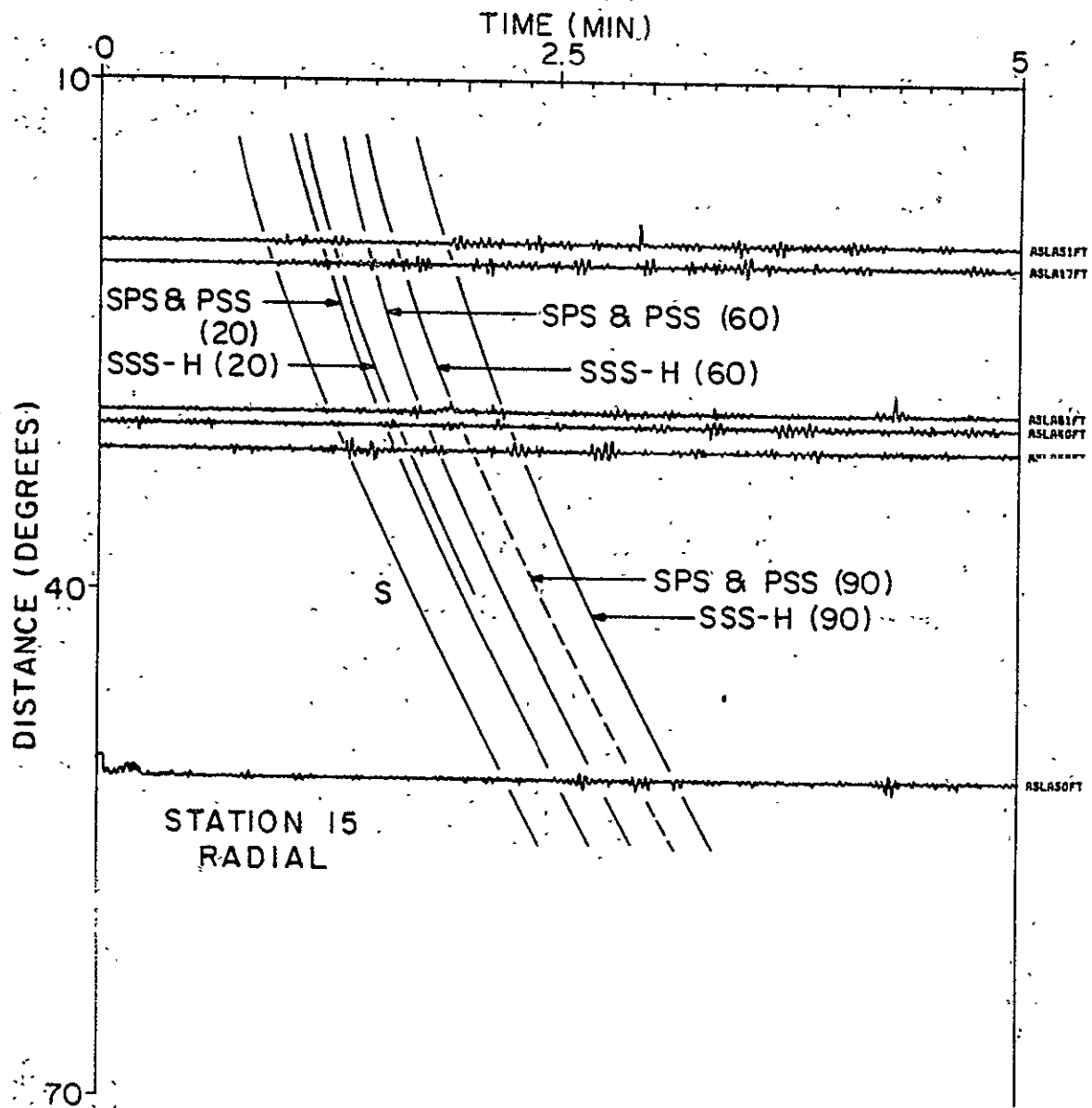
Figure 2-12d
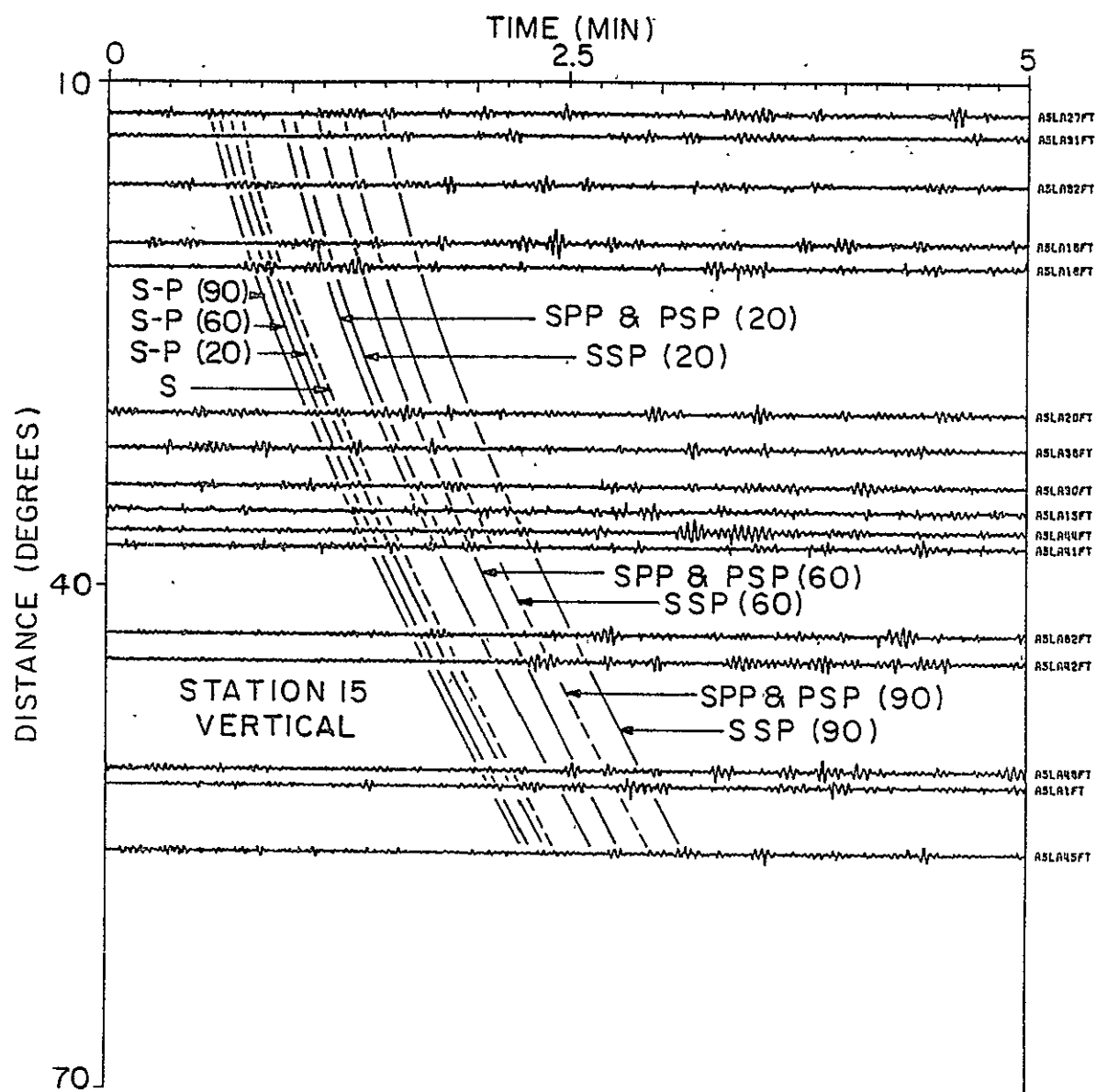
Figure 2-12e
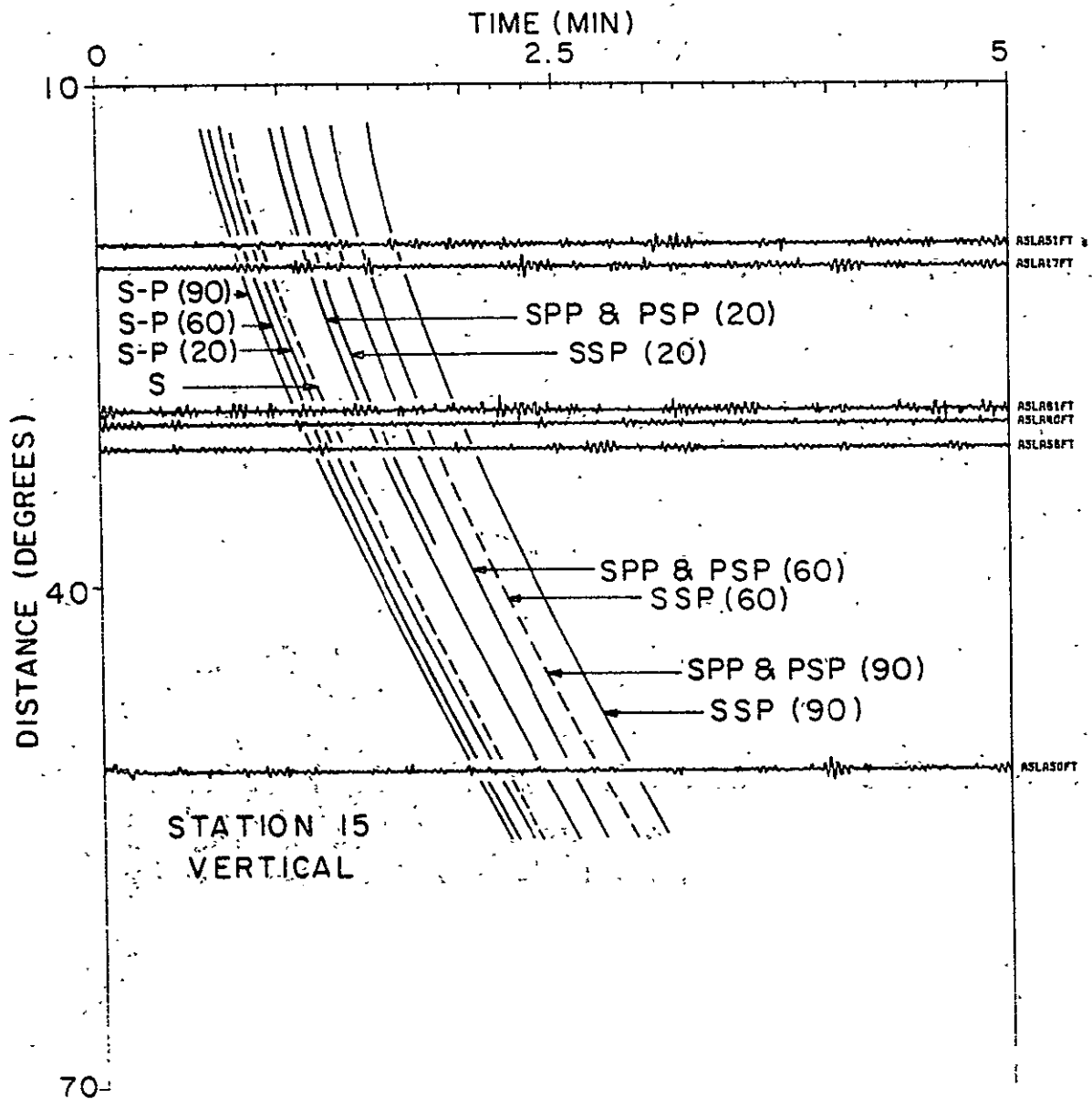
Figure 2-12f

Figure 2-12

Figure 2-12h

STATION

12　　　14　　　15　　　16

UPPER CRUST　　UC　　UC　　UC

LOWER CRUST　　LC　　LC　　LC

MANTLE　　M　　?　　

　　　　　　　　M

DEPTH (KM)
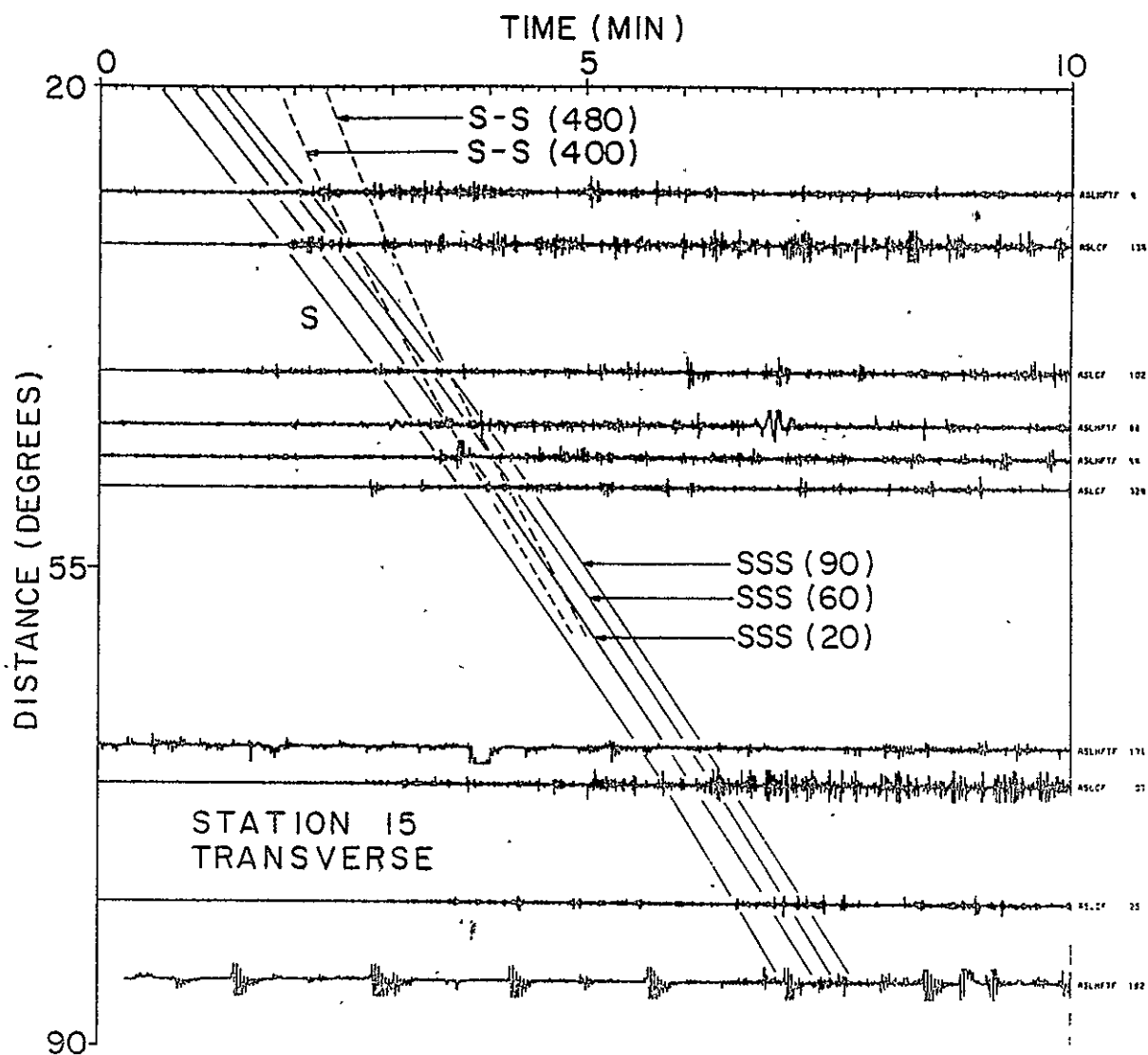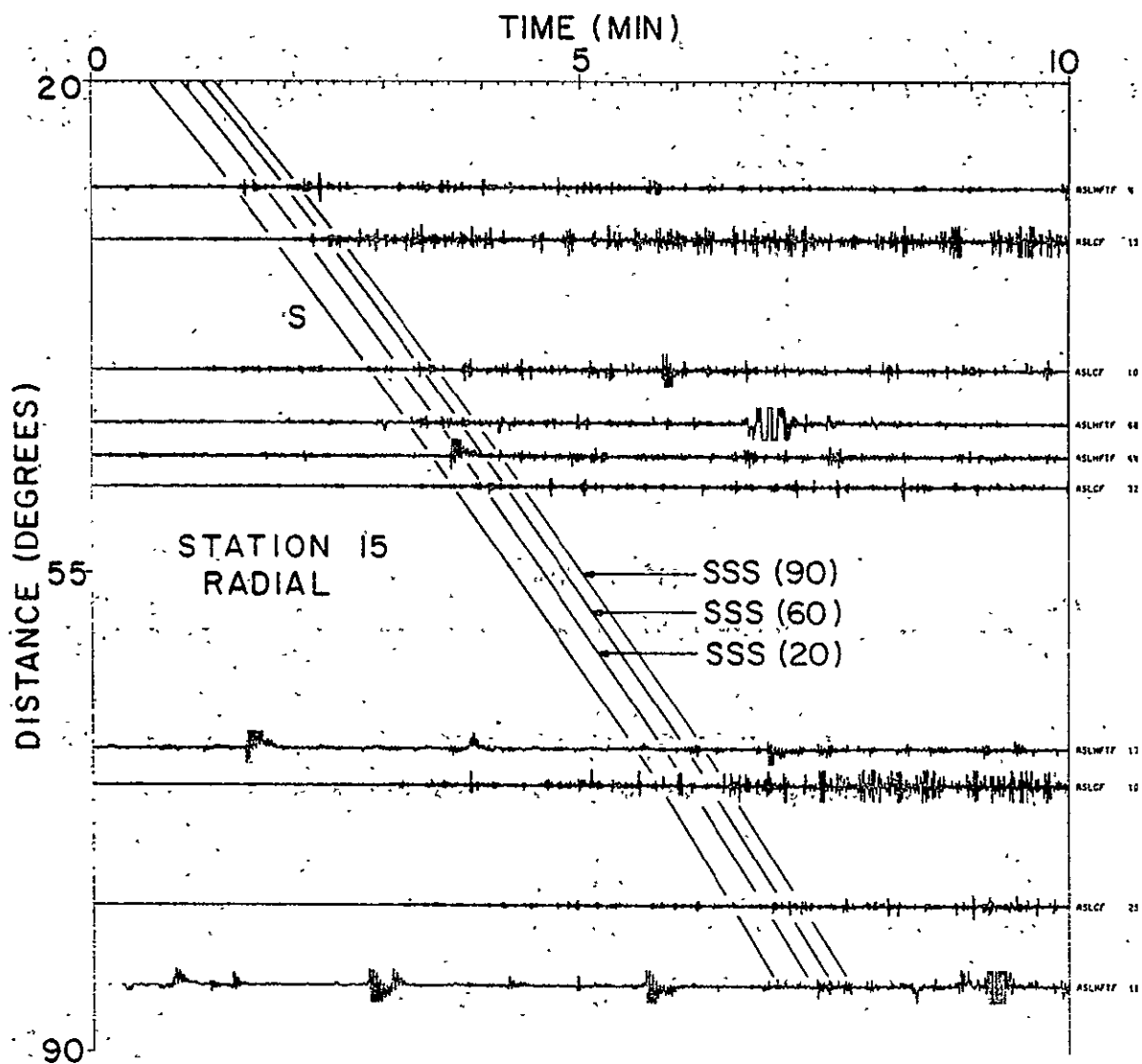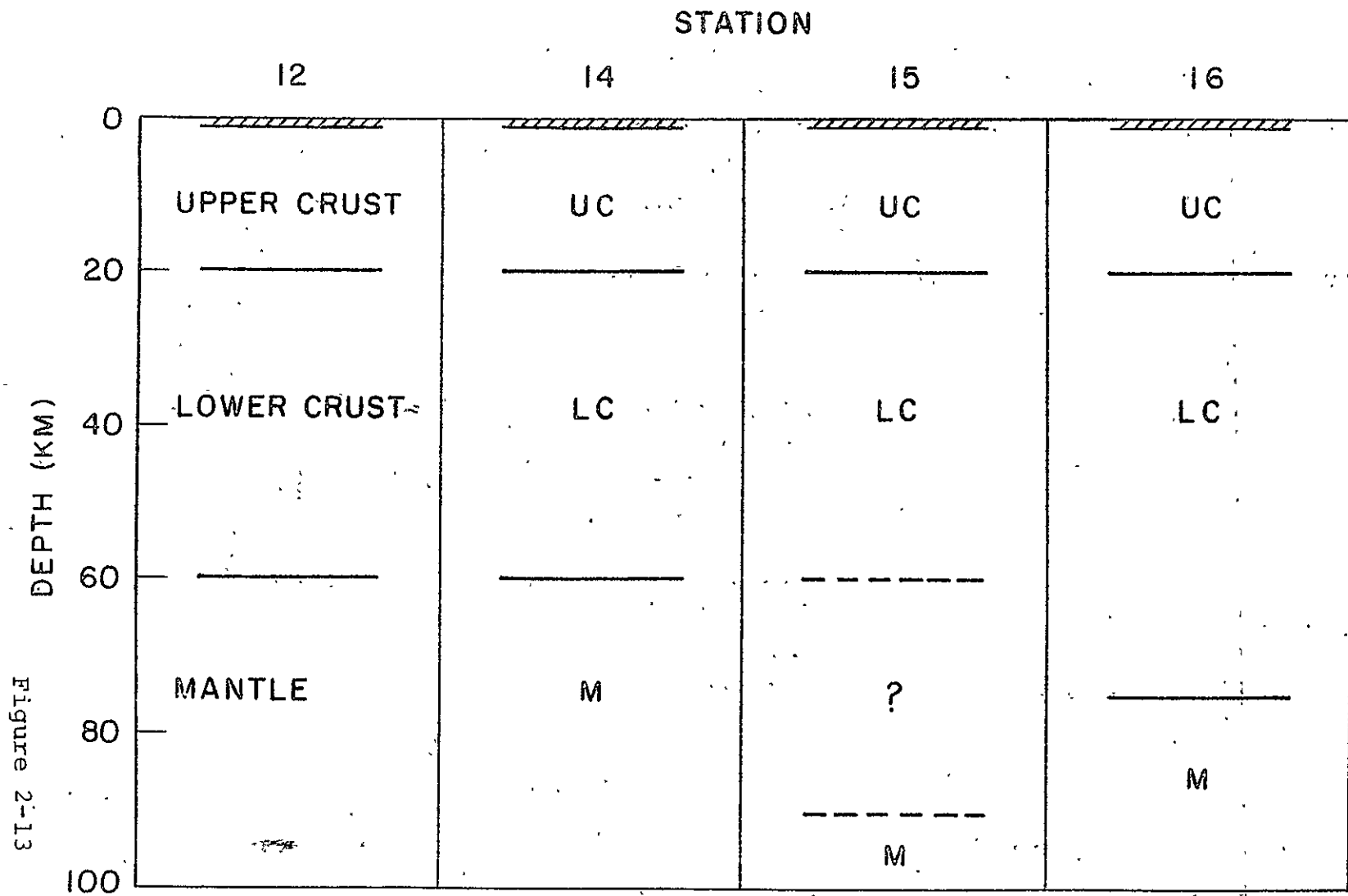
Figure 2-13

CHAPTER 3

MANTLE

3.1. Introduction

The next step in studying the seismic structure of the
moon is to determine the characteristics of the mantle region.
As discussed above, the artificial impact data suggest a P
wave velocity of either 7.7 km/sec or 9.2 km/sec for the top
of the mantle, although the higher value, if correct, must
be confined to a thin layer immediately below the crust.
Unfortunately, due to the limited source energies of the ar-
tificial impacts, they cannot provide any additional infor-
mation. Thus the structure of the lunar mantle must be deter-
mined almost entirely from the natural seismic events recorded
by the ALSEP array. These events occur at unknown locations
and times and so the available data consists of underlined arrival times
rather than travel times. (In addition of course the various
observed arrivals must be identified; the assumption that the
dominant phases are in fact direct P and S waves is discussed
in Chapter 1). As a result, a different set of analysis
techniques are needed, and the transition from crust to
mantle studies becomes a major step indeed.

The previous work concerning the lunar mantle and the
deep interior of the moon can be divided into two groups.
The work done at MIT prior to and during the inception of
this thesis is summarized in Toksöz et al. (1974a) and

Dainty et al. (1974b, 1976). The corresponding research ef-
forts of the Galveston group have been presented by Nakamura
et al. (1974b, 1976a, 1977). In addition a small number of
contributions have been made by other researchers (Burkhard
and Jackson, 1975; Voss et al., 1976; Jarosch, 1977).

A common problem that pervades all of these efforts is
the difficulty in using arrival time data, and thus having to
determine the event locations and origin times in addition to
trying to extract any useful structural information. This
dilemma is exacerbated by the paucity of seismic stations;
as discussed in Chapter 1 there are only four, two of which
are only partially independent due to their proximity to each
other, and at least three stations are needed to even tri-
angulate a seismic source even if the velocity structure is
known a priori. Furthermore, the initial knowledge of the
seismic characteristics of the moon is essentially zero, so
that any pathological combination of lateral heterogeneity
or anomalous structures may be present. Indeed two such
already analyzed and discussed are the very-low-velocity
surficial layer and the strong scattering zone.

Clearly some sort of bootstrapping operation combined
with a few judicious assumptions is necessary. The first
step was the determination of crustal structure from the ar-
tificial impact events, as discussed in the previous chapter.
In a sense the next link in the process was the Day 134, 1972
meteorite impact event which was large and close to the

ALSEP array. The rays received at station 14 bottomed in the crust providing a stepping stone from artificial impacts and the lunar crust to natural events and deeper structure. Finally, lateral homogeneity has been assumed, and is in a sense justified by the data as mentioned in Chapter 1. (Nakamura et al. (1977) have examined their data set for evidence of lateral heterogeneity; see discussion below.) From this point, several approaches have been tried.

Nakamura et al. (1974b) use an iterative procedure beginning with the assumption of a constant velocity mantle and correcting this model step by step to satisfy the data. Basically, six surface events are used; the four P wave from each arrival times are then inverted to determine an "average" mantle P wave velocity and the event location (four parameters from four data points). It is then observed that the calculated velocities decrease with increasing event range, and therefore with bottoming depth. To accommodate this a P wave velocity that decreases with depth is postulated and the events relocated. With the resulting origin times, the S wave travel times are computed and plotted as a function of distance. (A crucial assumption here is that the shear wave arrival times from impacts are accurately measureable. Two of the six events used were rejected in the work for this thesis on the grounds of poor arrivals.) This curve is then inverted to give the shear wave velocity profile in the mantle to a depth of about 300 km; the exact inversion method

is not given. Finally, four deep moonquake sources are examined to determine the S-P time difference versus P arrival times (a maximum of four points for each focus) and an average of the four slopes calculated. Since the moonquakes apparently occur beneath the 300 km boundary, the slope value (which is equivalent to V_p/V_s) can be used to estimate the shear wave velocity below 300 km given the above P and S wave velocity curves.

This work is extended in Nakamura et al. (1976a). Here the primary data set is the shear wave amplitude curve as a function of distance for surface events; on the basis of this the velocity gradients in the upper mantle are calculated. Then, using the absolute velocity values from the previous paper and (presumably) updated locations, the sudden drop-off of amplitudes at 90° distance implies a sharp velocity drop or (as they prefer) an abrupt steepening of the velocity gradient at 300 km depth. Finally, S-P vs. P times are again used to determine V_p/V_s ratios and further estimate velocities from those given in the first paper.

The last paper in this series (Nakamura et al., 1977) re-examines the data set for evidence of lateral heterogeneities. Essentially each event is considered individually; most of the arrival time data from a particular event is used to locate it given a laterally homogeneous velocity model, and then redundant data is examined for consistency. If the extra data is inconsistent, then lateral heterogeneity is a possible explana-

tion. Unfortunately, the results are not definitive. Both moonquakes and surface events were studied, and only surface events showed systematic trends of anomalous data. These trends, however, contain the effects of data uncertainties, radial variation of velocity, possible location bias, and finally, possible lateral heterogeneity. Considering that the uncertainty in arrival time measurements alone is probably sufficient to explain the magnitude of the observed trends, positive identification of lateral heterogeneity is impossible, and the assumption of lateral homogeneity is still justifiable as discussed in Chapter 1.

The stepwise procedure described above, while perfectly valid and in a sense effective, does have limitations. First, the essential ambiguous trade-off between event location and seismic velocities is obscured. It is difficult to understand how assumed locations and origin times may have biased the velocity results and vice-versa. More importantly it is not at all clear how much uncertainty there is in the presented models and locations, both in terms of standard errors of some sort for the given values and with regards to uniqueness of model type. (This last is very difficult to analyze effectively, even terrestrially.) This is a definite lack because in many ways, especially for non-seismologists attempting to correlate their results with the seismic information, it is at least if not more important to know the uncertainties in or allowable ranges of seismic models than the details of one

exact but possibly poorly constrained structure. In addition, the above approach involving many steps and various assumptions along the way does not provide a clear idea of which features of the final model are controlled by which data and how closely. For instance, in the final (or at least current for several years) Galveston model they feel that the tightest constraints are on the velocity gradients while the absolute velocity values are poorly defined (Nakamura, personal communication). Finally, it is not obvious that the particular sequence of steps used in the above method will extract all useful information from the observed data.

Clearly it is desirable to seek a more direct approach to the problem that will preserve and elucidate the relationship between event location and seismic velocities. In essence, a method of analyzing the arrival times directly is required. The technique of choice which will overcome most if not all of the above difficulties is to set up the data values (direct P and S wave arrival times) as functions of the desired parameters (event locations, origin times, and velocity structure) and solve the resulting set of simultaneous equations. This is the classic non-linear inverse problem, where the knowns can be written as some function of the unknowns, and there are two basic approaches to solving it.

First, the forward problem can be done many times using some systematic choice of values for the unknowns, and the theoretical observations compared with the actual data to

evaluate each trial solution. The model parameters can be iterated by some scheme to either improve the fit to the data (e.g. parameter search or steepest descent methods) or to explore the space of a given class of "acceptable" models (e.g. hedge-hog method or Monte Carlo technique, c.f. Keilis-Borok and Yanovskaya (1967) and Press (1970)).

The second approach is to do the forward problem once, using reasonably accurate initial values for the unknown parameters, and then form the differences (misfit) between the observed and predicted data. The functional relationships between the data and the model parameters are then linearized and corrections to the initial model values can be calculated from the misfit using one of several methods developed to solve linear inverse problems. (For example eigenvalue analysis and generalized inversion (Lanczos; 1961; Aki, 1975), stochastic inversion (Franklin, 1970), or Backus and Gilbert techniques (Backus and Gilbert, 1967, 1968, 1970)). The trial solution can then be updated and the inversion repeated.

Each of these solution methods provides different advantages; accordingly one technique from each group has been chosen for use in this thesis as described briefly below and at greater length in Appendix 4

The first method is a straightforward search through the parameter space. First, the seismic velocity model is fixed. Then for each seismic event, an initial location is chosen and calculated travel times to the four ALSEP stations sub-

tracted from the observed arrival times to obtain n estimates
of the event origin times (where n is the number of observed
arrival times). The variance of these origin time estimates
(σ^2) is a least-squares criterion for the adequacy of the ini-
tial values of location and seismic velocities. This is
repeated for a grid of locations, either on the surface or in
the interior of the moon, and the entire grid is moved step-
wise along decreasing σ^2. When a best location (i.e. minimum
σ^2) is found, the velocity values are changed systematically
and the entire process repeated, culminating in a comparison
of the σ^2 values for several velocity models.

This method has two advantages. First, we obtain a
complete picture of the parameter space, and can determine
the existence of local minima (i.e. local solutions), the
shape of the minima valleys, and the radius of convergence
to any particular solution. Second, the procedure is in-
sensitive to the choice of seismic velocity parameters to
be varied, and will not fail if the data cannot constrain
a particular model parameter or if the initial location or
velocity values are far from the true values preferred by
the data. In particular, during the work in this thesis the
event locations determined for any given velocity model were
unique in the sense that the grid of test locations would
move quickly to the same best location no matter where it
was started. Thus little a priori information about the
event locations required, minimizing the possibility of in-

advertent biasing. In contrast, there are three disadvantages
of this method. First, it is essentially a brute-force ap-
proach which is extremely inefficient in terms of computa-
tion time and cost. Second, there is no unique way to find
the optimum velocity values for several events simultaneously
although several such schemes were used in the preliminary
phases of this work. Finally, even when a solution is found
the calculations do not provide a quantitative estimate of
the accuracy of that solution.

The second inversion method used dovetails nicely with
the weaknesses in the first approach and takes advantage of
its strong points. As discussed in Appendix 4, the method
uses initial values for locations, origin times, and struc-
tural parameters (e.g. seismic wave velocity) that we wish to
determine, and calculates predicted arrival times. In ad-
dition, the equations relating initial model with the pre-
dicted data are linearized via a first-order Taylor series
expansion to produce a matrix of first derivatives. Correc-
tions to the initial model values (locations, origin times,
and velocities) can then be calculated all at once by finding
an inverse to the partial derivative matrix and multiplying
by the original misfit between the observed and predicted
data values. Naturally, the crux of this matter is to find
an inverse for the above matrix, given that the problem can
potentially be both over-determined and underconstrained.
This can be a complex procedure, and the appropriate solution

is dependent on the particular properties of each problem, as
discussed in Appendix 4. The problems treated herein turn
out to be just overconstrained, mostly because we do not
attempt to determine too many or inappropriate velocity model
parameters, thus producing a non-invertible matrix. The
actual choice of model parameters to be determined is dis-
cussed further below. Given that the problem is not under-
constrained, the matrix equation can be solved simply by
forming a square matrix $A^T A$ and inverting. The resulting
corrections are applied to the initial model values, and the
process is repeated a few times until hopefully convergence
occurs and the additional corrections go to zero. The
result is a model that fits the data best in a least-squares
sense.

A primary advantage of this method is that it is very
efficient computationally, usually requiring only three
iterations for convergence. In addition, we can obtain
several quantities that are of interest in describing the
solution and data. First, we can calculate the formal un-
certainties for the determined parameters, including the
effects of errors in the data, inconsistencies within the
data, and the degree to which the data constrain the unknowns.
Second, the correlation coefficients between the determined
parameters indicating which ones can be mutually adjusted
without overly damaging the fit to the data can be formed.
(Both of these quantities are contained in the parameter

covariance matrix.) Finally, the relative importance of each datum to the solution is obtained, and we can observe which data values are inconsistent with each other, thus identifying possibly erroneous data (all in the information density matrix). All of these quantities are of great help in understanding not only the characteristics of the inversion but also the physics of the problem. The disadvantages of this technique lie in the fact that when a solution is found it is difficult to ascertain the radius of convergence and determine the presence or absence of local minima. Furthermore, the method is sensitive and places strict requirements on the accuracy of the initial model; the inversion will fail to converge if the starting model is far removed from the true best values and outside the region where the linear approximation holds.

These two methods thus complement each other, and so both are used in this thesis. The first technique is applied in three ways. First, it is used in evaluating candidate arrival time data sets, as described in Chapter 1 and Appendix 1. Second, the final arrival times for each event are run to obtain initial event locations and origin times for use in the linearized inverse. Finally, the method served as a valuable learning tool, especially in the early phases of this work, for exploring the characteristics of the various parameter spaces considered herein. The second method, linearized matrix inversion, is then used to obtain the final results

presented, along with the various diagnostic quantities discussed above.

This combination of analysis methods obviates many of the difficulties confronted in the work of Nakamura et al. (1974b, 1976, 1977), by dealing directly with the arrival time data set, determining the event locations and structural parameters simultaneously, and quantitatively placing error bars on all of these. It remains to deal with secondary seismic data sets, namely secondary seismic wave arrivals and the direct P and S wave amplitudes. The additional seismic wave arrivals can be searched for using the techniques described in Appendix 3 and exemplified in Chapter 2. As will be observed the arrival times of these phases are nowhere near accurate enough to be used in a formal inversion procedure as above; it is sufficient to fit theoretical travel time curves in an effort to observe them and deduce structural implications. The same is true for the direct P and S wave amplitude data, for two reasons. First, the data as shown in section 3.3.3 contain a large scatter, much of which is probably real and caused by local and detailed structural effects. Furthermore, there are several assumptions involved in constructing quantitative amplitude curves, which make it difficult to draw strict quantitative conclusions. Finally, formal inversion of the amplitude data is not feasible due to the above factors and the extreme non-uniqueness of the problem. Thus it is appropriate to examine

both the secondary seismic wave arrivals and the amplitude data after the inversion of the primary arrival time data set, incorporating modifications as necessary.

Despite this systematic approach, two classes of initial assumptions are needed to begin the analysis procedure. First, the form of the velocity model for the lunar interior must be chosen. We begin by using the three-layer crustal structure discussed in Chapter 2; two constant-velocity regions supplemented by a time offset for the very-low-velocity zone. This is assumed to be the same at all ALSEP stations; as discussed below, travel-time corrections for the variation in crustal structure and topography at each station were included in various runs and the effects on the solutions were minimal. Next the form of the mantle structure must be defined. Given the number of seismic stations, it is clearly possible to obtain only a few structural parameters by inversion. Accordingly, a first pass is just to invert for the average P and S wave velocities in the entire mantle, thus effectively assuming that it has a constant velocity with depth. The results of this are given below. (In addition, of course, this postulates lateral homogeneity. As discussed in Chapter 1, this is a reasonable assumption based on the arrival time data although there are surely some lateral variations in velocity at least in the upper mantle; see Chapter 2.)

However, a dominant theme in the early work of both the

Galveston and M.I.T. groups has been the sudden decrease in

amplitudes and concurrent delay in arrival times experienced

by shear waves arriving from beyond a certain distance; vari-

ous velocity and location models place the critical distance

at about 90°. (This is re-examined in section 3.3.2.) This

suggests that there is a velocity drop and/or attenuation

increase for shear waves at some depth; for a constant-

velocity mantle of velocity 7.5-8.5 km/sec, this depth is

close to 500 km for a 90° critical distance. The S-P vs. P

times of the deep moonquakes (which seem to occur below 500 km

depth) seem to confirm this situation by giving a higher ap-

parent V_p/V_s ratio than that observed for near surface events

(<90° distant) whose rays do not penetrate below 500 km. Thus

on the basis of initial data indications it is appropriate to

consider a two-layer mantle model, again attempting to deter-

mine the average velocities in each. The boundary is initial-

ly chosen to be at about 500 km depth. Thus the initial form

of the structural model is four constant velocity layers.

(plus the surficial very-low-velocity (VLV) zone).

The second set of assumptions concerns the locations of

the three groups of natural seismic events that account for

the arrival time data used herein. As discussed in Chapter 1,

the events are classified as meteorite impacts, HFT's, or

deep moonquakes based on seismogram characteristics; all

authors are in general agreement concerning these interpre-

tations (c.f. Toksöz et al., 1974a; Latham et al., 1973a).

3.2 Results of Arrival Time Inversions

Initially, the arrival time data set was divided into two groups; surface events and deep moonquakes. The physical reasoning for this is that the two subsets are controlled by, and can therefore constrain, the velocities in different regions of the lunar mantle. Since most of the surface events are on the nearside (as will be seen below) most of the arrival times (~85%) are those of rays bottoming in the upper mantle (above 500 km depth). The few farside events are observed only by P waves due to the observed loss of shear wave energy. In contrast, the rays from all deep moonquakes traverse both the lower and upper mantle regions. Therefore our initial approach is to fix the lower mantle velocities and use the surface events to invert for the upper mantle velocities, and then fix the upper mantle values and use the deep moonquake events to obtain the lower mantle velocities.

The practical reasoning behind this is that the cost of finding a linearized matrix inversion solution to a problem with n events is observed to go roughly as $n^{2.5}$. Since there are many assumptions (given above) that we wish to test by re-solving the entire problem several times, it is much less expensive to do this on two halves of the data than on the full data set, by a factor of about three. Therefore the optimal approach is to solve for the event locations and structural parameters for the two data subsets, observing

the effects of various assumptions. Then the entire data set
can be inverted simultaneously, and only a few of the more
crucial assumptions re-tested.

The paragraphs below describe the results of inverting
the surface event data, the moonquake data, and finally the
complete data set. It is impossible to recount in complete
detail the many different inversions run during the analysis
procedure and all the numbers associated with each such solu-
tion. Therefore only the pertinent facts and results are
given, with details included as tables when appropriate.
Nevertheless, all aspects of the inversions were examined
closely during the research phase, both to ascertain the solu-
tion characteristics and to learn about the features of in-
verse problem solution in general. Three conventions are
followed below, unless stated otherwise. First, all solu-
tions were obtained by three iterations of the matrix inver-
sion routine. Second, all errors quoted are calculated from
the parameter covariance matrix and the data variance as dis-
cussed in Appendix 4. Finally, the quantity σ_d^2 is the
a _posteriori_ variance of the data, calculated from the final
least-squares fit to the data (see Appendix 4), and is used
as a measure of how closely a particular model and set of
parameters can fit the arrival time data.

3.2.1 Surface Events - Upper Mantle

The surface event data set is given in Tables 1-4 and

1-5. There are 16 events (eight meteorite impacts and eight
HFT events), and 88 arrival time measurements (58 for P
waves and 30 for S waves). The structural model assumes a
three-layer crust as given in Chapter 2, and a lower mantle
below 520 km depth with V_p = 7.8 km/sec and V_s = 4.2 km/sec
(chosen as reasonable values; since few of the surface
event rays penetrate this zone, the particular choice is not
crucial). The data can then be inverted to obtain the average
velocities between 60 and 520 km depth, along with the event
locations and origin times, for a grand total of 50 parameters
to be determined. The initial first-guess values for the
locations and origin times are obtained from the results of
the parameter search inversion method; they represent average
values for the various velocity structures considered (des-
cribed in Appendix 1) and are listed in Table 3-1. The ini-
tial upper mantle velocity values are V_p = 7.8 km/sec and
V_s = 4.4 km/sec, chosen on the basis of previous work and
indications from moonquake inversions, discussed below.

Note that this choice produces a shear wave shadow zone
beginning at 90° distance and extending to about 110°, as
mentioned above. A potential problem then arises because an
event location (and upper mantle velocity) may be such that
at some stage of the iteration the theoretical ray cannot be
traced for comparison with an observed arrival time datum.
In practice this has arisen only for those events that appear
to be located near the edge of the geometric shadow region

for one or more stations; the only such events are those occurring on Days 72, 192, and 3, perhaps coincidentally all are HFT events. The loss of a data point from one of these events can then occur for one of two reasons; a) the iterations may slightly overshoot the true location as convergence occurs, thus inadvertently entering the shadow zone while the true desired location is outside the zone; or b) the true desired location may be within the shadow zone for an arrival that is in fact observed, indicating that the location of the shadow zone is slightly inaccurate (very likely) or that the observed arrival is a diffracted wave around the velocity drop boundary that we have not accounted for in the ray theory calculations. Fortunately this occurred only occasionally and only for a few data points. In all cases each was re-included at some point by changing the parameters of the geometric shadow zone; a case study for Day 72, the most troublesome event, is described below. In addition, of course, such discrepancies can be used to infer the extent of the shadow region; this is discussed in the next section.

Returning to the main subject, the matrix inversion routine was run using the above data and starting parameters, and a least-squares solution was in fact obtained. Convergence was rapid; the third and final set of corrections to the model parameters were all less than 0.6 degress (~18 km) in latitude and longitude, one second in origin time, and 0.01 in velocities. In the three iterations the calculated σ_d^2 ·

(formula in Appendix 4) dropped from an initial value of
540.5 sec^2 to 34.6 sec^2 after one iteration, 30.8 after two,
and 30.7 after all three. This final value corresponds to
a standard deviation of ±5.5 sec for each data point, in good
agreement with the a priori estimate of ±4 sec for the accura-
cy of the data measurements. This suggests that the model
type is appropriate to the data and thus can fit it to within
the estimated accuracy.

The final event locations are given in Table 3-2, and
the final upper mantle velocities are V_p = 7.8 ± 0.16 km/sec
and V_s = 4.47 ± 0.05 km/sec. The ratio between the P and S
wave velocity uncertainties is about 3, as expected because
for a constant time error in the data (arrival times),

$$\Delta t \simeq V_p^{-2} \Delta V_p \simeq V_s^{-2} \Delta V_s$$

or

$$\frac{\Delta V_p}{\Delta V_s} \simeq \left(\frac{V_p}{V_s}\right)^2 \simeq 3$$

as observed.

The next step is to examine the characteristics of the
solution. First, three variations of the data set were run.
The "most confident" data, as listed in Tables A1-4 and A1-9,
using 11 of the original 16 events, gave velocity values of
V_p = 7.67 ± 0.20 km/sec and 4.45 ± 0.11 km/sec, in good
agreement with the full data set results. Also, HFT events
and meteorite impacts were run separately (using all eight

events of each), and the results were

$$HFT's: \quad V_p = 7.73 \pm 0.17 \text{ km/sec}$$
$$V_s = 4.47 \pm 0.06 \text{ km/sec}$$
$$Impacts: \quad V_p = 7.88 \pm 0.24 \text{ km/sec}$$
$$V_s = 4.44 \pm 0.09 \text{ km/sec}$$

again in good agreement with the original values considering

the standard deviation intervals. These comparisons indi-

cate that the overall solution is relatively stable with

respect to the data set, as also implied by the calculated

standard errors.

Returning to the full data set, the information density

and parameter covariance matrices were calculated in full

as described in Appendix 4. The results from the information

density matrix are summarized in Table 3-3, giving the total

importances of the P and S wave data at each station. The

main conclusion that can be drawn from this table is that

stations 12 and 14 are in fact each less important than either

stations 15 and 16, as expected due to their proximity to

each other. Note that the importances sum to 50, the number

of unknowns. The off-diagonal terms of this matrix indicate

that, as expected, the most averaging is necessary for the

data points observed at stations 12 and 14 since even small

errors are a significant percentage of the correct arrival

time difference. The parameter covariance matrix (diagonal

terms) produced the formal errors quoted above, and the off-

diagonal terms showed the expected correlations (e.g. origin time can trade off with distance or, to some extent, velocity) as discussed in Appendix 4.

.Finally, the starting values of locations, origin times, and velocities were changed to explore the uniqueness and radius of convergence of the above solution. This is difficult to explore thoroughly due to the presence of the geometric shadow zone caused by the velocity drop; as discussed above, a few events can be inadvertently placed just inside the shadow region. (In fact three data points, two arrivals from Day 72 and one from Day 3, were lost in the above inversion; see discussion below.) Nevertheless, most of the initial starting locations and origin times were varied randomly by about 5-10 degrees and 20 seconds, and the starting upper mantle velocities changed by as much as 0.2 km/sec; in all cases the iterations converged to the same result.

In sum, the surface event inversion appears to be stable and well-constrained, producing reasonable results. It remains then to re-examine some of the assumptions mentioned above that were necessary to obtain this solution. First, the effect of varying the crustal structure was calculated; the upper-lower crustal boundary was moved from 20 to 30 km. The effect was completely negligible. Next, the upper-lower mantle boundary depth was varied. Unfortunately, moving this boundary a significant distance upwards decreases the onset distance of the geometric shadow zone to less than 90°,

placing many of the observed arrivals in the shadow region.
In order to avoid this problem, a negative shear wave velocity
gradient of 6×10^{-4} km/sec/km was introduced in the upper
mantle, thus spreading the rays bottoming in the mantle so
that they reach further distances for a given bottoming depth.
This allows us to move the interface from 500 to 400 km depth,
and subroutine TRAVEL was then used to do the ray tracing.
The resulting inversion converged nicely, giving an upper
mantle P velocity of 7.7 ± 0.15 km/sec and a shear wave veloc-
ity at the top of the mantle immediately below the crust of
4.56 ± 0.05 km/sec, thus decreasing to 4.36 km/sec at 400 km
depth with a median value of 4.46 km/sec, in excellent agree-
ment with the initial results. With one exception, all loca-
tions were within 2° of the original values. The single ex-
ception is Day 72, 1973, an HFT event. As mentioned above,
in the initial constant-velocity inversion the two observed
shear wave arrival times from this focus were lost because
the event stumbled into the geometric shear wave shadow zone,
on the first iteration. With the loss of the shear wave data,
the event moved even further away, finally ending at about
100° distance from ALSEPS 12, 14, and 16, and thus within
the shadow zone, even though strong S arrivals are in fact
seen at these stations (although ALSEP 14 is not measured due
to the failure of the vertical component and resulting lack
of polarization filtering). In the iteration with velocity
gradient, however, the S arrivals were not lost and the

resulting location is about 90° away from the above three
stations, or just before the onset of the geometric shadow
zone. As discussed in Appendix 1, this is the preferred
location because the shear wave data are included in the solu-
tion. This location is indicated in parentheses in Table 3-2.

Overall, however, including a shear velocity gradient
and moving the upper-lower mantle interface up produced in-
significant changes in the results. (The final fit to the
data was 31.0 sec^2.) This is extremely important because it
implies that the average velocities obtained for the upper
mantle region from this inversion are in fact valid even if
a moderate velocity gradient exists; thus these values can be
considered as firm constraints independent of most of the
assumptions. On the other hand, this result also suggests
that the surface event arrival time data will not be able to
constrain the upper-lower mantle boundary depth or the magni-
tude of any velocity gradients. This is discussed further
below.

Finally, the assumption that the HFT events are con-
fined to the surface below the VLV zone was re-examined.
First, as mentioned above, the HFT events were inverted
separately, giving a σ_d^2 of 31.7. Then the inversion was re-
done assuming that the HFT's were at various common source
depths, as shown in Table 3-4. The σ_d^2 value consistently
increased, indicating that the best common source depth is in
fact at the surface. Of course the increase in σ_d^2 is only

significant beyond about 50 km depth, and it is possible that the HFT events are all located at different depths. In the absence of a priori information this is difficult to test, and so the simplest assumption consistent with the inversion results is that the HFT events are all in fact very near the surface. (In addition, the HFT polarization filtered records were searched for possible SS (surface reflected, see Richter (1958, p. 307) phases that would indicate source detph. None were observed.)

3.2.2 Deep Moonquakes - Lower Mantle.

The moonquake arrival time data set is given in Table 1-6. There are 24 events and 140 arrival time data (50 P and 90 S). The first structural model considered is simply a single-layer constant velocity mantle with a three-layer crust; thus the moonquake data inversion will yield average P and S wave velocities for the region between the moonquake depths and the crust. The starting locations and origin times (listed in Table 3-5) are again obtained from the parameter search inversion results, and the starting velocities are $V_p = 8.0$ km/sec and $V_s = 4.2$ km/sec, chosen to be near the middle of early velocity estimates. The resulting inversion converges quickly, giving maximum last-step corrections of 0.4°, 4 km, 0.8 seconds and 0.02 km/sec for the epicentral coordinates (latitude and longitude), depths, origin times, and velocities respectively. The least-squares fit to the data as measured

by the a posteriori data variance σ_d^2 begins at 193.7 sec^2 and decreases to 37.0, 10.4, and finally 10.2 sec^2 after the last iteration. This indicates an average error in the data of ±3.2 sec, in good agreement with the a priori estimate of ±4 sec given in Chapter 1. The resulting average velocities are 7.75 ± 0.55 km/sec and 4.44 ± 0.19 km/sec. These values are consistent with the surface event estimates of the upper mantle velocities; the larger uncertainties are due to the increased freedom in the solution provided by the necessity of determining the depth coordinate. The average depth turns out to be about 900 km, with values ranging from 700 km to 1100 km, in excellent agreement with the initial assumption that the moonquakes are situated below 500 km depth.

The next step is to consider a two-layer mantle model, assuming that the upper mantle velocities are known. Initially the upper-lower mantle boundary was placed at 520 km depth and the upper mantle velocities assumed to be V_p = 8.0 km/sec and V_s = 4.6 km/sec. (These velocities are different from the results reported in the previous section because the surface event and deep moonquake studies were done concurrently; further discussion below.) The moonquake data can then be inverted to obtain the lower mantle velocities.

The iterations again converged quite quickly, giving velocity values of V_p = 7.45 ± 0.63 km/sec and V_s = 4.13 ± 0.25 km/sec with a final σ_d^2 of 9.8 sec^2. The uncertainties are slightly larger than before probably because the path

length in the lower mantle is shorter than the whole mantle
path length, and so the arrival times are less affected by,
and therefore have less control over, the lower mantle
velocities. Note that the calculated lower mantle velocities,
given the assumed upper mantle values, are in good agreement
with the previous whole mantle average velocities. The final
moonquake locations from the two-layer mantle structure are
similar to those obtained above.

In order to examine the characteristics of this solution,
we follow the same procedure as discussed for the surface
event inversion. The most-confident data set (21 moonquake
events) as given in Table A1-14 was inverted, giving results
of $V_p = 7.66 \pm 0.90$ km/sec and $V_s = 4.12 \pm 0.33$ km/sec, in
good agreement with the full data set solution, implying that
the answers are reasonably stable with respect to modification
of the data set. The larger uncertainties are probably due
to the smaller number of picks per focus (5.1 vs. 5.8) than
in the full data set; thus fewer data are available for con-
straining the velocity values. The final σ_d^2 is similar at
10.7 sec^2.

Next the information density matrix was examined. The
results are summarized in Table 3-7, again showing that the
arrivals at stations 15 and 16 tend to be more important than
those measured at stations 12 and 14. The parameter covari-
ance matrix was somewhat more interesting than for surface
events, showing that the moonquake depths can be most effec-

tively traded off with origin times rather than with veloc-
ities, because a velocity change would produce an arrival
time change of reverse proportionality (more change with in-
creasing source-receiver central angle separation) than the
original depth change. V_p and V_s change with each other pro-
portionally and then compensate with the origin times.

Finally the initial locations, origin times, and veloc-
ities were changed to check the stability and radius of con-
vergence. Since as discussed below there is little problem
with shadow zones, the initial locations were perturbed ran-
domly by about 20°, 150 km, and 25 sec in epicentral distance,
depth, and origin time respectively, and the starting veloc-
ities for the lower mantle given as V_p = 8.2 km/sec and
V_s = 4.6 km/sec. Despite these large offsets and an initial
σ_d^2 of 4212.9 sec^2, the inversion converged within five itera-
tions to the same solution as above. Thus the solution is very
stable with a wide radius of convergence.

Three major assumptions were then tested. First, the
effects of varying the crustal structure were simulated by
applying different time offsets at each station to roughly
compensate for elevation differences (given in King et al.,
1976) and presumed subsurface crustal variations as discussed
in Chapter 2. For example, at ALSEP 16, the lower crustal
layer is 15 km thicker than at ALSEP 12, giving about 0.3 sec
additional travel time, and the surface is 1.5 km higher,
adding, say, 1.5 sec of travel time if the extra material is

surficial and of low (1 km/sec) velocity. Thus a total of 1.8 sec is added to each calculated P wave arrival time at station 16, and 3.1 sec to each S wave time. Similar estimates at ALSEPS 14 and 15 implied P wave corrections of 0.2 sec and -0.3 sec, respectively. The values of course are only rough estimates, but are probably of the correct magnitude and therefore sufficient for observing the effect of such corrections on the inversion solution. As expected, the changes in the solution were minimal, the maximum change being in the lower mantle P wave velocity, which was increased by 0.1 km/sec.

Next the fixed upper mantle velocities were varied to observe the resulting changes in the lower mantle velocities. In particular, the values obtained from the surface event data inversion (V_p = 7.8 km/sec; V_s = 4.5 km/sec) were used, and the results were lower mantle velocities of V_p = 7.62 ± 0.64 and V_s = 4.39 ± 0.25, again in agreement with the whole mantle average velocities desired by the moonquake data set. The moonquake locations and origin times were very similar to the previous inversion results, and are listed in Table 3-6.

The last structural assumption tested was the placement of the upper-lower mantle boundary. Since the deep moonquakes lie below this interface, there is no difficulty in moving it upwards. Locating the boundary deeper than about 560 km, however, places the shallower and more distant moonquake events in geometric shadow zones with respect to some of the

stations where arrivals are in fact observed. Accordingly the upper-lower mantle interface depth was varied between 300 km (the shallowest value given in previous work) and 560 km. The resulting lower mantle velocity values indicated that, for fixed upper mantle velocities, a smaller velocity drop was required as the interface moved upwards. This is consistent with the idea that the upper and lower mantle values must combine to give the average velocities required for the whole mantle by the same data set. The total variation in the lower mantle values was only 0.4 sec for V_p and 0.3 sec for V_s, well within the formal errors quoted above. In addition, the fit to the data as measured by σ_d^2 varied from 10.1 sec^2 for a 300 km interface depth to 9.7 sec^2 for a 560 km boundary, indicating that the moonquake data are also unable to satisfactorily constrain the upper-lower mantle boundary depth.

There are three major conclusions that can be drawn from the surface event and moonquake inversion results described above. First, the data are in fact able to constrain the average mantle velocities within reasonable uncertainty limits. The solutions are correspondingly stable with respect to the data sets, and appear to be unique with a significant radius of convergence. No indications of other local solutions have been found. Second, the solutions are relatively independent of the structural assumptions used, and tend to confirm the assumed location areas for the various classes of events

(HFT's and meteorite impacts on or near the surface, deep moonquakes below 500 km depth). Finally, the fact that the structural assumptions, in particular those of constant-velocity layers and a mantle interface depth of about 500 km, do not significantly affect the fit to the arrival time data when varied implies that the data will not be able to constrain such quantities as the interface depth or the slopes of velocity gradients. For example, the moonquake data were inverted to obtain the lower mantle velocities and the interface depth, and even with stochastic damping (see Appendix 4) it was not possible to obtain a stable solution.

3.2.3 Joint Inversion

Based on the above information, the complete data set can now be inverted to obtain a consistent set of average velocity values for the lunar mantle. The data are given in Tables 1-4, 5, and 6, and the initial locations and origin times are taken from the inversions discussed above. The usual crustal model was assumed, the upper-lower mantle boundary placed at 520 km depth, and starting velocity values of V_p = 7.8 km/sec, V_s = 4.5 km/sec; V_p = 7.8 km/sec, V_s = 4.2 km/sec were given for the upper and lower mantle velocities, respectively. The inversion was then done to determine all event locations and origin times and the four mantle seismic velocities simultaneously. The first attempt was unsuccessful, because the first iteration created both

P and S wave velocity drops at 520 km depth, and moved the
locations of two surface events (Days 3 and 192) so that
several P and S arrival time data points were lost for each
focus due to the resulting shadow zones. The inversion auto-
matically ceases when the number of data points for any
event falls below three (four for a moonquake event) because
then there are not enough data values to even locate the
focus, and so the matrix becomes non-invertible (at least one
eigenvalue is zero); this occurred for the above two events.
A similar problem did not arise in the surface event inver-
sion work because the lower mantle seismic velocities were
fixed and the calculated upper mantle velocities only produced
a shear wave shadow zone. In the joint data set inversion,
however, the lower mantle velocities are free to change and
are apparently decreased substantially by the moonquake data.

In order to examine this situation further, two ap-
proaches were taken. First, the two offending events were
removed, and the inversion attempted again. This time con-
vergence was achieved; the final velocity values were

$$
\begin{aligned}
\text{upper mantle:} \quad V_p &= 7.70 \pm 0.13 \ \text{km/sec} \\
V_s &= 4.45 \pm 0.04 \ \text{km/sec} \\
\text{lower mantle:} \quad V_p &= 7.54 \pm 0.56 \ \text{km/sec} \\
V_s &= 4.25 \pm 0.13 \ \text{km/sec}
\end{aligned}
$$

and the final data a posteriori variance was $\sigma_d^2 = 19.2 \ \text{sec}^2$,
indicating an overall fit to the data of ± 4.4 sec, in good

agreement with the previous results and the a _priori_ estimate of data accuracy. The above results indicate that there is in fact a significant shear wave velocity drop from the upper to the lower mantle, as expected from earlier observations (discussed in the previous section). Note that the lower mantle velocities were not required to be lower than those in the upper mantle; they were simply allowed to be different and the data produced the above results. The P wave velocity drop is much smaller proportionally, and in view of the large uncertainty in the lower mantle P velocity, is not considered significant.

The second approach to inverting the full arrival time data set is based on the supposition that the true P wave velocity drop is indeed negligible as indicated by the above results; furthermore, in contrast with the shear wave data, no distinctive P wave shadow zone is seen on the surface event seismograms for any distance. Thus it is likely that in fact essentially no P wave velocity drop occurs at the boundary, or a small drop is gradual over an extended area. In either case no shadow zone will exist, and the two events previously omitted from the data set can be retrieved. Accordingly, the full data set was re-inverted and the upper and lower mantle P wave velocities were required to be the same at each step of the inversion; essentially there is no mantle interface for the P wave velocity structure and the quantity returned will be the best average velocity for the

whole mantle on the basis of the entire data set.

The starting values used were as before, and this time the iterations converged successfully, giving a final σ_d^2 of 19.4 sec^2. The resulting velocity values are

upper mantle: $V_S = 4.44 \pm 0.04$ km/sec

lower mantle: $V_S = 4.20 \pm 0.06$ km/sec

and: $V_p = 7.65 \pm 0.13$ km/sec

Note that the formal variance of the lower mantle shear wave velocity is much decreased from the previous inversion results; this is because the average whole mantle P wave velocity is much better constrained than was the original lower mantle value, and so the moonquake data can place tighter error bars on the shear wave value through determination of the V_p/V_S ratio. In essence, of course, the same data is being used to constrain only three velocity values instead of four. The final event locations from the inversion are given in Tables 3-8a and 3-8b. (Note that the location for Day 72 is given in parentheses; again the shear wave arrival times at stations 12 and 16 were lost inadvertently as the event location entered the edge of the geometric shadow zone. The preferred location including the constraints of these shear wave times is as given in Table 3-2 in parentheses; the resulting location is not in the shadow region with respect to stations 12 and 14, as discussed above.)

It remains to discuss the conclusions that can be drawn

from the above inversion results. First, the average P and
S wave velocity values in the upper and lower mantle regions
are well-constrained to be about

$$\text{upper mantle:} \quad V_p = 7.7 \pm 0.15 \text{ km/sec}$$
$$V_s = 4.45 \pm 0.05 \text{ km/sec}$$

$$\text{lower mantle:} \quad V_p = 7.6 \pm 0.6 \text{ km/sec}$$
$$V_s = 4.2 \pm 0.1 \text{ km/sec}$$

$$\text{average:} \quad V_p = 7.65 \pm 0.15 \text{ km/sec}$$

using a compendium of the values given above. These quan-
tities are relatively independent of the position of the
upper-lower mantle boundary, and are still valid if moderate
velocity gradients are present. The formal error bounds as
constrained by the entire seismic data set are reasonably
narrow, and therefore these velocity values constitute fairly
stringent constraints which any model of the lunar interior
must satisfy.

Second, the shear wave velocity results require that the
average values in the lower and upper mantle regions be sig-
nificantly different; a velocity decrease of about 0.25 km/sec
is indicated. This result is very satisfying because it is
independent of arguments concerning amplitude envelopes, a
few anomalously delayed and hard-to-measure arrival times,
or S-P vs. P times which are not easy to interpret; yet it
is in agreement with these preliminary observations (see
next section). The actual velocity drop can be due to a

C-3

sharp interface, a transition region, or a steadily decreasing gradient throughout the entire mantle. These alternatives are discussed below.

The P wave velocity drop indicated is much less significant and may not exist. The entire mantle is equally well represented by an average P wave velocity value that is well-constrained; moderate gradients are allowed if they satisfy the average value.

Finally, it is clear that the above average velocity values constitute nearly all the information that can be extracted from the primary data set, i.e. the direct P and S wave arrival times. Due to the small number of stations, the data cannot effectively constrain the characteristics of any velocity gradients that may be present. Similarly, the exact nature and position of the shear wave velocity drop cannot be determined. In addition, it is not feasible to attempt to determine the average velocities in a greater number of mantle layers in an effort to obtain more detail; the resulting uncertainties in the calculated velocities (assuming that a stable solution could be found) would be much larger than those given above, thus rendering the greater detail useless. In formal terms, as discussed in Appendix 4, we are clearly near the optimum point on the trade-off curve between resolution and accuracy.

The final epicentral location of the seismic events used in this work are shown in Figs. 3-1a and 3-1b. The approxi-

mate uncertainties are indicated by the size of the symbols, and open symbols are on the farside. Note that the moonquake foci are all marked with the same size symbol because the uncertainties as given in Table 3-7b are reasonably uniform; those indicated in Fig. 3-1b are average values. In Fig. 3-1a, as expected, the uncertainties generally increase as the events move farther from the center of the ALSEP array, although other factors such as the number of and amount of inconsistency in the arrivals observed for each focus also contribute to the formal error bars.

The locations shown are those given in Table 3-7 (with the exception of Day 72); other locations given by other inversions are nearly all within the error limits shown. These represent in a sense the best values as they result from the joint inversion of the entire data set. It is important to note, however, that when theoretical arrival time curves are compared with record sections of the events, it is generally sufficient to use any of the velocity models considered above as long as the model obtained jointly with the locations and origin times is also used to calculate the arrival time curves. For instance, the record section shown in Fig. 3-2 (transverse components of moonquake events at all stations) was constructed using an early velocity model; the agreement between the theoretical and observed S arrivals is clear.

3.3 Secondary Data Sets

3.3.1 Upper-Lower Mantle Interface Reflections

In order to constrain the nature and location of the
interface or transition region between the upper and lower
mantles it is necessary to turn to the secondary data sets.
On the basis of the observed shear wave shadow zone as dis-
cussed in early papers (and re-examined below) it has
been considered likely that the velocity drop from the upper
mantle region to the lower mantle region is not simply due to
a gradual velocity decrease beginning at the base of the
crust; rather, the decrease is confined to a limited region
so that at some point the velocity decrease with depth ap-
proaches or exceeds the critical gradient ($\frac{dV}{dr} < \frac{V}{r}$) thus pro-
ducing an effective shadow zone for surface events. The
simplest possible such velocity structure (as used above) is
of course a two-layer mantle with a zero-order velocity
discontinuity at a single interface. More complex models
could contain several step decreases in velocity, higher
order discontinuities such as a sharp change in the slope of
velocity with depth (c.f. Nakamura et al., 1976a), or a
continuous velocity profile with a steep velocity decrease
in some depth range.

If there are any such zero-order (or possibly even first-
order) velocity discontinuities, then it is possible that
the energy from surface seismic sources would be reflected

and produce visible secondary arrivals on the surface event
seismograms. As discussed in Chapter 2 and Appendix 3, we
can search for such phases on the lunar records by applying
a·polarization filter designed to enhance the rectilinear
particle motion of body wave arrivals. Previous work in
this area has been done by Dainty et al. (1976), Voss et al.
(1976), and Jarosch (1977). The former paper used the same
polarization filter as implemented herein, and processed
and examined about 23 records from eight artificial impacts
and six natural surface seismic events covering a distance
range of about 3° to 140°. Possible reflections were iden-
tified for boundaries at 400 and 500 km depth (with upper
mantle velocities of $V_p = 8.0$ km/sec and $V_s = 4.6$ km/sec;
the velocities used herein would change the above depths to
about 380 and 480 km). Both reflected P and reflected S
waves were tentatively observable, along with the accompany-
ing converted reflections S-P and P-S.

The latter two papers used a different polarization
filtering technique (described in Shimshone and Smith (1964))
which, as discussed in Appendix 3, may not be as effective
for the lunar situation as the one used herein because it
cannot detect arrivals that appear on only one component.
In addition, both papers analyze only the artificial impact
records. Voss et al. (1976) report a possible reflector at
300 km depth based on a PP reflection observed on seven
seismograms, all recorded at less than 13° of source-

receiver separation. Jarosch (1977) studied the same records plus two at about 30°-35° distance, and suggested that multiple surface-reflected phases were visible (e.g. PPP, P_4, etc.). It is desirable to confirm these observations by examining the natural event records from greater distances.

Thus it appears possible that reflectors are in fact present in the lunar mantle, although their placement is uncertain. This uncertainty is almost certainly caused by the large amount of scattered energy on the raw lunar seismograms and the resulting large number of pulses on the polarization filtered records (see filtered plots in Chapter 2 and Appendix 1); it is possible, even with the use of record sections, to mis-identify false-alarm noise pulses as true body wave arrivals. The only solution to this dilemma is to examine as many records as possible over a large distance range in order to reduce the chances that a series of noise pulses will apparently line up across the traces of a record section.

Accordingly, we have examined the seismograms from the surface events used in this thesis in an effort to resolve the above uncertainties. Following the procedure outlined in Chapter 2, the first step is to calculate and examine the theoretical amplitudes for reflected phases from interfaces at various depths. There are four such waves, two from each of the incident P and S waves. The ray tracer programs are described in Appendix 2.

The velocity models used are shown in Table 3-9, and the resulting amplitudes and times are given in Table 3-10. Tables 3-10a and 3-10b contain the values for reflectors at 400 km and 480 km depths, respectively, while Table 3-10c gives the direct P and S wave amplitudes (and times) for the same velocity model. An interesting effect is seen in this last table; the direct wave amplitudes increase with distance out to about 50°. This is a result of the $(di_1/d\Delta)$ factor in the ray-tube spreading calculation (see Appendix 2) which temporarily dominates the $1/R^2$ term at close distances for surface events. (Note that columns labeled P and S (S-H or S-V) in the first two tables refer to PP and SS reflected phases from the mantle interfaces.)

The following conclusions can be drawn from these tables. First, the reflected wave amplitudes can be as much as 0.1 to 0.2 times the direct wave amplitudes. Such ratios are comparable to those calculated for the crustal peg-leg multiples, and so the reflected phases may also be visible if reflectors do indeed exist in the lunar mantle. Second, the larger amplitudes tend to occur at greater distances, and the same-type reflections are generally larger than the converted reflected waves. Beyond 40° the S-H reflection is invariably the largest. As discussed in Chapter 2, the shear wave contains substantially more energy than the P wave (particularly for HFT events), and so it is appropriate to search for the S-H, S-V and SP reflections, which

should be seen on the transverse, radial, and vertical components respectively due to the near-vertical incidence of all surface-arising waves. The S-H reflection should be the most prominent, followed by the S-V, and finally the SP conversion should be the smallest by a factor of two or so.

The record section plots of all available polarization-filtered surface event records are shown in Figs. 3-3. The first two (3-3a and 3-3b) show the transverse components of ground motion split up into two figures to provide better clarity. There are 17 records plotted, representing 11 of the 16 surface events. All other records are either at less than 20° source-receiver separation, where only low amplitudes are expected for reflected phases, or beyond 60° where it is difficult to separate the direct S arrival from any reflections that may be present. The theoretical curves shown mark the expected arrival times of direct S and the SS reflected phases from interfaces at depths of 400 km and 480 km (on the transverse component the S-H waves are seen). The observed and predicted S arrival times are in good agreement as expected from the inversion results. There is good correlation for the 480 km interface, and weaker but nevertheless prominent arrivals occur along the 400 km curve. Little evidence is seen for a 300 km reflector. Thus it seems that there are possibly at least two velocity discontinuities in the lunar mantle, with the major boundary at 480 km depth.

To further examine this possibility, the radial and ver-
tical components of ground motion are shown in Figs. 3-3c,
d, and e. The first two are the radial records which should
contain S-H reflected and direct phases as marked. The corre-
lations are not quite as convincing as on the transverse com-
ponent record sections, but there is substantial supporting
evidence, as can be seen, which strengthens the interpre-
tation made above. Finally, the smallest amplitudes are ex-
pected on the vertical components from the S-P converted
reflection, and as seen in Fig. 3-3e there are only a few
correlations between observed arrivals and the predicted
arrival times. (Notice that the S-P reflection from a
400 km boundary only exists at source-receiver separations
less than about 45°.)

The final step is to examine the moonquake event record
sections to see if any corroborating phases are present. The
most likely possibilities are the transmitted converted phases
S-P, which leave the source as S and are converted to P at
a mantle interface. Theoretical amplitudes for such converted
phases are given in Table 3-12 along with the amplitudes
of the direct P and S waves; the velocity model used is given
in Table 3-11. As can be seen, the maximum amplitude of any
converted phase is only .06 times the direct wave amplitudes,
making their potential observation somewhat questionable.
As usual, we would only expect to see the S-P conversion;
moonquake direct P wave arrivals are very small. This phase

only exists to about 35° for a mantle interface at 520 km
depth, but is theoretically present at all ranges for a 300
km interface depth.

Thus the only possibility is to look for the S-P phase
from deep moonquakes on the filtered vertical components;
the optimal range should be between 20 and 40 degrees.
Again, the necessary origin time corrections as discussed
in Chapter 2 are all very similar (within 2 seconds) for the
S-P phase from any interface depths between 300 and 500 km,
and so an S-P (400) correction was used for all record
sections. All moonquake records were then examined and a
typical subset is shown as Fig. 3-4. No consistent cor-
relations between arrival time curves and the seismograms
were found, as might be expected from the predicted ampli-
tudes, and so the moonquake data can provide no corroborat-
ing evidence.

In sum then there appears to be fairly convincing evi-
dence from surface event reflected waves for a discontinuity
in the mantle at a depth of about 480 km, and weaker evi-
dence for another interface at about 400 km depth, in reason-
able agreement with Dainty et al. (1976). Assuming that
we are indeed correct in identifying the observed phases
as mantle interface reflections, the allowable error bars
including ±2 cycles (equal to ±4 seconds) for properly
aligning the arrival time curve with the observed arrivals
and ±.05 km/sec in upper mantle velocity are about ±20 km

for each interface. (The uncertainty in origin time is not a factor because it can be eliminated by using the time difference between the reflected and direct S arrivals.)

Given that a shear wave velocity drop from the upper to lower mantle regions is required by the arrival time data, a simple structural interpretation of the interfaces tentatively identified above is that they represent zero-order velocity discontinuities where the velocity decrease occurs. If only the 480 km boundary is real, then all of the velocity drop could occur there. If the 400 km interface is also present, then the velocity decrease could be accomplished by a series of two smaller velocity drops or by some sort of transition zone with complex structure and generally negative velocity gradients between 400 and 480 km depth.

3.3.2 Shear Wave Shadow Zone

To further study these possibilities, it is necessary to examine the characteristics of the shear wave shadow zone observed for surface events. (The existence of the shadow zone has been noted in Toksöz et al. (1974a) and Nakamura et al. (1976).) The optimal way to approach this is to construct a record section of the short-period vertical records, for two reasons. First, even though they measure the vertical component of ground motion, there is significant shear wave energy present, primarily as a result of scattering effects. Second, the rise time of the shear

wave envelope is shorter on the short-period records than on the long-period records, as mentioned in Chapter 1, thus making the onset of the shear wave energy envelope easier to see.

The resulting record section plot is shown in Fig. 3-5. Unfortunately due to the necessary reduction to page size not all of the traces are clearly visible; expanded versions of each trace are shown in Figs. A1-5 and A1-10. The distance in central angle is given for each record as calculated from the locations given in Table 3-8. (Table 3-2 could also have been used; the event epicentral distances vary by at most 2-3° for all the structural models used in the previous section, including those with velocity gradients in the upper mantle.) All available records from HFT events are included since they produce the largest shear wave amplitudes, along with the four impact events that produce any records beyond 90° distance. The other four impacts are all within 90° of all stations and so do not add any information concerning the shadow region. The impact records are marked by dots in Fig. 3-5, and the source and receiving station for each trace are listed in Table 3-13.

The arrows mark the predicted shear wave arrival times, which are aligned on the section (rather than the origin time). Up until about 85 degrees, with only a few possible exceptions every trace shows a distinctive shear wave envelope at the expected time. Beginning with the records

at 86°, the envelope onset begins to be less pronounced on
a few records, and past 96° little shear wave envelope is
visible at the expected time. The triangles mark the expected
onset of the SS surface-reflected phase, and several of the
more distant records show a corresponding envelope. This
can be seen more clearly for example in Fig. A1-10a (at
station 15 S is expected at about minute 67.5 and SS at
minute 69.3), and in Fig. A1-10c (at station 14 S expected
at minute 56.8, SS at 58.3). Thus it seems that there is in
fact a substantial loss of shear wave amplitude beginning
at about 90° ± 10°, the large error bars being due to the
formal errors in event locations combined with the uncer-
tainty observed in Fig. 3-5. The delayed envelopes that ap-
pear on records beyond 100° seem to often represent the SS
surface-reflection arrival.

This can be further studied by examining the long-
period records for source-receiver pairs omitted from Fig.
3-5, i.e. the twelve records at station 12 where the SP
instrument is inoperative and four records from other stations
where the SP record was not retrievable from the data tapes.
This can be done by examining the plots included in Appendix
1, and the results are summarized in Table 3-14. In addition
the long-period records corresponding to the short-period
traces in Fig. 3-5 have been examined. The observations
generally confirm those seen on the short-period records,
implying a shear wave amplitude loss beginning at about 90°

distance.

There two mechanisms which can account for the loss of energy in the seismic shear waves from surface events. Velocity decreases with depth spread the seismic rays arriving at the surface. If the negative velocity gradient approaches or exceeds the critical value, then little or no energy is returned to the surface over a certain distance range (except diffracted energy not considered in ray theory). This relationship is quantified in the next section. The other mechanism is an increase in attenuation with depth, so that rays will be more attenuated as they bottom at greater depths and reach greater epicentral distances (assuming a prograde travel time curve).

The characteristics of the lunar shadow zone suggest that both of these mechanisms are operating simultaneously. First, the onset of the shear wave amplitude loss appears to occur in a small range of distances, in the sense that most records (especially those of HFT events) have either a clear shear wave envelope or only little or no shear wave expression. This is true for both long-period and short-period records. Of course, in view of the formal location uncertainties given above, and the relatively small number, and variable quality, and signal-to-noise ratio of the seismograms it is difficult to ascertain the precise characteristics of the amplitude loss onset. Nevertheless, to date no clear-cut transitional records have been observed.

This suggests that there is a velocity decrease that approaches the critical gradient, creating at least a small region of low shear wave amplitudes that begins rather sharply beyond a critical distance. Even a sudden attenuation increase at some depth would only gradually affect the shear wave envelopes as the rays penetrated deeper into and therefore traveled further in the attenuating zone. (This assumes that the attenuation increase is not excessive, based on the fact that the deep moonquakes apparently occur within the attenuating region and yet produce clearly observable shear waves. This is discussed below.)

A velocity drop then typically produces a shadow zone of limited extent. For example, the inversion models used that had a shear wave velocity drop from $V_S = 4.45$ km/sec to $V_S = 4.20$ km/sec at a 500 km boundary would produce a geometric shadow zone from only 90° to about 107° distance. A negative velocity gradient that is near the critical value $dv/V \sim dr/r$ becomes non-critical rather quickly as the radius decreases, unless the negative velocity gradient increases proportionally, and thus typically gives an even smaller shadow region. Figure 3-5 indicates that the shadow zone reaches to at least 140°, and so it is likely that there is an attenuation increase along with the velocity decrease so that the rays received beyond the shadow zone will be attenuated as a result of their extended travel path in the region below the velocity decrease.

Thus it appears that a fairly sharp velocity decrease and an attenuation increase for shear waves at some depth in the lunar mantle are implied by the short-period record section; the resulting low-amplitude zone must begin no closer than about 90° (source-receiver separation). This last feature is required by the short-period record section, which is relatively independent of velocity model assumptions, and by the surface event inversion results which show that a shadow zone beginning before 90° encompasses a significant number of clearly observed shear wave arrivals when the final best event locations are obtained.

The next step is to relate the average velocities obtained from inversion of arrival time data, the tentative mantle boundaries identified by reflected surface event waves, and the constraints provided by the existence of the shear wave shadow zone. There are basically two models that will satisfy all of these results.

1) If the 480 km boundary in fact represents the sharp velocity decrease, then the upper mantle shear wave velocity gradient must be nearly zero (i.e. a constant-velocity upper mantle) so that the shadow zone from this velocity drop will commence at 90° distance. The upper mantle velocities will then be V_p = 7.7 km/sec, V_s = 4.45 km/sec, and the lower mantle velocities V_p = 7.6 km/sec and V_s = 4.2 km/sec. As mentioned before, there may be no P wave velocity decrease.

2) If the 400 km interface indeed exists and represents

the beginning of the shear wave velocity decrease, then the upper mantle must have a negative velocity gradient so that the rays bottoming immediately above 400 km will reach 90° distance. The required gradient is about -6×10^{-4} km/sec; to satisfy the required average shear wave velocity a profile with $V_s = 4.57$ immediately below the crust to 4.37 at 400 km depth is appropriate. The accompanying P wave velocity profile may decrease from 7.75 to 7.65, still satisfying the average upper mantle P wave velocity required by the arrival time data. Between the 400 km and 480 km boundaries the shear wave velocity decreases sharply, possibly in a series of two or more steps which would produce the observed reflections. Since the structure of such a zone is likely to be complex, in the absence of more detailed information it is appropriate to model it as a smooth transition zone from $V_s = 4.37$ km/sec at 400 km to $V_s = 4.20$ km/sec at 480 km, while noting that velocity discontinuities of some sort at the upper and lower interfaces are probably required by the observed reflected phases. The overall gradient is then 2.1×10^{-3} km/sec/km, or about 64% of the critical gradient. This is sufficient to produce an effective shadow zone from 90° to about 110° (discussed below). The P wave velocity could decrease a small amount also, from 7.65 km/sec to 7.60 km/sec, satisfying the average velocity requirements while producing essentially no shadow zone for P waves (the negative velocity gradient is only about 10%

of the critical value).

This second model is slightly preferred because a) it includes the 400 km interface and b) the possible P wave velocity drop can be accomodated easily without creating a significant shadow zone. The velocity profiles are shown in Fig. 3-6 as a function of depth and approximate pressure (the pressure and relation to terrestrial velocities are discussed in Chapter 5), and the actual values listed in Table 3-15. This model satisfies the average velocity values required by the arrival time data inversions, the tentative mantle interfaces, the onset point of the surface event shear wave amplitude loss, and the absence of any observable P wave shadow region. In addition, it satisfies the observation that the velocity drop must occur above 560 km depth to avoid creating shadow zones that interfere with the observed moonquake arrivals.

3.3.3 Amplitude vs. Distance Curves

The final step is to examine the quantitative implications of these models on amplitudes over the entire disstance range 0° to 140°, including the effects of anelastic attenuation, thus quantifying the above discussions. In order to do this it is necessary to obtain some estimates of the attenuation at various depths in the moon. The quantity of interest is the quality factor Q as defined and discussed in Appendix 2. On the basis of diffusion

modeling of the scattering zone, the crustal Q_p and Q_s are
about 5000 (Dainty et al., 1974a). Nakamura et al. (1976b)
report similar values. The Q structure of the lunar mantle
has been studied by Dainty et al. (1976) and Nakamura et al
(1976a); both papers use a similar technique (also used
terrestrially, c.f. Solomon and Toksöz, 1970). Basically,
the analysis assumes that Q values are constant in each
layer of lunar structure, and then an approximate estimate
of Q for a layer can be extracted from the slope of a plot
of log (A_2/A_1) vs. frequency, where A_2 and A_1 are the ob-
served amplitudes of two rays that bottom at different depths
in the layer.

Dainty et al. (1976) applied this technique to five
natural surface seismic events, analyzing a total of nine
seismogram pairs (naturally only records from the same event
were compared in order to eliminate source effects on the
spectral content of the seismograms; the frequency response
of the SP instruments at different stations is assumed to be
the same). The slope values were computed by fitting a best
straight line to the smoothed ratio of the Fourier amplitude
spectra, calculated from the first two minutes of P wave coda
on the SP seismograms. (The peaked response LP records
do not have a large enough bandwidth to permit a useful
slope value to be measured.) An example is shown in Fig. 3-7.
The primary conclusion from this work is that there is a
marked Q decrease for records beyond 90° to 100° distance,

in excellent agreement with the above discussion suggesting that a low Q (high attenuation) region is required to explain the continued shear wave shadow zone. Furthermore, the distance range indicated suggests that the Q decrease roughly coincides with the velocity decrease. The actual values obtained are $Q_p \sim 5000$ in the upper mantle, and $Q_p \sim 1500$ for the lower mantle. In view of the necessary assumptions and scatter in slope values, error bars of about 20% are given.

Now these are Q values for compressional waves; it is not a simple matter to deduce the corresponding values for Q_s. If all attenuation occurs as a result of shear anelastic losses, i.e. the bulk attenuation factor Q_B is ∞, then for a Poisson solid $Q_s = 4/9\ Q_p$ (Knopoff, 1964), giving Q_s values of about 2200 and 700 for the upper and lower mantle regions, respectively. However, it is entirely possible that the above assumption is not correct. Another estimate of the shear wave Q values has been obtained by Nakamura et al. (1976a). The method used is essentially the same as described above, except that 1) each slope is calculated from only two amplitude ratio values (one at 1.0 Hz and one at 8.0 Hz, and 2) the amplitudes were obtained from the section of the seismogram dominated by the shear wave coda. The values obtained are $Q_s = 4000$ and $Q_s = 1500$ for the upper and lower mantle regions, but error bars are probably larger than for the previous study (say 30-40%) since only two points were used to obtain the

spectral ratio slopes. (For example, the possible slope variations obtainable in Fig. 3-7 by choosing different pairs of points are quite large.)

In order to obtain hopefully representative values for Q_s, the above two sets have been averaged. The appropriate formula is

$$\frac{1}{Q_s} = \frac{1}{2}[\frac{1}{Q_1} + \frac{1}{Q_2}]$$

thus averaging the energy loss per cycle; the resulting values are approximately 3000 and 1000 for the upper and lower mantle. (Note that this value of Q_s for the lower mantle is still quite high by terrestrial standards; for a moonquake at 1100 km depth the resulting attenuation of the shear wave at 0.5 Hz in the lower mantle is only 20% in amplitude. The attenuation at 2 Hz, however, is about 60%, at least in part accounting for the lack of moonquake energy seen on the short-period records.) The complete Q model used in this thesis is summarized in Table 3-16. The values are listed by region only; the depth of the Q decrease along with the major shear wave velocity decrease is dependent on the bottoming depth of the seismic waves and thus on the velocity gradients in the upper mantle. As mentioned above, though the Q and velocity decreases appear to roughly coincide no matter what upper mantle velocity structure is chosen; this is because in general the same surface event records which show the onset of the shear wave shadow zone

also indicate the decrease in Q.

The only quantitative surface event amplitude data as a function of distance that is available is given in Nakamura et al. (1976a), Figure 1. They show a series of points from 3° to about 160° distance that represent the amplitude measured on the long period records (Z component for ALSEP 12 and Y component for the other stations) near the signal peak over a small range of frequencies. HFT's meteorite impacts, and artificial impacts are all included. There are several assumptions involved in constructing the resulting amplitude vs. distance plot which should be noted.

1) Since the amplitude is measured at the signal peak, it represents the amplitude of whatever wave coda is dominant at that point. As we have seen, in general for distances closer than 90°, this is usually the shear wave, although for impact events the P wave contribution is probably more significant and so the "apparent" S wave amplitude will be larger than the true value. Beyond 90° it is likely that the measured amplitude value represents predominantly the SS surface reflected phase, along with smaller contributions from the P wave coda, secondary wave codas, and what little direct S wave coda is seen. The SS arrival can be seen for instance in Fig. 3-5 on the SP traces beyond about 100°, and on the LP records in Figs. Al-2b (stations 12, expected SS at about minute 66), Al-2f (station 12, SS expected ~minute 11 and 55 seconds), and Al-7c (station 12, SS expected

at minute 59 and 10 seconds), all of which were recorded

beyond 90° distance. In addition, the SS phase is occasion-

ally seen at closer ranges superimposed on the direct S wave

coda (Fig. Al-2g, station 12, SS at minute 12 and 55 seconds),

and so may bias the amplitude measurements at close distances

also. Considering these caveats, then, the measured ampli-

tudes from the signal peaks are assumed to be roughly pro-

portional for a given event to the direct S wave amplitude

up to 90° distance, where the true shear wave amplitude

decreases markedly and the measurements may represent SS or

other phases.

2) The resulting values were then corrected for dif-

ferential station sensitivity, using values estimated from

amplitude ratios for a large number of signals. To the

extent that these corrections are approximate further possible

errors are introduced into the data.

3) Finally, the principle of smoothness is used to

overcome the effect of source energy variation and match the

sets of at most four amplitude values to a single level.

In principle, this is a valid approach, but in practice

errors in the relative amplitude values for a given event

will tend to propagate through the curve to further distances

as the smoothness principle is involved iteratively. This

can be more or less serious depending on the amount of over-

lap achieved by the various data sets (maximum distance

range for any event is 39°, the maximum station separation).

Despite all these assumptions and possible sources of error, it is probable that the plotted points (shown in Fig. 3-9) are roughly representative of the shear wave amplitude curve out to 90°, at least within the 5-7 dB (linear factor of 2) scatter shown. Therefore, it is appropriate to see how well our proposed velocity and Q models fit the amplitude data.

In order to calculate the theoretical amplitudes over the distance range 5° to about 140° (the region beyond 140° is considered in Chapter 4) it is necessary to use the detailed crustal velocity model as shown in Fig. 2-7 (and listed in Table 4 of Toksöz et al. (1974a)), rather than the simplified two-layer model used previously. In fact, the two-layer model produces very similar results but for the sake of completeness the detailed structure is appropriate. The programs used are described in Appendix 2, and they consider only the effects of ray-tube spreading and anelastic attenuation on the amplitude values. As mentioned therein, transmission coefficients at the various interfaces do not contribute a significant effect.

The first step is to calculate the expected amplitudes for near distances where the arriving waves bottom in the crust; these values will be the same no matter what mantle velocity model is used. Since the observed data points in Fig. 3-9 begin at about 3°, we are interested only in the amplitudes beginning with rays bottoming in the lower crust

(see Figs. 2-1 and 2-3).

The calculated amplitudes on a linear but arbitrary scale are shown in Fig. 3-8 as the solid and short-dashed line. (The dashed lines represent regions where ray theory is not adequate and are approximations to the true curve.) They begin at about 2° falling from the amplitude of the last sub-critically reflected wave from the upper-lower mantle velocity increase. The ensuing solid portion gives the low amplitudes of waves bottoming in the lower crust, followed by the retrograde high amplitude arrivals of the reflected wave from the base of the crust. The last portion that ends at the outward pointing arrow is the amplitude of waves returning from immediately below the crust in the upper mantle; the values are of course somewhat dependent on the velocity in the upper mantle (actually on the proportional velocity increase across the crust-mantle boundary) but as discussed below for reasonable models the amplitude levels vary only by 10%. Now all of these waves arrive within at most 15 to 20 seconds of each other, which is a small fraction of the rise time observed for seismic arrivals on the moon (typically 5 to 10 minutes). Thus the amplitude as measured at the signal peak will include contributions from all three arrivals, and should represent approximately the square root of the sum of the arriving energies.

This quantity is shown by the long-dashed curve in Fig. 3-8. It is smoothed somewhat over the sharp amplitude

discontinuities produced from ray theory, particularly in the range from 25° to 30° where the end of the crustal contributions is continued smoothly into the mantle amplitudes at 30°. This curve then is the theoretical amplitude distribution that should be fit to the observed data between 3° and 25° distance.

Fig. 3-9a shows the data points measured by Nakamura et al. representing the shear wave amplitude profile with distance. The solid line is the theoretical amplitude curve predicted by the model described above with a shear velocity drop at the 480 km reflector and a constant velocity in the upper mantle. The part of the curve between 5° and 25°-30°. is taken from Fig. 3-8, as discussed. As can be seen, the fit out to 90° is excellent; the relative level of crust phase amplitudes and mantle phase amplitudes is correct. At 90° the expected geometric shadow zone occurs, extending to about 107°. From about 107°-109° distance there is a sharp amplitude spike caused by the turning point of the T-Δ curve (see Fig. A2-1) and the resulting confluence of rays. The magnitude of the spike is partially an artifact of ray theory, and the narrow distance range and true wave nature of seismic arrivals make it unlikely that it would be observed with the present rather sparse coverage of amplitude measurements. Beyond 110° the amplitudes are low as a result of the Q values ($Q_s = 1000$ in the lower mantle, significantly lower than the data points, confirming the view that the measured amplitudes

beyond 90° represent SS and other contributions. The predicted
amplitudes beyond 90° are down by factor of 2 to 4 from the
arrivals in the 30°-90° zone, which is sufficient to account
for the observed absence of strong shear wave arrivals beyond
the geometric shadow zone (>110°). Furthermore, the model
used has a constant shear wave velocity profile in the lower
mantle region; it is possible (and perhaps likely if tem-
peratures are increasing) that the gradient is somewhat nega-
tive, which would decrease the amplitudes in the 110°-140°
range even further. However, we have no constraint on this
gradient except for the average velocity value as determined
from the arrival time inversion and so it is not included
in the amplitude calculations.

Fig. 3-9b shows a similar plot for the "transition zone"
model described above which includes boundaries at both 400
and 480 km with a sharp velocity decrease between them. The
velocity model for this case is shown in Fig. 3-6. The
agreement between the predicted and observed amplitudes at
distances less than 90° is not quite as good as the previous
figure, but still perfectly adequate in view of the scatter in
the data and the uncertainties discussed above. Beyond 90°
there is not an absolute shadow zone, but rather a sharp
velocity minimum between 90° and 100°, followed again by a
very narrow spike, and then decreasing velocities out to
140°. As before, the amplitudes between 100° and 140° average
about 1/2 to 1/3 of those between 30° and 90°, and may be

decreased still further by a negative velocity gradient in the lower mantle.

Finally, it is interesting to compare these results with those of the latest Galveston lunar velocity model given in Nakamura et al. (1976a). In order to do this, the same crustal model is used (it is very similar to the Galveston crustal model), and the mantle velocities are measured from Fig. 3 of Nakamura et al. (1976a). Unfortunately these values are only approximate because the paper does not include a table of velocities. The Q_s values reported by them are also used; the values are mentioned above. The resulting curve is shown in Fig. 3-9c. It is immediately obvious that the predicted mantle amplitudes are far too low relative to the crustal amplitudes. The source of this discrepancy is the steep negative velocity gradient (-13×10^{-4} km/sec/km) required in the upper mantle in order to enable the rays bottoming immediately above 300 km depth to reach 90° distance, at 300 km begins a sharp velocity decrease which produces the amplitude loss shown at 90° in Fig. 3-9c. For comparison, the velocity gradients in the upper mantle of the models for Figs. 3-9a and 3-9b are 0 and -6×10^{-4} km/sec/km respectively. As can be seen, the amplitude level between 30° and 90° relative to the crustal phase amplitudes decreases systematically from Fig. 3-9a through Fig. 3-9c, in direct response to the increasing negative upper mantle velocity gradient, which increasingly spreads the rays traversing the region. Thus

the amplitude data seem to imply that the maximum negative velocity gradient in the upper mantle is about -6×10^{-4} km/sec/km, and given the fact that the shear wave amplitude loss onset is near 90°, this constrains the sharp velocity decrease responsible to be no shallower than 400 km depth. This is an important constraint, and it is gratifying that our models proposed from independent data are in close agreement.

It will be noticed that Nakamura et al. (1976a) do in fact present a theoretical amplitude curve that agrees with the above data points. It is very similar to the curve shown in Fig. 3-9c; the difference lies in that they fit the measured amplitude values between 5° and 20° to the predicted amplitudes of the rays bottoming in the lower crust. The much larger amplitudes expected from the sub-critical reflection at the base of the crust are ignored, the line representing these is drawn well above all observed data points. This alignment does permit the mantle phase amplitudes (30°-90°) to fit the data (essentially the whole curve in Fig. 3-9c is shifted up by about 6 dB relative to the data), but only as a result of improperly fitting the crustal arrival amplitudes.

Nakamura (personal communication) has suggested that the discrepancy may be resolved by varying the magnitude of the velocity jump at the crust-mantle boundary. As expected, the net effect of varying the velocity increase from .7 km/sec

to 1.1 km/sec with a variety of absolute velocity values produces a maximum relative change between crustal and mantle amplitude levels of about one dB, an insignificant amount. As asserted above, the velocity gradient in the upper mantle is the principle controlling factor. A final difficulty with the curve shown in Fig. 3-9c is that the amplitudes between 115° and 140° are quite high, only about 30% below those for the 30°-90° range, implying that more shear wave amplitude should be observable at far distances than is in fact the case.

In spite of the above difficulties and the inherent and potentially large uncertainties in the observed amplitude data curve, Nakamura et al. (1976a) use the velocity gradient in the upper mantle (-13 x 10^{-4} km/sec/km as derived from the amplitude vs. distance curve) in conjunction with the observed shadow zone onset at 90°, to obtain 300 km for the depth of the sharp velocity decrease. On the basis of the above discussion, this value must be considered suspect; a more reasonable estimate from the amplitude data is 400 km to 500 km, in agreement with the observed reflected phases mentioned above.

Finally, the P wave amplitude curve was calculated for the curve shown in Fig. 3-6. Although there is no qualitative data available for comparison, the resulting predicted amplitudes are reasonable, showing a slow, smooth decrease as a function of distance with only minor perturbations caused

by the small velocity gradient variations in Fig. 3-6. There is no region of decreased amplitudes.

In summary, the final preferred velocity model for the lunar interior is as shown in Fig. 3-6 and listed in Table 3-15. The upper mantle extends from 60 km to 400 km depth with negative velocity gradients of 3×10^{-4} km/sec/km (~6% of critical value) and 6×10^{-4} km/sec/km (~20% of critical value) for P and S waves, respectively. The average values are $V_p = 7.7$ km/sec and $V_s = 4.45$ km/sec. From 400 km to 480 km depth the gradients increase sharply to 6×10^{-4} km/sec/km (~10% of critical) and 21×10^{-4} km/sec/km (~64% of critical for P and S, creating an effective shadow zone for shear waves. Below 480 km to the depth of the moonquakes (900 km - 1000 km), the average velocities are $V_p = 7.6$ km/sec and $V_s = 4.2$ km/sec, with decreased Q values as given in Table 3-16.

The uncertainty in the average velocity values are as listed above. Additional uncertainties are 1) the transition zone may well be more complex and contain step decreases in velocity rather than a smooth gradient, especially in view of the observed reflected waves which suggest zero-order discontinuities, 2) the 400 km interface is only weakly constrained and the bulk of the shear wave velocity drop may occur at 480 km depth, and 3) the P wave velocity may be essentially constant throughout the lunar mantle. Nonetheless, the main and important features of the velocity

model are well constrained and satisfy all the available lunar seismic data.

The final two figures 3-10a and 3-10b show the seismic ray paths of waves from a surface event and a deep moonquake (900 km depth). The crust-mantle and transition zone boundaries are shown. The structural and compositional implications of the results in this chapter are discussed in Chapter 5.

Table 3-1

Starting locations and origin times for surface event inversion

| Event | | Starting Model | | Origin Time |
Yr	Day	Colatitude (deg)	Longitude (deg)	(sec)*
72	134	88.8	-16.2	-18.6
72	199	55.6	147.4	-387.9
72	213	54.3	4.8	-53.8
72	324	26.5	-39.8	-171.3
75	102	86.6	36.7	-121.4
75	124	120.1	-125.1	-36.4
76	25	94.9	-69.6	-195.9
77	107	109.4	-59.5	-156.6
73	72	165.2	-150.0	-272.7
73	171	84.1	-63.0	-166.6
74	192	73.8	87.2	-289.6
75	3	60.1	-90.0	-272.2
75	44	104.4	-21.6	-62.9
76	4	51.9	27.8	-106.0
76	66	43.3	-22.5	-145.8
76	68	105.3	-11.5	-38.4

*Relative to reference times given in Tables 1-4 and 1-5.

Table 3-2

Final event locations and origin times for
surface event inversion

Starting Model

Event		Colatitude (deg)	Longitude (deg)	Origin Time (sec)*
Yr	Day			
72	134	88.9+0.7	-16.3+0.8	-18.0+2.4
72	199	56.3+6.0	129.4+7.3	-366.5+12.6
72	213	54.2+1.5	5.6+2.0	-54.6+8.24
72	324	24.7+2.7	-43.8+10.5	-178.3+16.3
75	102	87.2+1.9	38.7+2.7	-127.6+11.1
75	124	123.6+5.4	-124.5+6.4	-343.9+13.0
76	25	96.5+2.7	-71.2+2.6	-201.0+12.3
77	107	104.5+4.4	-56.0+9.2	-140.0+32.0
73	72	163.4+8.5 (173.1∓2.4)	-166.9+14.9 (-139.0∓21.1)	-314.7+18.7 (-292.9∓9.6)
73	171	84.2+3.5	-64.8+3.0	-171.9+12.4
74	192	74.9+4.4	95.7+9.2	-312.8+20.0
75	3	62.8+5.9	-106.7+4.2	-273.1+12.8
75	44	104.9+1.5	-20.1+1.9	-57.3+9.5
76	66	41.7+2.2	-23.5+2.0	-151.2+10.7
76	68	106.0+1.6	-11.8+1.0	-40.4+6.7

*Relative to reference times given in Tables 1-4 and 1-5.

Table 3-3

Importance of data to surface event inverse
solution, grouped by station and wave type

Wave Type	Station 12	14	15	16	All	Average per data point
P	5.881	4.667	11.297	10.572	32.417	0.569
S	6.608	2.365	5.452	3.152	17.577	0.651
Total	12.489	7.032	16.749	13.724	50.0	0.595

Table 3-4

Comparison of the final fit to the HFT data as a function
of average source depth

HFT average depth (km)	fit to data (σ_d^2 in sec^2)
0	31.67
15	32.90
30	34.02
100	36.15

Table 3-5

Starting locations and origin times for moonquake inversion

Focus	Colatitude (deg)	Longitude (deg)	Depth	Origin Time (sec) [3]
A1	100.5	-26.6	805.3	-101.0
A15	96.1	3.2	912.9	-95.5
A16	83.5	2.8	928.9	-128.0
A17	68.6	-16.7	754.7	-124.9
A18	71.6	20.7	854.2	-92.1
A20	72.1	-22.6	877.3	-141.0
A27	73.3	11.1	912.9	-91.1
A30	80.2	-24.2	836.4	-97.7
A31	76.1	7.9	1127.0	-156.0
A32	72.6	18.8	782.2	-96.5
A33	79.4	83.1	1094.0	-199.0
A34	83.2	-5.7	849.8	-88.7
A36	46.9	-4.2	1016.0	-93.8
A40	89.9	-9.3	805.0	-70.6
A41	68.8	-36.3	790.9	-100.8
A42	70.9	-35.7	949.3	-103.0
A44	36.8	20.9	968.0	-117.9
A45	102.1	-28.0	927.1	-113.0
A46	100.5	-26.3	841.8	-73.1

Table 3-5 (cont'd)

Focus	Colatitude (deg)	Longitude (deg)	Depth	Origin Time (sec)
A50	81.2	-39.9	872.9	-106.0
A51	81.4	11.7	769.8	-79.0
A56	81.4	-25.2	736.0	-57.5
A61	66.9	37.7	868.0	-203.0
A62	50.4	40.1	963.5	-137.5

*Relative to reference times in Table 1-6.

Table 3-6

Final locations and origin times for moonquake inversion

Focus	Colatitude (deg)	Longitude (deg)	Depth	Origin Time* (sec)
A1	103.2±1.9	-31.1±2.6	840.2±24.9	-111.2±6.9
A15	99.6±2.8	4.4±1.4	1012.7±51.3	-108.7±10.7
A16	83.5±1.3	2.3±1.3	1029.9±49.0	-140.4±7.8
A17	66.5±1.6	-19.1±1.9	786.3±34.2	-131.6±6.6
A18	68.9±1.8	26.2±3.0	913.0±33.2	-104.7±7.9
A20	69.3±1.8	-28.5±3.3	942.1±32.8	-153.3±8.2
A27	70.4±2.0	14.6±2.5	989.8±49.6	-101.2±9.7
A30	79.3±1.3	-28.6±2.9	884.0±34.1	-106.0±7.7
A31	76.6±2.3	7.5±2.2	1101.3±58.8	-154.0±10.8
A32	73.2±1.2	17.8±1.8	760.3±38.7	-94.4±6.6
A33	83.6±2.8	109.0±5.7	997.0±118.8	-247.8±16.4
A34	82.7±1.2	-6.8±1.4	933.2±54.8	-94.7±9.5
A36	32.6±5.5	-9.4±4.6	1049.8±33.9	-116.6±12.3
A40	90.8±1.3	-10.6±1.3	869.0±39.3	-77.7±6.9
A41	67.2±1.5	-37.5±3.0	707.0±42.5	-111.7±8.7
A42	68.1±2.0	-45.5±4.6	973.9±35.3	-117.0±8.9
A44	45.6±2.7	44.2±5.8	943.2±43.0	-124.5±10.9
A45	105.9±2.6	-34.8±3.6	957.0±27.7	-123.9±7.9
A46	102.6±2.1	-30.5±2.7	873.8±25.7	-79.5±7.2
A50	80.8±1.5	-47.6±3.8	875.7±35.2	-117.0±7.9
A51	80.9±0.9	13.9±1.6	830.6±38.4	-86.7±6.4

Table 3-6 (Cont'd)

Focus	Colatitude (deg)	Longitude (deg)	Depth	Origin Time (sec)
A56	81.5±1.0	−23.9±2.2	715.1±40.4	−55.5±8.4
A61	67.9±1.8	35.9±4.1	847.4±38.6	−199.2±12.0
A62	46.6±2.4	53.2±6.1	955.3±49.5	−149.9±11.2

*Relative to reference times in Table 1-6.

Table 3-7

Importance of data to mooonquake inverse solution,
grouped by station and wave type

Wave Type	Station					Average per data point
	12	14	15	16	All	
P	3.718	10.112	9.665	6.355	29.850	0.597
S	10.463	13.134	22.317	22.229	68.143	0.757
Total	14.181	23.246	31.982	28.584	98.0	0.700

Table 3-8a

Final locations and origin times for
all events from joint inversion

Surface Events

Yr	Day	Colatitude (deg)	Longitude (deg)	Origin Time (sec)*,
72	134	88.9±0.6	-16.1±0.6	-18.8±1.9
72	199	56.9±4.4	130.8±5.7	-376.2±12.1
72	213	53.4±1.4	5.6±1.6	-59.7±7.3
72	324	23.7±2.2	-47.0±8.9	-187.8±13.7
75	102	87.0±1.5	39.2±2.3	-132.2±9.3
75	124	123.0±4.4	-126.1±5.1	-353.8±12.4
76	25	96.8±2.2	-72.4±2.1	-209.4±10.4
77	107	105.4±3.4	-59.5±7.1	-155.0±24.9
73	72	(161.8±6.2	-168.3±10.8	-325.0±16.0)
73	171	84.0±2.8	-65.6±2.5	-178.6±10.5
74	192	75.2±3.5	98.1±6.6	-324.8±17.8
75	3	65.1±3.7	-112.4±5.4	-291.4±14.7
75	44	105.2±1.2	-20.4±1.5	-60.4±7.8
76	4	44.7±2.0	29.6±2.0	-130.6±10.1
76	66	41.1±1.8	-24.1±1.7	-156.2±9.0
76	68	106.1±1.3	-11.6±0.8	-41.8±5.4

*Relative to reference times in Tables 1-4 and 1-5.

Table 3-8b

Final locations and origin times
for all events from joint inversion

Moonquakes

Focus	Colatitude (deg)	Longitude (deg)	Depth	Origin Time* (sec)
A1	102.9±1.9	-30.5±2.1	837.8±26.2	-111.4±6.5
A15	99.2±3.1	4.3±1.8	1003.4±54.9	-108.6±11.5
A16	83.5±1.8	2.2±1.6	1019.6±43.3	-140.3±7.3
A17	66.8±1.5	-18.8±1.8	783.7±44.3	-132.2±7.8
A18	69.2±1.8	25.6±2.2	907.9±37.2	-104.7±7.3
A20	69.6±1.8	-27.8±2.7	936.3±34.8	-153.1±7.4
A27	70.7±2.0	14.2±2.5	982.8±59.0	-101.3±11.5
A30	79.4±1.6	-28.0±2.5	879.5±41.2	-106.2±8.5
A31	76.8±2.8	7.3±2.7	1090.5±60.9	-153.7±11.7
A32	73.4±1.3	17.5±1.8	756.8±50.0	-153.7±11.7
A33	83.3±3.6	107.4±4.4	1006.9±109.4	-245.7±10.3
A34	82.8±1.6	-6.7±1.7	925.1±63.4	-97.7±11.2
A36	34.0±4.1	-8.9±5.3	1048.0±33.4	-115.6±9.4
A40	90.7±1.6	-10.5±1.4	862.6±43.6	-78.2±7.6
A41	67.4±1.7	-36.9±3.0	708.7±45.9	-112.3±11.3
A42	68.4±2.3	-44.5±3.2	972.4±40.4	-116.8±8.7
A44	46.2±2.6	42.9±4.4	943.6±32.7	-123.7±9.0
A45	105.5±2.6	-34.0±2.7	963.5±34.9	-124.0±8.5
A46	102.3±2.2	-29.9±2.1	870.8±29.2	-79.6±7.2

Table 3-8b (Cont'd)

A50	80.8±2.1	-46.8±2.8	876.3±36.9	-117.2±8.6
A51	81.0±1.2	13.6±1.5	824.3±43.0	-87.0±7.0
A56	81.6±1.4	-23.5±2.4	713.3±54.4	-56.3±11.3
A61	68.2±2.0	35.0±4.0	844.3±39.3	-198.6±12.0
A62	47.1±2.5	51.7±4.0	956.7±33.3	-148.9±8.0

*Relative to reference times in Table 1-6.

Table 3-9

Velocity models used in calculating Tables 9a,b, and c

	Depth to Bottom of Layer (km)	V_p (km/sec)	V_s (km/sec)	ρ (g/cm^3)
a)	20	5.10	2.94	3.04
	60	6.80	3.90	3.06
	400	7.75	4.47	3.40
	1738	7.60	4.20	3.45
b)	20	5.10	2.94	3.04
	60	6.80	3.90	3.06
	480	7.75	4.47	3.40
	1738	7.60	4.20	3.45
c)	20	5.10	2.94	3.04
	60	6.80	3.90	3.06
	480	7.75	4.47	3.40
	1738	7.60	4.20	3.45

Table 3-10a

Travel times and amplitudes for surface event waves
reflected from an interface at 400 km depth

Distance (Degrees)	Travel Time (sec)				Amplitudes x 10^3				
	P	S	PS	SP	P	S-V	S-H	PS	SP
10	117.0	202.9	159.4	159.4	0.003	0.000	0.011	0.010	0.010
20	132.5	229.7	178.4	178.4	0.009	0.018	0.002	0.003	0.003
30	154.5	267.9	204.4	204.4	0.008	0.019	0.009	0.006	0.006
40	180.4	312.9	233.5	233.5	0.003	0.010	0.020	0.008	0.008
50	208.5	361.6	--	--	0.005	0.008	0.031	--	--
60	237.8	412.4	--	--	0.016	0.022	0.042	--	--
70	267.8	464.3	--	--	0.029	0.031	0.044	--	--
80	--	--	--	--	--	--	--	--	--
90	--	--	--	--	--	--	--	--	--

Table 3-10b

Travel times and amplitudes for surface event waves
reflected from an interface at 480 km depth

Distance (degrees)	Travel Time (sec)				Amplitudes x 10^3				
	P	S	PS	SP	P	S-V	S-H	PS	SP
10	136.5	236.6	186.1	186.1	0.002	0.003	0.010	0.008	0.008
20	149.0	258.3	201.6	201.6	0.006	0.010	0.004	0.005	0.005
30	167.6	290.6	224.1	224.1	0.007	0.017	0.003	0.003	0.003
40	190.3	329.9	250.3	250.3	0.005	0.013	0.011	0.007	0.007
50	215.5	373.7	278.3	278.3	0.001	0.006	0.020	0.004	0.004
60	242.3	420.1	--	--	0.006	0.010	0.029	--	--
70	270.0	468.2	--	--	0.016	0.022	0.038	--	--
80	298.2	517.0	--	--	0.027	0.028	0.038	--	--
90	--	--	--	--	--	--	--	--	--

Table 3-10c

Travel times and amplitudes for direct P and S
waves from surface events

Distance (degrees)	Travel time (sec)		Amplitudes x 10^3		
	P	S	P	S-V	S-H
10	53.3	92.6	.122	.135	.134
20	91.3	158.5	.134	.158	.149
30	128.6	223.0	.176	.187	.195
40	165.1	286.3	.195	.195	.214
50	200.5	347.8	.202	.197	.220
60	234.7	407.0	.204	.190	.220
70	267.2	463.3	.203	.181	.217
80	297.9	516.5	.200	.177	.212
90*	--	--	--	--	--

*shadow zone begins at about 87 degrees distance

Table 3-11

Velocity model used in calculating values in Table 3-12

Depth to Bottom of Interface (km)	V_p (km/sec)	V_s (km/sec)	ρ (gm/cc)
20	5.1	2.94	3.04
60	6.8	3.9	3.06
520	8.0	4.6	3.40
1738	7.5	4.1	3.50

Table 3-12

Travel times and amplitudes for direct P and S waves and
waves converted at a 520 km boundary.
Moonquake source is at 1000 km depth.

Distance	Travel times (sec)				Amplitudes x 10^3				
(Degrees)	P	S	PS	SP	S-H	P	S-V	PS	SP
10	135.8	242.1	187.4	190.0	.930	.946	.929	.022	.019
20	143.1	255.2	195.7	200.5	.881	.891	.876	.038	.034
30	154.3	275.3	208.1	216.7	.815	.820	.805	.046	.045
40	168.2	300.6	223.1	--	.749	.748	.726	.047	--
50	184.0	329.3	239.6	--	.689	.683	.676	.045	--

Table 3-13

Listing of events used in record section of Figure 3-5

Distance (deg)	Event Yr	Day	Station
14	76	68	14
28	76	68	16
28	76	4	15
31	76	66	15
36	75	44	16
45	76	68	15
48	75	44	15
49	72	324	15
49	73	171	14
53	76	66	14
56	76	4	16
64	76	4	14
67	76	66	16
69	73	171	15
72	72	324	14
79	76	25	15
82	73	171	16
82	74	192	16
84	74	192	15
86	72	324	16
86	76	25	16
89	73	72	16

Table 3-13 (Cont'd)

Distance (deg)	Event Yr Day		Station
92	73	72	14
92	75	3	14
96	75	3	15
102	72	199	15
112	74	192	14
115	72	199	16
123	73	72	15
124	75	3	16
135	75	124	15
137	72	199	14

Table 3-14

Summary of S and SS (surface bounce) observations
for events and stations for which short-period
records are not available; observations refer to
long-period records (see Appendix 1 for plots)

Distance (deg)	Event Yr	Day	Station	S	SS
11	75	44	14	+	X
12	75	44	12	+	X
17	76	68	12	+	X
42	73	171	12	+	X
48	76	25	12	+	X
51	76	66	12	+	X
54	76	25	14	--	X
67	76	4	12	--	X
70	72	324	12	+	X
85	75	3	12	?	X
91	73	72	12	+	X
98	75	124	12	--	+
102	75	124	14	--	?
119	74	192	12	?	?
123	75	124	16	--	--
141	72	199	12	--	+

x = not considered, + = observed, - = not observed

Table 3-15

Final velocity model for the lunar mantle

Depth (km)	V_p (km/sec)	V_s (km/sec)
60	7.75	4.57
400	7.65	4.37
480	7.6	4.20
?	7.6	4.20

Table 3-16

Q values used in theoretical calculations in Figs. 3-9a
and 3-9b.

Layer	Q_p	Q_s
Crust	5000	5000
Upper mantle	5000	3000
Transition zone	5000	3000
Lower mantle	1500	1000

Figure Captions

Fig. 3-1. Locations of surface events and deep moonquakes used in this work; size of symbol gives one standard deviation in location estimate. Open symbols indicate farside locations.

Fig. 3-2. Record section of polarization-filtered transverse component records from all deep moonquakes.

Fig. 3-3. Record sections of polarization-filtered surface event records.

Fig. 3-4. Record section of selected polarization filtered moonquake records (vertical component).

Fig. 3-5. Record section of short-period seismograms from surface events.

Fig. 3-6. Final velocity model for the lunar mantle.

Fig. 3-7. Spectral ratio plot for surface event records (from Dainty et al., 1976).

Fig. 3-8. Crustal wave theoretical amplitude curves.

Fig. 3-9. Comparison of shear wave amplitude data with predicted values.

Fig. 3-10. Ray-trace diagrams through velocity model of Fig. 3-6; program kindly supplied by Dr. Bruce Julian.
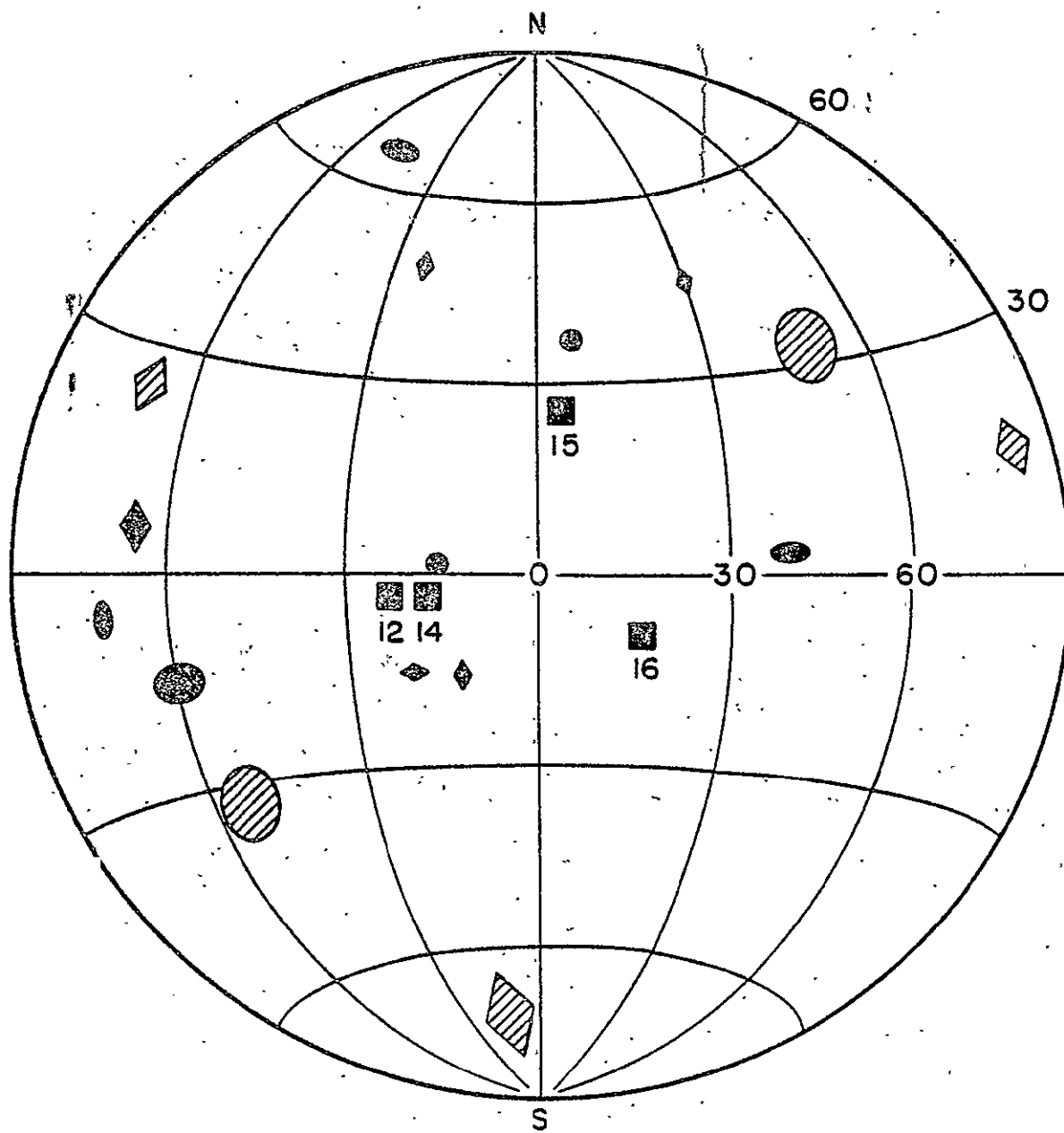
SEISMOMETERS

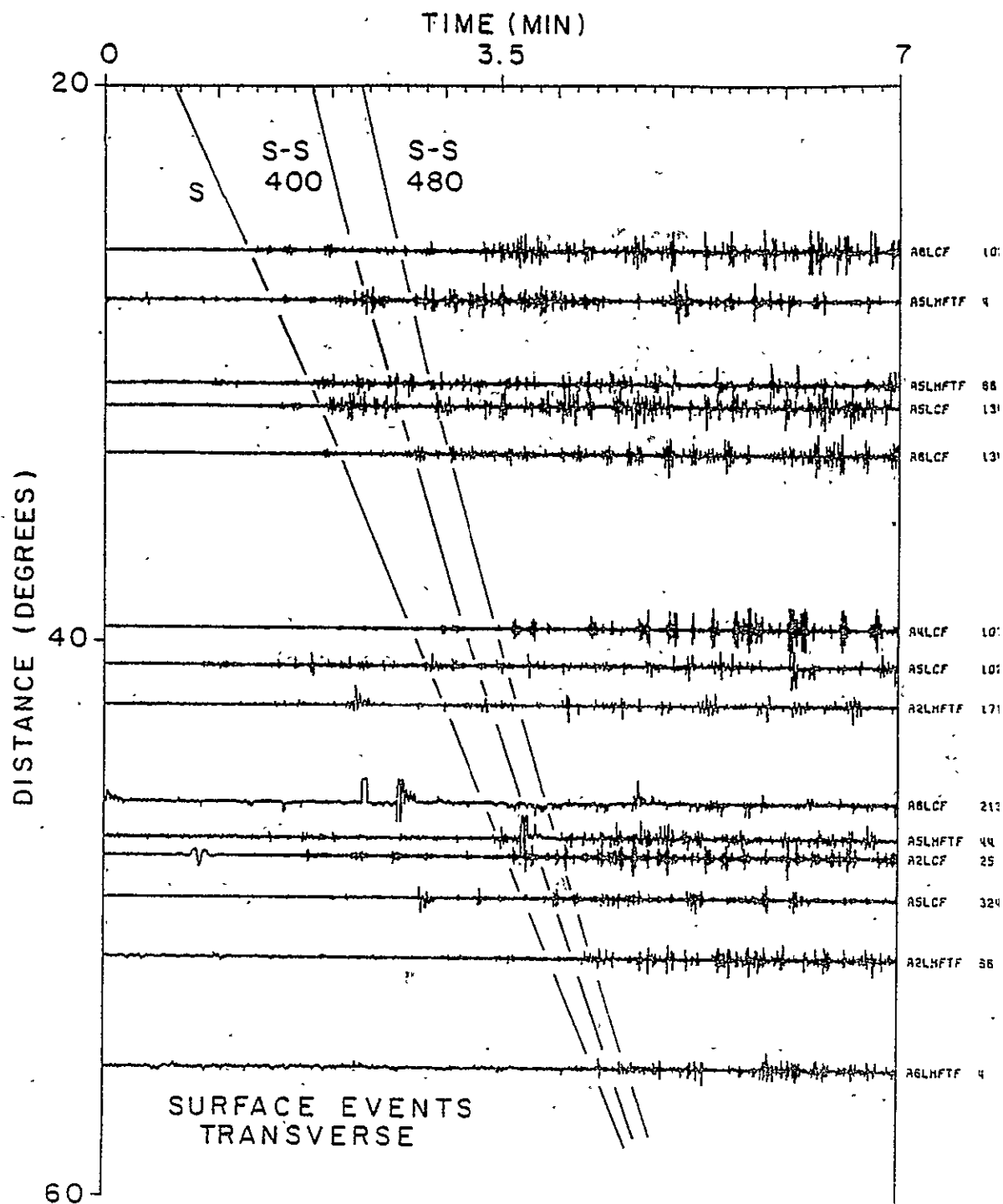METEORITE IMPACTS

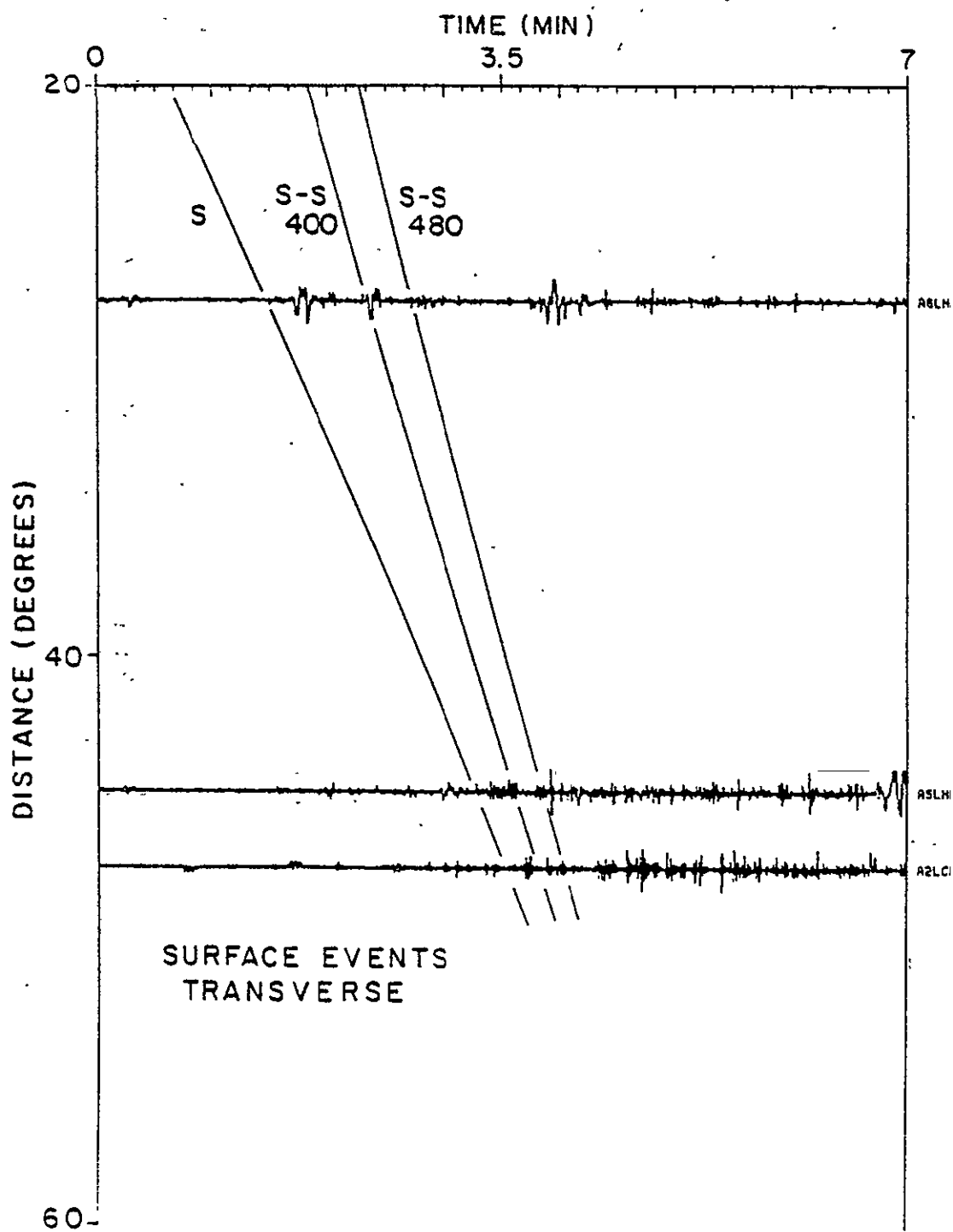NEAR-SURFACE MOONQUAKE

Fig. 3-1a
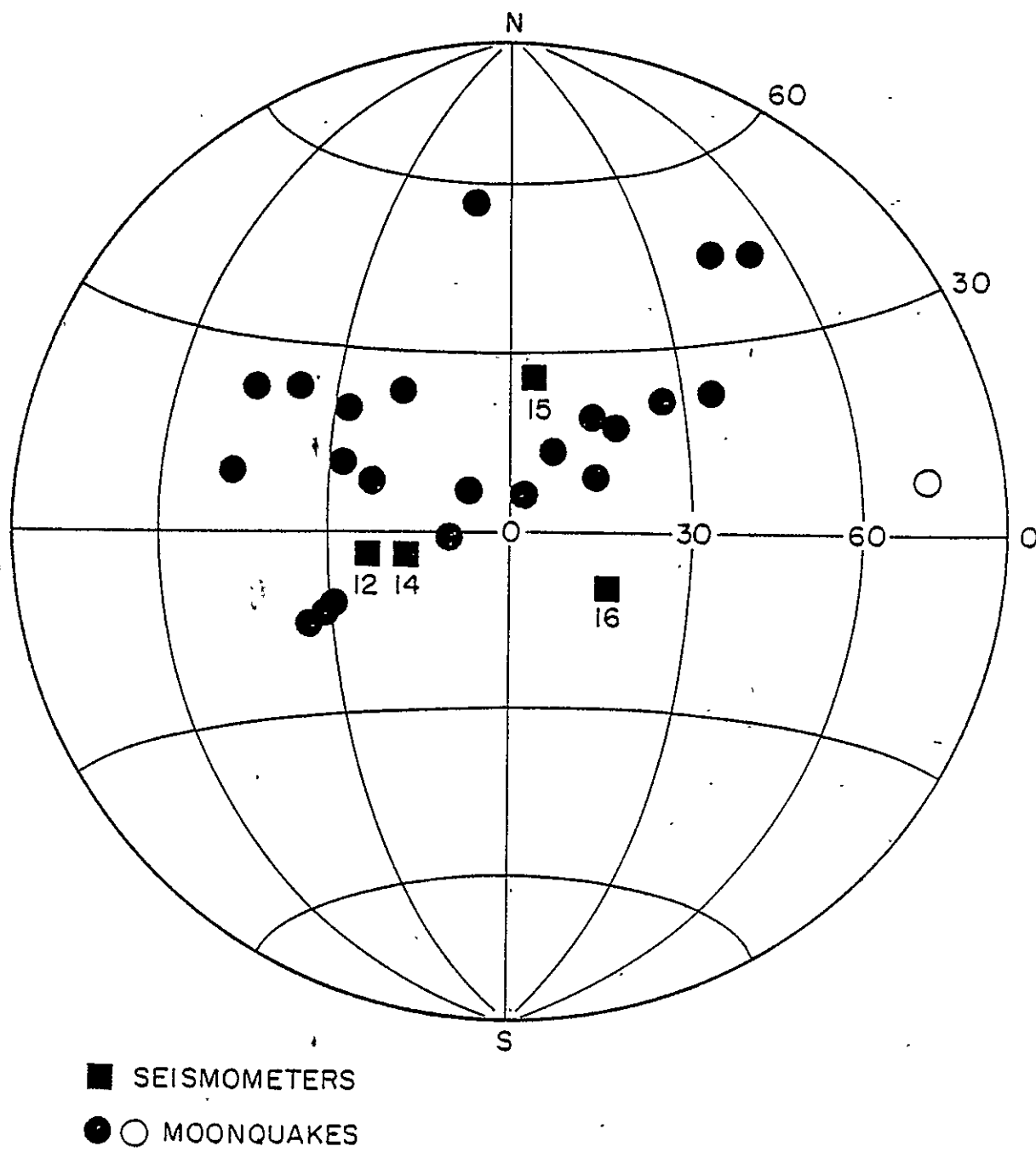
Fig. 3-1b
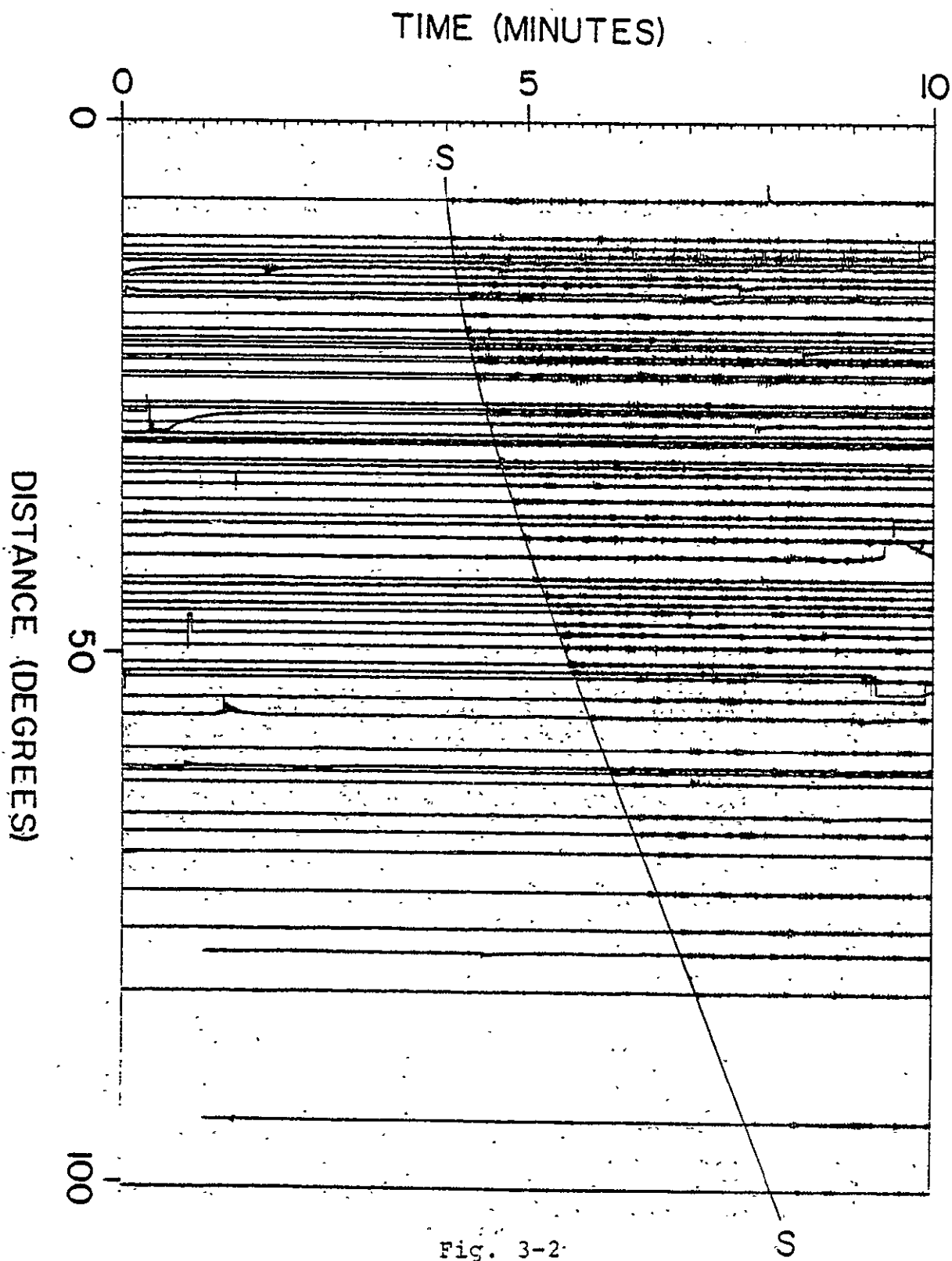
254

TIME (MINUTES)

Fig. 3-2

Fig. 3-3a

Fig. 3-3b

Fig. 3-3c

Fig. 3-3d

Fig. 3-3￼
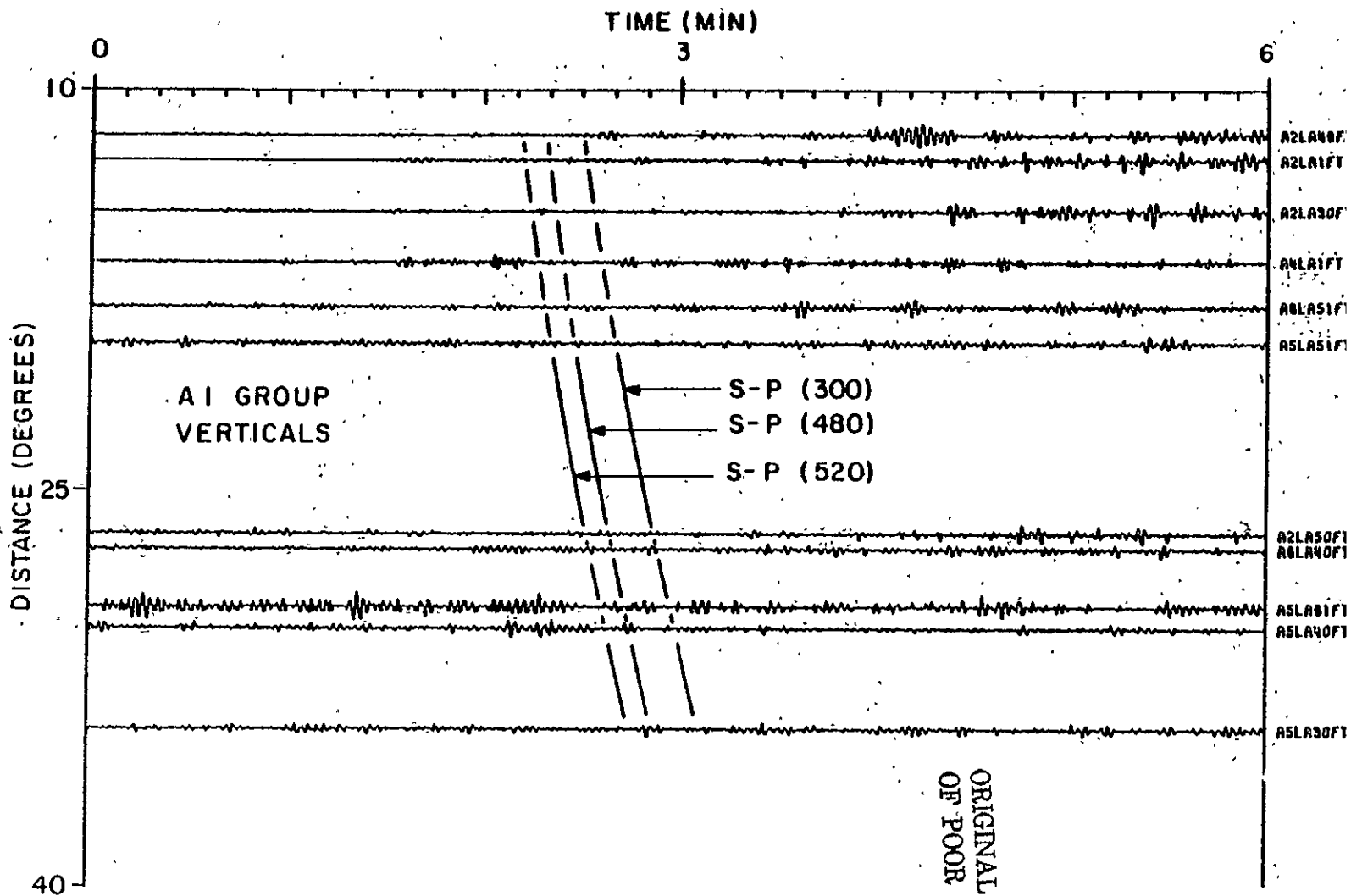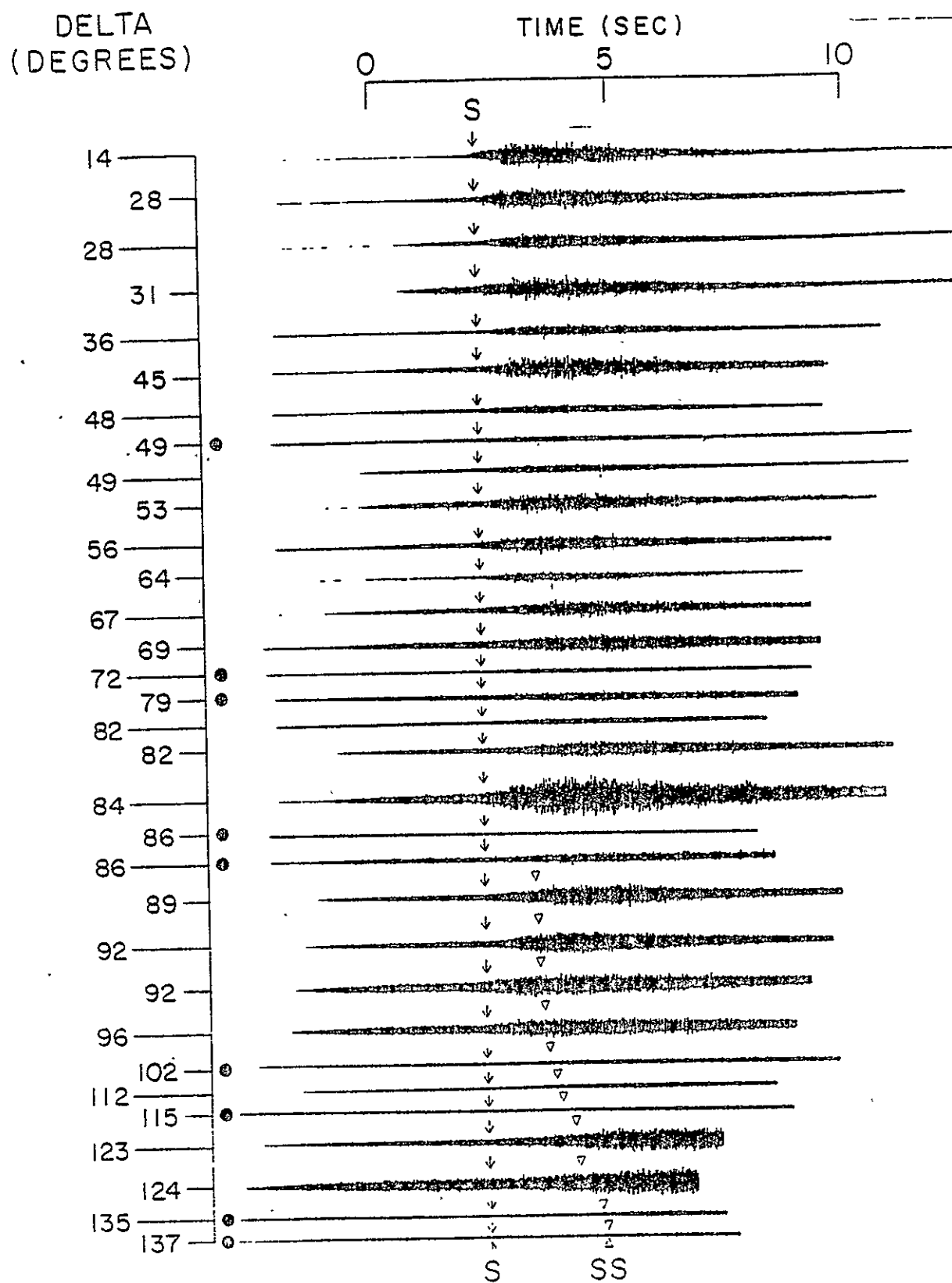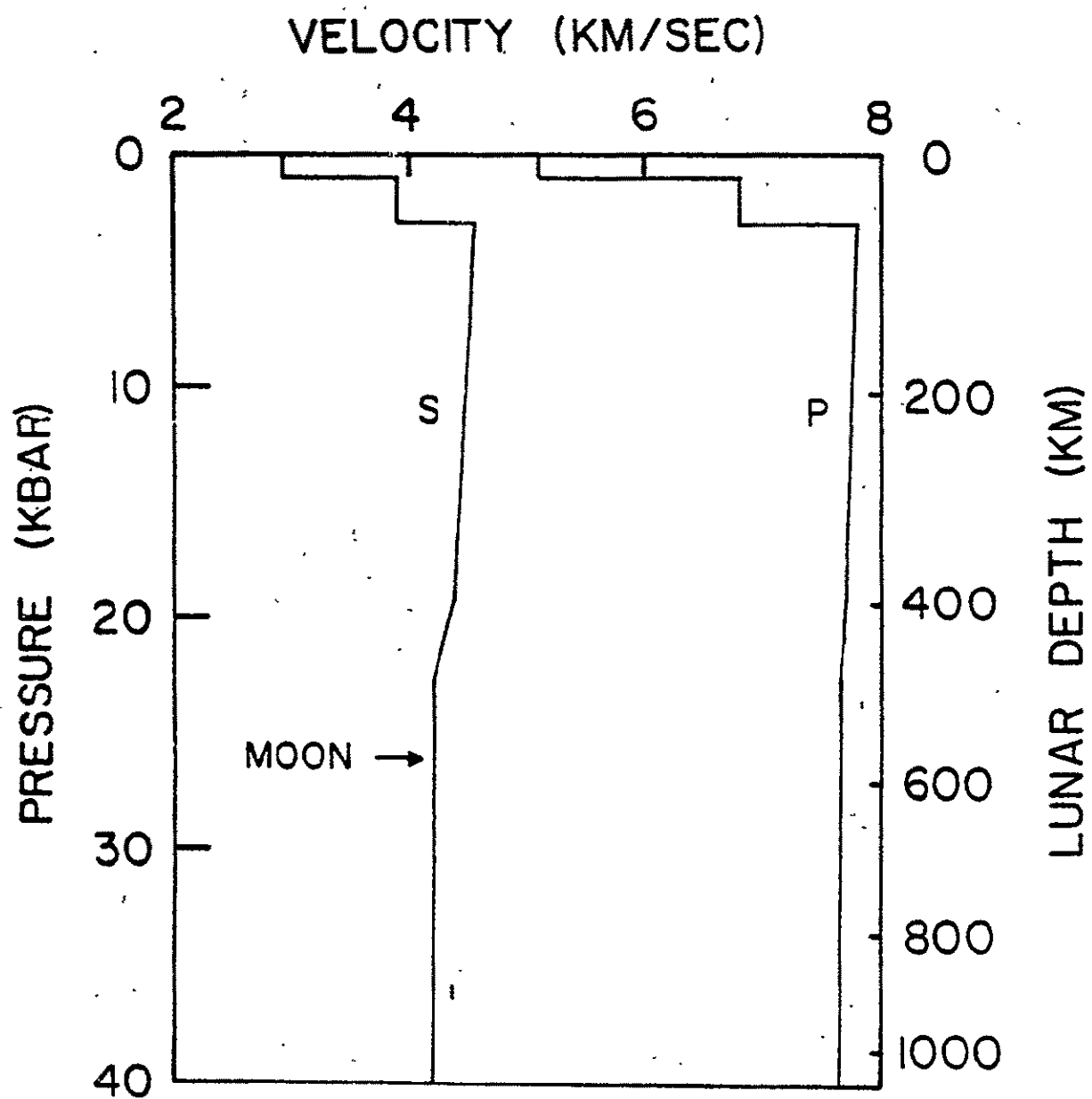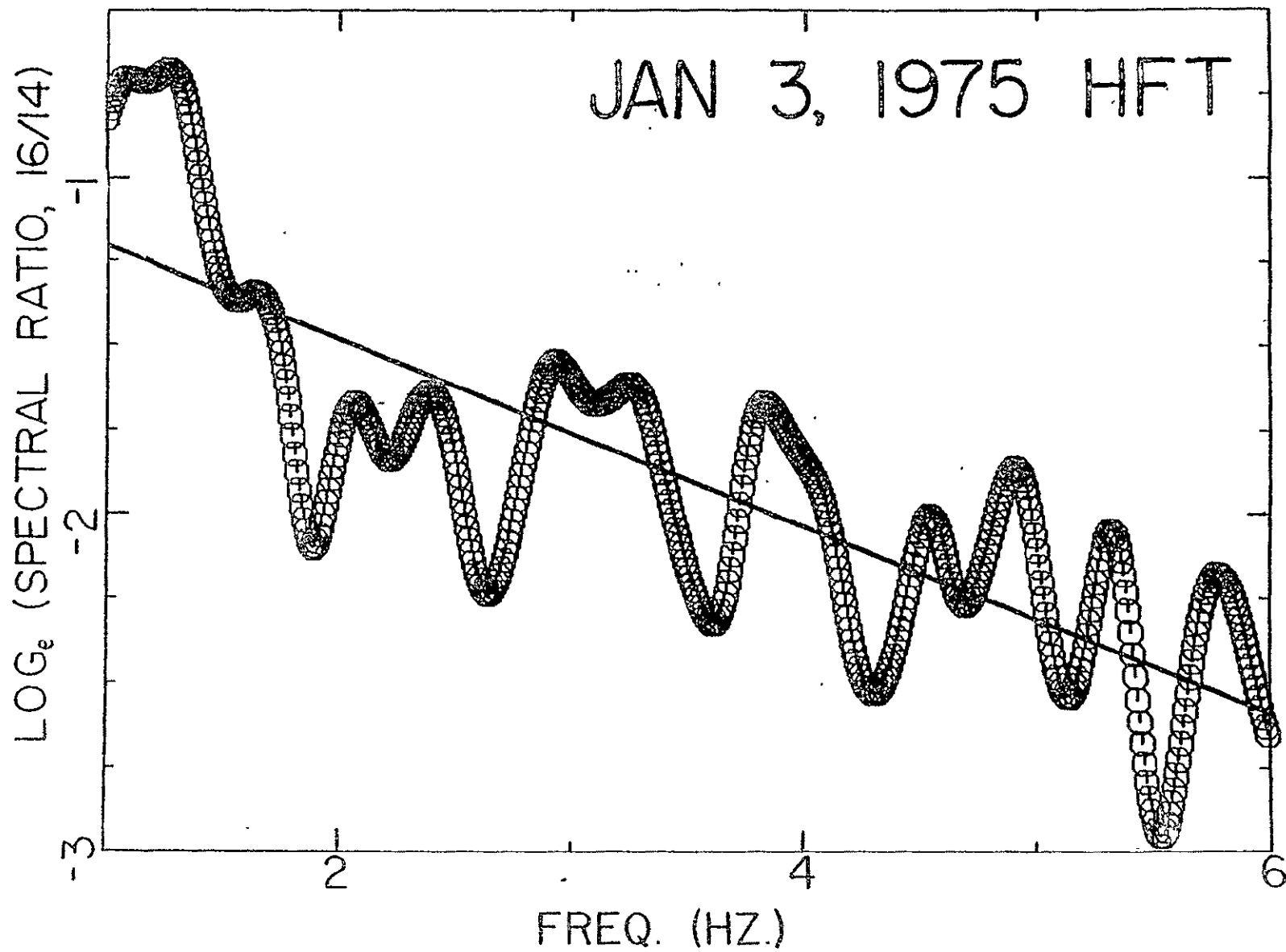
Fig. 3-4

TIME (MIN)

S-P (300)
S-P (480)
S-P (520)

A1 GROUP
VERTICALS

DISTANCE (DEGREES)

A2LA40F
A2LA1FT
A2LA30F
A4LA1FT
A8LA51F1
A5LA51F1

A2LA50F1
A8LA40F1

A5LA81F1
A5LA40F1

A5LA30F1

Fig. 3-5

Fig. 3-6

Fig. 3-7

263

Fig. 3-8

CURRENT MODEL –
CONSTANT VELOCITY

Fig. 3-9a

265

Fig. 3-9b

NAKAMURA et.al.
MODEL

Fig. 3-9c

Fig. 3-10a

SURFACE EVENT

Fig. 3-10b
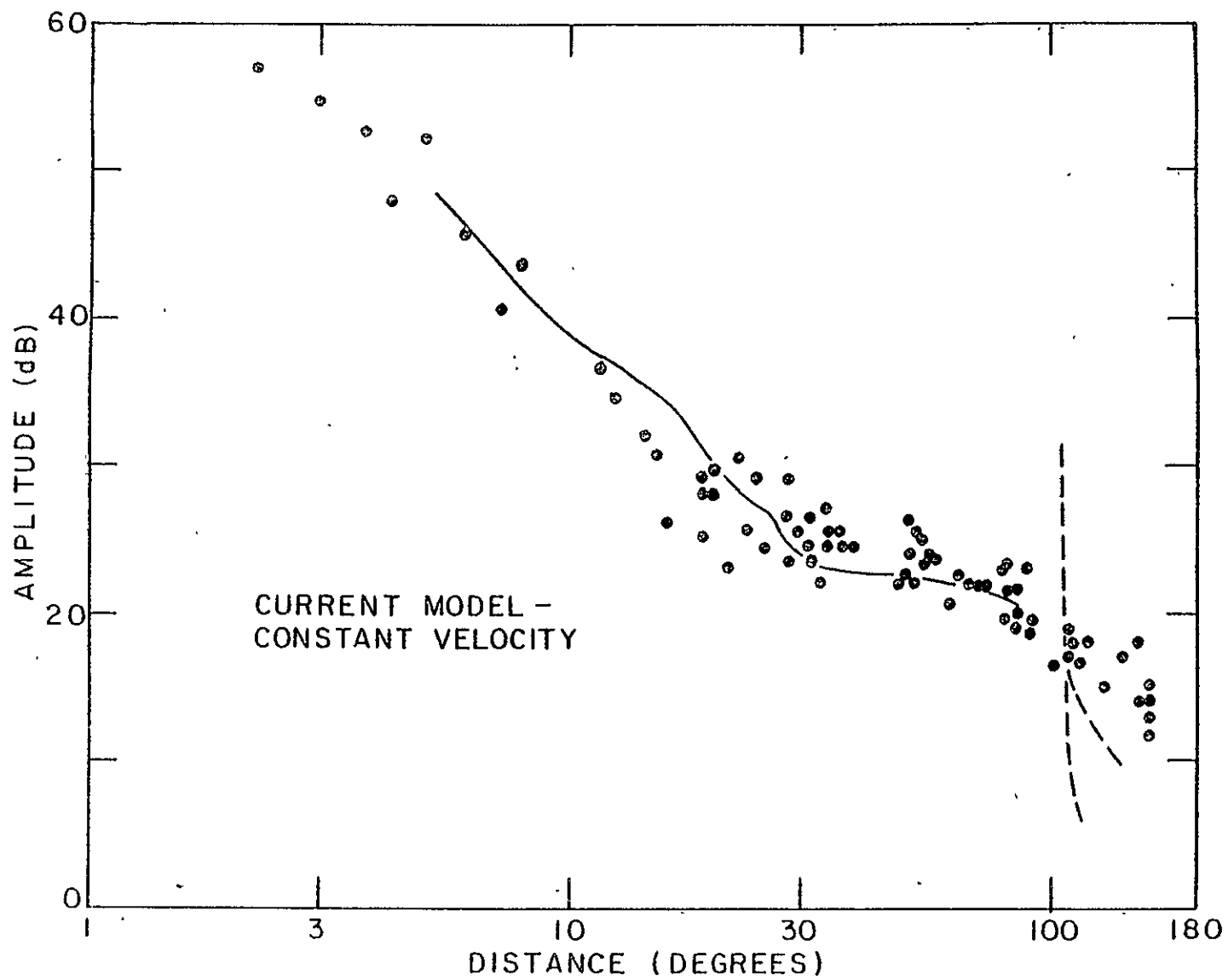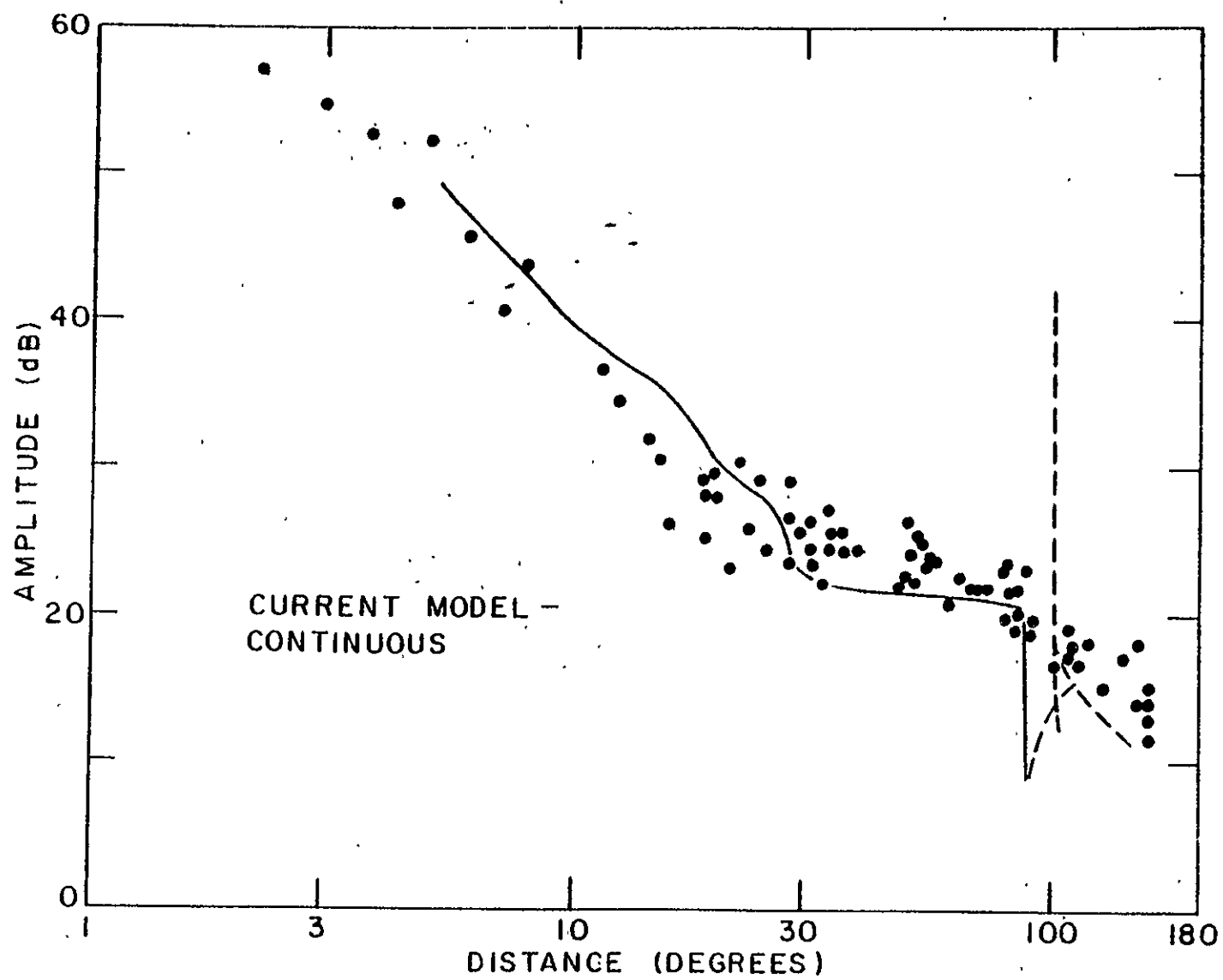
DEEP MOONQUAKE

CHAPTER 4

DEEPER STRUCTURE

The results in the previous chapter extend to a
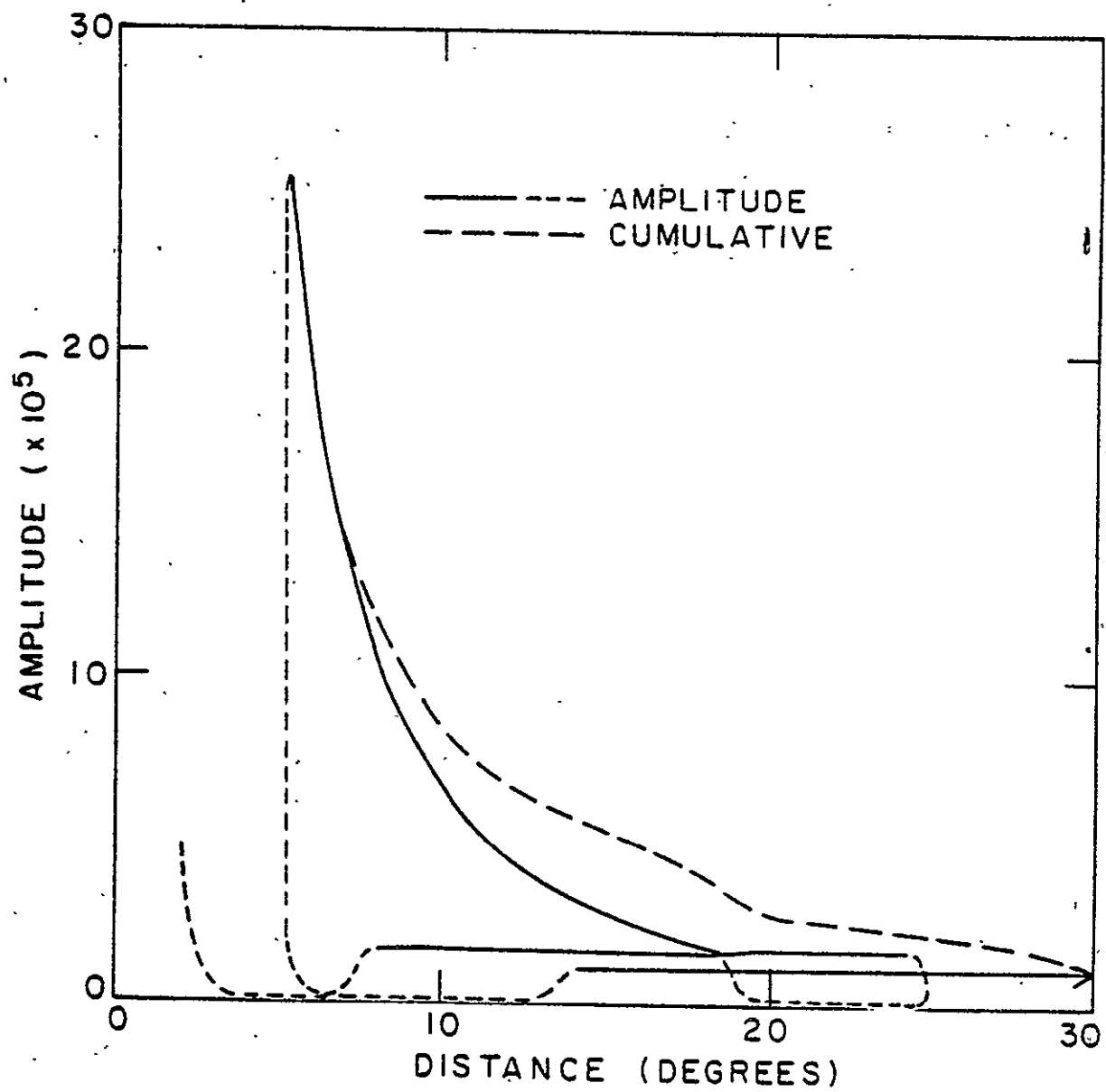depth of about 1100 km, the location of the deepest
locatable moonquake source. However, between 950 km,
the average moonquake source depth, and 1100 km there is
only loose control, as provided by the average velocity
values for the whole lunar mantle and the observation
that the characteristics of signals from deeper moonquakes
are essentially the same as for the shallower (700 km-900 km)
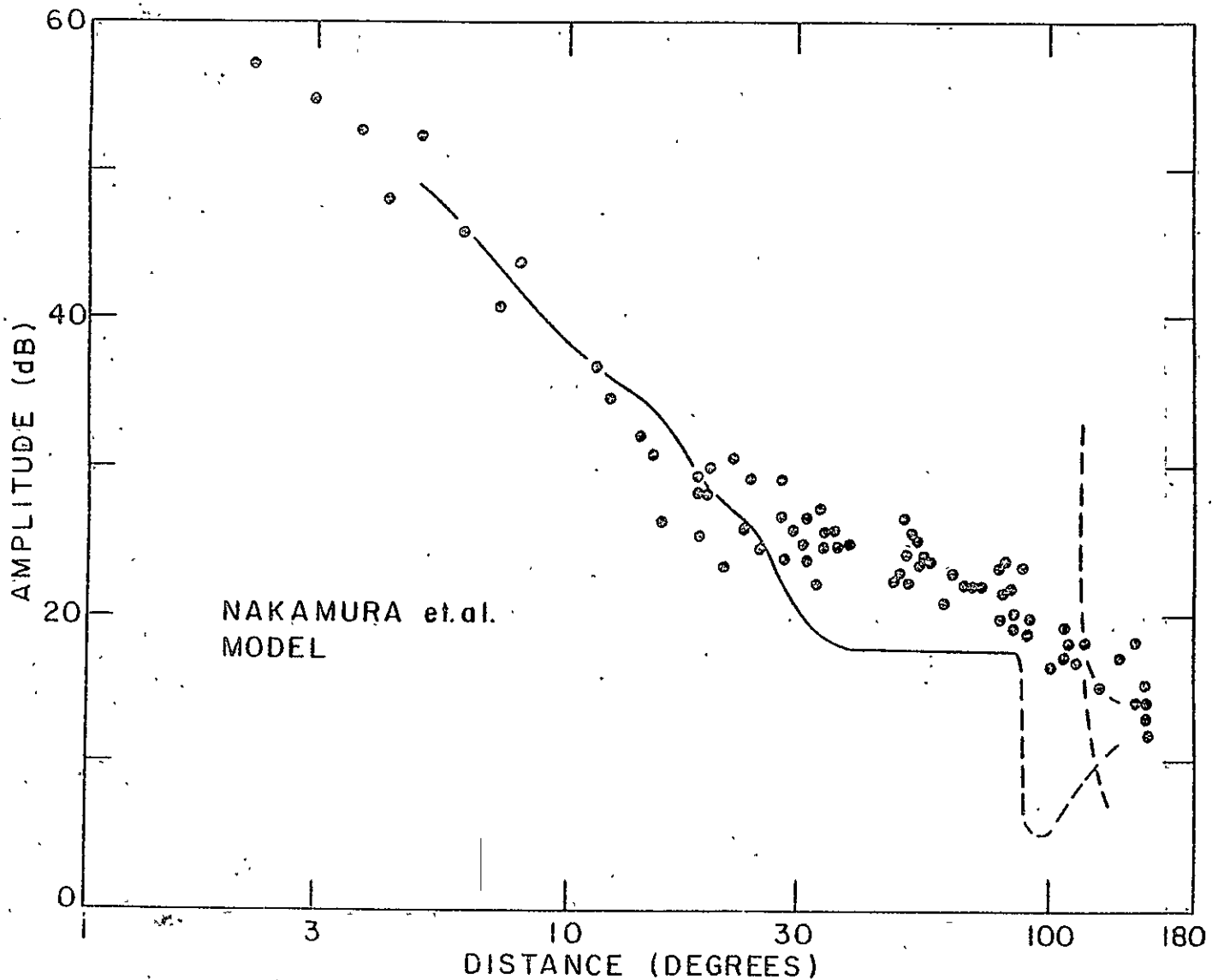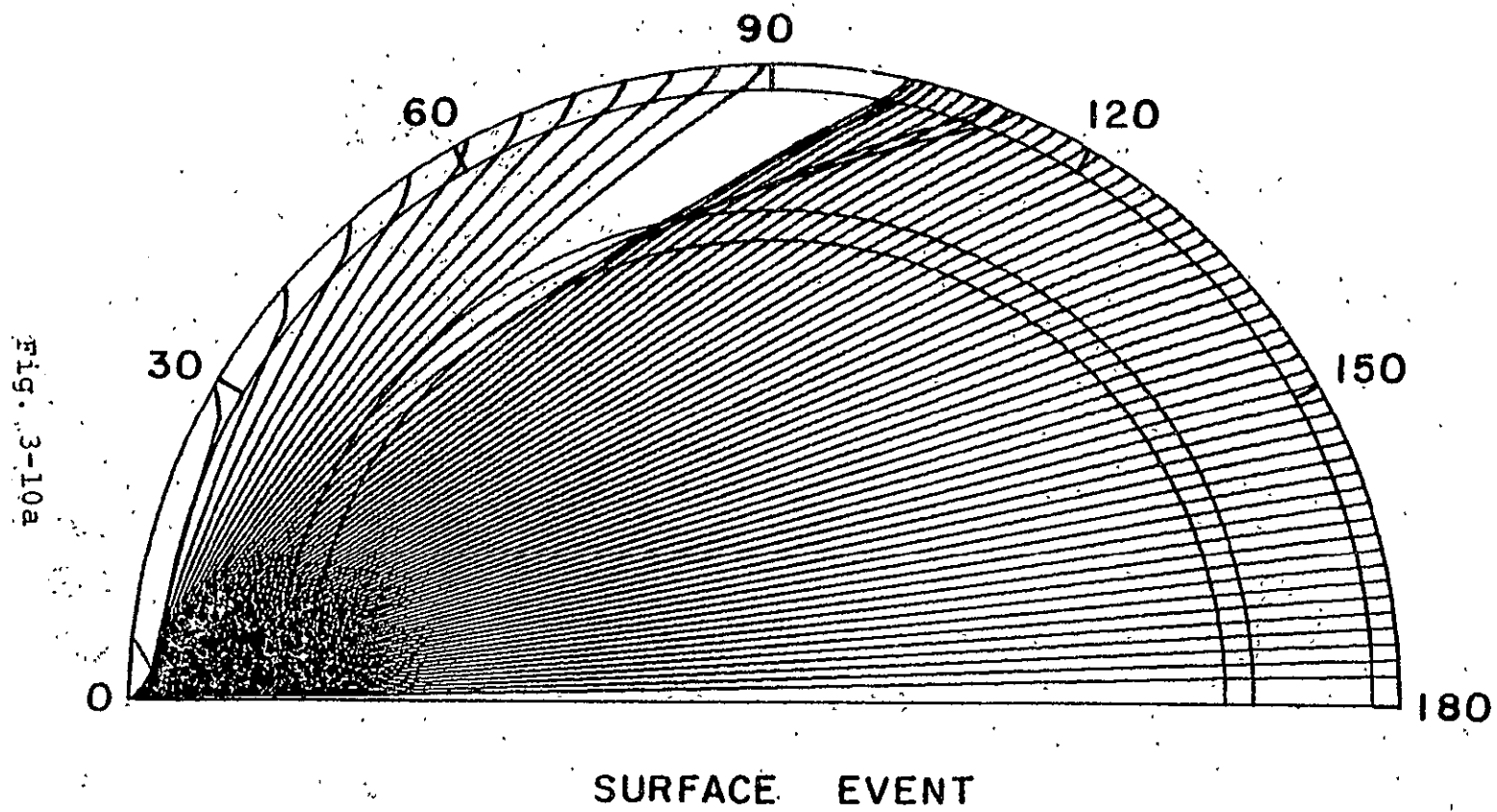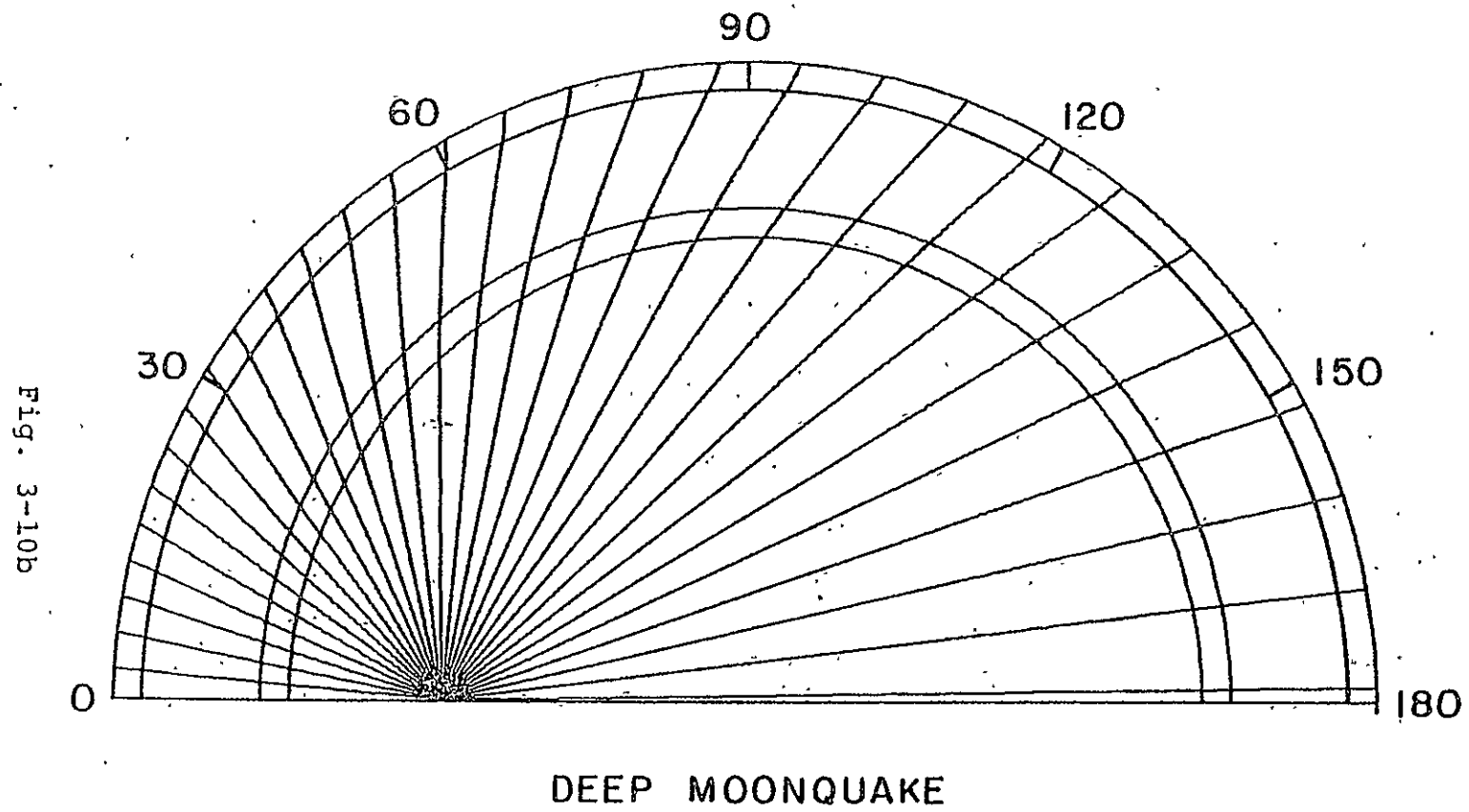foci. The structure below 1100 km depth down to the center
of the moon (1738 km) is even less constrained; the availa-
ble evidence is presented and discussed in this chapter.

4.1 Attenuating Zone

With the exception of A33 (discussed below) all of
the 24 moonquake foci used in this thesis are located on
the nearside of the moon, generally within 60° of the center
of the ALSEP array and within 90° of the farthest seismic
station. This can be seen in Fig. 4-1, the moonquake
source locations are plotted in depth and longitude.
(This figure is used herein only to illustrate the
moonquake event locations relative to the center of the
moon and the ALSEP stations; further discussion of the

other features shown is given in Chapter 5). However, these locatable moonquake sources by no means represent all of the deep moonquake events; there are approximately 56 other matching classes of seismic signals that have similar characteristics as the moonquakes discussed herein and so presumably represent other deep moonquake foci. In addition there are many smaller signals received by the ALSEP seismometers which are non-classifiable due to low signal amplitudes. It is likely that at least some if not most of these represent small moonquake events. Two questions then arise: 1) are these non-locatable deep moonquake sources also on the nearside of the moon, and if so 2) are there any deep moonquake events on the farside at all?

It is not possible to answer these questions definitively. Lammlein (1977) reports the locations of about 20 moonquake sources besides the ones used in this thesis. Although the location uncertainties are probably substantial, they too are all on the nearside, bringing the number of known nearside repeating moonquake foci to about 45, with 35 still unaccounted for. Lammlein (1977) tentatively places another 15 (all that were considered) on the nearside on the basis of occurrence history

similarities. Thus it is possible that many if not all of the presently identified categories of deep moonquakes are in fact on the nearside. Nevertheless this conclusion is far from definitive and the many potential small moonquake events which are un-matchable and unlocatable remain an open question.

Given that there is no solid evidence for any farside moonquake source (except A33, see below) in the present data set, it is of interest to speculate on the reasons for this. There are basically two possibilities; either there are truly no farside events, or there are but they are unobservable. The first option implies that either the causative factors for the moonquakes are absent on the farside or that the rheology is different in such a way that moonquakes cannot occur. Assuming that the moonquakes are at least triggered and controlled by tidal stresses (Toksöz et al., 1977), these explanations are in fact connected because the elastic parameters of the lunar interior control the distribution of the applied tidal stress (Cheng and Toksöz, 1978). There is no evidence at present to suggest an absence of tidal or ambient stresses on the farside relative to the nearside, although there is a small chance that the center-of-figure center-of-mass

offset or absence of major mare on the farside could have
an effect (c.f. Runcorn, 1975). Another possibility is tha
the locations of the moonquakes on the nearside are
controlled by local inhomogeneities or "weak spots" which
are for some reason absent on the farside.

The other option is that there are in fact farside
moonquake events (perhaps represented by a few small but
non-analyzable signals seen at the ALSEP seismometers), but
for some reason they are not generally observable by the
ALSEP array. Again there are two possibilities here. The
moonquakes are small events even on the nearside, and the
greater distances and perhaps smaller source energies as
the events move towards the limb of the moon could account
for the observed source distribution. This explanation,
though, has a few weak points. First, as can be seen in
Fig. 4-1, the cessation of moonquake activity is relatively
sudden rather than a gradual fall-off in source density.
Second, on a statistical basis it would perhaps be expected
that at least a few farside sources would be able to
produce large enough signals to travel the extra distance.

These objections can be partially obviated by the
final possibility that there is an attenuating zone that
begins immediately beneath the moonquake source depth

region, as marked by the dashed circle in Fig. 4-1. Then as the moonquake sources move beyond a certain distance the waves begin to bottom in this zone (and perhaps are bent into it by a velocity decrease) and thus are too severely attenuated to be observable at one or more of the ALSEP stations. A minimum depth for the onset of such a region would be about 1100 km based on the deepest moonquakes, although locally it could be shallower. Given the distribution of nearside moonquakes reported here and by Lammlein (1977) the zone is also constrained to begin no deeper than about 1100 km so as to explain the apparent cut-off distance for moonquake epicenters at 60° to 80°. In fact, there remains a small range between say 70° and 90° where perhaps more moonquakes should be seen unless the attenuating zone is in general shallower than 1100 km and the few deepest moonquakes are contained in anomalously deep intrusions of non-attenuating material. It is also important to note that in principle the attenuating zone need only affect shear waves since most P wave arrivals from even the largest nearside moonquake sources are only marginally observable.

In view of the above evidence it is difficult to be more quantitative. The last possibility seems in some sense to be the most satisfactory since it does not require

the postulation of significant nearside-farside assymetry
and is in keeping with the general trend of increasing
attenuation with depth in the moon.

Further data on this potential attenuating zone can
be obtained by examining the lone farside moonquake focus,
A33 (located about 100°E longitude in Fig. 4-1). The
signal amplitudes at stations 14, 15, and 16 are among the
larger of all moonquake signals, as can be seen in Figs.
4-2a and 4-2b. Given the far greater distance of the
source (see Fig. 4-1; it is a factor of 1.5 to 2, or at
least 600 km, farther from the ALSEP array than any other
focus used in this work), this implies that the A33 focus
may be the largest moonquake source yet observed. As can
be seen in Figs. 4-2, good P and S wave arrivals are seen
at both stations 15 and 16; they are the closest stations
and receive rays that bottom at about 900-1100 km depth.
At station 14, however, the rays have presumably bottomed
at about 1200 km depth (assuming that the constant lower
mantle velocities extend to this region), and there is
absolutely no evidence for a shear wave arrival at the
expected time (about minute 44 and 40 seconds) or at any
time after up to about four minutes. In contrast there
is a strong P wave arrival as shown; in fact it is one of

the clearest and largest P arrivals on any moonquake seismogram, along with the P picks at stations 15 and 16. Furthermore, only little energy of any sort is seen at ALSEP 12, which is even more distant from A33.

Now this situation of a good P arrival with no subsequent shear wave energy is completely unique on deep moonquake records as can be seen by scanning through Figs. Al-13. Although it is possible that a node in the shear wave radiation pattern for A33 is responsible, the fact that this is not observed for any other focus besides the lone farside source suggests that the deep attenuating region proposed above is responsible. To account for the essentially zero shear wave energy at ALSEP 14, the Q would have to decrease substantially (from $Q_S \sim 1000$ to say $Q_S \sim 200$) in a small depth range between about 1000 and 1200 km. (Alternatively, a sharp shear wave velocity drop at about 1100 km depth could also be responsible, with or without an accompanying Q_S decrease. However, a decrease in Q is the simplest explanation to cover both the lack of farside moonquakes and the A33 signal characteristics; a simple velocity drop would not explain the absence of all farside moonquakes, especially near the antipode. Needless to say, though, an accompanying velocity drop is allowed by the information available.)

A slower decrease in Q_p could perhaps explain the absence of energy at ALSEP 12, but since station 12 is typically less sensitive than station 14 and there is some P wave energy present, this is not necessarily required.

Thus the deep moonquake data provide consistent, if somewhat weak evidence for a zone of increased shear wave attenuation beginning at about 1100 km depth. If this zone exists, Q_s probably drops quite rapidly from the lower mantle value of 1000 to at most a few hundred. Unfortunately, there is at present no corroborating evidence from surface event records. It is perhaps significant that the surface events selected for use in this thesis are all less than 140° distant from any seismic station; the bottoming depth of a surface event wave for 140° source-receiver separation is just about 1100 km. It should be noted that Nakamura et al. (1973) discuss several of the same matters concerning an attenuating region below 1100 km. They include evidence from the Day 199, 1972 meteorite impact event (also used herein) claiming that the direct S arrival is seen at ALSEP 15 and absent at stations 16 and 14. Their location for this event is such that the respective distances are 114°, 130° and 150°, with ray bottoming depths of 800,

1000, and 1300 km. The source of the discrepancy between their location and the one obtained herein lies in that the P arrival times used in this thesis for stations 15 and 16 are about 15 seconds earlier than reported in Nakamura et al. (1973), placing our location within 140° of ALSEP 14. Furthermore, as discussed in Chapter 3 and shown in Figs. 3-5 and Al-5b, there is little direct shear wave energy at any station for this event and the decreased velocities and increased attenuation in the lower mantle are sufficient to account for that. In all fairness, the P pick at ALSEP 16 is arguable due to the possible presence of noise on the vertical LP record, but even so the overall shear wave loss is easily explained by the characteristics of the lower mantle region, the bottoming depths of the rays, and the calculated amplitudes in Chapter 3. It is not necessary to postulate a sharp Q decrease at 1100 km to explain the surface event data.

In sum, then, the deep moonquake data suggest that there may be a sharp shear wave attenuation increase below about 1100 km, but in view of the scarcity of pertinent data this interpretation must remain tentative.

4.2 Core

The seismic evidence concerning a possible lunar core is almost non-existent, and this section is included primarily for completeness. Nakamura et al. (1974b) report that a meteorite impact event occurred on Day 262, 1973 near the center of the backside. The location and origin time are determined from the three closest stations and then the arrival time for the fourth P wave is predicted. Given their calculated location, this P wave should traverse the moon along a diameter; the observed arrival time is in fact delayed by about 50 seconds. This value and the bottoming depth of the other three P waves allows them to tentatively propose the existence of a lunar core of radius 170-360 km and P wave velocity 3.7-5.1 km/sec. (For reference, a typical ray trace diagram for a surface source is shown in Fig. 4-3; a 200 km low-velocity core region is included resulting in the ray spreading seen.) While this is certainly possible, the Day 262 event is very weak with extremely low signal to noise ratios (much smaller than those seen on the surface event records used herein). Independent measurements (Dainty, personal communication; this author) show that the uncertainty in

the actual P wave arrivals is sufficient to explain the proposed arrival time delay. In essence, the true location of the onset of the emergent P wave arrivals is ambiguous, and an equally convincing set can be chosen that will not yield an arrival time delay. Thus the present seismic evidence for a core remains inconclusive.

It is appropriate to mention here that potential evidence for a lunar core (and other lunar structure) may exist on the lunar records recorded in the broad-band response mode. It is possible that the larger surface events are capable of significantly exciting the long-period normal modes of the moon; the fundamental period should be about 13 minutes. Since the frequency response of the ALSEP seismometers even in the broad-band mode begins to drop sharply for periods beyond a minute, it is not likely that the very low-order vibrational modes would be recorded. Frequencies between 20 sec and 100 sec could well be observable, if in fact the long-period energy seen on the records is not just instrument induced noise. An example of a broadband record that has been narrow bandpass filtered at 12, 20, and 50 sec periods is shown in Fig. 4-4; the origin time of the event is marked by the arrow. The increase in rise time as the center period increases and the extended decay times are apparent.

Efforts to analyze such records are currently underway at Penn State (Smith, personal communication) and MIT (this author and co-workers). To date, however, no results have been obtained or reported, and so the potential usefulness of the broad-band information remains in doubt.

In sum, then, there is little evidence for or against the existence of a lunar core.

4.3 Secondary Seismic Phases

If there are any sharp discontinuities below 1000 km depth, for example the onset of a high attenuation zone or a mantle-core boundary, it is again possible that reflected waves will be visible on polarization-filtered record sections. Since these boundaries would occur below both the surface events and moonquakes, five possible phases could occur for each source; SS-H, SS-V, PP, SP, and PS. (For surface events the SP and PS phases are identical.)

The theoretical amplitudes for such phases are given in Tables 4-2a and 4-2b for surface events and deep moonquakes respectively. The velocity models used are shown in Tables 4-1a and 4-1b. The values for the lower-most region are somewhat arbitrary; several models were run, including different source depths and mantle velocities.

The cases shown are representative. For surface events
(reflector at 300 km radius) the largest amplitudes in
general are expected for the SS-H reflected phase. The
direct wave amplitudes vary between .134 and .220 (x 10^{-3})
(Table 3-10c) and so the deep structure reflections are
at most about .07 times the direct wave amplitudes. From
the experience in previous chapters, this appears to be
a minimum value for observation. The reflected phases
from deep moonquakes (source depth 1000 km) are shown
in Table 4-2b, and reach a maximum of about .045 for the
SS-H reflection, for a ratio to direct wave values of
less than .05. This is as expected since the direct wave
travel paths are much shorter than those for deep
reflections; thus it is doubtful that such phases, even
if present, would be visible.

Now if there is a sudden increase in shear wave
attenuation below 1100 km depth, then for boundaries deeper
than 1100 km the shear wave reflections would be
substantially attenuated and so it is appropriate to
look for the PP (and possibly PS) reflections rather than
just those arising from the incident S wave, as has been
the practice in previous sections.

The final step then, is to examine the record sections

for evidence of the above arrivals. All possible phases from a variety of depths were considered and searched for; in view of the negative results only two examples are shown below. Fig. 4-5a shows the transverse component filtered traces from surface events; the lines shown are the expected arrival times of reflected phases from interfaces of 300 km and 400 km radius. The object is to look for arrivals that line up along the trends of these lines. As can be seen, there are many such possible trends; in fact there are too many. It is clearly impossible to distinguish between possible arrivals and random noise alignments. No dominant trend is obvious. The other components of ground motion and other expected phases were also examined with the same results.

The moonquake record sections were obtained after correcting the origin time values for a given phase and structure, as discussed in Chapter 2 and Appendix 3. The relative corrections are similar for any boundary depth and same initial wave type, but in order to avoid inadvertent biasing the record sections were plotted by groups of foci chosen to have similar source depths. All such records and components were examined, and a typical one is shown in Fig. 4-2b (A20 depth group, transverse components). The expected arrival time curves are as

drawn, and again there are several possible alignments.
The correlation along the SS (400) curve is actually
fairly good, but supporting correlations from other
components, foci groups, or expected arrivals did not
appear.

In sum there is no dominant supporting evidence for
any sharp discontinuities below the lower mantle. It is
possible that reflections are present on the seismograms,
but the random noise pulses passed by the polarization
filter obscure any possible observations. Essentially there
is too much scattered energy arriving in the appropriate
portion of the records and we are unable to clearly
distinguish any true body wave arrivals.

Thus the deeper structure of the lunar interior
remains in doubt. The best evidence is for a sudden shear
wave attenuation increase beginning immediately below the
moonquakes at about 1100 km depth. The existence of a
core is allowed but not required by the present seismic
information.

Table 4-1

Velocity and density models used in Table 4-2

Depth to Bottom of layer (km)		Vp (km/sec)	Vs (km/sec)	ρ (gm/cm^3)
a)	20	5.1	2.94	3.04
	60	6.8	3.9	3.06
	520	7.75	4.5	3.4
	1438	7.6	4.2	3.45
	1738	5.0	2.5	3.5
b)	20	5.1	2.94	3.04
	60	6.8	3.9	3.06
	520	8.0	4.6	3.4
	1400	7.5	4.1	3.37
	1738	5.0	2.5	3.38

Table 4-2a

Calculated travel times and amplitudes of "core"
reflected phases from a surface event;
reflection at radius of 300 km.

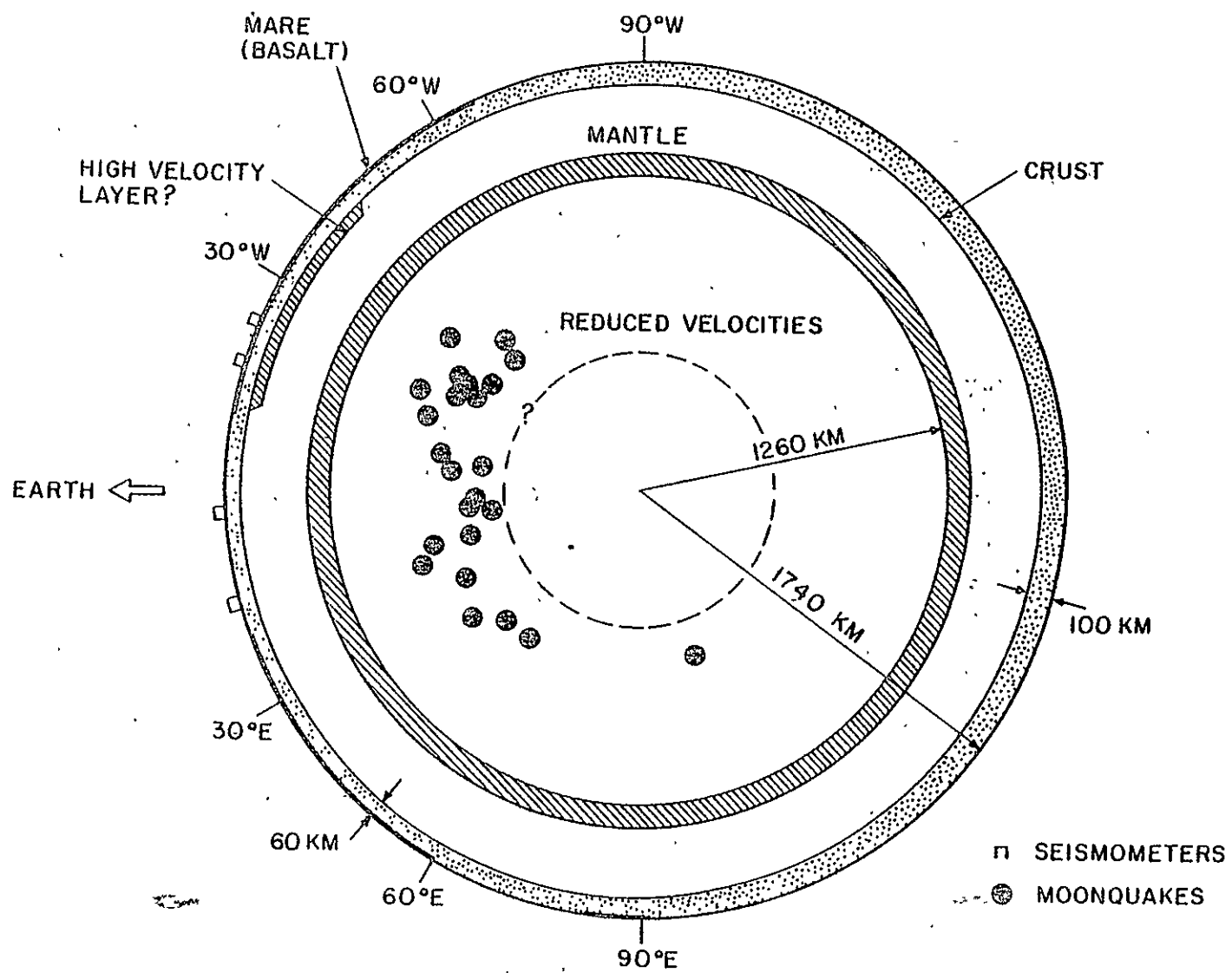| Distance	Travel Times (sec)			Amplitudes x 1000			
(degrees)	P	S	SP(PS)	PP	SS-V	SS-H	SP(PS)
10	384.3	683.2	533.7	.007	.009	.010	.003
20	385.3	685.1	535.1	.007	.007	.010	.005
30	387.1	688.3	537.4	.006	.005	.009	.007
40	389.6	692.8	540.5	.005	.001	.009	.008
50	392.7	698.4	544.5	.005	.003	.008	.008
60	396.5	705.2	549.2	.004	.006	.007	.007
70	400.8	712.9	554.6	.003	.007	.006	.006
80	405.6	721.6	560.5	.003	.007	.004	.004
90	410.9	731.1	566.9	.003	.008	.002	.003

Table 4-2b

Same as 2a, for a moonquake focus at 1000 km depth;
reflection at radius of 338 km.

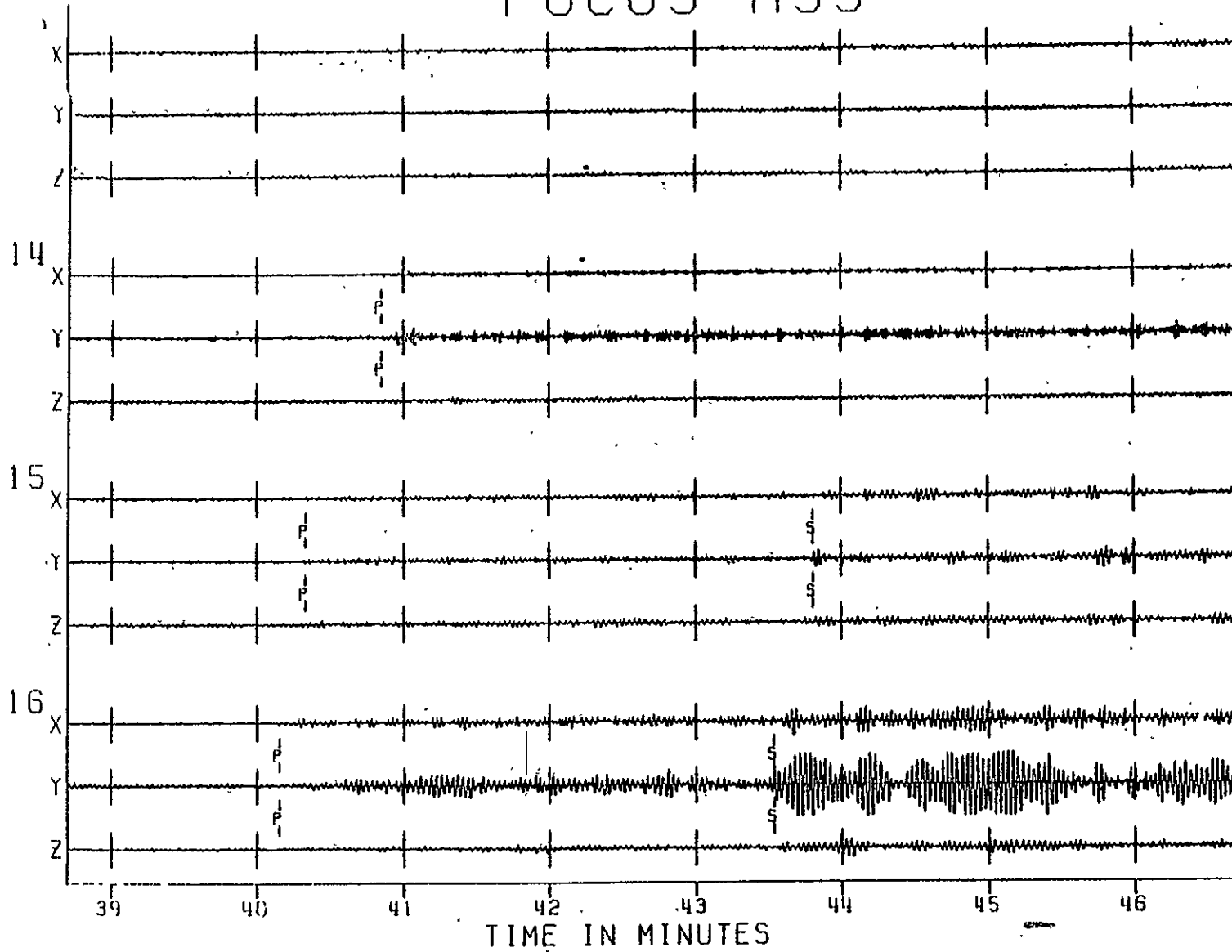| Distance	Travel Times (sec)				Amplitudes x 1000				
(degrees)	P	S	PS	SP	PP	SS-V	SS-H	PS	SP
10	240.5	433.7	389.2	284.8	.037	.041	.045	.017	.007
20	242.0	436.4	391.3	286.7	.033	.028	.043	.030	.014
30	244.5	440.9	394.6	289.7	.028	.010	.040	.038	.018
40	247.9	447.1	399.2	293.8	.023	.009	.035	.039	.019
50	252.1	454.8	404.7	298.9	.018	.025	.030	.033	.018
60	257.1	463.9	411.2	304.9	.014	.029	.023	.025	.015
70	262.7	474.3	418.3	311.6	.012	.032	.014	.015	.011
80	269.0	485.7	425.9	318.9	.013	.044	.005	.007	.006
90	275.7	497.9	--	--	.017	.056	.005	--	--

Figure Captions

Fig. 4-1. Deep moonquake locations plotted in depth and longitude. Depths are shown to scale and further details are described in the caption for Fig. 5-3.

Fig. 4-2. Raw (a) and scaled rotated (b) stacked records from the A33 moonquake focus.

Fig. 4-3. Ray path diagram for a surface source. Velocity model is for P waves as given in Table 3-15 except for the addition of a core of radius 200 km and Vp = km/sec.

Fig. 4-4. Narrow-bandpass filtered plots from a broad-band response mode lunar seismogram.

Fig. 4-5. Surface event and moonquake record sections used in searching for deep reflected phases. Boundary locations are given as radii in km (e.g. R = 300 means a depth of 1438).

Fig. 4-1

MARE
(BASALT)
90°W
60°W
MANTLE
CRUST
HIGH VELOCITY
LAYER?
30°W
REDUCED VELOCITIES
1260 KM
EARTH ⇐
?
1740 KM
100 KM
30°E
60 KM
60°E
90°E

⊓ SEISMOMETERS
⊕ MOONQUAKES

FOCUS A33

Fig. 4-2a

TIME IN MINUTES

290

Fig. 4-2b

TIME IN MINUTES
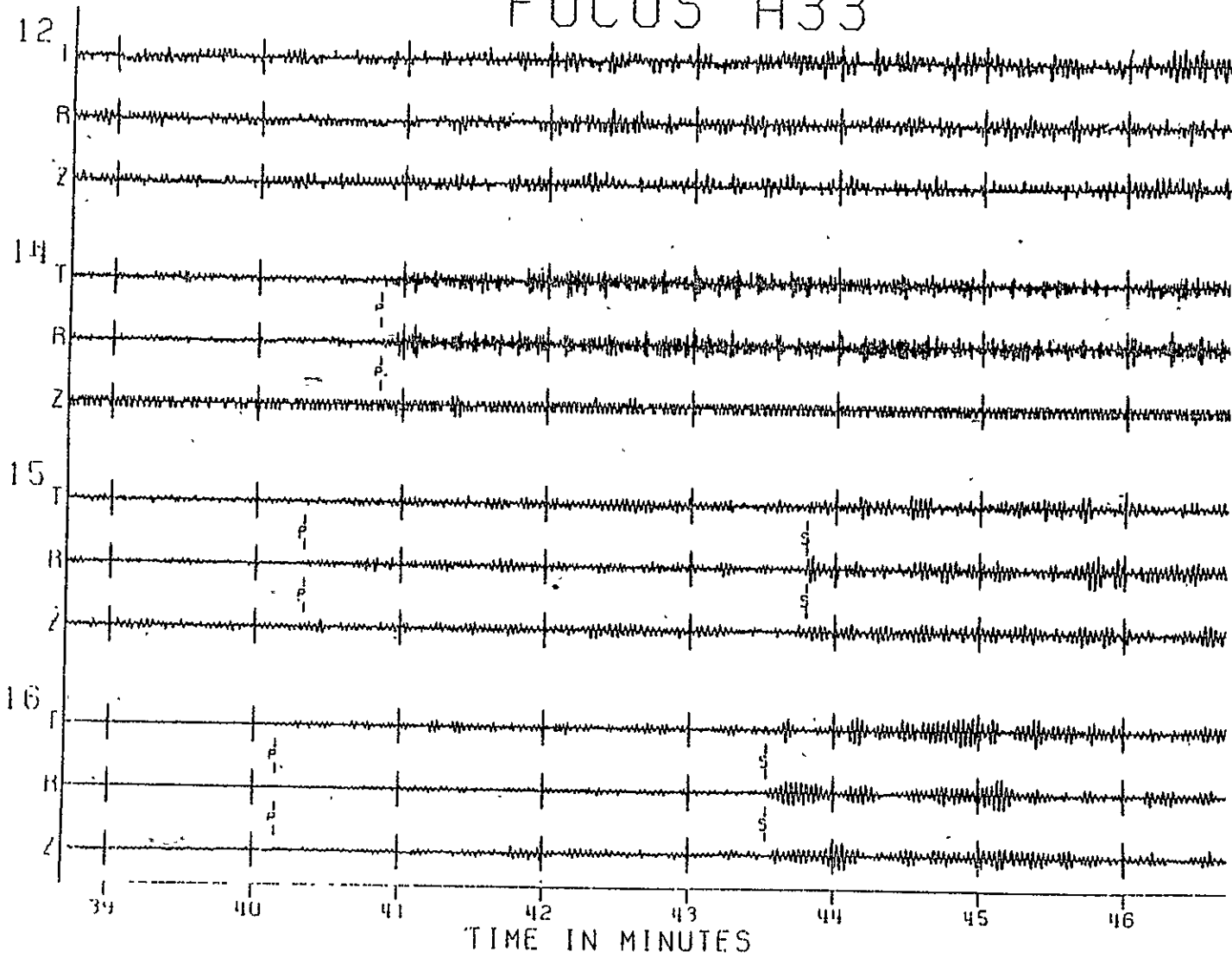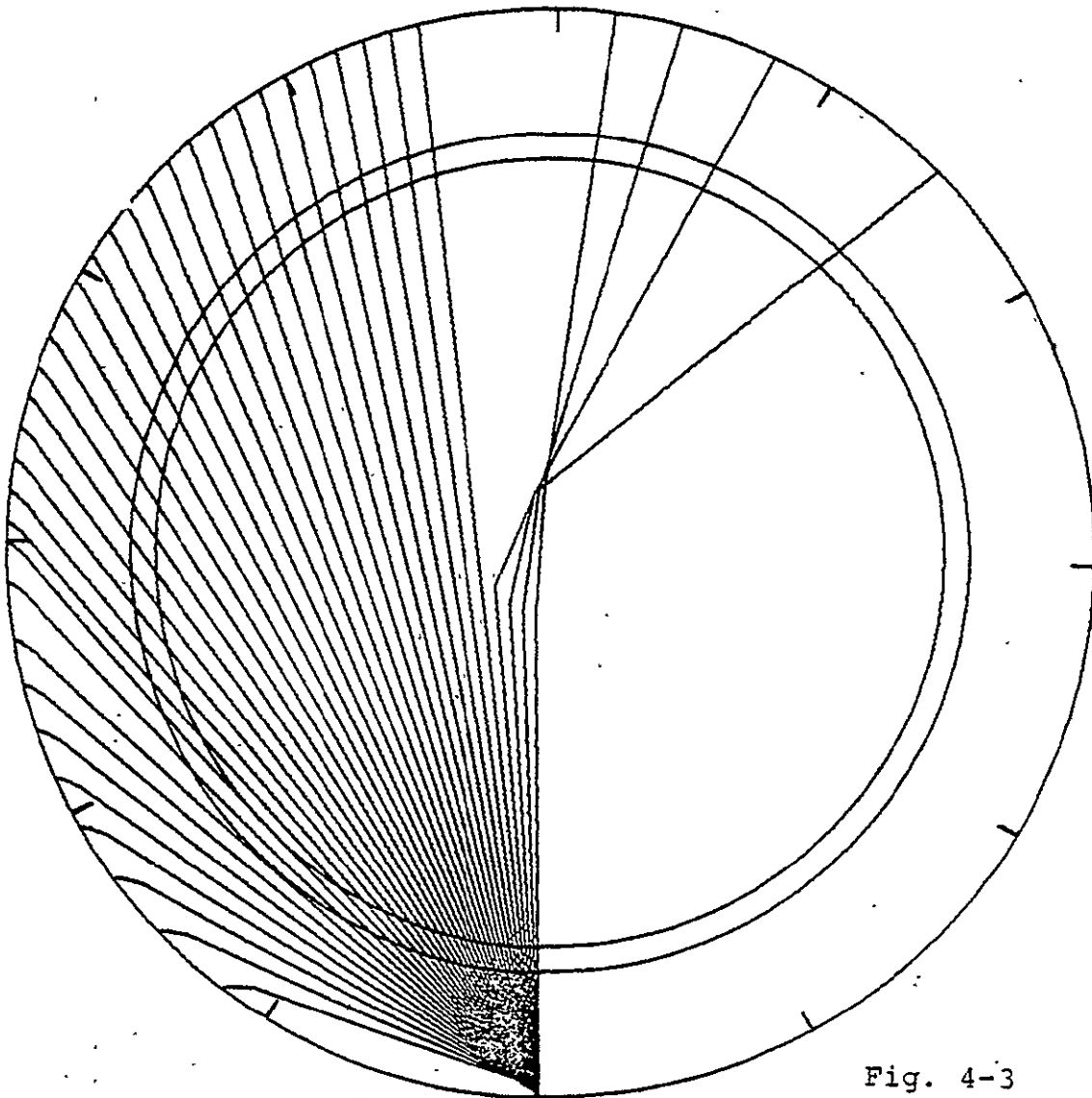
Fig. 4-3

DAY 3, 1976   HFT   STATION 12 VERTICAL

CENTER PERIOD (SECONDS)

TIME (MINUTES)

293

DISTANCE (DEGREES)

TIME (MIN)

SURFACE EVENTS
TRANSVERSE

S-S
(400)

S-S
(300)
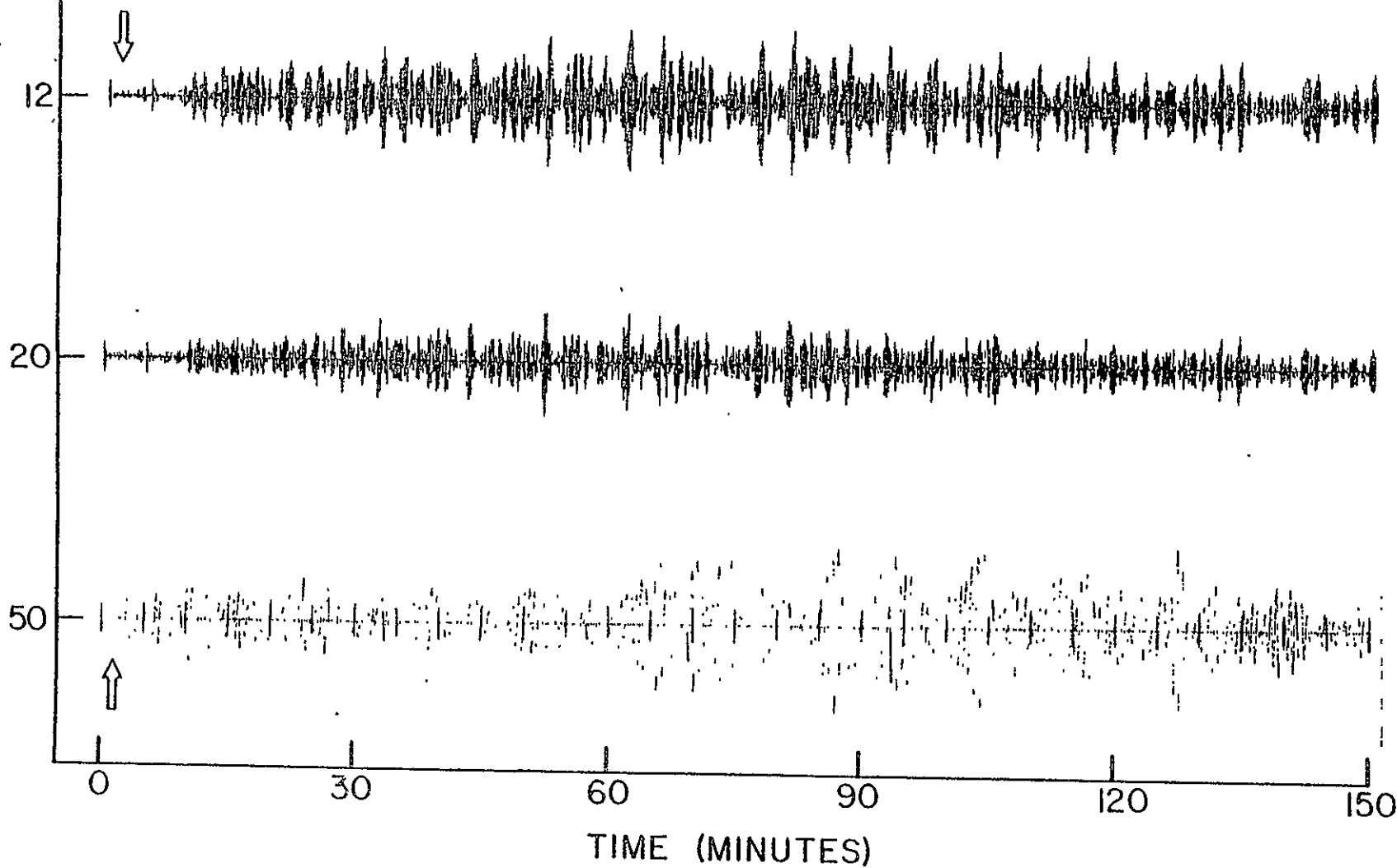
Fig. 4-5a

ORIGINAL PAGE IS
OF POOR QUALITY

294

Fig. 4-5b

DISTANCE (DEGREES)

TIME (MIN)
3.5

A2O GROUP
TRANSVERSE

S-S (400)

S-S (300)

ORIGINAL PAGE IS
OF POOR QUALITY

295

CHAPTER 5

IMPLICATIONS AND CONCLUSIONS

As discussed in the introduction, the seismic structure of the moon, as presented in this thesis, can provide direct constraints on the possible composition, temperature, and physical state of the lunar interior, and indirectly suggest evolution scenarios and present-day structural interpretations. The proper and complete evaluation of the implications of the seismic model in terms cf these areas remains to be accomplished. The purpose of this chapter is to discuss some of the first-order conclusions that can be drawn from the seismic results and identify major questio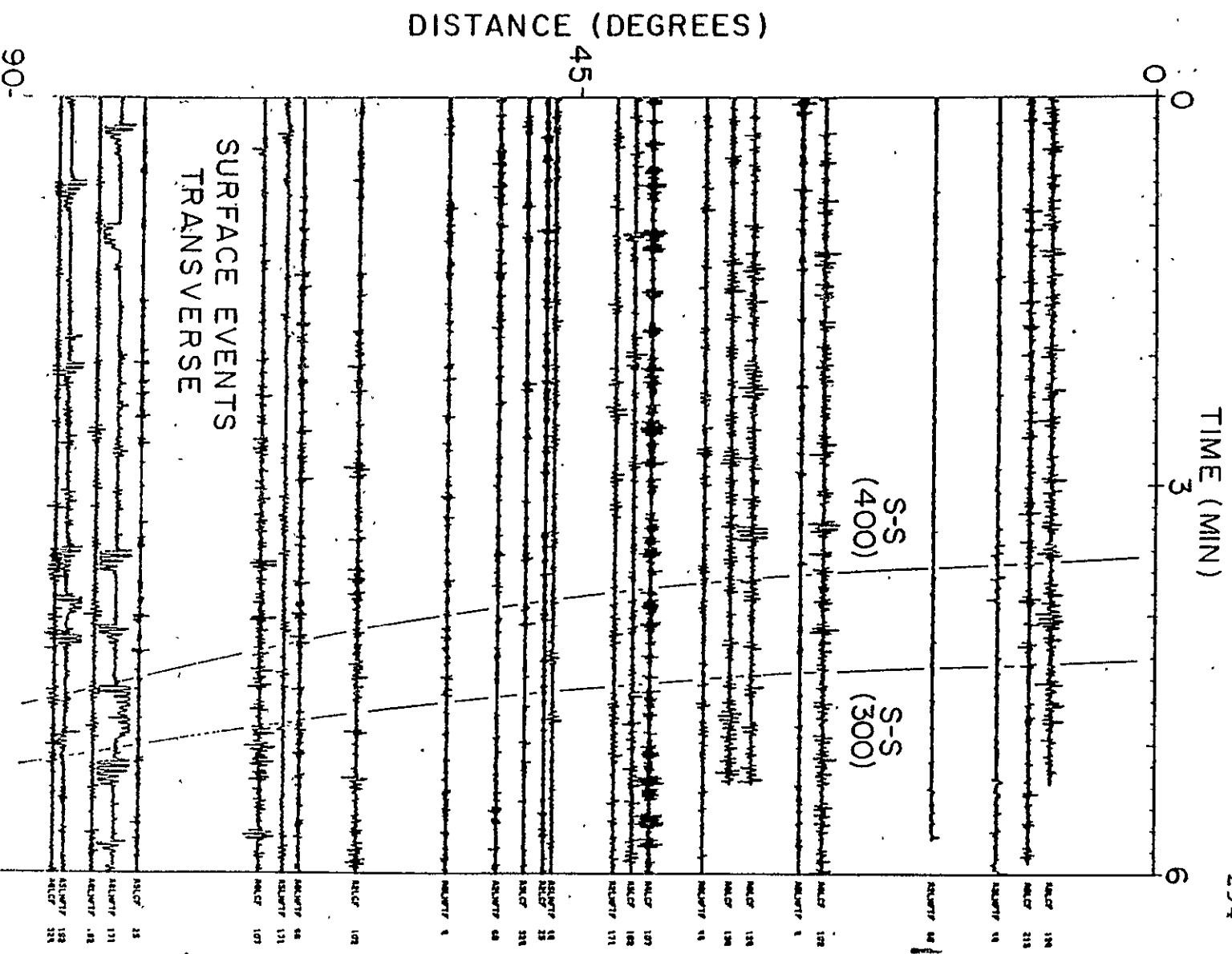ns that remain to be answered. Herein only the mantle and deeper regions of the moon are considered; the crustal structure results are discussed in Chapter 2.

5.1 Other Geophysical Data

Before discussing the implications of the seismic model, it is appropriate to briefly consider the other geophysical data that may provide information on the nature of the lunar interior. More complete reference lists

are included in the introduction.

The gravity and topographic analyses of the moon yield two integrated factors that must be satisfied by any lunar model. The average density of the moon is known to be 3.344 gm/cc, and the latest moment of inertia value is given as $I/mR^2 = 0.391\pm.002$ (Bills and Ferrari, 1977; Blackshear and Gapcynski, 1977). Although these values can of course be satisfied by an infinite number of density distributions, some conclusions can be drawn. The low average density seems to suggest that the moon is depleted in high-density materials such as iron and refractory siderophiles relative to the earth (c.f. Kaula, 1977). The moment of inertia value implies that a moderate density increase with depth is required; previous work (Toksöz et al., 1974a; Solomon and Toksöz, 1973; Solomon, 1974; Kaula et al., 1974) has shown that the contribution of a low density crust (3.0 gm/cc, 60 km thick) overlying a chemically homogeneous mantle only reduces the moment of inertia value to about 0.398 as compared to a homogeneous sphere ($I/mR^2 = 0.4$). (In these models the density within the moon is calculated as a function of temperature and pressure using elastic parameters for olivine, and the mantle STP density is determined so as to fit the mean lunar density.) If the crustal density is decreased to

2.8 and the crustal thickness increased to 100 km, then the predicted I/mR^2 could be as low as 0.395. The measured value of 0.391 thus implies that there is a further density increase within the lunar mantle. For example, Dainty et al. (1976) used a mantle with two homogeneous layers (upper mantle and lower mantle, boundary at 520 km depth) and found that the moment-of-inertia value and average density could be fit with an upper mantle density of 3.33 gm/cc and a lower mantle of 3.66 gm/cc.

The electromagnetic soundings of the moon have produced several curves of electrical conductivity with depth (see references in Introduction), summarized in Wiskerchen and Sonett (1977). If a) the temperature and compositional dependence of the conductivity, and b) the composition of the moon is known, then the conductivity profiles may be inverted to obtain the temperature distribution in the lunar interior (c.f. Duba and Ringwood, 1973). Due to the many necessary assumptions in the process and the variability in the reported conductivity profiles, the resulting constraints on temperature are rather loose, generally implying steeply rising temperatures in the first 200 km of depth, with a slower increase after that;

values at a 500 km depth range from 1000°C to 1500°C (c.f. Duba et al., 1976). It is uncertain whether or not the solidus is reached at some depth.

Finally, rock properties measurements are useful in interpreting the seismic model of the lunar mantle. In particular, Tittman et al. (1976, 1977, 1978) and others have shown that the high Q values in lunar rocks are strongly connected with the lack of volatiles, especially water, that characterize the returned samples. Chung (1970, 1971), Frisillo and Barsch (1972), Kumazawa (1969), and Mueller (1965) have reported on the stability fields and various physical parameters (e.g. V_p, V_s, ρ, and temperature and pressure derivatives) for candidate compositions (chiefly olivine and pyroxene) of the lunar interior.

In general then the above results can only act as guides and broad constraints in interpreting the seismic model. The seismic data remains the best evidence on the structure and state of the lunar interior.

5.2 Implications of Seismic Results

The seismic structure of the moon obtained in this thesis is summarized in Fig. 5-1a; velocities are plotted

as a function of depth and pressure. The pressure-depth curve for reasonable density and temperature profiles was kindly provided by Dr. S.C. Solomon. For comparison, the dashed lines represent typical velocity profiles at the same pressures in the earth; 40 kbars correspond to roughly a terrestrial depth of 125 km (Bullen, 1965, p. 235). Thus the velocities shown are all within the earth's lithosphere, where there are considerable lateral variations of velocity values. The shear wave velocity profile is actually taken from Toksöz et al. (1967) representing a mixed-path model derived from surface waves passing over Mongolia, oceanic areas, and the western U.S. The values are closely compatible with recent values reported by Helmberger and Engen (1974) from body wave data for the western U.S. The P wave velocity profile is taken from Bullen (1965) and probably represents average continental values with no low-velocity zone above 125 km. The comparison with lunar velocities shows that the profiles are roughly similar, with the lunar values generally lower than most terrestrial velocity profiles given in the literature. Figure 5-2 shows a pie diagram of the moon, with the structural units as marked based on the seismic results. In the paragraphs below, each zone

is discussed in turn. Again, the following comments are preliminary only; a complete analysis invoking geochemical, petrological, and evolutionary modeling is not within the scope of this thesis.

Upper mantle: the in situ average values of the seismic velocities in this region are compatible with several possible compositions, including an olivine-pyroxene mixture. Various combinations of iron content and olivine/pyroxene ratio could fit the observed velocities, but density, chemical equilibria, and petrological constraints need to be factored in. The negative shear wave velocity gradient of -6×10^{-4} km/sec/km corresponds to a velocity-temperature gradient of about

$$\frac{\partial V_s}{\partial T} \sim -3.2 \times 10^{-4} \; km/sec/°C$$

using the temperature vs. depth curve of Toksöz et al. (1977) and ignoring pressure effects. This value is fairly consistent with the thermal velocity gradients reported for rocks of composition that are reasonable for the lunar mantle. This suggests that the velocity decreases in the upper mantle may be due solely to the effects of increasing temperature. (This is in contradiction to the

recent assertion of Keihm and Langseth, which is based on
the upper mantle shear wave velocity gradient reported by
Nakamura et al. (1976a)). Thus no major compositional
gradients are required in the upper mantle. The average Q
values in the region (Qp $\sim$ 5000, Qs $\sim$ 3000) are quite
high compared to terrestrial values at comparable
pressures and temperatures and suggest that the rocks are
still extremely depleted in volatiles as observed at the
surface and that the temperatures are not sufficiently close
to the solidus to produce a significant amount of melt and
resulting anelastic attenuation.

Transition zone: the question of interest here concerns
the cause of the sharp shear wave decrease (and possible
accompanying small P wave drop) and attenuation increase.
(It is of course possible that the Q decreases and velocity
decrease are unrelated and that different factors are
responsible for each. However, that fact that both occur
at roughly the same depth argues for a single dominant
mechanism.) There are basically three possibilities, a
compositional change, a phase transition caused by
temperature or pressure gradients, or the onset of partial
melting. Of the middle possibilities a temperature induced
phase change is more likely because increasing pressure

typically produces a transition to phases with higher velocities rather than lower. To date no specific suggestions for either temperature or pressure phase transitions that could produce the observed velocity drops have appeared in the literature, and so they must remain speculative. The onset of partial melting is also a possibility, but the relatively high Q values in the lower mantle and the existence of the deep moonquakes argue against this (see below). A possible compositional change that could produce the velocity decreases has been tentatively proposed by Dainty et al. (1976), namely an increase in the iron content of an olivine-pyroxene mixture. A change in the (Mg/Mg + Fe) ratio from say 80 to about 60 would provide approximately the correct shear wave velocity drop. This would have a smaller effect on the P velocity, and would in addition increase the density somewhat and lower the solidus; this last change could lower the Q values. All of these effects are in at least qualitative agreement with the observations, and so such a model should be given serious consideration and tested against geochemical and petrological constraints. In fact, similar models have been proposed by Ringwood and Kesson (1977b) and Taylor (1978) on geochemical grounds.

Many other compositional changes are of course conceivable, and proposed models should be examined to see if they can satisfy the seismic constraints presented herein. A *sine qua non* for this is that laboratory measurements of velocities, densities, and attenuations as a function of temperature and pressure be available for the compositions in question.

Lower Mantle: the seismic velocity values in this region are again compatible with an olivine-pyroxene composition, among others, tied closely of course to the possible compositional change represented by the transition zone. The seismic data cannot constrain the velocity gradients; a moderate velocity decrease perhaps as a result of increasing temperature is possible. The Q values ($Q_p \sim 1500$, $Q_s \sim 1000$) are still reasonably high but may also decrease slowly with depth. An additional seismic datum is that all the deep moonquakes apparently occur in the lower mantle region (see Fig. 5-3). As mentioned before, the calculated shear stresses due to tides peak in this region when elastic parameter distributions consistent with the above velocity model are used. These moonquakes presumably represent brittle

fractures, suggesting that a significant percentage of partial melt is not present in the lower mantle. It is difficult to place a quantitative constraint on this especially in view of the small magnitude of the moonquake events, but it is qualitatively in agreement with the reasonably high Q values.

Deep interior: As discussed in Chapter 4, the seismic data for this region are extremely sparse. It is possible that beginning below the deepest moonquakes, say at 1100 km, there is a region of increased shear wave attenuation (Qs on the order of a few hundreds). One possible explanation for this of course is that the temperature is approaching the solidus. The possibility of a lunar core remains an open question. Perhaps coincidentally, all lunar data (moment-of-inertia, density, seismic, electrical conductivity) allow but do not require a core.

In closing this section, it is appropriate to touch briefly on some of various geochemical, petrological, and thermal evolutionary models that have been proposed and perhaps now can be constrained by the seismic results. There is a reasonable consensus that the outer few hundred kilometers of the moon have been melted and differentiated,

early in the moon's evolution. This event probably
produced the lunar highland-type crust; the mare basalts
formed later after the major meteorite impacts, perhaps
by remelting portions of the upper mantle (c.f. Taylor and
Jakes, 1974). The depth of the initial melt zone has
been variously reported as between 200 and 600 km, based
on a variety of constraints (c.f. Solomon and Chaiken,
1976; Keihm and Langseth, 1977). Below this, there is
little agreement. Suggestions that the region has been
totally differentiated (c.f. Binder and Lange, 1977) and
is completely primitive lunar material (c.f. Taylor, 1978)
are both in the recent literature. It is tempting to
identify the upper-lower mantle boundary as the division
between the melted, differentiated region and the
primitive lunar material, especially since a recent report
(Taylor, 1978) favors a 400 km depth for the base of the
melted zone and predicts an iron increase in the primitive
region.

However, this correlation with the seismic results is
speculative, it is mentioned here only as a possibility
that has recently emerged. It is likely that equally
valid and consistent models will be proposed.

5.3 Conclusions and Suggestions for Future Work

The purpose of this thesis has been to obtain a seismic model of the lunar interior. Considering the limitations inherent in a four-station array and the analysis difficulties presented by the data, the seismic results as reported herein and elsewhere that have been achieved by the Apollo program are impressive and augur well for future seismic exploration of other planets. A final schematic view of the lunar seismic structure reported in this thesis is shown in Figs. 5-3. With the exception of the mare basalt and high velocity layers, all depths are drawn to scale. The drawing is an equatorial slice through the moon; thus only longitude and depth coordinates are plotted. The ALSEP seismic stations are as shown, followed by mare basalt layers (schematically and roughly representing Mare Imbrium, Mare Serenitatis, and Mare trisium) imbedded in a lunar crust of 60-100 km thickness. A possible thin high-velocity layer beneath the crust is shown, followed by the upper mantle, transition zone, and lower mantle. The deep moonquake events used in this thesis are as shown; the dot size corresponds to the

average uncertainties in the locations as discussed in
Chapter 3. Possible deeper structure is indicated by
the dashed line, below which an attenuating zone and
conceivably a core could exist. Coupled with the
discussions in the preceeding chapters, this model
represents the structure of the lunar interior envisioned
on the basis of the results reported in this thesis.

There are three areas of possible future work on lunar
seismology. First, a small amount of data remains to be
processed and, as new analysis methods become available,
they should be applied as appropriate. Second, specific
compositional and thermal lunar models should be
quantitatively tested against the seismic model to
determine which classes of models are acceptable. The
reverse procedure is also feasible; models designed to
satisfy the seismic parameters can be checked against the
constraints from other fields. Finally, though not
directly germane to the structural problem, some work
remains to be done in analyzing the source characteristics
of the deep moonquakes; a definitive correlation between
the causative tidal stresses and the occurrence history
of each repeating source has not yet been produced.

Figure Captions

Fig. 5-1. Final lunar velocity model obtained in this
thesis.

Fig. 5-2. Schematic view of the structural units of the
lunar interior.

Fig. 5-3. Equatorial slice through the moon showing
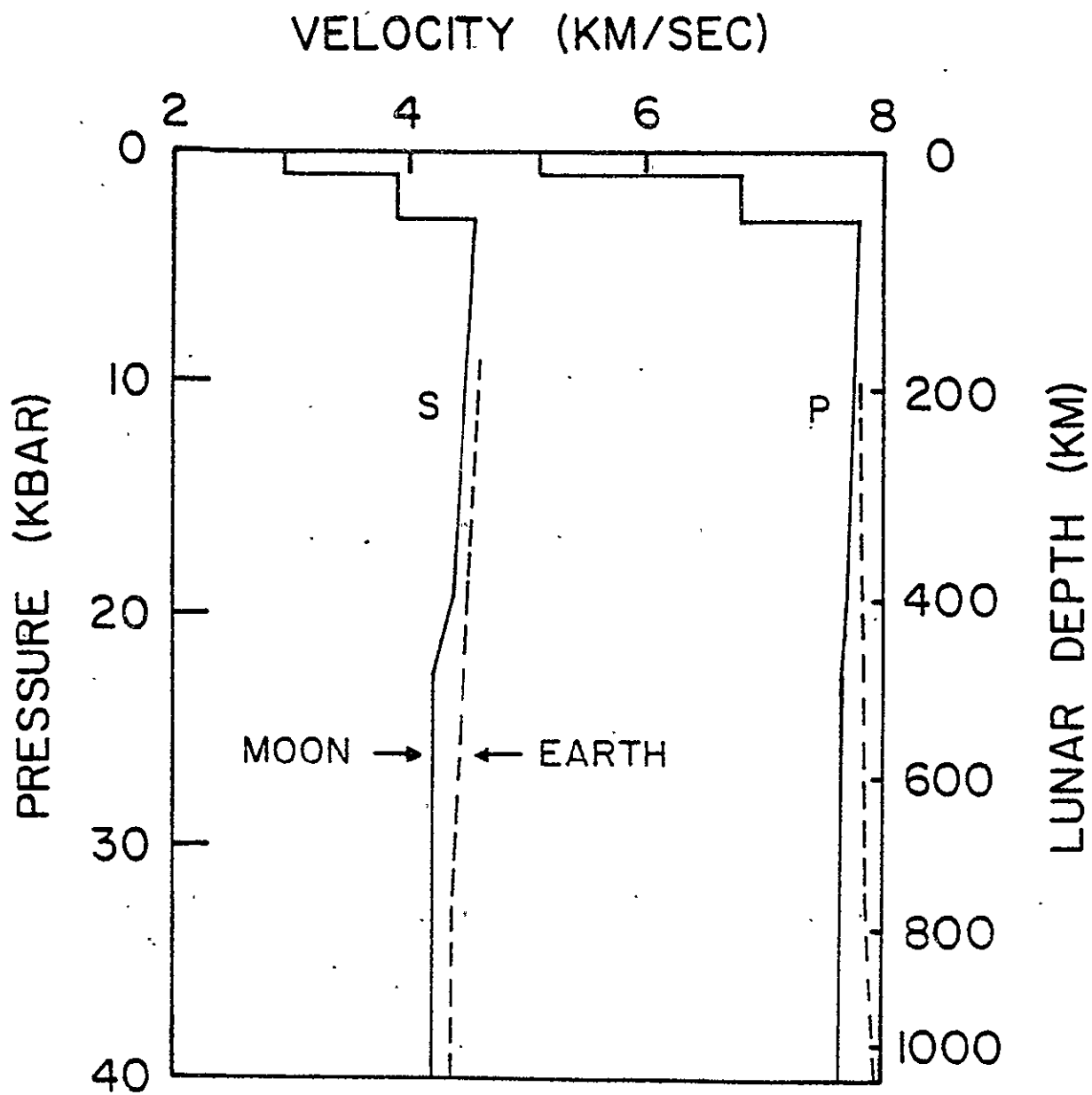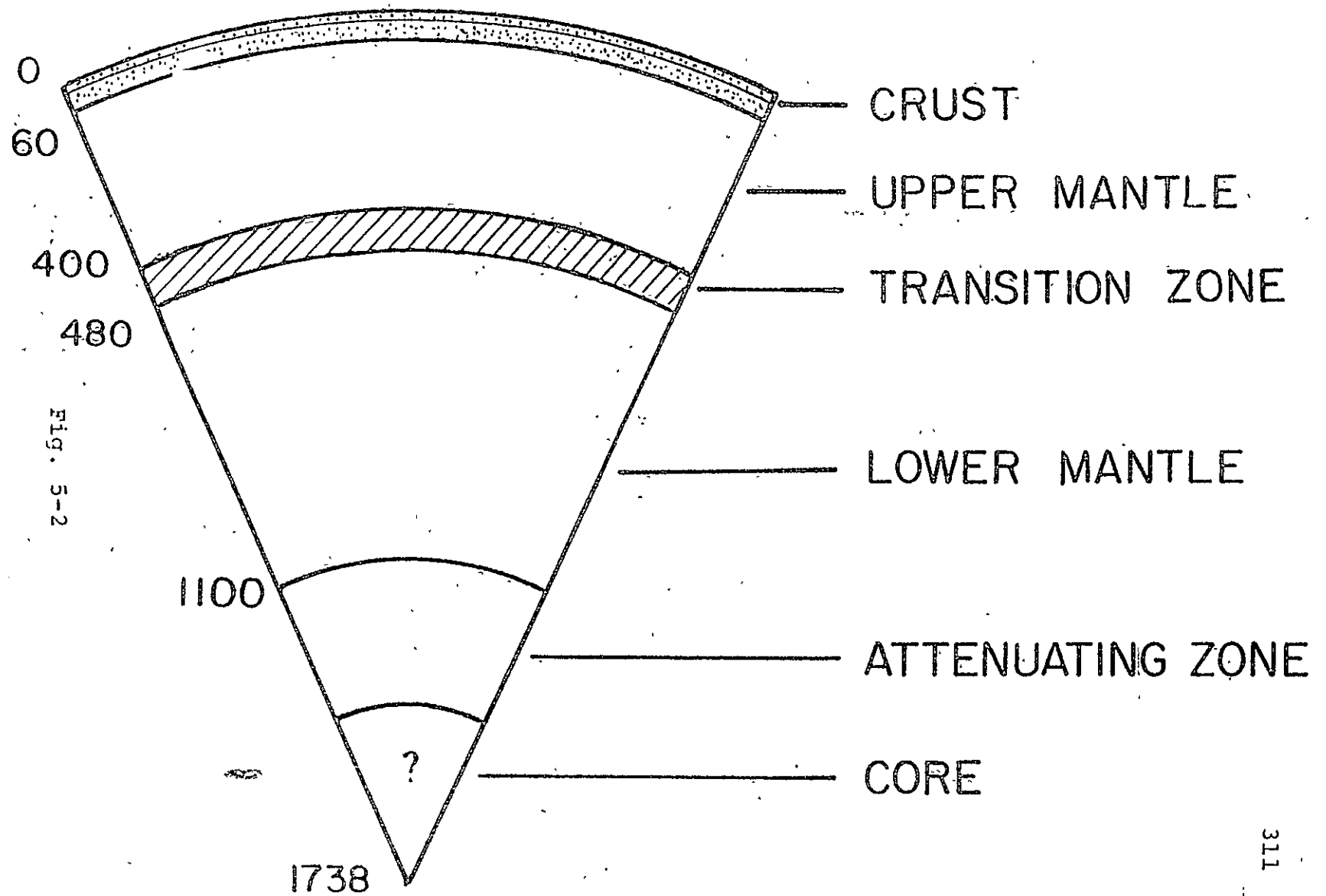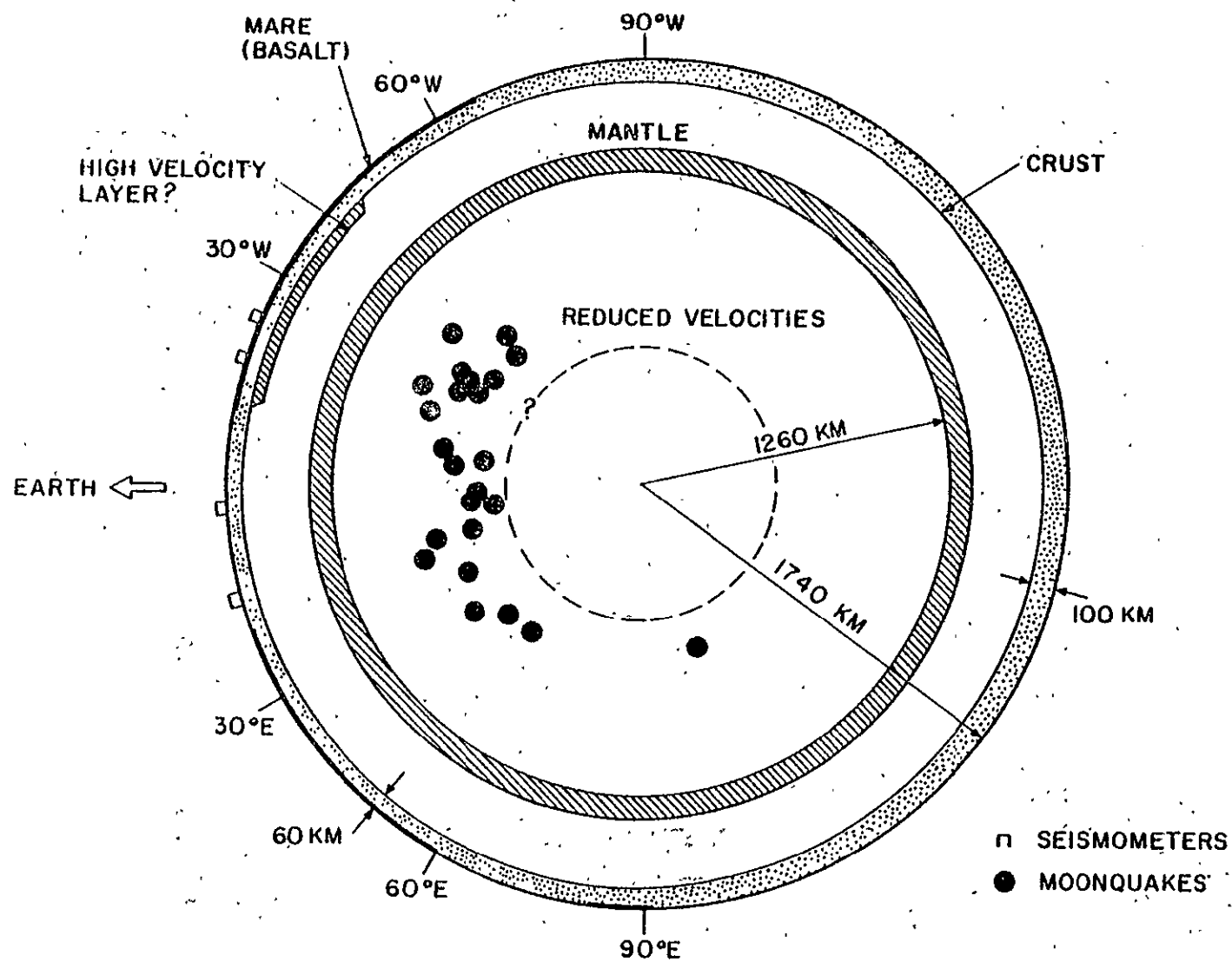structural units.

310

Fig. 5-1

Fig. 5-2

0
60
400
480
1100
1738

CRUST

UPPER MANTLE

TRANSITION ZONE

LOWER MANTLE

ATTENUATING ZONE

?

CORE

311

Fig. 5-3

References

Acton, F.S., _Numerical Methods that Work_, Harper and Row, New York, 1970.

Aki, K., Analysis of the seismic coda of local earthquakes as scattered waves, _J. Geophys. Res._, 74, 615, 1969.

Aki, Scattering of P waves under the Montana LASA, _J. Geophys. Res._, 78, 1334, 1973.

Aki, K., Class notes, 1975.

Aki, K. and B. Chouet, Origin of coda waves: source, attenuation and scattering effects, _J. Geophys. Res._, 80, 3322, 1975.

Aki, K. and W.H.K. Lee, Determination of three-dimensional velocity anomalies under a seismic array using first P arrival times from local earthquakes, 1. A homogeneous model, _J. Geophys. Res._, 81, 4381, 1976.

Aki, K., A. Christoffersson and E. Husebye, Determination of the three-dimensional seismic structure of the lithosphere, _J. Geophys. Res._, 82, 277, 1977.

Alfvén, J. and G. Arrhenius, Origin and evolution of the Earth-Moon system, _Moon_, 5, 210, 1972.

Ananda, M.P., Lunar gravity: a mass point model, _J. Geophys. Res._, 82, 3049, 1977.

Anderson, D.L., The moon as a high temperature condensate, _Moon_, 8, 33, 1973a.

Anderson, D.L., The composition and origin of the moon, _Earth Plan. Sci. Lett._, 18, 301, 1973b.

Anderson, D.L., On the composition of the lunar interior, _J. Geophys. Res._, 80, 1555, 1975.

Arkani-Hamed, J., Stress differences in the moon or an evidence for a cold moon, _Moon_, 6, 135, 1973a.

Arkani-Hamed, J., Density and stress distribution in the moon, _Moon_, 7, 84, 1973b.

Backus, G. and F. Gilbert, Numerical applications of a formalism for geophysical inverse problems, _Geophys. J. R. astr. Soc._, 13, 247, 1967.

Backus, G. and F. Gilbert, The resolving power of gross earth data, Geophys. J. R. astr. Soc., 16, 169, 1968.

Backus, G. and F. Gilbert, Uniqueness in the inversion of inaccurate gross earth data, Phil. Trans. R. Soc. Lond. A., 266, 123, 1970.

Berckhemer, H., A possible scattering mechanism for lunar seismic waves, Z. Geophys., 36, 523, 1970.

Bessonova, E.N., V.M. Fishman, V.Z. Ryaboyi and G.A. Sitnikova, The tau method for inversion of travel times, 1, Deep seismic sounding data, Geophys. J. R. astr. Soc., 36, 377, 1974.

Bills, B.G. and A.J. Ferrari, A lunar density model consistent with typographic, gravitational, and seismic data, J. Geophys. Res., 82, 1306, 1977.

Binder, A.B., On the origin of the moon by rotational fission, Moon, 11, 53, 1974.

Binder, A.B., On the petrology and early development of the crust of a moon of fission origin, Moon, 15, 275, 1976a.

Binder, A.B., On the compositions and characteristics of the mare basalt magmas and their source regions, Moon, 16, 115, 1976b.

Binder, A.B., On the implications of an olivine dominated upper mantle on the development of a moon of fission origin, Moon, 16, 159, 1976c.

Binder, A.B. and M. Lange, On the thermal history of a moon of fission origin, Moon, 17, 29, 1977.

Binder, A.B. and M.A. Lange, The mare basalt magma source region (abstract), in Lunar and Plan. Sci. IX, 91, 1978.

Blackshear, W.T. and J.P. Gapcynski, On improved value for the lunar moment of inertia, J. Geophys. Res., 82, 1699, 1977.

Bowin, C., B. Simon and W. Wollenhaupt, Mascons: a two-body solution, J. Geophys. Res., 80, 4947, 1975.

Bullen, K.E., An Introduction to the Theory of Seismology, Cambridge University Press, Cambridge, U.K., 1965.

Burdick, L.J. and D.V. Helmberger, The upper mantle P wave velocity structure of the western United States, J. Geophys. Res., 83, 1699, 1978.

Burkhard, N. and D.D. Jackson, Extremal inversion of lunar travel time data, Proc. Lunar Science Conf. 6th, 2881, 1975.

Butt, R.V.J. and J.A. Bastin, Latitutde effects in lunar thermal evolution, Moon, 16, 339, 1977.

Cameron, A.G.W., Properties of the solar nebula and the origin of the moon, Moon, 7, 377, 1973.

Cassen, P.M. and R.E. Young, On the cooling of the moon by solid convection, Moon, 12, 361, 1975.

Cheng, C.H. and M.N. Toksöz, Tidal stresses in the moon, J. Geophys. Res., 83, 845, 1978.

Cheng, C.H., S. Hannahs and M.N. Toksöz, Tidal stresses in central California (abstract), EOS, Trans. Am. Geophys. Un., 59, 331, 1978.

Chung, D.H., Effects of iron/magnesium ratio on P- and S-wave velocities in olivine, J. Geophys. Res., 75, 7353, 1970.

Chung, D.H., Elasticity and equations of state of olivines in the $Mg_2SiO_4-Fe_2SiO_4$ system, Geophys. J. R. astr. Soc., 25, 511, 1971.

Cooper, M.R. and R.L. Kovach, Energy, frequency and distance of moonquakes at the Apollo 17 site, Proc. Lunar Sci. Conf. 6th, 2863, 1975.

Cooper, M., R. Kovach and J. Watkins, Lunar near-surface structure, Rev. Geophys. Space Phys., 12, 291, 1974.

Dainty, A.M. and M.N. Toksöz, Elastic wave propagation in a highly scattering medium - a diffusion approach, J. Geophys., 43, 375, 1977.

Dainty, A., M.N. Toksöz, K. Anderson, P.J. Pines, Y. Nakamura and G. Latham, Seismic scattering and shallow structure of the moon in Oceanus Procellarum, Moon, 9, 11, 1974a.

Dainty, A.M., M.N. Toksöz, S.C. Solomon, K. Anderson and N. Goins, Constraints on lunar structure, Proc. Lunar Sci. Conf. 5th, 3091, 1974b.

Dainty, A.M., N.R. Goins and M.N. Toksöz, Natural lunar seismic events and the structure of the moon, Proc. Lunar Sci. Conf. 6th, 2887, 1975a.

Dainty, A.M., S. Stein and M.N. Toksöz, Variation in the number of meteoroid impacts on the moon with lunar phase, Geophys. Res. Lett., 2, 272, 1975b.

Dainty, A.M., M.N. Toksöz and S. Stein, Seismic investigation of the lunar interior, Proc. Lunar Sci. Conf. 7th, 3057, 1976.

Dolginov, Sh. Sh., On the origin of ancient lunar magnetic fields, Moon, 14, 255, 1975.

Dorman, J., Y. Nakamura and G.V. Latham, The meteoroid population viewed from the lunar science network (abstract), in Lunar and Plan. Sci. IX, 261, 1978.

Drake, M.J., Evolution of major mineral compositions and trace element abundances during fractional crystallization of a model lunar composition, Geochim. Cosmochim. Acta, 40, 401, 1976.

Drake, M.J. and G.J. Consolmagno, Critical review of models for the evolution of high-Ti mare basalts, Proc. Lunar Sci. Conf. 7th, 1633, 1976.

Duba, A. and A.E. Ringwood, Electrical conductivity, internal temperatures and thermal evolution of the moon, Moon, 7, 356, 1973.

Duba, A., H. Heard and R. Schock, Electrical conductivity of orthopyroxene to 1400°C and the resulting selenotherm, Proc. Lunar Sci. Conf. 7th, 3173, 1976.

Duennebier, F., Thermal movement of the regolith, Proc. Lunar Sci. Conf. 7th, 1073, 1976.

Duennebier, F. and G.H. Sutton, Thermal moonquakes, J. Geophys. Res., 79, 4351, 1974a.

Duennebier, F. and G. Sutton, Meteoroid impacts recorded by the short-period component of Apollo 14 lunar passive seismic station, J. Geophys. Res., 79, 4365, 1974b.

Duennebier, F., D. Lammlein, G. Latham, J. Dorman and Y. Nakamura, Passive Seismic Experiment Long Period Event Catalog I-VI, Marine Science Institute, University of Texas, Galveston, Texas, 1975a.

Duennebier, F., J. Dorman, D. Lammlein, G. Latham and Y. Nakamura, Meteoroid flux from passive seismic experiment data, Proc. Lunar Sci. Conf. 6th, 2417, 1975b.

Duennebier, F., Y. Nakamura, G. Latham and J. Dorman, Meteoroid storms detected on the moon, Science, 192, 1000, 1976.

Dyal, P., C.W. Parkin and W.D. Daily, Magnetism and the interior of the moon, Rev. Geophys. Space Phys., 12, 568, 1974.

Dyal, P., C.W. Parkin and W.D. Daily, Lunar electrical conductivity and magnetic permeability, Proc. Lunar Sci. Conf. 6th, 2909, 1975.

Dyal, P., C.W. Parkin and W.D. Daily, Structure of the lunar interior from magnetic field measurements, Proc. Lunar Sci. Conf. 7th, 3077, 1976.

Ewing, M., W. Jardetzky and F. Press, Elastic Waves in Layered Media, McGraw-Hill Book Co., New York, 1957.

Ferrari, A.J., Lunar gravity: a harmonic analysis, J. Geophys. Res., 82, 3065, 1977.

Flinn, E.A., Signal analysis using rectilinearity and direction of particle motion, Proc. IEEE, 53, 1874, 1965.

Franklin, J., Well-posed stochastic extensions of ill-posed linear problems, J. Math. Anal. Appl., 31, 682, 1970.

Frisillo, A.L. and G.R. Barsch, Measurement of single-crystal constants of bronzite as a function of pressure and temperature, J. Geophys. Res., 77, 6360, 1972.

Fuller, M., Lunar magnetism, Rev. Geophys. Space Phys., 12, 23, 1974.

Ganapathy, R. and E. Anders, Bulk compositions of the moon and earth estimated from meteorites, Proc. Lunar Sci. Conf. 5th, 1181, 1974.

Ganapathy, R., R.R. Keays, J.C. Law and E. Anders, Trace elements in Apollo 11 lunar rocks: implications for meteorite influx and origin of moon, Proc. Apollo 11 Lunar Sci. Conf., 1117, 1970.

Gast, P.W. and R.T. Giuli, Density of the lunar interior, Earth Plan. Sci. Lett., 16, 299, 1972.

Goins, N.R., A. Dainty and M.N. Toksöz. Moonquake locations and seismic properties of the lunar mantle (abstract), EOS, Trans. Am. Geophys. Un., 56, 1141, 1974.

Goins, N.R., C.H. Cheng and M.N. Toksöz, Deep moonquake polarity reversals and tidal stress in the moon (abstract), EOS, Trans. Am. Geophys. Un., 57, 272, 1976a.

Goins, N.R., A.M. Dainty and M.N. Toksöz, Moonquakes and the structure of the lunar interior (abstract), EOS, Trans. Am. Geophys. Un., 57, 962, 1976b.

Goins, N.R., A.M. Dainty and M.N. Toksöz, The structure of the lunar interior as determined from seismic data (abstract), in Lunar Science VIII, 354, 1977a.

Goins, N.R., A.M. Dainty and M.N. Toksöz, The deep seismic structure of the moon, Proc. Lunar Sci. Conf. 8th, 471, 1977b.

Goins, N.R., A.M. Dainty, M.N. Toksöz and L. Shure, The structure of the lunar interior (abstract), EOS, Trans. Am. Geophys. Un., 58, 427, 1977c.

Goins, N.R., M.N. Toksöz and A.M. Dainty, Constraints on the structure of the lunar upper mantle, in Lunar and Plan. Sci. IX, 385, 1978a.

Goins, N., M.N. Toksöz, and A.M. Dainty, Seismic energy release of the moon (abstract), EOS, Trans. Am. Geophys. Un., 59, 315, 1978b.

Gold, T. and S. Soter, Apollo 12 seismic signal: indication of a deep layer of powder, Science, 169, 1071, 1970.

Goswami, J.N., Constraints on the nature of the ancient lunar magnetic field, Nature, 261, 695, 1976.

Hanks, T.C. and D.L. Anderson, Origin, evolution and present thermal state of the moon, Phys. Earth Planet. Int., 5, 409, 1972.

Hart, R.S., D.L. Anderson and H. Kanamori, The effect of attenuation on gross earth models, J. Geophys. Res., 82, 1647, 1977.

Head, J.W. III, Lunar volcanism in space and time, Rev. Geophys. Space Phys., 14, 265, 1976a.

Head, J.W., The significance of substrate characteristics
    in determining morphology and morphometry of lunar
    craters, Proc. Lunar Sci. Conf. 7th, 2913, 1976b.

Head, J.W., C.A. Wood and T.A. Mutch, Geologic evolution of
    the terrestrial planets, Am. Scientist, 65, 21, 1977.

Heaton, T.H., Tidal triggering of earthquakes, Geophys. J. R.
    astr. Soc., 43, 307, 1975.

Helmberger, D.V. and G.R. Engen, Upper mantle shear structure,
    J. Geophys. Res., 79, 4017, 1974.

Herbert, F., M.J. Drake, C.P. Sonett and M.J. Wiskerchen, Some
    constraints on the thermal history of the lunar magma
    ocean, Proc. Lunar Sci. Conf. 8th, 573, 1977a.

Herbert, F., C.P. Sonett and M.J. Wiskerchen, Model 'Zero-Age'
    lunar thermal profiles resulting from electrical
    induction, J. Geophys. Res., 82, 2054, 1977b.

Herbert, F., M.J. Drake and C.P. Sonett, Geophysical and
    geochemical evolution of the lunar magma ocean, in Lunar
    and Plan. Sci. IX, 494, 1978.

Herzberg, C. and J.A. Wood, Spinel cataclasites as samples of
    the lower crust of the moon, in Lunar and Plan. Sci. IX,
    500, 1978.

Horedt, G.P., Pre-capture orbits of the moon, Moon, 15, 439,
    1976.

Hörz, F., R. Gibbons, R. Hill and D. Gault, Large scale
    cratering of the lunar highlands: some Monte Carlo
    model considerations, Proc. Lunar Sci. Conf. 7th, 2931,
    1976.

Howard, K.A., D. Wilhelms and D. Scott, Lunar basin formation
    and highland stratigraphy, Rev. Geophys. Space Phys.,
    12, 309, 1974.

Hubbard, N.J. and J.W. Minear, A physical and chemical model
    of early lunar history, Proc. Lunar Sci. Conf. 6th, 1057,
    1975.

Hubbard, N.J. and J.W. Minear, Petrogenesis in a modestly
    endowed moon, Proc. Lunar Sci. Conf. 7th, 3421, 1976.

Irving, A.J., Chemical, mineralogical and textural systematics of non-mare melt rocks: Implications for lunar impact and volcanic processes, Proc. Lunar Sci. Conf. 6th, 363, 1975.

Jarosch, H.S., The use of surface reflections in lunar seismograms, Bull. Seism. Soc. Am., 67, 1647, 1977.

Julian, B.R. and D. Gubbins, Three-dimensional seismic ray tracing, J. Geophys., 43, 95, 1977.

Kanamori, H., A. Nur, D.H. Chung, D. Wones and G. Simmons, Elastic wave velocities of lunar samples at high pressures and their geophysical implications, Science, 167, 726, 1970.

Kanasewich, E.R., Time Sequence Analysis in Geophysics, 274-298, U. of Alberta Press, Canada, 1973.

Kaula, W.M., Interpretation of the lunar gravitational field, Phys. Earth Planet. Int., 4, 185, 1971.

Kaula, W.M., The seven ages of a planet, Icarus, 26, 1, 1975a.

Kaula, W.M., The gravity and shape of the moon, EOS, Trans. Am. Geophys. Un., 56, 309, 1975b.

Kaula, W.M., On the origin of the moon, with emphasis on bulk composition, Proc. Lunar Sci. Conf. 8th, 321, 1977.

Kaula, W.M. and A.W. Harris, Dynamics of lunar origin and orbital evolution, Rev. Geophys. Space Phys., 13, 363, 1975.

Kaula, W.M., G. Schubert, R.E. Lingenfelter, W.L. Sjogren and W.R. Wollenhaupt, Apollo laser altimetry and inferences as to lunar structure, Proc. Lunar Sci. Conf. 5th, 3049, 1974.

Keihm, S.J. and M.G. Langseth, Lunar thermal regime to 300 km, Proc. Lunar Sci. Conf. 8th, 499, 1977.

Keilis, Borok, V. and T. Yanovskaya, Inverse seismic problems (structural review), Geophys. J., 13, 223, 1967.

Kesson, S.E. and A.E. Ringwood, Further limits on the bulk composition of the moon, Proc. Lunar Sci. Conf. 8th, 411, 1977.

King, R.W., C. Counselman III, and I. Shapiro, Lunar dyanamics and selenodesy: results from analysis of VLBI and laser data, J. Geophys. Res., 81, 6251, 1976.

Klein, F.W., Earthquake swarms and the semidiurnal solid Earth tide, Geophys. J. R. astr. Soc., 45, 245, 1976.

Knopoff, L., Q, Rev. Geophys., 2, 625, 1964.

Knopoff, L. and J.A. Hudson, Scattering of elastic waves by small inhomogeneities, J. Acoust. Soc. Am., 36, 338, 1964.

Kovach, R. and J. Watkins, The velocity structure of the lunar crust, Moon, 7, 63, 1973a.

Kovach, R. and J. Watkins, Apollo 17 seismic profiling - probing the lunar crust, Science, 180, 1063, 1973b.

Kovach, R. and J. Watkins, The structure of the lunar crust at the Apollo 17 site, Proc. Lunar Sci. Conf. 4th, 2549, 1973c.

Krähenbühl, U., R. Ganapathy, J.W. Morgan and E. Anders, Volatile elements in Apollo 16 samples: implications for highland volcanism and accretion history of the moon, Proc. Lunar Sci. Conf. 4th, 1325, 1973.

Kumazawa, M., The elastic constants of single-crystal orthopyroxene, J. Geophys. Res., 74, 5973, 1969.

Lammlein, D., Lunar seismicity and tectonics, Phys. Earth Planet. Int., 14, 224, 1977.

Lammlein, D.R., G.V. Latham, J. Dorman, Y. Nakamura and M. Ewing, Lunar seismicity, structure, and tectonics, Rev. Geophys. Space Phys., 12, 1, 1974.

Lanczos, C., Linear Differential Operators, Chap. 3, Van Nostrand, New York, 1961.

Latham, G., Selected Seismic Event Catalog from the Apollo 12, 14, 15, 16 Passive Seismograph, Data Set No. 69-099C-03Q, 71-008C-04Q, 71-063C-01Q, 72-031C-01Q, National Space Science Data Center, 1975.

Latham, G.V., M. Ewing, F. Press and G. Sutton, Apollo passive seismic experiment, Science, 165, 241, 1969a.

Latham, G.V., M. Ewing, F. Press, G. Sutton, J. Dorman, N. Toksöz, R. Wiggins, Y. Nakamura, J. Derr and F. Duennebier, Passive seismic experiment, NASA Spec. Publ. SP-214, 143, 1969b.

Latham, G.V., M. Ewing, J. Dorman, F. Press, N. Toksöz,
    G. Sutton, R. Meissner, F. Duennebier, Y. Nakamura,
    R. Kovach and M. Yates, Seismic data from manmade
    impacts on the moon, Science, 170, 620, 1970a.

Latham, G.V., M. Ewing, F. Press, G. Sutton, J. Dorman,
    Y. Nakamura, N. Toksöz, R. Wiggins, J. Derr and F.
    Duennebier, Passive seismic experiment, Science, 167,
    455, 1970b.

Latham, G.V., M. Ewing, F. Press, G. Sutton, J. Dorman,
    Y. Nakamura, N. Toksöz, R. Wiggins, J. Derr and F.
    Duennebier, Apollo 11 passive seismic experiment,
    Apollo 11 Lunar Sci. Conf., 2309, 1970c.

Latham, G.V., M. Ewing, F. Press, G. Sutton, J. Dorman,
    Y. Nakamura, N. Toksöz, R. Wiggins and R. Kovach,
    Passive seismic experiment, NASA Spec. Publ. SP-235,
    39, 1970d.

Latham, G., M. Ewing, J. Dorman, D. Lammlein, F. Press,
    N. Toksöz, G. Sutton, F. Duennebier and Y. Nakamura,
    Moonquakes, Science, 174, 687, 1971a.

Latham, G.V., M. Ewing, F. Press, G. Sutton, J. Dorman,
    Y. Nakamura, N. Toksöz, F. Duennebier and D. Lammlein,
    Passive seismic experiment, NASA Spec. Publ. SP-272,
    133, 1971b.

Latham, G., M. Ewing, J. Dorman, D. Lammlein, F. Press, N.
    Toksöz, G. Sutton, F. Duennebier and Y. Nakamura,
    Moonquakes and lunar tectonism, Moon, 4, 373, 1972a.

Latham, G.V., M. Ewing, F. Press, G. Sutton, J. Dorman,
    Y. Nakamura, N. Toksöz, D. Lammlein and F. Duennebier,
    Passive seismic experiment, NASA Spec. Publ. SP-289,
    8-1, 1972b.

Latham, G., M. Ewing, F. Press, G. Sutton, J. Dorman, Y.
    Nakamura, N. Toksöz, D. Lammlein and F. Duennebier,
    Moonquakes and lunar tectonism, Proc. Lunar Sci. Conf.
    3rd, 2519, 1972c.

Latham, G.V., M. Ewing, F. Press, G. Sutton, J. Dorman, Y.
    Nakamura, N. Toksöz, D. Lammlein and F. Duennebier,
    Passive seismic experiment, NASA Spec. Publ. SP-315,
    9-1, 1972d.

Latham, G., J. Dorman, F. Duennebier, M. Ewing, D. Lammlein and Y. Nakamura, Moonquakes, meteoroids, and the state of the lunar interior, <u>Proc. Lunar Sci. Conf. 4th</u>, 2515, 1973a.

Latham, G., M. Ewing, J. Dorman, Y. Nakamura, F. Press, N. Toksöz, G. Sutton, F. Duennebier and D. Lammlein, Lunar structure and dynamics, results from the Apollo passive seismic experiment, <u>Moon</u>, <u>7</u>, 396, 1973b.

Latham, G.V., M. Ewing, F. Press, J. Dorman, Y. Nakamura, N. Toksöz, D. Lammlein, F. Duennebier and A. Dainty, Passive seismic experiment, <u>NASA Spec. Publ. SP-330</u>, 11-1, 1973c.

Latham, G., Y. Nakamura, J. Dorman, F. Duennebier, M. Ewing and D. Lammlein, Results from the Apollo passive seismic experiment, Soviet-American Conf. on Cosmochemistry of the Moon and Planets, <u>NASA Spec. Publ. SP-370</u>, Part 1, 389, 1977.

Latham, G.V., J. Dorman, P. Horvath, A. Ibrahim, J. Koyama and Y. Nakamura, Passive seismic experiment: a summary of current status, in <u>Lunar and Plan. Sci. IX</u>, 634, 1978.

Lewis, J.S., The chemistry of the solar system, <u>Sci. Am.</u>, <u>230</u> 50, March 1974.

Longhi, J., Magma oceanography 2: Chemical evolution and crustal formation, <u>Proc. Lunar Sci. Conf. 8th</u>, 601, 1977.

Longhi, J., Pyroxene stability and the composition of the lunar magma ocean, in <u>Lunar and Plan. Sci. IX</u>, 657, 1978.

Malin, P.E. and R.A. Phinney, First order surface wave scattering solution for synthesizing lunar seismograms (abstract), in <u>Lunar and Plan. Sci. IX</u>, 688, 1978.

Mark, N. and G.H. Sutton, Lunar shear velocity structure at Apollo sites 12, 14, and 15, <u>J. Geophys. Res.</u>, <u>80</u>, 4932, 1975.

Marquardt, D.W., An algorithm for least-squares estimation of non-linear parameters, <u>J. Soc. Indust. Appl. Math.</u>, <u>11</u>, 431, 1963.

Meissner, R. and M. Lange, An approach for calculating temperatures and viscosities in terrestrial planets, <u>Proc. Lunar Sci. Conf. 8th</u>, 551, 1977.

Meissner, R., J. Voss and J.H. Kaestle, A_1 moonquakes, problems of determining their epicenters and mechanisms, Moon, 6, 292, 1973.

Metzger, A., J. Trombka, R. Reedy and J. Arnold, Element concentrations from lunar orbital gamma-ray measurements, Proc. Lunar Sci. Conf. 5th, 1067, 1974.

Michael, W.H. and W.T. Blackshear, Recent results on the mass, gravitational field and moments of inertia of the moon, Moon, 3, 388, 1972.

Minear, J.W. and C.R. Fletcher, Crystallization of a lunar magma ocean, in Lunar and Plan. Sci. IX, 741, 1978.

Minster, J.B., T.H. Jordan, P. Molnar and E. Haines, Numerical modeling of instantaneous plate tectonics, Geophys. J. R. astr. Soc., 36, 541, 1974.

Mitler, H.E., Formation of an iron-poor moon by partial capture, or: yet another exotic theory of lunar origin, Icarus, 24, 256, 1975.

Mizutani, H., H. Spetzler, I. Getting, R.J. Martin III and N. Soga, The effect of outgassing upon the closure of cracks and the strength of lunar analogues, Proc. Lunar Sci. Conf. 8th, 1235, 1977.

Montalbetti, J.F. and E. Kanasewich, Enhancement of tele-seismic body phases with a polarization filter, Geophys. J. R. astr. Soc., 21, 119, 1970.

Mueller, R.F., System $Fe-MgO-SiO_2-O_2$ with applications to terrestrial rocks and meteorites, Geochimica et Cosmochimica Acta, 29, 967, 1965.

Nakamura, Y., Seismic energy transmission in the lunar surface zone determined from signals generated by movement of lunar rovers, Bull. Seism. Soc. Am., 66, 593, 1976.

Nakamura, Y., HFT events: shallow moonquakes?, Phys. Earth Planet. Int., 14, 217, 1977a.

Nakamura, Y., Seismic energy transmission in an intensely scattering environment, J. Geophys., 43, 389, 1977b.

Nakamura, Y., A_1 moonquakes: source distribution and focal mechanism, in Lunar and Plan. Sci. IX, 796, 1978.

Nakamura, Y., D. Lammlein, G. Latham, M. Ewing, J. Dorman, F. Press and N. Toksöz, New seismic data on the state of the deep lunar interior, Science, 181, 49, 1973.

Nakamura, Y., J. Dorman, F. Duenneber, M. Ewing, D. Lammlein and G. Latham, High-frequency lunar teleseismic events, Proc. Lunar Sci. Conf. 5th, 2883, 1974a.

Nakamura, Y., G. Latham, D. Lammlein, M. Ewing, F. Duennebier and J. Dorman, Deep lunar interior inferred from recent seismic data, Geophys. Res. Lett., 1, 137, 1974b.

Nakamura, Y., J. Dorman, F. Duennebier, D. Lammlein and G.V. Latham, Shallow lunar structure determined from the passive seismic experiment, Moon, 13, 57, 1975.

Nakamura, Y., F. Duennebier, G.V. Latham and J. Dorman, Structure of the lunar mantle, J. Geophys. Res., 81, 4818, 1976a.

Nakamura, Y., G.V. Latham, J. Dorman and F. Duennebier, Seismic structure of the moon: a summary of current status, Proc. Lunar Sci. Conf. 7th, 3113, 1976b.

Nakamura, Y., G.V. Latham, J. Dorman, P. Horvath and A. Ibrahim, Seismic indication of broad-scale lateral heterogeneities in the lunar interior: a preliminary report, Proc. Lunar Sci. Conf. 8th, 487, 1977.

Nuttli, O., The effect of the earth's surface on S wave particle motion. Bull. Seism. Soc. Am., 51, 237, 1961.

Nyland, E. and E.J. Roebroek, Bounds on the P velocity for the whole moon, Nature, 253, 179, 1975.

Oberli, F., M.T. McCulloch, F. Tera, D.A. Papanastassiou and G.J. Wasserburg, Early lunar differentiation constraints from U-Th-Pb, Sm-Nd, and Rb-Sr model ages, in Lunar and Plan. Sci. IX, 832, 1978.

O'Keefe, J.A., III, The formation of the moon, Moon, 9, 219, 1974.

Olhoeft, G.R., A.L. Frisillo, D.W. Strangway and H. Sharpe, Temperature dependence of electrical conductivity and lunar temperatures, Moon, 9, 79, 1974.

Palme, H. and H. Wänke, A unified trace-element model for the evolution of the lunar crust and mantle, Proc. Lunar Sci. Conf. 6th, 1179, 1975.

Papike, J.J., F.N. Hodges, A.E. Bence, M. Cameron and J.M. Rhodes, Mare basalts: crystal chemistry, mineralogy, and petrology, _Rev. Geophys. Space Phys._, _14_, 475, 1976.

Parkin, C.W., P. Dyal and W.D. Daily, Iron abundance in the moon from magnetometer measurements, _Proc. Lunar Sci. Conf. 4th_, 2947, 1973.

Pines, P.J., Model seismic studies of intensely scattering media, M.Sc. Thesis, M.I.T., 1973.

Piwinskii, A.J. and A.G. Duba, Feldspar electrical conductivity and the lunar interior, _Proc. Lunar Sci. Conf. 6th_, 2899, 1975.

Press, F., Regionalized earth models, _J. Geophys. Res._, _75_, 6575, 1970.

Richter, C.F., _Elementary Seismology_, W.H. Freeman and Co., San Francisco, 1958.

Ringwood, A.E., Limits on the bulk composition of the moon, _Icarus_, _28_, 325, 1976.

Ringwood, A.E., Basaltic magmatism and the bulk composition of the moon, I., major and heat-producing elements, _Moon_, _16_, 389, 1977.

Ringwood, A.E., Origin of the moon, in _Lunar and Plan. Sci. IX_, 961, 1978.

Ringwood, A.E. and S.E. Kesson, Basaltic magmatism and the bulk composition of the moon, II. siderophile and volatile elements in Moon, Earth and Chondrites: implications for lunar origin, _Moon_, _16_, 425, 1977a.

Ringwood, A.E. and S.E. Kesson, Composition and origin of the moon, _Proc. Lunar Sci. Conf. 8th_, 371, 1977b.

Runcorn, S.K., On the origin of mascons and moonquakes, _Proc. Lunar Sci. Conf. 5th_, 3115, 1974.

Runcorn, S.K., Solid-state convection and the mechanics of the moon, _Proc. Lunar Sci. Conf. 6th_, 2943, 1975.

Runcorn, S.K., Physical processes involved in recent activity within the moon, _Phys. Earth Planet. Int._, _14_, 330, 1977.

Ryder, G. and J. Wood, Serenitatis and Imbrium impact melts: implications for large-scale layering in the lunar crust, Proc. Lunar Sci. Conf. 8th, 655, 1977.

Schreiber, E., The moon and Q, Proc. Lunar Sci. Conf. 8th, 1201, 1977.

Schultz, P.H. and D.E. Gault, Seismically induced modification of lunar surface features, Proc. Lunar Sci. Conf. 5th, 2845, 1975.

Schwerer, F.C., G.P. Huffman, R.M. Fisher and T. Nagata, Electrical conductivity of lunar surface rocks: Laboratory measurements and implications for lunar interior temperatures, Proc. Lunar Sci. Conf. 5th, 2673, 1974.

Shih, C. and E. Schonfeld, Mare basalt genesis: a cumulate-remelting model, Proc. Lunar Sci. Conf. 7th, 1757, 1976.

Shimshoni, M. and S.W. Smith, Seismic signal enhancement with three-component detectors, Geophysics, 29, 664, 1964.

Simmons, G., T. Todd and H. Wang, The 25-km discontinuity: implications for lunar history, Science, 182, 158, 1973.

Singer, S.F., Origin of the moon by tidal capture and some geophysical consequences, Moon, 5, 206, 1972.

Sjogren, W. and J. Smith, Quantitative mass distribution models for Mare Orientale, Proc. Lunar Sci. Conf. 7th, 2639, 1976.

Smith, J.C., W. Banerdt, C. Sammis and S. Alexander, Tidal stress concentrations in a laterally heterogeneous moon (abstract), in Lunar Science VIII, 879, 1977.

Smith, J.V., Possible controls on the bulk composition of the earth: implications for the origin of the earth and the moon, Proc. Lunar Sci. Conf. 8th, 333, 1977.

Solomon, S.C., Density within the moon and implications for lunar composition, Moon, 9, 147, 1974.

Solomon, S.C., Mare volcanism and lunar crustal structure, Proc. Lunar Sci. Conf. 6th, 1021, 1975.

Solomon, S.C., The relationship between crustal tectonics and internal evolution in the moon and Mercury, Phys. Earth Planet. Int., 15, 135, 1977.

Solomon, S.C. and J.Chaiken, Thermal expansion and thermal stress in the moon and terrestrial planets: clues to early thermal history, Proc. Lunar Sci. Conf. 7th, 3229, 1976.

Solomon, S.C. and J. Longhi, Magma oceanography: 1. Thermal evolution, Proc. Lunar Sci. Conf. 8th, 583, 1977.

Solomon, S.C. and M.N. Toksöz, Lateral variation of attenuation of P and S waves beneath the United States, Bull. Seism. Soc. Am., 60, 819, 1970.

Solomon, S.C. and M.N. Toksöz, Internal constitution and evolution of the moon, Phys. Earth Planet. Int., 7, 15, 1973.

Sonnet, C.P. and S.K. Runcorn, Electromagnetic evidence concerning the lunar interior and its evolution, Moon, 8, 308, 1973.

Steg, R.G. and P.G. Klemens, Scattering of Rayleigh waves by surface irregularities, Phys. Rev. Lett., 24, 381, 1970.

Strangway, D.W. and H.N. Sharpe, A model of lunar evolution, Moon, 12, 369, 1975.

Strobach, K., Scattering of seismic waves and lunar seismograms, Z. Geophys., 36, 643, 1970.

Sutton, G.H. and G.V. Latham, Analysis of a feedback-controlled seismometer, J. Geophys. Res., 69, 3865, 1964.

Talwani, P., A. Nur and R.L. Kovach, Implications of elastic wave velocities for Apollo 17 rock powders, Proc. Lunar Sci. Conf. 5th, 2919, 1974.

Taylor, S.R., Geochemical evolution of the moon: Th, U, and K abundances: depth of initial melting and pre-accretion element fractionation, in Lunar and Plan. Sci. IX, 1152, 1978.

Taylor, S.R. and A.E. Bence, Evolution of the lunar highland crust, Proc. Lunar Sci. Conf. 6th, 1121, 1975.

Taylor, S.R. and P. Jakes, The geochemical evolution of the moon, Proc. Lunar Sci. Conf. 5th, 1287, 1974.

Taylor, S.R. and P. Jakes, Geochemical evolution of the moon revisited, Proc. Lunar Sci. Conf. 8th, 433, 1977.

Thurber, C.H. and S.C. Solomon, An assessment of crustal thickness variations on the lunar near side: models, uncertainties, and implications for crustal differentiation, in Lunar and Plan.Sci. IX, 1169, 1978.

Tittman, B.R., L. Ahlberg and J. Curnow, Internal friction and velocity measurements, Proc. Lunar Sci. Conf. 7th, 3123, 1976.

Tittman, B.R., L. Ahlberg, H. Nadler, J. Curnow, T. Smith and E.R. Cohen, Internal friction quality-factor Q under confining pressure, Proc. Lunar Sci. Conf. 8th, 1209, 1977.

Tittman, B.R., H. Nadler, J. Curnow and J.M. Richardson, Internal friction and modulus measurements in lunar and lunar analogue rocks, in Lunar and Plan. Sci. IX, 1172, 1978.

Todd, T., H. Wang, W.S. Baldridge and G. Simmons, Elastic properties of Apollo 14 and 15 rocks, Proc. Lunar Sci. Conf. 3rd, 2577, 1972.

Todd, T., D.A. Richter, G. Simmons and H. Wang, Unique characterization of lunar samples by physical properties, Proc. Lunar Sci. Conf. 4th, 2639, 1973.

Toksöz, M.N., Geophysical data and the interior of the moon, Ann. Rev. Earth Plan. Sci., 2, 151, 1974.

Toksöz, M.N., Lunar and planetary seismology, Rev. Geophys. Space Phys., 13, 306, 1975.

Toksöz, M.N. and S.C. Solomon, Thermal history and evolution of the moon, Moon, 7, 251, 1973.

Toksöz, M.N., M.A. Chinnery and D.L. Anderson, Inhomogeneities in the earth's mantle, Geophys. J. R. astr. Soc., 13, 31, 1967.

Toksöz, M.N., F. Press, K. Anderson, A. Dainty, G. Latham, M. Ewing, J. Dorman, D. Lammlein, Y. Nakamura, G. Sutton and F. Duennebier, Velocity structure and properties of the lunar crust, Moon, 4, 490, 1972a.

Toksöz, M.N., F. Press, K. Anderson, A. Dainty, G. Latham, M. Ewing, J. Dorman, D. Lammlein, G. Sutton, F. Duennebier and Y. Nakamura, Lunar crust: structure and composition, Science, 176, 1012, 1972b.

Toksöz, M.N., F. Press, A. Dainty, K. Anderson, G. Latham, M. Ewing, J. Dorman, D. Lammlein, G. Sutton and F. Duennebier, Structure, composition and properties of the lunar crust, Proc. Lunar Sci. Conf. 3rd, 2527, 1972c.

Toksöz, M.N., S.C. Solomon, J.W. Minear and D.H. Johnston, Thermal evolution of the moon, Moon, 4, 190, 1972d.

Toksöz, M.N., A. Dainty, S.C. Solomon and K. Anderson, Velocity structure and evolution of the moon, Proc. Lunar Sci. Conf. 4th, 2529, 1973.

Toksöz, M.N., A.M. Dainty, S.C. Solomon and K. Anderson, Structure of the moon, Rev. Geophys. Space Phys., 12, 539, 1974a.

Toksöz, M.N., F. Press, A. Dainty and K. Anderson, Lunar velocity structure and compositional and thermal inferences, Moon, 9, 31, 1974b.

Toksöz, M.N., N.R. Goins and C.H. Cheng, Moonquakes: mechanisms and relation to tidal stresses, Science, 196, 979, 1977.

Toksöz, M.N., A.T. Hsui and D.H. Johnston, Thermal evolutions of the terrestrial planets, Moon, in press, 1978.

Trice, R., N. Warren and O. Anderson, Rock elastic properties and near-surface structure at Taurus-Littrow, Proc. Lunar Sci. Conf. 5th, 2903, 1974.

Turcotte, D.L., A.T. Hsui and K.E. Torrance, Thermal structure of the moon, J. Geophys. Res., 77, 6931, 1972.

Turner, G., The first 100 millions years, Geophys. J. R. astr. Soc., 49, 302, 1977.

Vanyan, L.L. and I.V. Egorov, The lunar lithosphere from electromagnetic sounding data, Moon, 17, 3, 1977.

Vermillion, R.E., On the center-of-mass offset of the moon, Am. J. Phys., 44, 1014, 1976.

Voss, J., W. Weinrebe, F. Schildknecht and R. Meissner, Filter processes applied to the scattering parts of lunar seismograms for identifying the 300 km discontinuity and the lunar grid system, Proc. Lunar Sci. Conf. 7th, 3133, 1976.

Walker, D., J. Longhi and J.F. Hays, Differentiation of a very thick magma body and implications for the source regions of mare basalts, Proc. Lunar Sci. Conf. 6th, 1103, 1975.

Warren, N., Q. and structure, Moon, 4, 430, 1972.

Warren, N., R. Trice, N. Soga and O.L. Anderson, Rock physics properties of some lunar samples, Proc. Lunar Sci. Conf. 4th, 2611, 1973.

Watkins, J.S. and R.L. Kovach, Seismic investigation of the lunar regolith, Proc. Lunar Sci. Conf. 4th, 2561, 1973.

Wesley, J.P., Di-fusion of seismic energy in the near range, J. Geophys. Res., 70, 5099, 1965.

Wiggins, R.A., The general linear inverse problem: implication of surface waves and free oscillations for earth structure, Rev. Geophys. Space Phys., 10, 251, 1972.

Wiskerchen, M.J. and C.P. Sonett, A lunar metal core?, Proc. Lunar Sci. Conf. 8th, 515, 1977.

Wood, J.A., Thermal history and early magmatism in the moon, Icarus, 16, 229, 1972.

Wood, J.A., Lunar petrogenesis in a well-stirred magma ocean, Proc. Lunar Sci. Conf. 6th, 1087, 1975.

APPENDIX 1

DATA PROCESSING

A1.1. General Considerations

The purpose of this appendix is to describe and list the data used in this thesis, culminating in the direct P and S wave arrival times shown in Tables 1-4 thru 1-6, and the seismograms included herein. The justification for and overview of the procedures used in this appendix are discussed in Chapter 1 (and Appendix 3).

The lunar seismic data are originally received at Galveston in the form of day tapes, containing 24 hours of digital data from one seismic station, four 2400 ft. tapes per day, or more than 10,000 tapes for the eight-year ALSEP net operation. The data are plotted on a compressed time scale and all seismic events logged. From these, event tapes containing only seismic events are made, averaging about 9 days of data from one station per tape. Generally 20-30 minutes of data from each event are put on the event tapes beginning ten minutes before the earliest observable signal. These tapes are regularly sent to MIT with catalogues listing their contents. To date event tapes through Day 50, 1976 have been received and catalogues through Day 90, 1975 are on hand. The major events occurring after these times up to the

network shutdown time are contained in special event
tapes and listings that are sent by Galveston shortly
after receiving such an event, so the data set at MIT
is essentially complete insofar as structural analyses
are concerned.

. In addition, compendium tapes are made which contain
groups of the largest events. For example, the largest
meteorite impacts are on a series of six tapes per station,
and the HFT's are all on one tape per station. Unfortunate-
ly, more than half of these tapes seem to be unreadable
(terminal tape read errors) at the MIT computer facility,
possibly because refurbished NSSDC tapes are used at
Galveston. In any case, these have been of limited use,
and by and large it was necessary to extract each event
from the event tapes which, due to the small number of
days of data per tape rarely contained more than one
event of interest. Thus effectively every event of
interest necessitated the reading of four event tapes.

The tape format is standardized, beginning with two
header records. The data from all instruments at a station
is multiplexed as a function of time, stored in logical
records, 90 logical records per physical record, physical
record length 1823 words. The ALSEP 12 record length is
only 912 words, because the defunct SP (short-period)

seismometer does not produce data. Each physical record
contains about 54 seconds of data; LP (long-period)
digitized at about 0.2 second intervals and SP (short period) at
0.025 seconds. These tapes are read and decoded at MIT using
program SCNLP, written by Ralph Wiggins and rewritten and
modified by Ken Anderson, Anton Dainty, and this author.
The program searches through an ALSEP tape for the
requested data, specified by year, day, hour, minute, and
second, and cracks out the required components (LP or SP).
Many sections of data, ordered chronologically, can be
read from the same tape if desired but to obtain the SP
and LP data from the same time segment requires two runs.
SCNLP is most commonly used to transfer the decoded data
to disc. The disc can hold about 6.8×10^6 data points,
or 500 15-minute 3-component LP records. The catalogue
has 600+ available entries. Thus a great number of
seismograms can be stored and randomly accessed on a
single device, greatly increasing the data accessibility
and allowing further computer processing.

The data on disc is read using program MASSAG, a
generalized data processor. Again the desired time
segment is selected, and options include deleting data
on disc (actually just the catalogue entry), removing
data spikes, removing the mean, scaling, tapering the
ends of the data, rotating horizontal components,

frequency filtering, polarization filtering, and plotting any resulting data from the above operations. Anton Dainty and Ken Anderson are the principle authors of this program. In the work described below MASSAG was primarily used only for plotting; special-purpose programs were written for the other data manipulation tasks in order to achieve greater efficiency than is possible in a generalized program.

As mentioned in Chapter 1, a fraction of the LP seismic data used in this thesis was actually recorded in the broad-band response mode, reducing the maximum sensitivity and widening the frequency response to include long-period (2-50 sec) energy. At periods longer than about 30 seconds, there is a large amount of energy that is continuously present on the lunar records; it does not correlate with the onset of seismic events. It is unclear whether this energy originates in the instrument itself or is actually present in the ground motion; further discussion is included in Chapter 4. In most of the data analysis procedures discussed below, it is best to eliminate this long-period "noise" making the short-period onsets more clearly observable. This is done with subroutines BNDPAS, PLYDV2, and BNDPS2 which design and implement a Chebyshev low-pass auto-regressive

frequency filter. The programs were authored by Ralph Wiggins. The application of a high-pass filter to the data was accomplished by first applying the low-pass and subtracting the result from the original data. In general the cutoff period was 10 seconds; typically a filter length of 5 and a ripple (allowable deviation from flat response) of 0.01 was used, giving about an order of magnitude drop-off at 20 seconds and two orders of magnitude at 30 seconds.

In addition to the event tapes and catalogues, microfilm copies of the seismic records from selected events are available at MIT. Specifically, all HFT events and the larger meteorite impacts are on microfilm in both compressed-time and expanded playout form. The difficulty involved in using the microfilm records is that the vertical scaling factor is constant so that the larger events saturate the plots and make the identification of S arrivals impossible. Accordingly, they were used only for preliminary scanning and arrival time measurement designed to learn the data characteristics, and to make a few final arrival time measurements when the corresponding event tapes were found to contain terminal tape read errors, precluding computer replotting of the data.

A1..2 Meteorite Impact Data

The initial selection criterion of at least 10 du
(5 mm Galveston amplitude as listed in the catalogue)
produced a total of 33 events, listed in Table A1-1,
excluding ones listed as containing timing errors on the
seismograms (only about five smaller events). The start
times are those given in the catalogues, representing the
approximate time of the earliest visible phase. The
records from all these events except the last three are
on microfilm, and they were examined to determine which of
the events produced enough observable arrivals to meet
the triangulation and minimum number of picks requirement
(in this case, at least four arrivals spread over the
network triangle). The last three events were transferred
from tape to disc and then plotted for examination.

Eight events survived this final culling, as listed
in Table A1-2. In order to ensure that a sufficient length
of seismogram was available for this work and possible
later studies, 25 minutes of both LP and SP records at
all four stations from the eight events were transferred
from tape to disc. The three-component LP data is on disc
234055 (LUNSEISK), while the SPZ data is on disc 234046
(LUNSEISJ). The beginning and ending times of the data
are listed in Table A1-2; they are the same for both data

types and all stations for a given event, with the exception of Day 199 ALSEP 14 whose start time is at second 6 rather than 1. The start times were chosen to be close to initial estimates of the event origin times. The records not on disc (Table A1-3) excluding the short-period traces at ALSEP 12 (instrument not operational), are 1) Day 25, ALSEP 14 (LP and SP) due to temporary instrument malfunction when no data was received and 2) Day 124, ALSEP 14 (SP) and ALSEP 16 (LP and SP) due to terminal tape read errors. Thus a total of 30 three-component LP records and 21 SPZ records were put onto disc, necessitating about 40 computer runs costing roughly $30 each on an average.

Assuming reasonable seismic velocities, the maximum S-P time difference for a surface event is about six or seven minutes. This would be for an event 180° away from a seismic station. The maximum travel time across the ALSEP array occurs for an event next to one of the stations, and is about five minutes for the direct S wave. Since these cases cannot occur simultaneously, a comfortable overestimate for the maximum time difference between first P and last S is 12 minutes. Accordingly 15 minutes of each record on disc was processed, beginning about three minutes before the earliest onset at any station. Thus direct P and S will be included on every

record as well as at least several minutes after S to allow the observation of secondary phases. Processing only 15 of the 25 minutes of data on disc saves a large amount of computation time and if it had been necessary to examine more data it was easily available. The data sections that were used extend from three minutes before to 12 minutes after the reference times listed in Table A1-2 (and 1-4) which represents roughly the time of the earliest observable arrival.

Initially, small-scale plots as shown in Figs. A1-1a thru A1-1h were made in order to have a complete picture of the records available at a given focus. Events which were recorded in the broad-band response mode were passed through a high-pass frequency filter as described above; a list of the records requiring filtering is given in Table A1-3. The P and S arrivals marked are the final ones listed in Table 1-4; the initial versions of these plots naturally were not so marked. The vertical scale is 120 du between component traces at any station; the great variation in amplitudes is clear (compare Day 134 with Day 324). In addition, the SP records were plotted at a scale of 2 in/min, or 30 inches per 15-minute record. This is about the maximum length that permits convenient handling, and picks are measurable to within about 0.2 or 0.3 seconds, using a ruler marked in sixtieths of an inch,

so that one division is 0.5 seconds. Photographically reduced versions of these plots are shown in Figs. Al-5a thru Al-5h. In each case the top trace, when present, is the SP record at ALSEP 14. The middle trace is ALSEP 15, and the bottom ALSEP 16. The vertical scale is about 217 du between traces, except for Day 134 which is plotted at 4333 du between traces due to the large amplitudes. The final P and S wave arrival times are as marked.

Initial arrival time measurements were made on the microfilm records, supplemented by selected SP plots and expanded LP plots of the data on disc as necessary. The arrival times were nearly all those of the direct P waves. From these, preliminary event locations were determined, using the techniques described in Appendix 4. Armed with these locations, it was then possible to further process the LP seismograms on disc, using the program described in Appendix 3. First, each trace at each station was automatically scaled to a common average amplitude, pre-applying the frequency filter as necessary. The horizontal components were then rotated from the original X and Y directions to radial and transverse relative to the preliminary epicenter. These scaled, rotated records were stored on disc (LUNSEISK) and plotted as Figs. Al-2a thru Al-2h. The vertical scale is now 16 du between component traces. These are now scaled du; the scaling

factors are given in Tables A3-1. These records are
equivalent to the raw seismograms but are easier to use
and plot due to the uniform scaling. Figs. Al-3a thru
Al-3h show amplified versions (vertical scale 4 du between
traces) of the first seven minutes of the scaled records
so that the initial P arrival is easier to see (for a few
of the larger events, it is better to use the raw plots,
Al-la thru Al-hl). Finally, the scaled traces were
polarization filtered and stored on disc (LUNSEISK),
producing the records shown as Figs. Al-4a thru Al-4h.
The vertical scale is 8 du between traces, half that of
regular scaled plots because the polarization filter
eliminates a great deal of energy. The filter could not
be applied to several records because not all three
components of ground motion were present, as is often
true at ALSEP 14 because of the poor functioning of the LP
vertical seismometer. The non-filtered records are
listed in Table Al-3.

In order to accurately measure the arrival times,
expanded plots of these last two data sets were made
using MASSAG. First, the scaled and rotated records were
plotted from two minutes before the reference time to five
minutes after, in order to observe the P arrival. The
scales were 2 in/min and 10 du/in. Second, all 15

minutes of the polarization-filtered records were plotted
at scales of 2 in/min and 5 du/in. The P picks are
measured primarily on the SP records, the LP scaled
vertical components, and the LP filtered vertical
components, since a vertically-arriving wave should
produce P energy primarily on the vertical components.
Correspondingly, the S arrivals are located roughly by
the SP envelopes when possible to take advantage of the
shorter rise times, and then measured on the filtered
horizontal components with confirmation on the small-scale
raw and scaled plots. These schemes insure that each pick
is compatible with all the appropriate information.

As discussed in Chapter 1, the above procedure
generally produced several possible arrival time sets for
each event. Once obvious inconsistencies were eliminated,
the rest were compared by using each to locate the event
and observing the relative squared arrival time residuals.
As described in Appendix 4, nine velocity models were
used. The upper mantle velocities were varied (Vp = 7.5,
7.8, 8.1, Vs = 4.4, 4.4, 4.7) while the crustal structure
and lower mantle velocities (Vp = 7.5, Vs = 4.1) were held
constant (all values in km/sec). The upper-lower mantle
boundary was placed at 520 km depth. This type of
structure is appropriate because most surface event rays
bottom above 500 km assuming a constant velocity below

the crust, and so the upper mantle velocities dominate the surface event travel times. Furthermore, previous work has suggested the existence of a shear wave shadow zone beginning at 90°; most of the above models predict such a zone because of the velocity drop at 520 km. Each arrival time set was then used to find a best event location for each velocity structure, and the locations and residuals are printed in a grid map. Examples are given in Appendix 4.

It is impossible to recount in a reasonable space all the factors that were considered in selecting among the various pick alternatives. The methodology outlined in Chapter 1 was rigidly adhered to, and in the following paragraphs the major points in choosing each set of "best" arrival times will be discussed. Emphasis will be placed primarily on the analysis of the residual grids and the final selection procedures, since this is where the most judgment is required. In addition, pertinent descriptions of the seismograms are included, and for each focus the final picks that are considered less well-observed (LWO) than usual will be listed. Thus the end result will be the primary data set, as well as a "most confident" data set with far fewer but possibly more reliable picks. All seismograms referred to are in Figs. A1-1 thru A1-5 as

discussed above; they will not be explicitly referenced
further. The final picks are marked on the plots;
computer generated symbols are accurate only to 0.5 seconds.
The arrival times referred to below are all relative to the
reference times given in Tables 1-4; the year of each event
is also listed therein.

Day 134: The only uncertain pick is 12S; the three
possibilities are 60.2, 62.7, and 69.7 seconds. The
residual grid indicates that the first two are very
comparable, with minimum residuals of 1 or 2 sec^2 at
intermediate velocities. The third pick produces
somewhat larger residuals, around 10-20 sec^2, and
seems to want very low upper mantle velocities (7.5 and
4.1 km/sec); as a result it was eliminated. Of the
remaining two, the 62.7 pick seems best when viewed on
the scaled plot (Fig. A1-9), while the filtered records
are inconclusive. The location and residual differences
are small, so the 62.7 value was chosen for the final data
set. LWO picks: none.

Day 199: There were two alternative P picks and one
weak possible S pick at both stations 15 and 16 (15 P =
-13.7, -6.2; 15 S = 242.0, 16 P = 16.7, 28.9; 16 S = 278.8).
First the four combinations of P picks were run, without
any S picks. The residuals were all reasonable and
similar, around 70 sec^2. Upon examination of the scaled

vertical LP records the earlier pick was chosen in both cases, because they appear slightly more convincing and probably represent the true first arrival. Then the S picks were tried singly and together. In each case the residuals jumped to 350 sec^2 and since the arrivals were considered weak originally, they were eliminated. LWO; none.

Day 213: Three possible P picks at station 16 were measured (132.5, 139.5, 162.8) due to the noisy character of the record caused by intermittent leveling. The last option produced residuals on the order of 10 sec^2; i.e. the data were very inconsistent. The other two produced comparable grids with residual values around 50 sec^2; it was decided that the middle value was fractionally more convincing on the seismograms. The 12 S pick was considered weak when it was measured, but when it was included the residuals increased only fractionally and so it was retained in the final data set. LWO: 12 S. (Note that the 15 P pick may appear early; it is constrained by the SP plot.)

Day 324: The four P arrivals are well-constrained, but due to an irretrievable data error on tape, there is a data gap at the time of the 12 P arrival. That pick was measured on microfilm. There were two possible S arrivals, a good one at station 12 (284.2) and a poorer one at station 15 (139.0). The residuals remained small

($\sim$1 sec^2) when the 12 S pick was included, but grew larger ($\sim$20) when the weak 15 S was used. Accordingly, the 15 S pick was rejected. LWO: 12 S.

Day 102: The 12 P pick was considered uncertain; grids run with and without it showed nearly identical residuals ($\sim$7 sec^2) and preferred reasonable velocities; and so it was retained. Two S arrivals were observed; a good 12 S and a slightly weaker 16 S. These were accomodated easily with no degradation in residual values. LWO: 14 P and 15 S. (The 14 P is particularly weak.)

Day 124: The only option at this focus was a weak 15 S pick. The event was located using the four P arrivals with and without the 15 S value. The residuals remained about the same, around 6 sec^2, and so it was included. Note that the ALSEP 16 record is missing due to terminal tape error; the picks were measured on microfilm. LWO: 15 S.

Day 25: Station 14 was not operational during this period. Pick options were available at station 12 (S: 133.5, 140.9) and station 16 (P: 110.7, 115.7). The later picks in both cases produced higher residuals, and so the earlier ones were used. LWO: none.

Day 107: The P picks are well-constrained. There are

possible S picks at station 14 (157.9, 194.5). The
residuals from both are reasonable, but the best locations
are significantly different. In view of the excellent-
quality P arrivals, the very emergent character of the
14 records (especially the radial component), and the
large possible variation in the true arrival time, this
pick was omitted altogether. LWO: none.

The final data set is listed in Table 1-4. The
"most-confident" data set is given in Table Al-4.

Al.3   HFT Event Data

The steps involved in processing the HFT's are very
similar to those used for meteorite impacts; the reader is
referred to Al.2 for more complete discussions than those
in this section.

There are a total of 27 HFT events identified to date;
22 of these have measurable amplitudes at a triangle of
stations, as listed in Table Al-5. All of these twenty-two
events were examined for measurable picks; 17 on microfilm
and 5 on plots made from special tapes copied onto disc.
In several instances additional plots were made of the
events that are on microfilm in order to optimize the time
and amplitude scales for measuring arrivals. Every effort
was made to find as many useful HFT events as possible.

As a result, eight events met the final criteria of at
least four measurable arrivals at a triangle of stations,
as listed in Table A1-6. Again, 25 minutes of data from
each event was transferred from tape to disc as for
meteorite impacts. The start and stop times are in
Table A1-6. Day 72 ALSEP 16 has a start time at second
16; all the other times represent all four stations. As
listed in Table A1-7, the records from station 14 for Day
44 are not on disc due to terminal tape read errors. In
addition of course no ALSEP 12 SP records are available.
Thus 31 LP and 23 SP seismograms were placed on disc.
The records received in the LP broadband response mode
are also listed, along with the stations where the lack of
three-component LP data precluded polarization filtering.

As for meteorite impact data, 15 minutes of data were
processed, beginning three minutes before the reference
time in Table A1-6. Reduced-scale plots of the three-
component LP data were made, as shown in Figs. A1-6a thru
A1-6h. Frequency-filtering was applied as necessary; the
vertical scale is 120 du between traces. Figs. A1-10a thru
A1-10h show the corresponding SP records. As for meteorite
impacts, the traces are those from stations 14, 15, and 16,
in order from the top. However, due to the great
variability in HFT event size and distance and the large

amounts of high-frequency energy produced, it was necessary to change the vertical scale from trace to trace. Table Al-8 gives the number of du between traces for each record. All P and S arrival times marked are the final picks as given in Table 1-5.

Arrival time measurements were first made on microfilm records and selected expanded-plot SP and LP seismograms from disc. After initial location of the events, the LP records were scaled, rotated, and polarization filtered (Appendix 3). Figs. Al-7a thru Al-7h show the scaled and rotated seismograms while Figs. Al-8a thru Al-8h contain the filtered records. In order to better illustrate the P arrivals, expanded versions of the first part of the scaled traces are shown in Figs. Al-9a thru Al-9h. The vertical scales in Figs. Al-7, 8, 9, are 16 du, 8 du, and 6 du between component traces, respectively. All traces are stored on disc as described for meteorite impacts.

Final arrival time measurements were made on expanded versions of the above records. P picks were measured on the LP scaled records (2 in/min; 5 du/in) the SP traces (2 in/min; average 114 du/in), and confirmed on the LP filtered records (2 in/min; 3 du/in). The S arrivals were measured primarily on the LP filtered

records after locating the shear wave envelope on the SP traces, and then confirmed on the LP raw and scaled reduced plots (Figs. A1-6 and 7). Thus all picks are based on the maximum amount of information available, and were measured at appropriate scales to ensure that small first arrivals were not overlooked and that an accuracy of 0.2-0.3 seconds was maintained.

As in the previous section, the following paragraphs will discuss the significant decisions made in the pick selection process. The velocity models used in calculating location and residual grids for each arrival time data set are the same as used for meteorite impact events. Less-well-observed picks are as noted. (Reference times for picks and year of each event given in Table 1-5).

Day 72: This event was the most difficult to analyze, and so it correspondingly received more attention. Of the P picks, the only uncertainty was at station 15. The pick used (99.7) was preferred, but a slightly earlier pick (93.2) was an outside possibility. The residuals favored the later pick and so it was chosen. The location, based on these arrivals, is on the farside down near the south pole (small residuals), about 100° away from stations 12, 14, and 16, and 130° away from station 15. There are also good S arrivals at stations 12, 14, and 16; unambiguous picks

were made at stations 12 and 16, but not at ALSEP 14 because 1) no polarization-filtered record was available, 2) the S arrival was only visible on the radial component of ground motion and experience indicates that often the initial S onset is seen primarily on the transverse trace (c.f. Al-2a, station 15; Al-7b, station 14), and 3) the ALSEP 12 and 14 arrivals are partially redundant. Now, as discussed in Chapter 3, there is considerable evidence, even prior to this work, for a shear wave shadow zone beginning at 90° distance. This distance is relatively independent of the velocity model chosen for the lunar interior. Unfortunately, that means that the well-observed S waves at stations 12, 14, and 16 should not in fact be there. Furthermore, the S picks cannot be used by the grid location program except when there is no velocity drop across the upper-lower mantle boundary. Since S-P times are the strongest constraint on epicentral distance, it was decided to locate the Day 72 event with a program (kindly provided by Dr. Anton Dainty) that uses an entered travel time curve rather than calculating theoretical travel times from a velocity model. The input travel time curve was typical of the models discussed in Chapter 3, except that interpolated values were given to

cover the shadow zone region. The result was that, when the S arrival times were included, the epicenter moved about 10° closer to the ALSEP array, with still quite reasonable residuals. This result indicates that 1) the S-P interval, when available, is in fact important in determining epicentral distance, especially for the farther events, and 2) the Day 72 event is located near the edge of the observed shadow zone, and so care is needed in using location programs that may stumble into the theoretical shadow zone during a location search or iteration. This latter issue is discussed in Chapter 3. The important point for this section is that the observed S arrivals are in agreement with the shadow zone location obtained from other events, and a consistent location can be found. LWO: none.

Day 171: The only options available for this event were the S arrivals at stations 14 and 16. A possible 14 S pick was not used because the two horizontal traces do not agree as to the arrival time and no polarization filtered plot is available to reconcile the difference. The 16 S pick was considered very weak, and locations were made with and without it. Its inclusion did not degrade the residual map, and so it was retained. LWO: 16 S.

Day 192: Two options were available for the 12 P pick

(66.5, 78.5). The residuals for the earlier choice (150 sec^2) were significantly larger than for the later pick (14 sec^2) and so the later option was chosen. The 15 P arrival is best seen on the SP record; it is consistent with but unmeasurable on the LP records. The 14 P pick is well-constrained on the SP record; it could also be seen clearly on the Y-component on the LP raw plot (A1-6c) if the trace were enlarged. The scaled, rotated ALSEP 14 records are not useful because a noise pulse on the X component at the P arrival time contaminates both horizontal components. No S arrivals were used although some suggestive envelopes can be seen; no discrete picks are observed. LWO: 15 P is considered weak because the primary evidence for the arrival is on the SP record. Without this pick, the triangulation criterion is no longer met and so the entire event was excluded from the "most-confident" data set.

Day 3: There were two options for the 16 P pick (127.5, 135.2). Both were seen on the SP and LP vertical records. (The LP vertical is off-scale due to long-period noise.) The grid residuals were comparable, and so the earlier one was chosen on the grounds that it was the earliest reasonable pick. The 15 P pick is weak; it can be seen somewhat on the SP record but the LP traces contain a

·noise pulse at the apparent P arrival time. Nevertheless
the pick was used because a) the LP noise pulse is only
about 8 seconds wide and it is clear that the P wave
onset occurs somewhere therein and b) if the pick were
thrown out, the event would be unusable. Two S picks
were measured and included on a trial basis; they did
not degrade the residual grid and so were included.
LWO: 12 S, 15 P; thus the entire event was excluded
from the "most-confident" group.

Day 44: the ALSEP 14 records are missing due to tape
problems; P and S picks were made on microfilm records and
are reasonably well-observed. The 15 P pick is weak, but
is based on the SP vertical and LP horizontal records.
16 P is similarly weak; some evidence exists on the LP and
SP vertical records. Although an S envelope is visible at
ALSEP 12, no distinct pick is possible. Two options were
available for 16 S (168.3, 197.0). They were tried
alternately with the other picks (16 P was omitted when
the earlier pick was run due to relative incompatibility).
The grid values (130 sec^2 vs. 20 sec^2) clearly favored the
later choice. LWO: most picks from this event are weaker
than usual; the event was included in the final data set
only because the six picks as initially measured were
consistent and produced reasonable residuals and location

maps. The entire event was excluded in the most-confident
data set.

Day 4: the 15 P and 16 P picks are primarily seen on
the SP records; they are both weak. 14 S is also weak
because polarization filtered records are not available.
There were two options for 15 S; 78.3 and 82.0 sec. The
latter is favored by the polarization-filtered records;
the former is a possible early pick on the scaled
seismograms. The residual grids are comparable (10 sec^2),
but the later pick was chosen because the polarization
filtered traces are perhaps more reliable. In any case
the two picks are not significantly different. LWO: the
entire focus.

Day 66: the 12 P pick was considered weak although it
is reasonably well-observed on the LP filtered records.
Its inclusion did not degrade the residual maps. The P
picks at stations 14 and 15 are well-observed on the SP
records and they are consistent with the LP seismograms.
LWO: 12 P.

Day 68: the three P picks were measured on the SP
records, 14 P is the weakest. 15 P and 16 P are somewhat
consistent with the LP records. Two options were
available for the 12 S pick (86.0, 98.8) the later pick
produced smaller residuals (1 sec^2 vs. 9 sec^2), and is
most clearly observed on the transverse filtered component.

The earlier is only observed on the vertical and radial components, and so the latter option was chosen. LWO: the entire focus.

The final data set is listed in Table 1-5; the "most confident" group is shown in Table A1-9. The large number of weak HFT events used relative to the number of weak meteorite impact events is due to the increased confidence placed in the HFT S picks. The impact event S picks were generally so emergent that strong P arrivals were required to even meet the minimum data requirements. The more prominent S arrivals from HFT events resulted in more available picks and if six weak arrivals produced consistent results, the event was considered for the primary data set but excluded from the select data set. No effort was made, however, to adjust a weak HFT pick set to produce consistent results; such events were eliminated completely.

A1.4 Moonquake Data

The deep moonquake data set is at once easier and more difficult to analyze and process than the surface event data. On the credit side, the moonquake seismograms are remarkably uniform. The LP record amplitudes vary only between 0 and about 15 du (except for a few Al events),

while essentially no energy is observed on the SP records. As will be shown later, the locatable moonquake sources are confined to within about 60° of the center of the ALSEP array and seem to occur in a restricted depth range. As a result, the S-P time difference is remarkably constant for all events, averaging about two minutes. On the other hand, the individual moonquake amplitudes are too small to permit accurate arrival time measurement. Fortunately, the moonquake sources repeatedly produce nearly identical events which can be used to increase the arrival time measurement accuracy. Of course, one way to do this would be to measure the observable arrivals on each event from a particular focus and average the results to hopefully obtain more accurate estimate for each arrival time. A far superior method is to stack the individual event records at each focus to improve the signal-to-noise ratio, thus creating an artificially large event summarizing all the individual moonquakes at a given focus.

There are 68 identifiable categories of deep moonquakes listed in the Galveston event catalogues through 1975. Each category contains between two (e.g. A68) and 99 individual events (A1). The category numbers are ordered more or less chronologically in order of their recognition as a distinct category. Generally speaking, later

categories contain fewer and smaller events than the
earlier ones. The moonquake events are assigned to a
category on the basis of occurrence time in the lunar
monthly cycle and matching signals. Of course, many
other moonquake-type signals are received that are too
small to be matched. Since 1975, about 12 new categories
have been assigned (Latham et al., 1978). In addition,
more events from the previous categories have been
received. Nevertheless, this additional data is not
likely to add significantly to the results obtained in
this thesis, for three reasons. First, no major new
focus such as A1 has appeared. Thus the 12 new moonquake
categories are probably very similar in occurrence and
amplitude characteristics to the present data set available
at MIT. Second, based on the first observation and the
results of processing this pre-1976 data set, only about
three or four of the new event categories could be
expected to contribute to the structural studies. Third,
the increased number of events in the previously analyzed
moonquake categories would only increase by about 25%
the theoretical signal-to-noise enhancement already
produced by stacking, due to the $\sqrt{n}$ flattening of the
enhancement curve. Naturally, this new data should
be incorporated into the structural analyses as it

becomes available, but the data used in this thesis probably represents the bulk of the structurally useful moonquake information.

The first step in processing the moonquake data was to go through the event catalogues and punch the year, day, and category number of every moonquake event on cards. These were then sorted by computer to produce a chronological list of the events that occurred at each focus. (This information has also been useful in studying the correlations between tidal stresses and moonquake time histories.) The catalogued amplitudes observed at each station are then listed alongside all the events. If, for a given focus, at least one observable amplitude is not listed at each of the ALSEP array corners, then that focus is eliminated from consideration. In addition, any focus that has only one observable signal at an array corner is further examined by plotting that single record to see if a measurable arrival is present. If not, the focus is eliminated. In all, 39 of the 68 foci were eliminated by these criteria; they are listed in Table Al-10 along with the stations where arrivals are not observable. Note that since all events from a particular focus produce nearly identical signals with roughly proportional amplitudes at each station, it is not likely that the post-1975 data set contains additional events which will

remedy these deficiencies.

The remaining 29 foci are listed in Table A1-11. As for the surface events, it is necessary to put the moonquake seismograms on direct-access discs to facilitate further processing. However, a total of 543 events were observed at the 29 foci, implying more than 1600 seismograms if each event on average produces observable amplitudes at three stations. Now in fact there are only about 1000 event tapes containing all the lunar data, so clearly some of the tapes contain more than one event of interest. Nevertheless, the required data is spread over at least 600-800 magnetic tapes. It is quite impossible to process this many tapes at the MIT IBM 370 computer due to handling problems. On the other hand, the Lincoln group's PDP 7's, while set up to handle many tapes, is inadequate for the later processing that must be done on the seismograms. Therefore a two-stage process was devised.

First, the necessary event tapes were transported to the PDP 7's. A program was written to search through the tapes to locate the desired data times, and then the seismogram was copied onto a master tape. The next event tape was then mounted, and the pertinent seismogram copied to the master tape sequentially following the previous record. Since, as mentioned, the S-P time difference is

relatively stable for the moonquakes and in order to conserve storage space, only 15 minutes of each seismogram were transferred to the master tape beginning 5 minutes before the catalogued start times. As a result, it was possible to get about 100 seismograms on a master tape, and about 15 master tapes were required to contain all the desired data, agreeing well with the initial estimate of the number of seismograms of interest. The transfer program is very efficient. All three tape drives are used so that while one tape is being copied the next is being mounted. No data processing is done at all except to read the time words of each physical record in order to locate the appropriate seismogram (time de-coding program supplied by Dr. D. McCowan). The actual transfer is simply tape-to-tape copy, and so it was possible to transfer about 10-12 records per hour.

The next step was to dump the master tapes onto disc at the IBM facility, using the program SCNLP. Each master tape cost about $100 and about two master tapes were sufficient to completely fill a disc; the raw moonquake seismograms are contained on discs LUNSEISA-G. Roughly 5% of the desired data was not obtained for several reasons. Occasionally, it had simply not been included on the event

tapes; in other instances the time codes were incorrect
due to dirty or damaged tapes, making the desired time
section impossible to locate. During the transfer to disc
similarly erroneous data streams were encountered and it
was impossible to decode the data and write it on disc.

The 543 events that occurred at the 29 foci of
interest are listed in Tables A1-11a thru A1-11cc. In
addition the observed amplitudes at ALSEP 12 are given;
station 12 is chosen because its operation period covers
all observed events. Due to the large number of events
and the relative uniformity mentioned before, the other
station amplitudes are not included; they may be found in
the Galveston event catalogues.

In order to stack the seismograms, it was necessary to
first plot them to measure approximate alignments for
stacking and eliminate noisy traces from the eventual
stacked records. Since the moonquake S-P interval never
exceeds three minutes, in view of the number of events it
was decided to plot only five minutes of each record
beginning at the catalogued start time; thus the middle
five minutes of each 15 minute seismogram on disc was
displayed, at scales of 5 in/min and 7 du/in. Due to
variations in the start times, it was occasionally
necessary to plot extra segments for some events. Note

also that the variation of the 15 minute data segment relative to, say, the first P arrival means that during stacking the ends of each event record are not exactly aligned, and so the final stacked records will be complete only in the region where all stacked segments overlap.

The individual records from one station and one focus were examined as a group. First, noisy records were eliminated so that the stacked traces would not be contaminated. In general, a noise-free interval from about one minute before P to two or three minutes after S was desired, allowing additional phases between P and S and after S to be seen if present. Naturally, this time interval was not always totally included in the five minute plots; if noise appeared in the resulting stacked record (which was plotted in its entirety), further plots of the individual events were made as necessary and the noisy trace removed from the stack. In addition, it was occasionally necessary to include records with noise pulses because so few events were available. When this occurred the resulting noise on the stacked records was marked to insure that it later was not mistaken for an arrival. In sum, the goal was to enhance the signal-to-noise ratio as much as possible while including as little noise as possible.

Next the records were matched and aligned visually, and relative times measured to about 0.2 second accuracy. Occasionally, due to poor signal amplitudes, an event could not be matched to the others, even using relative times from other stations where it had been matched. Such records were discarded on the grounds that the low amplitudes and possible subtle noise contamination would not enhance the stacked traces.

The relative times were then used to stack the events at each station and focus by computer. The procedure was as follows. One of the events to be stacked is designated as the base record; the absolute time of that event is thereafter used to refer to the stacked record. This event is read in from disc (all 15 minutes), the mean removed, and the resulting traces put in the stack buffer. The next record is then read, the mean removed, the amplitudes reversed (multiplied by -1) if necessary (for a reverse-polarity event), and frequency filtered if the event had been received in the broad-band response mode (see Table 1 1-3). The records are then aligned with the event in the stack buffer using the measured relative times, and either the X, Y, or Z components of both are passed to a cross-correlation subroutine. For each event to be added the

largest and cleanest component is chosen for the cross-correlation. In general four minutes of the traces are used in calculating the cross-correlation extending from one minute before S to three minutes after; zeroes are filled in at the ends as the traces are shifted. The cross-correlation coefficient, defined as

$$\sigma_j = \frac{\sum_{i=1}^{n} f_i\, g_{i-j}}{\left[\left(\sum_{i=1}^{n} f_i \right)^2 \left(\sum_{i=1}^{n} g_{i-j} \right)^2 \right]^{1/2}}$$

where n is the number of points to be cross-correlated (four minutes = 1200 points), j is the offset in points varying from -10 to +10, f_i is the first signal, and g_i is the second signal (of length n + 2j) is calculated for 21 offsets centered around the visually obtained relative time and extending ±2 seconds in steps of 0.2 seconds (the digitization interval). All of these parameters are variable as needed, especially the trace section used in cross-correlation which must be nearly noise-free. The maximum cross-correlation coefficient in an absolute sense is chosen automatically by the program, and if 1) the value is positive, 2) the value is greater than 0.2, and 3) the value is not at either +2.0 or -2.0 seconds shift, then the visual relative times are modified to the position of the maximum. If one of these conditions is not met, the

event is rejected and the next one read in. If they are
met, the event is added to the stack buffer using the
revised relative alignment time. All three components
need not be added; only those specified in each case by
the user. Thus noise on one component of ground motion
does not result in rejecting the entire record, and the
maximum possible information is included in the stacked
records. Finally, the entire process is repeated until
all records from that station and focus have been stacked.

At the end of this process, the program outputs
various important parameters. The number of traces stacked
into each component are counted, and the stacked traces
divided by those numbers. Thus the resulting stacks
represent an average event at that focus, both in absolute
amplitudes and relative trace amplitudes. Hopefully, though,
the noise component is reduced. The stack is stored on
disc (LUNSEISG), and 13 1/2 minutes are plotted (omitting
the last 1 1/2). The final relative times of all events
to the base event are listed, and the region of the stack
where all records overlap is given. This last is termed
the region of validity since outside of it there will be
artificial amplitude jumps where each added record ends
or begins. Finally, the program incorporates procedures
for removing traces that are subsequently found to contain

noise from the stacks.

The results of the stacking effort are listed in Tables A1-11 thru A1-13. Table A1-11 summarizes the number of records stacked into each component at each station for each of the 29 foci. Tables A1-12a through A1-12cc list the events occurring at a given focus, the ALSEP 12 catalogued amplitude (in Galveston mm), and the components that were added to the various stacked records. 1, 2, and 3 refer to the X, Y, and Z components of ground motion respectively; the orientations are given in Table 1-2. Dashes imply that no records were stacked from that event at that station, and X's mean that the station was not yet in operation. The underlined entries indicate the event that was used as a time base for the stack at that particular station; usually it is the strongest event that could be used at the most stations. The large number of records not stacked in is the cumulative result of missing data on tapes, tape read errors, noise, and weak amplitudes resulting in being unable to confidently match the events; all these effects caused the exclusion of the event from stacking. The most common problem was noise on the records, mostly caused by the frequent automatic releveling of the

seismic instruments. Often this only affects the horizontal records, which is why there are more vertical component records stacked overall than horizontals (except at station 14). Other noise sources included temporary instrument malfunction, thermal noise caused by terminator crossing, and overlapping events.

It is significant that the cross-correlation functions were sufficiently stable to allow automatic positioning of the events relative to each other; this indicates the remarkable similarity of matching moonquake records. The cross-correlation coefficient values were printed out for each time a record was stacked; some examples are shown in Table A1-13. Zero offset corresponds to the visual match. Note the sinusoidal character of the correlation function; this is caused by the sinusoidal nature of the seismograms which is in turn due to the narrow frequency response of the seismometers. The maximum cross-correlation coefficient is underlined, and was generally between 0.4 and 0.8; occasionally values greater than 0.9 were obtained. The criteria for poor matches were rarely met. If the maximum value was at either end of the four-second cross-correlation function range, or was less 0.2, almost invariably the problem was an incorrectly punched visual relative time. Negative maximum values signified that a record matched better if it was flipped over relative to

the current stack. This in fact was how the reverse-polarity events were initially observed at MIT, and nearly all of the time the available stations agreed as to the preferred polarity of the event. Thus it was initially assumed that such events resulted from a complete reversal of the slip vector at the source, and the reversed records were added to the stack simply by "flipping" them at all stations and then stacking. It has recently been suggested by Nakamura et al. (1978) on the basis of the S/P amplitude ratio variation, that the slip vector in fact rotates continuously thus producing events with reverse polarity signals at some stations and normal polarity at others. Accordingly, all available traces from each suspected reversed event and many normal events have been cross-correlated against the stacked record; a maximum of three components times four stations or 12 possible traces to test. By and large all the available traces from an event agree as to its polarity, and the few that don't are invariably either noisy records or have insignificant differences between the negative and positive maxima due to the sinusoidal nature of the cross-correlation function. Nakamura (1978) agrees that except for possibly one case, no definite "split-polarity" events are observed. Thus, while the true slip vector variation has important

consequences for the moonquake source mechanisms (Goins et al., 1976a) and the apparent dichotomy between the amplitude ratio evidence and the observed signal polarities should be studied further, for stacking purposes it appears to be adequate and correct to assume that a moonquake event is either of reverse or normal polarity at all stations.

Relatively few reversed events have been observed, and only at two foci (A1 and A20); they are indicated by negative amplitudes in Tables A1-12a and A1-12f. Positive amplitudes imply either a normal event or that no records were cross-correlated. The principle result is that automatic alignment via cross-correlation techniques worked extremely well in refining the visual relative times. The few rejected events were caused by overlooked noise, gross errors in visual matching, and reversed signals, and the program was indispensible in locating these anomalies.

After the stacking was completed the relative times between events obtained from different stations and components were compared, and none differed by more than 0.4 seconds (two digitization intervals) except in the case of known timing errors. It should be noted here that another method, suggested by Nakamura et al. (1978) is available for determining relative times. In essence, the

cross-phase spectra are calculated and the slope of the resulting phase vs. frequency plot represents a time difference that may be measured to considerably more accuracy than the digitization interval, depending on the ratio and values of the autocovariance length to the signal length. This method is impractical for the purpose of stacking due to the increased computation cost, and the extra accuracy is unnecessary because to stack the signals at offsets that are not an integral number of digitization steps would require interpolation between points, an unjustifiable complexity.

The signal-to-noise ratio enhancement obtained by stacking is illustrated in Fig. A1-11. The bottom five traces are individual event records; the top trace is the stack resulting from summing the five events shown and four others. The dashed lines connect matching features on the records, and the P arrival enhancement on the stacked trace is obvious.

The complete stacked record data set is shown in Figs. A1-12a thru A1-12x, plotted at a vertical scale of 16 du between component traces. The P and S wave arrival times were measured primarily from the expanded versions of these plots that were produced by the stacking program

in comparing the arrival time sets. For reference, the events discussed are shown in Figs. Al-12, 13, and 14.

. It should be noted here that many of the P arrivals are far weaker than those seen from the surface events, as a result of the small magnitude of the moonquakes. Often the picks are not clearly visible on the reduced plots; the original measurements were made on the expanded versions. Nevertheless there is good evidence for each pick shown; this can usually be seen by comparing the signal before the indicated P with the signal immediately after. Alternative picks are considered and noted, and fully a third of the measured P arrivals are excluded from the "most confident set".

Al: The only uncertain pick was 15 P; the alternatives were 73.0 and 78.1. The earlier pick produced smaller residuals by a factor of four, and so it was chosen. Notice that the 14 S arrival is clearly observed on the raw records as a long-period onset but is less obvious on the filtered traces. LWO: none.

Al5: There were three options for the 15 P pick; 20.1, 54.3, and 78.5. The residuals were smallest for 54.3, and on the whole it is more convincing on the seismograms because there is some expression on both the

vertical and horizontal components. Therefore it was used in the final data, but considered as a weak pick. 16 S is seen primarily on the transverse raw record. LWO: 15 P.

A16: There were two options each for 14 P (9.8, 22.0), 15 P (6.0, 13.3), and 12 S (129.0, 137.4). In each case the earlier pick produced smaller residuals, and so they were chosen. The P pick at 14 is seen mainly on the expanded plot horizontal components, while the 15 P in pick is fairly well-observed on all expanded components, even though its onset is fairly gradual. LWO: 14 P and 12 S.

A17: The options were at 16 S; 132.2 and 172.6. Surprisingly enough, although the locations differed by 10-20°, the residual grids were similar with small values (1 sec^2). The later value was ultimately chosen because it is somewhat more convincing on the seismograms. LWO: none.

A18: The alternatives were whether or not to use the ALSEP 16 picks at all. When they were run, the results were reasonable, and so it was decided to use the focus, especially since the P pick is fairly confident as seen on the Y component. The 15 P arrival can be seen on the R component of the scaled, rotated traces, while 14 P is visible on the raw horizontal records. Unfortunately, the vertical component at ALSEP 14 is not reliable. LWO:

16 S.

A20: The major question at this focus was whether or not to use the 15 S pick. Its inclusion did not degrade the residuals, and so it was retained. The 15 P pick as marked seems slightly (~2 seconds) late as seen on the filtered vertical component. The raw vertical component is inconclusive, however, so the original pick was retained. In either case, the difference is insignificant. LWO: 15 S.

A27: Two alternatives were available for 15 S, 162.1 and 168.5. As expected, they produced very similar locations and residuals, and ultimately the later pick was chosen as being more convincing. 12 S is observed primarily on the scaled horizontals, and 15 P is seen best on the raw horizontals. LWO: none.

A30: There were essentially no alternatives for the arrival times at this focus, and all the picks as marked are well-observed. LWO: none.

A31: This was a difficult data set. There are good S picks at stations 15 and 16, and a weak S at station 14. No records from station 12 are available. There were two possible P picks; one at station 14 (28.8) and the one as shown at station 16. The ALSEP 14 record is noisy, and so

the 16 P time was used. The residual grids do not provide any information since only four arrival times are available and thus the event can be located with zero residual for any of the velocity models. LWO: the entire focus.

A32: Possible P picks were considered at stations 14 (44.7) and 15 (as shown), but the 14 P was finally judged too weak to use. The 15 P was retained and produced reasonable grid values. 16 P is seen most clearly on the raw Y component. LWO: 15 P.

A33: This focus is unique in that stations 12 and 14 show no sign of an S arrival at all, in spite of a strong P arrival at station 14. (It was even considered that the station 14 arrival was in fact S; the resulting grid had residuals in excess of 10^3 sec^2.) The picks as shown are quite convincing, and produce small residuals ($\sim$1 sec^2). The anomalous shear wave absence is discussed in Chapter 4.

A34: There were two distinct possibilities for 15 P; 40.7 and 47.3. The earlier pick yielded the smallest residuals and seems somewhat more convincing on the scaled records, and so it was used. LWO: 15 P.

A36: This was also a difficult focus; no records were available at station 12, and there were several options. There were two alternatives for 16 S (208.0 and 268.8) and three for 14 S (171.4, 203.8, and 245.2). The only

A61: Despite the large leveling noise and temporary failure of the X component instrument, the P and S arrivals at station 14 are clearly measurable. The scaled plots are of no interest because the automatic scaling routine reacted to the leveling noise amplitudes. Only four picks were available for this focus; thus no direct structural can be obtained. LWO: none.

A62: Two options were considered for the 15 P pick; 11.0 and 26.7. The residuals are of nearly the same size, although different velocity values are preferred in each case. The later pick was chosen as being the more convincing. 16 P is best observed on the raw Y component trace. LWO: 14 P and 15 P'.

The final data set is given in Table 1-6 and the "most-confident" picks listed in Table A1-14. In concluding the section on the moonquake arrival time measurements, it is appropriate to make a few general comments now that the picks have been described individually. The account of the decisions made for each focus has been brief due to the number of events and the many factors considered as the final arrival time sets were developed. When the picks were first measured, all possibilities for arrivals were read; later they were compared to see which ones were most

convincing based on experience gained as more data was examined. Thus this phase was essentially iterative. A good number of additional weak picks and thus many more residual and location grids were examined that were not explicitly discussed above. These were not mentioned because their elimination was reasonably straightforward and obvious, using the criteria described previously, and a complete discussion would be of prohibitive length. The decisions highlighted above are those which were less certain and more judgemental in character. Most of these additional picks were substantially weaker than the ones retained.

In sum all possible picks, however remote were considered at least to some extent, and systematic methods applied to narrow the range of possibilities. Obviously, it is not possible to show nor is it likely that in every case the correct final pick was obtained. One problem is that the expanded plots are much more illuminating than the reduced figures shown herein, but I preferred to show all stations for a given focus together, rather than devote one page to each station-focus pair. There are 228 picks in the moonquake and surface event data sets, and hopefully most errors will average out. In fact, the "most confident" data sets were chosen mostly to see what the effect of

choosing a different data set (albeit a subset of the
original) would be on the structural results, rather than
to obtain a unique, clearly defined elite data group. As
is discussed in Chapter 3, the two "answers" were very
similar, which suggests that random errors in the data do
not in fact dominate the solutions. In any case, the
seismograms are all included in this thesis so that
future workers may use the present data as a starting
point.

Table A1-1

Meteorite impact events with 10 du amplitude at all four
stations.

	Start	Time		Galveston	Amplitude	(mm)	
Year	Day	Hour	Min	12	14	15	16
72	132	13	35	10	35	12	31
72	134	8	46	700	2500	170	450
72	199	7	50	6	30	5	15
72	199	21	56	58	90	110	320
72	202	2	30	5	24	6.5	13
72	213	18	8	13	40	100	40
72	242	22	59	5	21	8.5	20
72	319	19	25	9	18	5	10
72	324	18	24	11	44	24	27
73	83	19	23	6	17	6.5	13
73	113	13	56	20	50	27	50
73	220	17	19	48	22	5	13
73	233	12	17	6	27	8	30
73	262	9	32	20	30	16	58
73	269	20	48	6	28	10	19
74	38	6	21	9	35	6	28
74	109	18	34	11	30	5.5	13
74	187	2	57	7.8	20	10	17.7
74	198	12	5	5	20	15	19
74	275	13	27	6.7	15	6.1	10
74	305	11	42	5.5	18	13	35
74	312	16	48	5.1	39	5.8	13.5
74	325	13	16	10	50	16.5	120
74	349	9	8	16	150	11	27
75	64	21	52	8	65	12	63
75	85	0	46	9	38.5	15	32.5
75	102	18	15	45	99	99	99
75	111	2	3	8	45	14	18
75	124	10	6	80	120	70	120
75	168	12	25	10	60	10	35
*76	25	X	X	X	X	X	X
*77	107	X	X	X	X	X	X

*not listed in latest catalogue; data on special tapes.

Table Al-2

Final set of meteorite impact events; reference times and time segments stored on disc are given.

Year	Day	Start Time Hour	Min	Sec	Reference Times Hour	Min	Stop Time Hour	Min
72	134	8	42	1	8	47	9	7
72	199	21	46	1(6)	21	57	22	11
72	213	18	-3	1	18	9	18	28
72	324	18	18	1	18	24	18	43
75	102	18	8	1	18	15	18	33
75	124	9	56	1	10	5	10	21
76	25	16	2	1	16	10	16	27
77	107	23	29	1	23	35	23	54

Table Al-3

Processing log of the meteorite impact events used in this thesis.

Event Year	Day	Missing Stations LP	SP	Frequency Filter Applied, Station	Not Polarization Filtered
72	134	--	--	--	14
72	199	--	--	--	14
72	213	--	--	--	14
72	324	--	--	--	14
75	102	--	--	--	14
75	124	16	14,16	--	14,16
76	25	14	14	12,15,16	14
77	107	--	--	--	12

Most confident arrival time data set for meteorite impact events.

Reference Time				Arrival Times (sec relative to reference times)							
Yr	Day	Hr	Min	12P	14P	15P	16P	12S	14S	15S	16S
72	134	8	47	25.2	12.5	114.3	120.6	62.7	36.8	217.0	--
72	199	21	57	55.0	63.8	-13.7	16.7	--	--	--	--
72	213	18	9	136.4	118.1	-8.7	139.5	--	--	35.5	--
72	324	18	24	87.6	94.3	21.3	131.3	--	--	--	--
75	102	18	15	111.8	--	40.4	-15.5	292.0	--	--	--
75	124	10	5	1.3	15.5	77.5	53.6	--	--	--	--
76	25	16	10	-8.9	--	94.5	110.7	133.5	--	312.2	--
77	107	23	35	6.9	18.3	127.9	126.5	--	--	--	--

Table A1-5

All known HFT events received at a triangle of stations.

Year	Day	Hour	Min	Amplitude (Galveston mm)			
				12	14	15	16
72	261	14	38	--	.01	.01	.01
72	341	23	10	--	2.2	3.4	3.7
72	344	3	53	1	3.4	.01	1.7
73	39	22	53	--	.01	.01	.01
73	72	8	1	35	40	17	45
73	171	20	25	17	56	10.5	28
74	54	21	17	--	2	1	1
74	86	9	16	--	3	.01	2
74	109	13	38	--	2	1	3
74	149	20	44	--	.01	.01	2.2
74	192	0	51	9	22	25	44
75	3	1	46	70	150	80	120
75	12	3	17	2	7	8	11
75	13	0	28	1	5	1	2
75	44	22	5	3	8	3	5
75	127	6	40	1	5	1	4
75	147	23	31	3	5	3	4
*75	314	(7	53)	X	X	X	X
*76	4	(11	19)	X	X	X	X
*76	12	(8	18)	X	X	X	X
*76	66	X	X	X	X	X	X
*76	68	X	X	X	X	X	X

*not listed in event catalogues; first three start times from Nakamura (1977a).

Table Al-6

Final set of HFT events; reference times and time segments
stored on disc are given.

		Start time			Reference time		Stop time	
Year	Day	Hour	Min	Sec	Hour	Min	Hour	Min
73	72	7	51	1(16)	8	1	8	16
73	171	20	17	1	20	25	20	42
74	192	0	45	1	0	51	1	10
75	3	1	37	1	1	46	2	2
75	44	21	58	1	22	5	22	23
76	4	11	14	1	11	21	11	39
76	66	10	8	1	10	15	10	33
76	68	14	37	1	14	43	15	2

Table Al-7

Processing log of HFT events used in this thesis.

Event		Missing Stations		Frequency Filter	Not Polarization
Year	Day	LP	SP	Station	Filtered
73	72	--	--	--	14
73	171	--	--	--	14
74	197	--	--	--	14
75	3	--	--	12	14
75	44	14	14	12	14
76	4	--	--	12, 15, 16	14
76	66	--	--	12, 15, 16	14
76	68	--	--	12, 15, 16	14

Table Al-8

Vertical scale factors for Figs. Al-10.

Event		SP Amplitude Scale (du between traces)		
Year	Day	14	15	16
73	72	1734	434	1300
73	171	866	216	216
74	192	216	434	866
75	3	1734	1734	434
75	44	--	216	216
76	4	216	434	216
76	66	866	866	434
76	68	650	216	434

Table Al-9

Most confident arrival time data set for HFT events.

				Arrival times (sec relative to reference time)							
Yr	Day	Hr	Min	12P	14P	15P	16P	12S	14S	15S	16S
73	72	8	1	34.1	35.9	99.7	27.8	--	--	--	259.4
73	171	20	25	-5.0	6.5	85.7	138.5	125.3	--	--	--
76	66	10	15	--	53.3	-20.8	--	202.0	208.7	75.8	286.0

Table A1-10

Stations not receiving signals from the listed moonquake foci

Focus	Missing Stations	Focus	Missing Stations
A2	14,15,16	A43	16
A3	15,16	A47	15
A4	14,15,16	A48	15
A5	15,16	A49	16
A6	15,16	A52	15
A7	16	A53	15
A8	16	A55	15
A9	16	A57	16
A10	15,16	A58	16
A11	16	A59	15
A12	14,15,16	A63	14,15,16
A13	14,15,16	A64	14,15,16
A21	15,16	A65	14,15,16
A22	15,16	A66	14,15,16
A23	16	A67	14,15,16
A24	16	A68	14,15,16
A25	16		
A26	16		
A28	16		
A29	16		
A35	16		
A38	16		
A39	15		

Table Al-11

Number of traces stacked into each component at each station for each moonquake focus used in this thesis.

Focus Number	Number of Records in Stack (components X,Y,Z)			
	Aℓ12	Aℓ14	Aℓ15	Aℓ16
A1	40,41,66	17,23,13	4,6,5	10,8,11
A14	9,10,20	5,6,3	1,1,1	3,3,5
A15	8,8,12	6,5,1	8,8,11	4,3,4
A16	8,7,12	10,10,3	6,6,8	1,1,1
A17	8,8,10	2,2,1	3,3,4	3,3,1
A18	8,8,10	15,17,4	6,7,7	3,4,5
A19	1,1,2	2,1,0	2,3,3	1,2,2
A20	20,21,28	17,16,1	18,18,20	11,10,15
A27	3,3,3	4,4,0	5,6,5	2,2,2
A30	10,10,18	14,14,0	8,8,8	10,9,9
A31	--	1,1,0	3,3,1	1,1,1
A32	1,1,1	2,2,1	5,5,5	1,2,2
A33	4,5,4	7,7,2	5,6,5	1,2,2
A34	3,3,4	3,3,3	4,4,0	4,4,4
A36	--	1,2,0	2,2,2	1,1,1
A37	1,1,1	1,1,0	1,1,2	1,1,1
A40	10,11,20	14,13,0	7,7,8	10,7,13
A41	4,4,7	5,6,3	4,4,4	1,2,4
A42	11,10,14	11,13,7	10,10,11	7,7,8
A44	7,7,10	8,8,0	6,8,8	7,7,7
A45	2,2,2	1,1,0	2,2,2	1,1,1
A46	5,6,6	5,5,1	6,6,6	2,2,2
A50	5,5,5	4,4,1	3,4,4	3,3,4
A51	2,2,1	1,3,0	2,1,2	3,2,3
A54	1,2,3	2,2,0	1,1,1	1,2,2
A56	1,2,3	1,1,1	2,2,2	1,1,1
A60	2,2,2	4,4,0	1,2,2	2,2,2
A61	1,1,1	1,1,1	1,1,1	1,2,2
A62	1,1,1	1,2,0	3,4,4	2,2,1

Tables A1-12

The following tables list the moonquake events stacked at each station for each focus used in this thesis. The X symbols indicate that the station was not yet emplaced, and the underlined records serve as the time base for each resulting stack (see text).

Table Al-12a (Al)

Stacking resumes of the deep moonquake foci

Event		Amplitude	Stacked Components			
Yr	Day	12	12	14	15	16
69	344	8.0	--	X	X	X
69	347	1.0	1,2,3	X	X	X
70	6	4.0	--	X	X	X
70	9	3.5	1,2,3	X	X	X
70	10	2.0	1,2,3	X	X	X
70	26	2.0	--	X	X	X
70	33	2.0	1,2,3	X	X	X
70	35	3.0	1,2,3	X	X	X
70	38	3.5	1,2,3	X	X	X
70	61	2.0	--	X	X	X
70	63	6.0	1,2,3	X	X	X
70	64	1.5	1,2,3	X	X	X
70	66	2.0	1,2,3	X	X	X
70	89	9.0	3	X	X	X
70	91	2.0	1,2,3	X	X	X
70	93	6.0	1,2,3	X	X	X
70	116	7.0	2,3	X	X	X
70	118	1.5	1,2,3	X	X	X
70	120	5.0	3	X	X	X
70	143	12.0	--	X	X	X
70	145	3.0	3	X	X	X
70	171	9.0	1,3	X	X	X

Table Al-12a (Al) (Cont'd)

70	175	1.5	3	X	X	X
70	197	2.5	3	X	X	X
70	199	4.0	3	X	X	X
70	201	9.0	3	X	X	X
70	204	2.0	--	X	X	X
70	226	9.0	--	X	X	X
70	229	2.5	--	X	X	X
70	232	1.5	--	X	X	X
70	252	3.0	--	X	X	X
70	254	3.0	--	X	X	X
70	256	2.0	--	X	X	X
70	257	1.5	--	X	X	X
70	280	1.0	--	X	X	X
70	284	4.0	--	X	X	X
70	307	4.5	--	X	X	X
70	334	4.0	--	X	X	X
70	336	1.5	--	X	X	X
70	337	-1.5	--	X	X	X
70	361	9.0	--	X	X	X
70	363	2.5	--	X	X	X
70	365	8.0	--	X	X	X
71	28	6.0	--	X	X	X
71	50	2.3	--	--	X	X
71	51	3.3	1,2,3	1,3	X	X
71	53	4.0	1,2,3	--	X	X

Table Al-12a (Al) (Cont'd)

71	56	2.6	1,2,3	1,2,3	X	X
71	80	2.3	3	1,2,3	X	X
71	82	2.8	--	1,2,3	X	X
71	85	2.0	--	--	X	X
71	107	1.8	1,2,3	--	X	X
71	110	2.1	1,2,3	3	X	X
71	137	1.5	2,3	3	X	X
71	160	2.0	1,2,3	--	X	X
71	163	2.5	--	3	X	X
71	187	3.0	3	--	X	X
71	189	0.9	1,	1,2,3	X	X
71	190	1.0	--	--	X	X
71	216	2.0	--	--	--	X
71	217	0.8	1,2,3	3	--	X
71	218	3.8	1,2,3	3	3	X
71	245	2.3	2,3	--	2	X
71	273	1.5	3	--	3	X
71	299	0.0	--	--	--	X
71	327	0.5	--	1,2	--	X
71	328	0.0	--	1,2	--	X
71	329	0.5	--	1,2	--	X
71	355	1.0	1,2,3	1	--	X
71	355	0.5	1,3	1	--	X
72	17	0.0	--	1,2	--	X

Table A1-12a (A1) (Cont'd)

72	44	-1.5	1,2,3	2,3	--	X
72	164	-1.0	2,3	1,2	--	1,2,3
72	195	-1.0	1,2,3	1,2	--	1,2,3
72	358	1.3	--	--	--	--
73	20	12	3	2,3	--	--
73	50	-1.0	--	--	--	--
73	127	-2.2	1,2,3	1,2,3	--	--
73	156	-5.0	1,2,3	1,2	2	--
73	184	-1.5	--	1,2	--	1,3
73	212	-1.0	2,3	1,2	--	1,3
73	241	-1.3	--	--	--	--
73	270	-1.8	1,2,3	--	1,2	--
73	321	-2.8	--	--	--	--
73	348	1.0	--	--	--	--
74	151	-3.4	3	--	--	3
74	315	1.5	1,2,3	2	1,2	--
74	317	1.5	1,2,3	2	--	--
75	86	7.0	3	--	3	1,2,3
75	113	14.5	2,3	--	--	2,3
75	140	4.3	3	--	--	--
75	168	2.0	1,2,3	2	--	--
75	250	4.0	1,3	2	1,2,3	1,2,3
75	276	3.5	3	2	--	1,2,3
75	278	3.0	--	2	--	1,2,3

Table Al-12a (Al) (Cont'd)

75	304	8.0	3	2	1,2,3	1,2,3
75	331	-3.0	--	--	--	1
75	331	0.0	--	--	--	--

Table Al-12b (Al4)

Event		Amplitude	Components Stacked			
Yr	Day	12	12	14	15	16
70	118	1.5	3	X	X	X
70	170	1.0	2,3	X	X	X
70	198	1.0	--	X	X	X
70	282	1.5	1,3	X	X	X
70	310	1.5	--	X	X	X
70	336	1.5	1,2,3	X	X	X
71	110	1.8	1,2,3	X	X	X
71	137	1.8	3	--	X	X
71	190	1.3	--	--	X	X
71	217	1.2	--	--	--	X
71	302	2.0	3	--	--	X
71	330	1.8	1,2,3	1,2	--	X
71	356	0.5	1,2,3	--	--	X
72	18	2.5	--	--	--	X
72	45	2.0	1,2,3	1,2,3	--	X
72	73	1.5	1,2,3	2	1,2,3	X
72	101	1.5	--	1,2,3	--	X
72	129	1.0	--	--	--	--
72	157	2.0	--	--	--	3
72	184	1.0	3	--	--	--
72	265	2.8	3	--	--	2,3
72	293	1.6	3	--	--	--

Table A1-12b (A14) (Cont'd)

72	322	2.0	3`	--	--	--
73	11	2.1	1,2,3	--	--	--
73	148	2.0	1,2,3	--	--	1,2,3
73	176	1.8	3	1,2	--	1,3
73	232	1.2	3	--	--	--
73	284	2.0	--	--	--	1,2,3

Table Al 12c (A15)

Event		Amplitude	Components Stacked			
Yr	Day	12	12	14	15	16
71	274	0.5	--	--	--	X
71	360	0.5	--	1,2	--	X
72	22	0.8	--	--	1,2,3	X
72	49	0.5	--	--	--	X
72	73	0.5	1,2,3	--	--	X
72	102	1.0	1,2,3	--	3	X
72	105	0.3	--	1,3	--	X
72	132	1.2	1,2,3	--	1,2,3	--
72	161	1.5	1,2,3	--	--	--
72	190	1.5	1,2,3	1,2	--	1,2,3
72	218	1.2	1,2,3	1,2	1,2,3	--
72	243	2.0	--	--	--	--
72	296	1.2	2,3	--	3	3
72	325	1.8	3	--	1,2,3	--
72	354	1.7	1,3	--	1,2,3	--
73	17	1.1	3	--	3	--
73	45	--	--	--	--	--
73	98	--	--	--	1,2,3	--
73	125	1.0	1,2,3	1,2	1,2,3	1,2,3
73	153	1.0	3	1,2	1,2,3	1,2.3

Table A1-12d (A16)

Yr	Event Day	Amplitude 12	Components Stacked 12	14	15	16
71	70	1.5	--	--	X	X
71	95	--	--	--	X	X
71	123	0.8	--	1,2,3	X	X
71	151	1.0	1,2,3	1,2,3	X	X
71	179	1.0	1,2,3	1,2	X	X
71	206	1.0	1,3	--	X	X
71	233	1.0	1,2,3	--	--	X
71	260	1.0	3	1,2,3	1,2,3	X
71	288	1.4	--	1,2	1,2,3	X
71	316	1.2	3	1,2	2,3	X
71	343	--	--	--	--	X
72	7	1.5	3	--	--	X
72	35	1.5	1,2,3	1,2	--	X
72	63	1.5	--	--	--	X
72	89	1.5	3	--	1,3	X
72	115	1.1	--	--	3	--
72	145	1.8	--	--	--	--
72	173	1.0	--	--	--	--
72	201	1.2	1,2,3	1,2	--	--
72	228	1.0	1,2,3	--	1,2,3	--
72	255	1.0	--	--	--	--
72	282	--	--	1,2	1,2,3	1,2,3
72	310	1.3	1,2,3	1,2	1,2,3	--

Table Al-12e (Al7)

Event		Amplitude	Components Stacked			
Yr	Day	12	12	14	15	16
71	270	1.0	--	1,2,3	--	X
71	351	1.5	1,2,3	--	--	X
72	13	1.1	1,2,3	--	--	X
72	40	1.0	--	--	--	X
72	93	--	--	--	--	X
72	148	2.0	3	--	--	1,2
72	176	1.5	--	--	--	1,2
72	203	1.5	3	--	--	--
72	230	1.8	1,2,3	--	--	--
72	258	2.0	1,2,3	--	1,2,3	--
72	284	1.0	1,2,3	1,2	--	--
72	312	2.0	1,2,3	--	3	1,2,3
72	339	2.0	1,2,3	--	1,2,3	--
73	1	1.8	1,2,3	--	1,2,3	--

Table A1-12f (A18)

Event		Amplitude	Components Stacked			
Yr	Day	12	12	14	15	16
71	51	1.2	--	1,2,3	X	X
71	78	1.1	--	--	X	X
71	106	1.9	--	--	X	X
71	132	--	--	1,2,3	X	X
71	134	1.0	--	1,2	X	X
71	160	1.0	1,2,3	--	X	X
71	186	0.9	--	--	X	X
71	188	1.0	--	--	X	X
71	214	1.0	3	--	--	X
71	241	1.0	--	--	--	X
71	242	1.5	--	--	--	X
71	269	1.0	--	1,2,3	--	X
71	270	1.0	--	1,2	--	X
71	296	1.0	--	1,2	--	X
71	298	1.5	1,2,3	1,2	--	X
71	325	1.0	--	1,2	1,2,3	X
71	351	1.0	--	--	--	X
71	357	0.5	--	--	--	X
72	14	1.0	1,2,3	1,2	--	X
72	41	1.2	1,2,3	2,3	1,2,3	X
72	69	1.5	--	--	--	X
72	97	1.0	--	--	--	X

Table A1-12f (A18) (Cont'd)

72	122	1.0	--	--	--	X
72	125	1.2	1,2,3	--	--	--
72	152	1.5	--	--	--	--
72	179	1.2	--	--	--	1,2,3
72	206	1.2	--	--	--	--
72	233	1.2	--	--	--	--
72	261	1.6	3	--	--	3
72	289	1.0	--	2	--	--
72	317	1.0	--	--	--	--
72	345	1.4	--	--	1,2,3	--
73	5	1.0	1,2,3	1,2	--	--
73	32	1.1	1,2,3	1,2	--	--
73	59	--	--	--	--	--
73	87	--	--	--	--	--
73	115	--	--	--	--	2,3
73	143	1.0	--	--	--	--
73	171	0.8	--	--	--	--
73	197	1.0	--	--	--	--
73	224	1.0	3	--	--	1,2,3
73	251	1.1	--	--	--	--
73	307	--	--	1,2	2,3	--
73	335	--	--	1,2	1,2,3	--

Table A1-12f (A18) (Cont'd)

73	363	0.7	--	--	--	--
74	26	0.5	1,2	1,2	1,2,3	--
74	52	--	--	--	--	--
74	79	--	--	1,2	1,2,3	1,2,3

Table A1-12g (A19)

Event		Amplitude	Components		Stacked	
Yr	Day	12	12	14	15	16
71	81	--	--	--	X	X
71	110	1.1	--	--	X	X
71	191	0.3	3	1	X	X
71	218	--	--	--	--	X
71	245	0.9	--	--	--	X
72	19	--	--	1,2	1,2,3	X
72	45	0.5	1,2,3	--	--	X
72	73	0.5	--	--	--	X
72	101	0.2	--	--	--	X
72	129	--	--	--	1,2,3	--
72	178	0.5	--	--	--	--
72	211	--	--	--	--	--
72	238	0.9	--	--	2,3	2,3
72	265	1.0	--	--	--	1,2,3

Table A1-12h (A20)

Event		Amplitude	Components Stacked			
Yr	Day	12	12	14	15	16
71	325	-1.0	1,2,3	1,2	1,2,3	X
72	81	0.5	1,2,3	1,2	1,2	X
72	108	1.0	--	1,2	1,2,3	X
72	136	2.5	1,2,3	1,2,3	1,2,3	1,2,3
72	151	-1.0	3	1,2	1,2,3	--
72	164	3.5	1,2,3	1,2	1,2,3	1,2,3
72	191	2.0	1,2,3	--	1,2,3	--
72	260	-2.2	1,2,3	1,2	--	--
72	272	1.6	--	--	--	--
72	300	2.5	--	--	--	--
72	328	1.2	--	1,2	1,2,3	--
72	355	1.3	--	--	--	--
73	17	2.0	3	--	3	2,3
73	44	2.0	3	--	--	1,2,3
73	71	1.0	1,2,3	1	--	--
73	98	2.0	1,2,3	--	--	--
73	111	-2.5	3	1	--	--
73	125	1.0	1,2,3	1,2	1,2,3	1,2,3
73	139	-3.3	3	--	--	--
73	235	2.5	1,2,3	--	3	--
73	262	3.0	--	--	1,2,3	--
73	289	2.0	--	--	--	--

Table Al-12h (A20) (Cont'd)

73	302	-2.8	1,2,3	1,2	1,2,3	--
73	329	-2.0	1,2,3	2	1,2,3	1,3
73	344	1.1	2,3	--	--	--
74	7	1.4	3	--	--	--
74	35	2.0	3	--	--	--
74	62	3.5	--	--	--	3
74	89	4.0	1,2,3	1,2	1,2,3	--
74	101	-0.0	--	--	--	--
74	116	4.0	1,2,3	1,2	1,2,3	1,2,3
74	143	3.0	1,2,3	1,2	1,2,3	1,2,3
74	170	2.0	1,2,3	--	--	1,2,3
74	198	2.5	1,2,3	1,2	--	1,2,3
74	226	2.5	1,2,3	1,2	1,2,3	--
74	254	1.0	--	--	1,2	1,2,3
74	334	0.9	1,2,3	--	3	--
74	362	1.0	1,2,3	--	3	--
75	25	1.2	--	--	1,2,3	3

Table A1-12i (A27)

Event		Amplitude	Components. Stacked			
Yr	Day	12	12	14	15	16
71	205	0.2	--	1,2	X	X
71	233	--	--	1,2	1,2,3	X
71	261	--	--	--	1,2,3	X
71	290	0.6	1,2,3	1,2	1,2,3	X
71	319	1.0	1,2,3	--	2,3	X
71	347	0.5	1,2,3	1,2	1,2,3	X
72	92	--	--	--	1,2	X
72	118	0.5	--	--	--	--
72	147	0.5	--	--	--	1,2,3
72	175	1.0	--	--	--	1,2,3

408

Table A1-12j (A30)

Event		Amplitude	Components Stacked			
Yr	Day	12	12	14	15	16
71	311	1.0	3	--	--	X
71	339	1.5	--	2	--	X
72	1	1.0	--	1,2	1,2	X
72	28	1.0	3	--	--	X
72	55	1.0	--	--	--	X
72	82	1.0	--	--	--	X
72	110	2.0	1,2,3	1,2	1,2,3	--
72	138	1.5	1,2,3	1,2	1,2	1,2,3
72	165	1.2	--	--	--	1
72	219	1.2	1,2,3	1,2	--	1,2,3
72	246	1.3	3	--	1,2	--
72	274	1.9	--	--	--	--
72	301	2.0	3	--	--	--
72	329	2.8	--	1,2	--	--
72	356	2.9	3	1,2	3	1,2,3
73	17	2.0	3	--	--	1,2,3
73	44	1.0	--	--	--	1,2,3
73	71	0.9	1,2,3	1	--	--
73	98	1.8	1,2,3	1,2	3	--
73	126	2.0	1,2,3	1,2	--	1,3
73	154	2.0	1,2,3	1,2	1,2,3	1,2,3
73	181	1.5	1,2,3	1,2	1,2,3	--

Table Al-12j (A30) (Cont'd)

73	208	1.5	1,2,3	1,2	--	--
73	262	1.5	--	--	--	1,2,3
73	289	2.0	--	1,2	--	--
73	316	1.2	3	--	3	--
73	344	1.4	--	--	--	--
74	6	2.0	3	--	--	--
74	34	1.0	--	--	--	2,3
74	61	0.5	--	--	--	--
74	88	--	--	--	--	--
74	115	1.0	1,2,3	1,2	1,2,3	--
74	142	--	--	--	1,2,3	1,2
74	197	--	--	--	--	--

Table Al-12k (A31)

Event		Amplitude	Components Stacked			
Yr	Day	12	12	14	15	16
71	270	--	--	--	1,2	X
71	351	--	--	--	--	X
72	41	--	--	--	1,2,3	X
72	161	0.2	--	1,2	1,2	1,2,3

Table Al-12l (A32)

Event		Amplitude	Components Stacked			
Yr	Day	12	12	14	15	16
71	258	0.8	1,2,3	--	1,2,3	X
71	286	--	--	--	1,2,3	X
71	349	--	--	1,2	1,2,3	X
72	120	--	--	--	1,2,3	1,2,3
72	148	--	--	1,2,3	1,2,3	2,3

Table A4-12m (A33)

Event		Amplitude	Components Stacked			
Yr	Day	12	12	14	15	16
71	264	0.5	--	--	--	X
71	292	0.3	1,2,3	1,2	1,2,3	X
71	320	0.5	1,2	--	1,2,3	X
71	348	--	--	--	--	X
71	348	0.8	1,2,3	1,2	2,3	X
72	10	0.5	--	--	--	X
72	92	0.5	--	--	--	X
72	120	--	--	--	--	--
72	148	1.0	--	--	--	3
72	176	0.5	--	--	--	2,3
72	203	--	--	--	--	--
72	230	0.8	--	--	--	--
72	258	--	--	--	2,3	--
72	285	--	--	1,2,3	1,2	--
72	313	1.0	--	1,2,3	--	2,3
72	341	0.8	1,2,3	--	1,3	2,3
73	3	0.8	--	--	1,2	--
73	30	--	--	--	--	--
73	57	--	--	--	--	--
73	111	--	--	--	--	--
73	139	1.0	--	--	--	--
73	167	--	--	--	--	--

Table A4-12m (A33) (Cont'd)

73	195	1.0	--	--	--	3
73	222	1.0	--	--	--	--
73	250	--	--	--	--	--
73	277	--	--	--	--	--
73	304	--	--	1,2	--	--
73	331	--	--	--	--	--
73	359	0.5	--	1,2	--	1,2,3
74	22	--	--	--	--	--
74	50	0.8	2,3	--	--	2,3
74	77	--	--	--	--	1,2,3
74	103	--	--	--	--	--
74	130	--	--	--	--	--
74	158	--	--	--	--	--
74	214	--	--	--	--	--
74	270	0.8	--	--	--	--
74	297	--	--	--	--	--
74	351	--	--	--	--	--
75	13	--	--	--	--	1,2,3
75	42	--	--	1,2	--	1,2,3

Table Al-12n (A34)

Yr	Day	Amplitude 12	Components Stacked 12	14	15	16
71	258	1.0	--	1,2,3	1,2	X
71	286	1.0	3	--	1,2	X
71	314	1.0	--	--	--	X
71	341	2.0	--	--	--	X
72	2	1.0	--	--	--	X
72	29	1.0	--	--	--	X
72	57	1.0	--	--	--	X
72	85	1.8	--	--	1,2	X
72	112	1.0	--	--	--	--
72	138	1.2	1,2,3	3	--	1,2,3
72	166	1.0	1,2,3	1,2,3	1,2	1,2,3
72	220	1.0	--	1,2	--	1,2,3
72	248	1.0	--	--	--	--
72	275	1.3	--	--	--	1,2,3
72	303	0.8	--	--	--	--
72	331	1.5	1,2,3	--	--	--

Table Al-12o (A36)

Event		Amplitude	Components Stacked			
Yr	Day	12	12	14	15	16
72	13	--	--	--	1,2,3	X
72	100	--	--	2	1,2	X
72	128	0.5	--	1,2	3	1,2,3

Table Al-12p (A37)

Event		Amplitude	Components Stacked			
Yr	Day	12	12	14	15	16
72	16	--	--	--	--	X
72	43	--	--	1,2	1,2,3	X
72	207	1.0	1,2,3	--	3	1,2,3

Table Al-12q (A40)

Event		Amplitude	Components Stacked			
Yr	Day	12	12	14	15	16
72	159	1.5	1,2,3	--	--	1,2,3
72	187	1.0	3	--	--	3
72	215	2.0	3	--	--	3
72	242	2.0	--	--	--	--
72	270	2.0	3	1,2	3	--
73	14	2.1	3	--	--	--
73	42	2.0	1,2,3	1,2	--	--
73	68	1.8	1,2,3	1	1,2,3	--
73	95	1.0	1,2,3	1,2	--	--
73	122	1.2	1,2,3	1,2	1,2,3	1,2,3
73	150	1.2	--	1,2	--	--
73	178	2.0	--	--	1,2,3	1,3
73	207	2.0	3	1,2	--	3
73	230	2.0	3	--	--	1,2,3
73	261	3.0	--	--	--	--
73	287	2.1	--	--	--	--
73	314	1.8	2,3	1,2	--	--
73	342	1.7	3	1,2	1,2,3	--
74	6	2.0	3	--	1,2,3	1,3
74	34	1.8	3	--	--	--
74	61	1.5	1,2	--	--	--
74	88	1.0	1,2,3	1,2	--	1,2,3

Table Al-12q (A40)(Cont'd)

74	115	1.2	1,2,3	1,2	--	1,2,3
74	115	1.0	--	--	--	--
74	142	1.1	1,2,3	1,2	--	1,3
74	170	1.3	3	1,2	1,2,3	1,2,3
74	198	1.5	1,2,3	1,2	1,2,3	1,2,3
74	225	0.8	--	--	--	--
74	253	1.1	--	--	--	--

Table A1-12r (A41)

| Event | | Amplitude | Components Stacked | | | |
Yr	Day	12	12	14	15	16
72	160	1.0	1,2,3	1,2	1,2,3	3
72	189	1.0	--	1,2	1,2,3	--
72	217	1.5	3	--	--	3
72	244	1.0	--	--	--	--
72	270	1.9	3	--	--	--
72	297	1.8	3	1,2,3	--	--
72	324	1.0	--	--	--	--
72	352	1.2	--	--	--	--
73	14	1.0	--	--	--	--
73	96	1.0	1,2,3	1,2,3	--	--
73	123	1.5	1,2,3	--	1,2,3	1,2,3
73	151	1.3	--	2	1,2,3	2,3
73	179	1.2	--	--	--	--
73	207	1.2	1,2,3	1,2,3	--	--
73	288	1.6	--	--	--	--

Table Al-12s (A42)

Event		Amplitude	Components Stacked			
Yr	Day	12	12	14	15	16
72	161	1.0	1,2,3	1,2	--	--
72	297	1.2	--	3	1,2	--
72	325	2.1	1,2,3	--	--	--
72	353	2.6	--	--	3	1,2,3
73	14	1.8	--	--	--	--
73	41	1.0	1,2,3	1,2,3	--	--
73	68	1.0	1,2,3	--	1,2,3	--
73	95	--	--	1,2,3	--	--
73	123	1.8	1,2,3	1,2,3	--	1,2,3
73	150	0.8	--	2	--	--
73	177	2.0	--	1,2,3	1,2,3	--
73	205	2.0	3	--	1,2,3	3
73	232	1.2	3	--	--	1,2,3
73	259	1.2	1,3	--	--	--
73	286	1.2	--	--	1,2,3	--
73	313	1.1	--	1,2	--	--
73	340	1.6	1,3	--	3	--
74	3	2.0	--	--	--	--
74	31	2.0	1,2,3	1,2	3	--
74	58	1.2	1,2,3	1,2	1,2,3	1,2,3
74	85	1.2	1,2,3	--	1,2,3	1,2,3
74	112	1.0	--	--	--	--

Table A1-12s (A42) (Cont'd)

74	138	1.1	1,2,3	1,2,3	1,2,3	--
74	166	1.4	2,3	1,2,3	--	1,2,3
74	194	1.8	--	--	1,2,3	--
74	221	1.5	--	--	--	--
74	248	1.0	--	--	--	--
74	357	1.0	--	--	--	--
75	20	1.1	--	2	--	--
75	47	0.8	--	1,2	1,2	1,2,3

Table A1-12t (A44)

Event		Amplitude	Components Stacked			
Yr	Day	12	12	14	15	16
73	120	--	--	--	--	1,2,3
73	148	1.0	1,2,3	1,2	--	1,2,3
73	176	1.0	--	--	--	--
73	204	1.0	3	--	1,2,3	--
73	258	1.5	--	1,2	--	--
73	285	1.0	--	--	1,2,3	--
73	312	0.7	3	--	1,2,3	1,2,3
73	340	1.5	3	--	2,3	--
74	3	1.5	--	--	--	--
74	31	1.0	1,2,3	1,2	--	--
74	58	1.0	1,2,3	1,2	1,2,3	1,2,3
74	84	1.2	1,2,3	1,2	1,2,3	1,2,3
74	111	1.0	--	1,2	1,2,3	--
74	139	1.1	1,2,3	1,2	2,3	1,2,3
74	167	0.9	1,2,3	1,2	--	1,2,3
74	194	1.0	--	--	--	--
74	222	1.0	--	--	--	--
74	249	1.2	1,2,3	--	--	--

Table A1-12u (A45)

Event		Amplitude	Components		Stacked	
Yr	Day	12	12	14	15	16
74	99	--	--	--	1,2,3	--
74	124	1.2	1,2,3	1,2	1,2,3	1,2,3
74	178	1.0	1,2,3	--	--	--

Table A1-12v (A46)

Event		Amplitude	Components		Stacked	
Yr	Day	12	12	14	15	16
73	60	3.0	1,2,3	--	1,2,3	--
73	88	2.5	2,3	--	1,2,3	--
73	116	1.8	--	--	1,2,3	1,2,3
73	144	2.0	--	--	--	--
73	243	2.0	1,2,3	1,2	--	--
73	273	3.0	1,2,3	1,2	1,2,3	--
73	303	3.0	1,2,3	1,2,3	1,2,3	--
73	330	1.9	1,2,3	1,2	1,2,3	--
74	343	1.0	1	1,2	--	1,2,3

Table A1-12w (A50)

Event		Amplitude	Components Stacked			
Yr	Day	12	12	14	15	16
73	120	0.5	1,2,3	--	1,2,3	1,2,3
73	149	1.0	1,2,3	1,2	--	3
73	177	1.2	1,2,3	--	1,2,3	--
73	205	2.0	--	1,2	--	--
73	232	1.0	--	--	--	--
73	260	1.0	--	--	--	--
73	340	1.2	--	--	2,3	--
74	112	1.0	--	--	--	--
74	139	1.3	1,2,3	1,2	--	1,2,3
74	167	0.8	1,2,3	1,2,3	--	1,2,3
74	194	1.0	--	--	1,2,3	--

Table A1-12x (A51)

Event		Amplitude	Components Stacked			
Yr	Day	12	12	14	15	16
73	330	1.0	--	--	--	--
73	358	1.0	1,2	1,2	1,3	1,2,3
74	21	--	--	2	1,2,3	1,3
74	49	1.0	1,2,3	2	--	1,2,3

Table A1-12y (A54)

Event		Amplitude	Components		Stacked	
Yr	Day	12	12	14	15	16
73	121	0.5	1,2,3	1,2	--	2,3
73	149	1.0	2,3	1,2	--	1,2,3
73	176	1.9	--	--	--	--
73	312	1.1	3	--	1,2,3	--

424

Table AI-12z (A56)

Event		Amplitude	Components Stacked			
Yr	Day	12	12	14	15	16
73	163	1.3	1,2,3	--	1,2,3	1,2,3
73	191	1.2	3	--	--	--
73	354	1.0	2,3	1,2,3	1,2,3	--

Table A1-12aa (A60)

Event		Amplitude	Components Stacked			
Yr	Day	12	12	14	15	16
74	37	1.0	1,2,3	1,2	--	--
74	59	1.0	1,2,3	1,2	1,2,3	--
74	86	--	--	1,2	--	1,2,3
74	112	1.2	--	1,2	2,3	1,2,3
74	139	1.3	--	--	--	--

Table A1-12bb (A61)

Event		Amplitude	Components Stacked			
Yr	Day	12	12	14	15	16
75	58	--	--	--	1,2,3	2,3
75	85	--	--	--	--	1,2,3
75	113	1.0	--	--	--	--
75	304	1.2	1,2,3	1,2,3	--	--

Table A1-12cc (A62)

Event		Amplitude	Components Stacked			
Yr	Day	12	12	14	15	16
75	59	0.4	--	1,2	--	--
75	86	--	--	--	2,3	--
75	114	1.2	--	--	1,2,3	1,2,3
75	140	4.0	--	--	--	--
75	167	2.0	1,2,3	--	1,2,3	--
75	304	1.2	--	2	1,2,3	1,2

Cross-correlation coefficients as a function of offset τ from eyeball matching, for representative cases from each station, and for the reversed A1 event shown in Fig. 4. Maximum absolute value is underlined.

	A17 Station 12	A18 Station 14	A19 Station 15	A34 Station 16	A1 Station 14 (reverse)
-2.0	.14	.13	.33	.68	.22
-1.8	.01	-.04	.14	.46	-.06
-1.6	-.15	-.13	-.12	.09	-.28
-1.4	-.30	.02	-.33	-.33	-.22
-1.2	-.36	.24	-.43	-.65	.08
-1.0	-.33	.17	-.40	-.76	.33
-0.8	-.17	-.29	-.29	-.61	.25
-0.6	-.10	-.65	-.14	-.24	-.13
-0.4	.41	-.32	.19	.25	-.43
-0.2	.57	.50	.63	.68	-.26
0.0	.46	.88	.69	.84	.29
.2	.14	.35	.27	.67	.65
.4	-.18	-.46	-.11	.26	.30
.6	-.37	-.65	-.26	-.23	-.46
.8	-.42	-.21	-.38	-.61	-.74
1.0	-.34	.23	-.46	-.76	-.19
1.2	-.17	.25	-.39	-.65	.53
1.4	.04	.01	-.18	-.34	.62
1.6	.21	-.13	.09	-.07	.09
1.8	.30	-.04	.31	.45	-.41
2.0	.29	.10	.41	.68	-.42

Table A1-14

Most-confident arrival times for deep moonquake events

Focus   Arrival times (relative to reference times in Table 1-6)

Focus	12P	14P	15P	16P	12S	14S	15S	16S
A1	8.10	10.20	73.00	58.30	99.80	103.00	212.90	193.30
A15	--	--	--	--	164.40	152.20	180.80	136.50
A16	--	9.80	--	6.20	--	127.20	119.30	120.00
A17	1.50	--	-10.80	--	102.20	100.90	85.10	172.60
A18	--	75.30	31.20	45.20	231.70	215.00	135.00	--
A20	--	-10.30	-1.80	33.30	99.30	104.10	--	178.20
A27	--	--	34.60	--	208.50	192.80	140.10	168.50
A30	--	22.80	46.00	--	114.30	123.90	162.00	207.20
A32	--	--	--	34.40	--	183.10	105.40	131.50
A33	--	51.20	19.50	8.70	--	--	228.00	211.70
A34	--	--	--	--	141.10	137.70	146.00	159.80
A40	--	--	--	61.50	136.40	133.20	177.40	169.00
A41	--	--	--	--	116.50	134.40	149.60	247.10
A42	--	46.10	--	--	160.20	172.30	193.00	262.00
A44	--	--	32.40	--	289.80	266.20	162.80	230.00
A45	--	14.40	--	--	--	121.70	220.20	200.10
A46	--	43.30	--	--	136.20	142.70	242.30	223.80
A51	--	61.90	--	37.20	193.60	171.80	135.30	131.00
A56	--	51.80	--	--	119.40	135.30	183.80	227.30
A61	--	-3.10	--	--	--	149.00	51.00	74.00
A62	--	--	27.30	53.40	279.50	266.60	151.40	215.70

Reference times for each focus given in Table 1-6.

Figure Captions

Fig. Al-1a,h. Raw long-period seismograms of the meteorite
impact events used in this thesis. Scales given in text.

Fig. Al-2a,h. Scaled and rotated seismograms from meteorite
impact events.

Fig. Al-3a,h. Polarization filtered seismograms from meteorite
impact events.

Fig. Al-4a,h. Expanded versions of Fig. Al-2 showing P arrivals.

Fig. Al-5a,h. Short-period seismograms from meteorite impact
events.

Fig. Al-6a,h. Raw long-period seismograms of the HFT events
used in this thesis.

Fig. Al-7a,h. Scaled and rotated seismograms from HFT events.

Fig. Al-8a,h. Polarization filtered seismograms from HFT events.

Fig. Al-9a,h. Expanded versions of Fig. Al-7 showing P arrivals.

Fig. Al-10a,h. Short-period seismograms from HFT events.

Fig. Al-11. Example of signal enhancement by stacking.

Fig. Al-12a,x. Raw stacked seismograms of the deep moonquake
foci used in this thesis.

Fig. Al-13a,x. Scaled and rotated seismograms from moonquake foci.

Fig. Al-14a,x. Polarization filtered seismograms from moonquake
foci.

Fig. A1-1a

72   134

12 X Y Z
14 X Y Z
15 X Y Z
16 X Y Z

45 46 47 48 49 50 51 52 53 54 55 56 57 58 59
TIME IN MINUTES

429

72 199

Fig. A1-1

TIME IN MINUTES

430

Fig. A1-1c

72 213

TIME IN MINUTES

431

Fig. A1-1d

72 324

TIME IN MINUTES

432

75 102

Fig. A1-1e

TIME IN MINUTES

433

75.124

Fig. A1-1f.

TIME IN MINUTES

434

Fig. A1-1g

76 25

TIME IN MINUTES

435

77 107

14

15

16

Fig. A1-1h

TIME IN MINUTES

72 134

Fig. A1-2a

TIME IN MINUTES

437

72 199

Fig. A1-2b

TIME IN MINUTES

55 56 57 58 59 60 61 62 63 64 65 66 67 68 69

438

72 213

Fig. A1-2c

TIME IN MINUTES

439

72 324

Fig. A1-2d

TIME IN MINUTES

440

Fig. A1-2e

75 102

TIME IN MINUTES

441

75 124

Fig. A1-2f

TIME IN MINUTES

442

76 25

Fig. A1-2g

TIME IN MINUTES

443

77 107

TIME IN MINUTES

A1-2a

72 134

TIME IN MINUTES

Fig. A1-3a

72 199

Fig. A1-3b

446

72 213

Fig. A1-3c

TIME IN MINUTES

447

72 324

Fig. A1-3d

TIME IN MINUTES

448

75 102

Fig. A1-3e

TIME IN MINUTES

449

Fig. A1-3f

75 124

TIME IN MINUTES

Fig. A1-3g

`76 25`

TIME IN MINUTES

451

Fig. A1-3h

77 107

TIME IN MINUTES

452

72 134

Fig. A1-4a

TIME IN MINUTES

453

72 199

Fig. Al-4b

TIME IN MINUTES

454

72 213

Fig. A1-4c

TIME IN MINUTES

455

72 324

Fig. A1-4d

TIME IN MINUTES

456

75 102

Fig. A1-4e

TIME IN MINUTES

457

75 124

Fig. A1-4f

TIME IN MINUTES

458

Fig. A1-4g

TIME IN MINUTES

Fig. A1-41

77 107

TIME IN MINUTES

Fig. A1-5a

Fig. A1-5b

STATION

14

72   199

P

15

P

16

P

55   60   65

TIME IN MINUTES

462

Fig. Al-5c

STATION

72 213

P (Station 14)

P (Station 15)
S

P (Station 16)

TIME IN MINUTES

463

72 324

Fig. A1-5d

STATION

14

15

16

P

P

P

TIME IN MINUTES

25

30

35

464

Fig. A1-5e

75 102

Fig. A1-5f

75   124

STATION

15

P   S

5   10   15

TIME IN MINUTES

466

Fig. A1-5g

76   25

STATION

15   P   S

16   P

TIME IN MINUTES

10   15   20

Fig. A1-5h

STATION

77 107

P

P

P

TIME IN MINUTES

14

15

16

35

40

45

468

Fig. A1-6a

23 171

Fig. A1-6b

TIME IN MINUTES

74 192

Fig. Al-6c

TIME IN MINUTES

471

Fig. A1-6d.

TIME IN MINUTES

472

75 44

Fig. A1-6e

TIME IN MINUTES

Fig. A1-6f

76 66

Fig. A1-6g

TIME IN MINUTES

475

Fig. A1-6h

TIME IN MINUTES

476

Fig. Al-7a

Fig. A1-7b

478

Fig. A1-7c

74 192

TIME IN MINUTES

479

Fig. A1-7d

TIME IN MINUTES

480

75 44

Fig. A1-7e

TIME IN MINUTES

481

Fig. A1-7f

TIME IN MINUTES

Fig. A1-7g

76 66

TIME IN MINUTES

483

Fig. A1-7h

Fig. A1-8a

Fig. A1-8b

486

Fig. A1-8c

74 192

TIME IN MINUTES

487

Fig. A1-8a

TIME IN MINUTES

488

75 44

Fig. A1-8e

489

76 4

Fig. A1-8f

TIME IN MINUTES

490

Fig. A1-8g

Fig. A1-8h

TIME IN MINUTES

492

73 72

Fig. A1-9a

TIME IN MINUTES

493

Fig. A1-9b

73 171

TIME IN MINUTES

494

74 192

Fig. A1-9c

TIME IN MINUTES

495

Fig. A1-9d

TIME IN MINUTES

75 44

Fig. A1-9e

TIME IN MINUTES

497

Fig. A1-9f

TIME IN MINUTES

Fig. A1-94

76 66

TIME IN MINUTES

499

76 68

Fig. A1-9h

TIME IN MINUTES

Fig. A1-10a

Fig. A1-10b

Fig. A1-10c

74 192

STATION

14
P

15
P

16
P

TIME IN MINUTES

50   55   60

Fig. A1-10d

75 3

STATION

14

P

15

P

16

P

S

45   50   55

TIME IN MINUTES

5.04

Fig. Al-10e

75 44

Fig. A1-10f

STATION

76   4

S

P   S

P   S

20   25   30

TIME IN MINUTES

Fig. A1-10g

Fig. A1-10h

TIME IN MINUTES

Fig. A1-11

P

STACK

DAY 156 (reverse)

I MIN

DAY 80

DAY 163

DAY 245

DAY 110

FOCUS A1   STATION 14   N-S COMPONENT

FOCUS A1

Fig. A1-12a

TIME IN MINUTES

FOCUS A15

Fig. A1-12b

511

FOCUS A16

Fig. A1-12c

TIME IN MINUTES

512

FOCUS A17

Fig. A1-12d

TIME IN MINUTES

513

FOCUS A18

Fig. A1-12e

TIME IN MINUTES

514

FOCUS A20

Fig. A1-12f

TIME IN MINUTES

FOCUS A27

Fig. A1-12g

TIME IN MINUTES

FOCUS A30

Fig. A1-12h
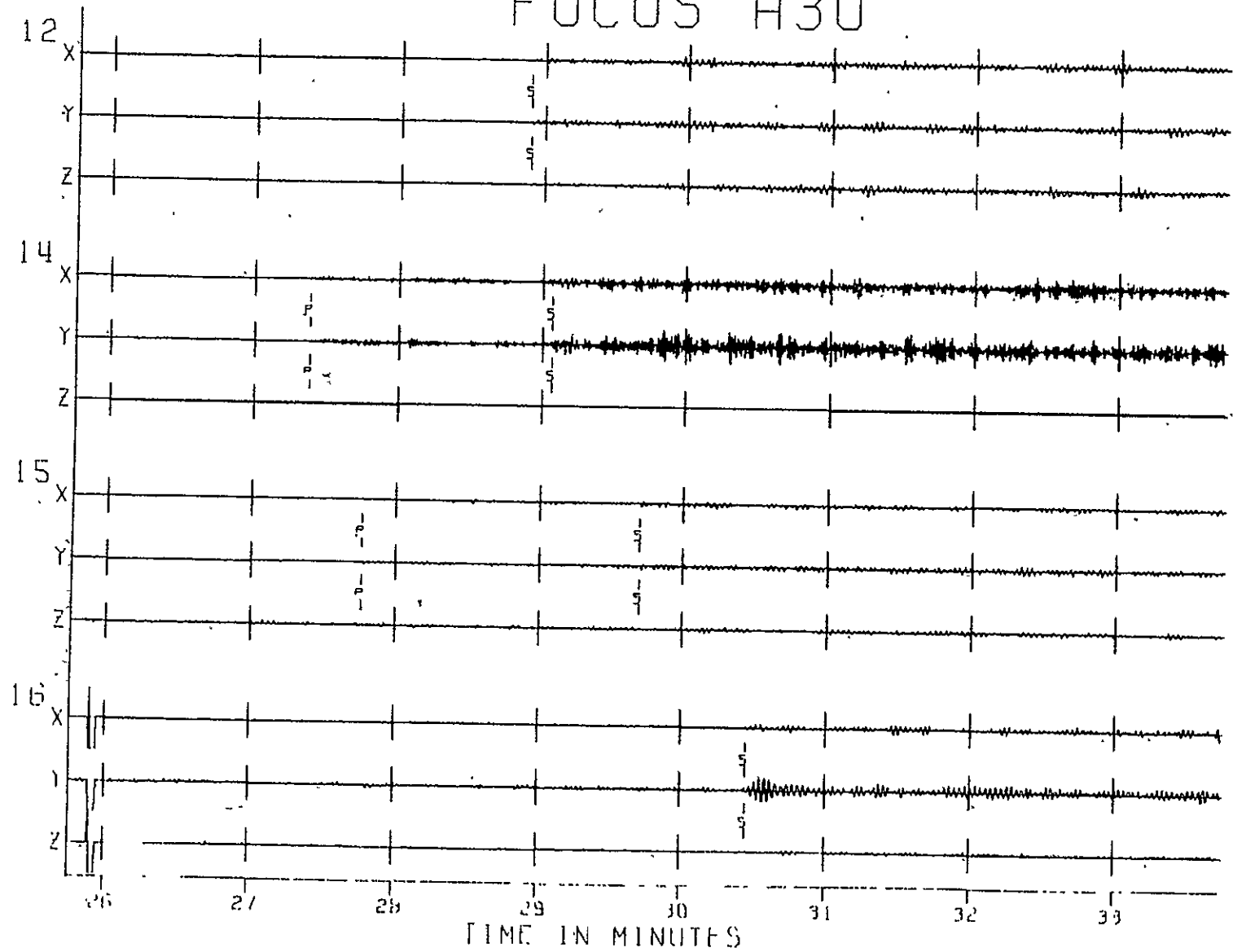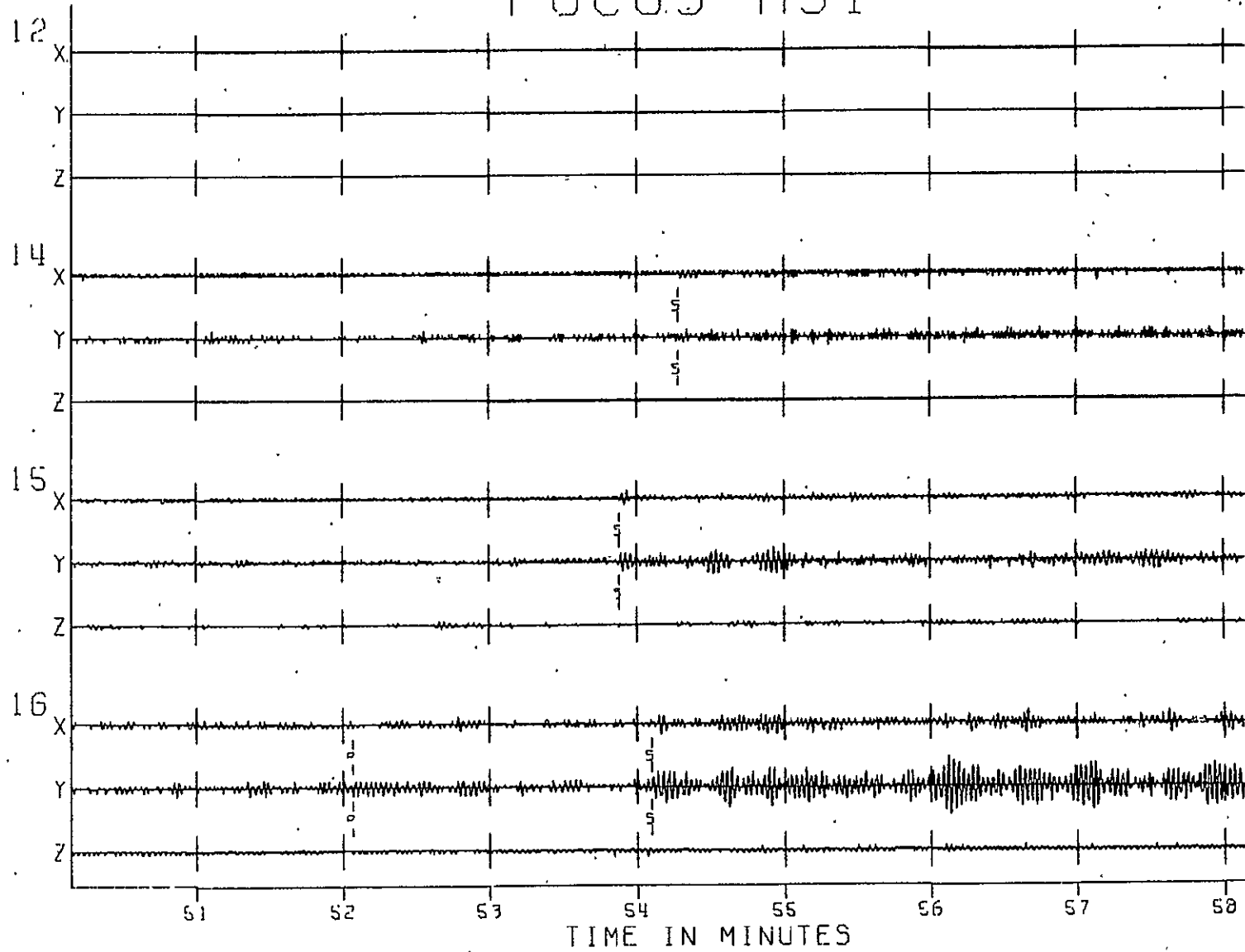
517

FOCUS A31

Fig. Al-12i

TIME IN MINUTES

FOCUS A32

Fig. A1-12j
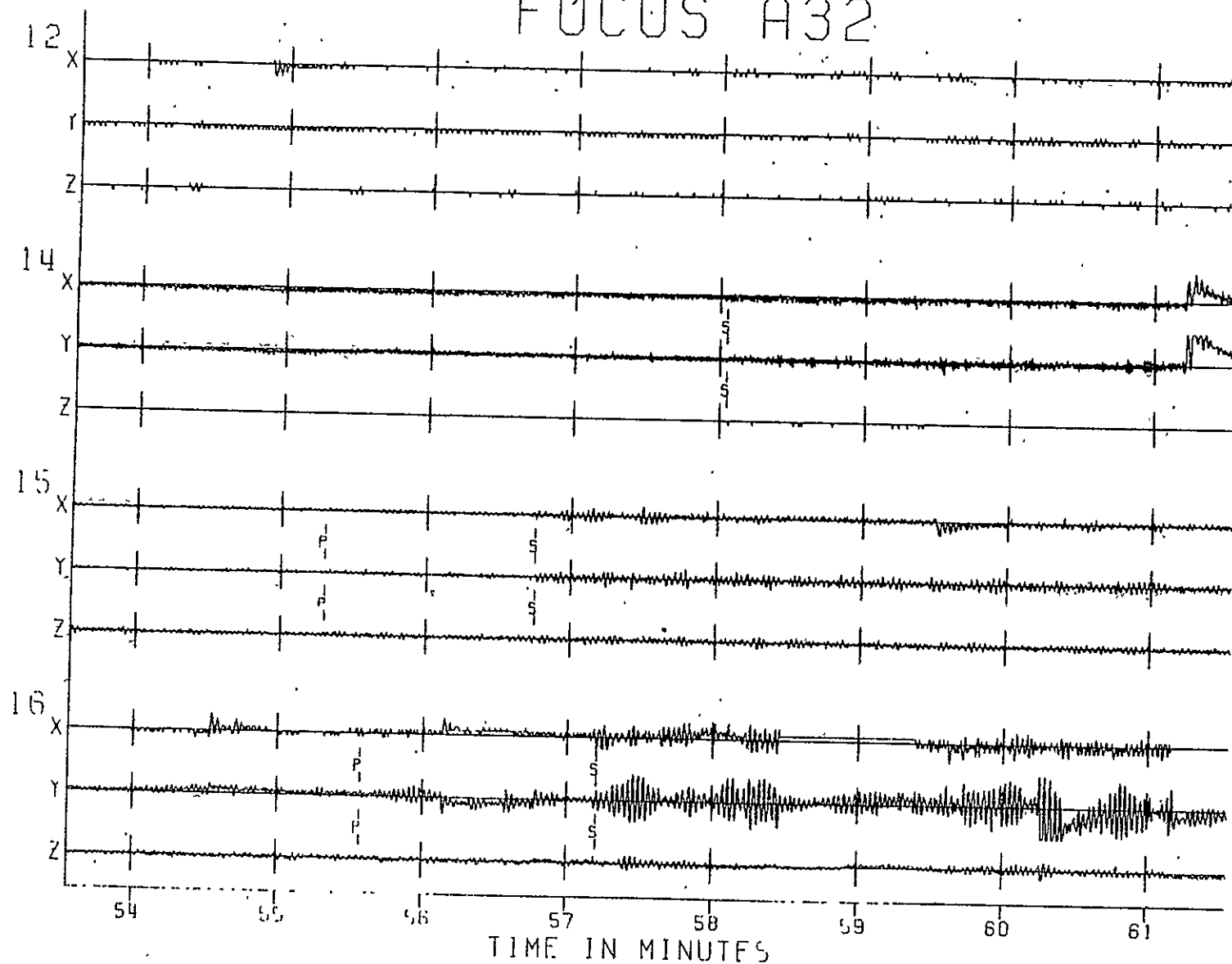
TIME IN MINUTES

FOCUS A33

Fig. A1-12k
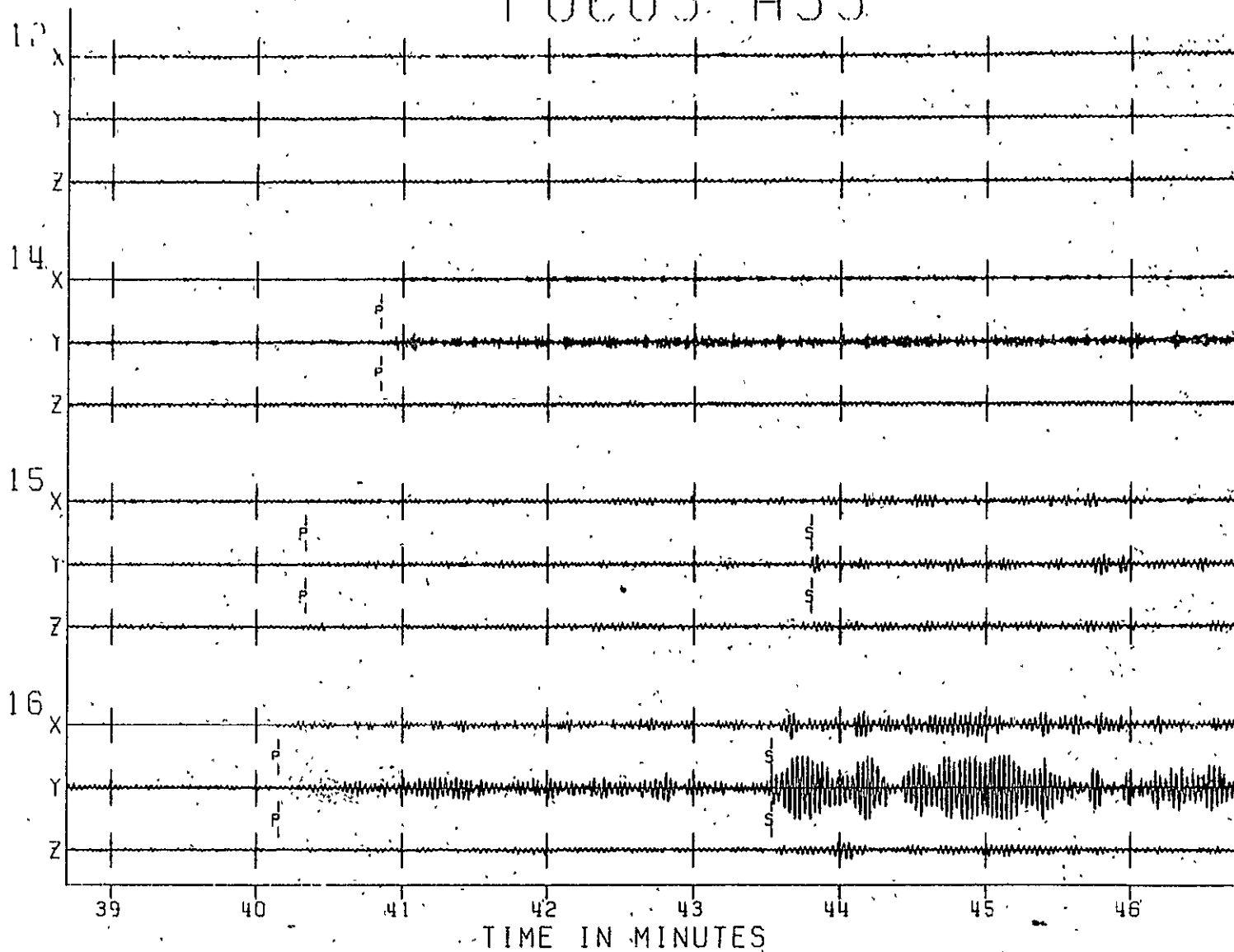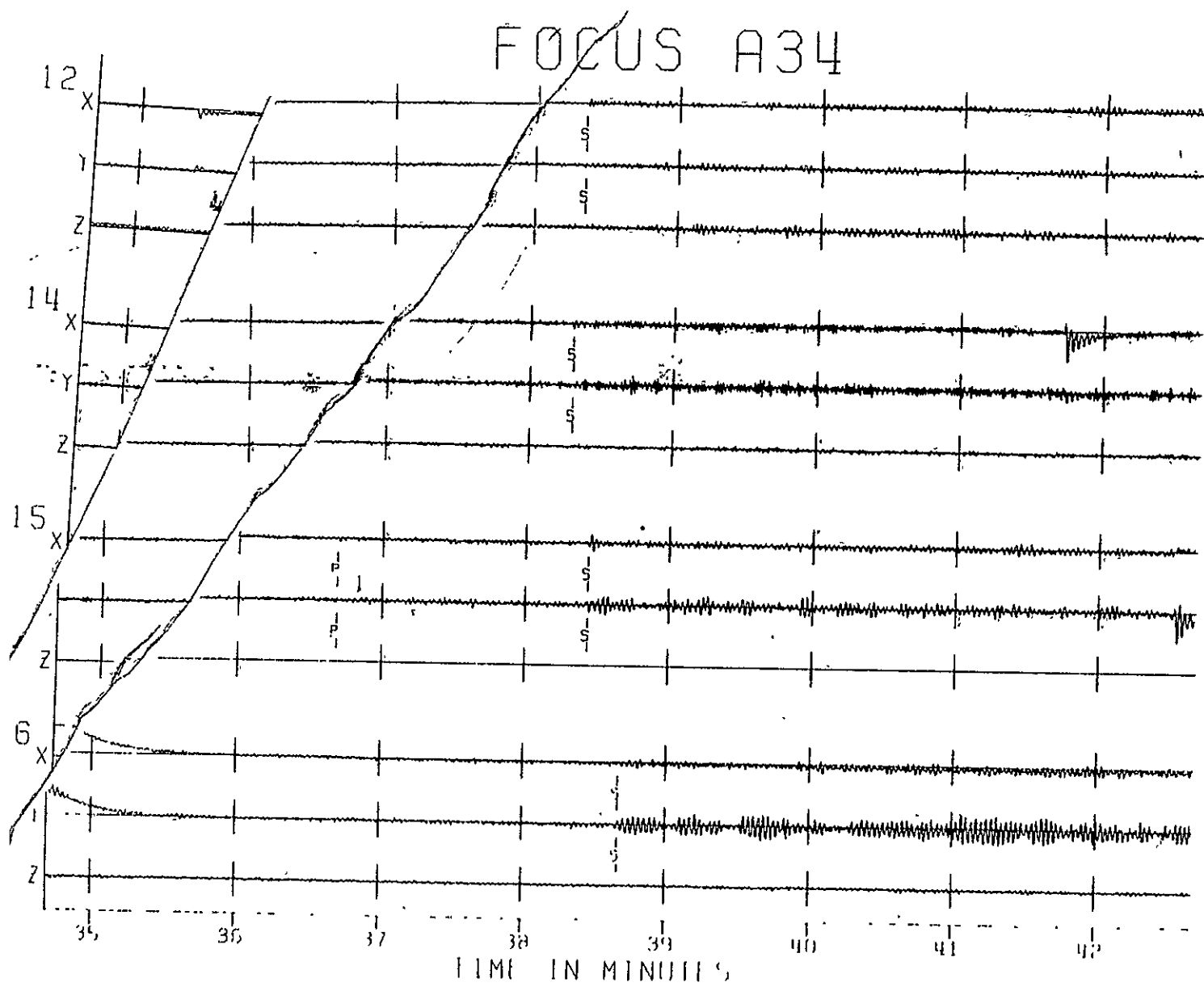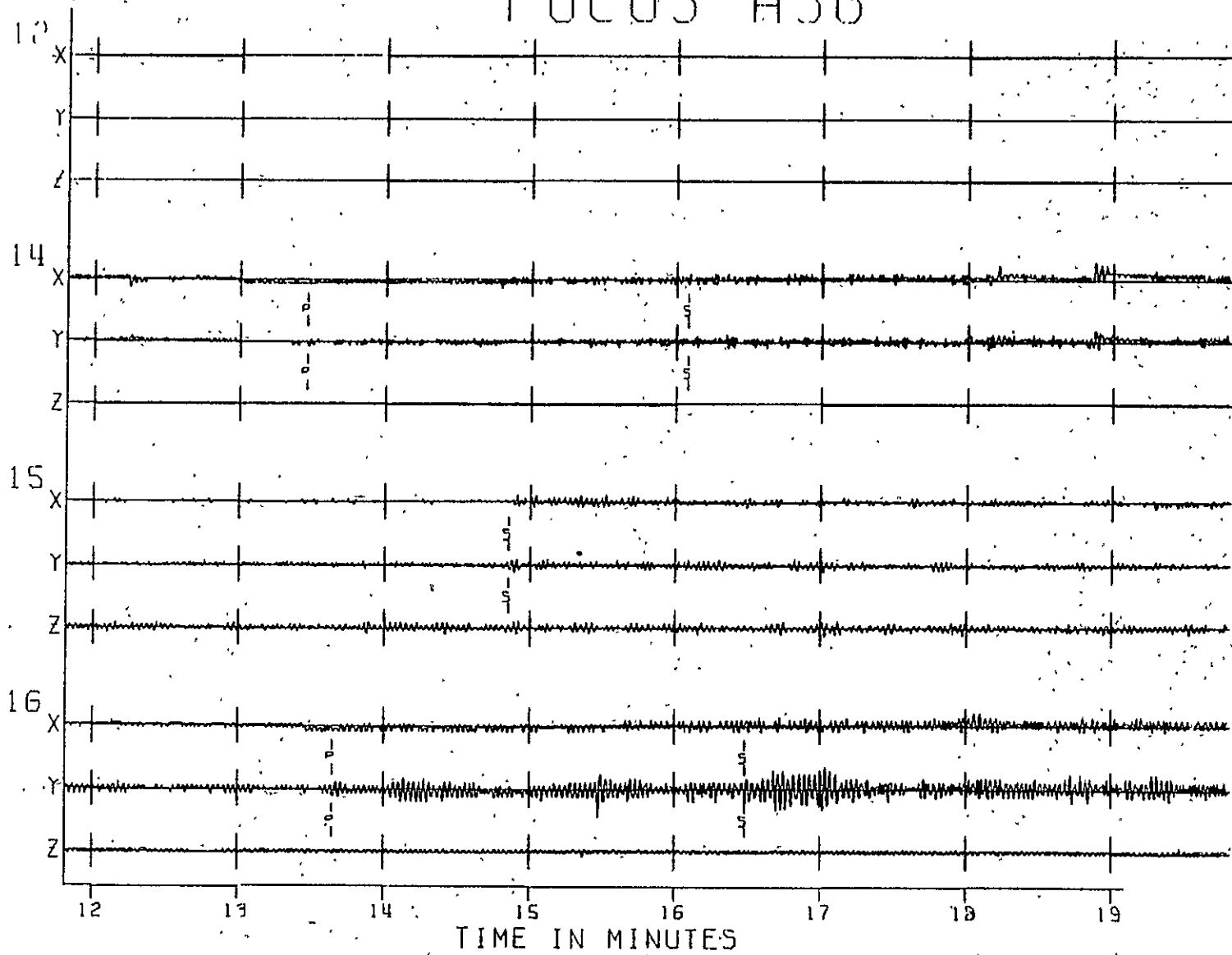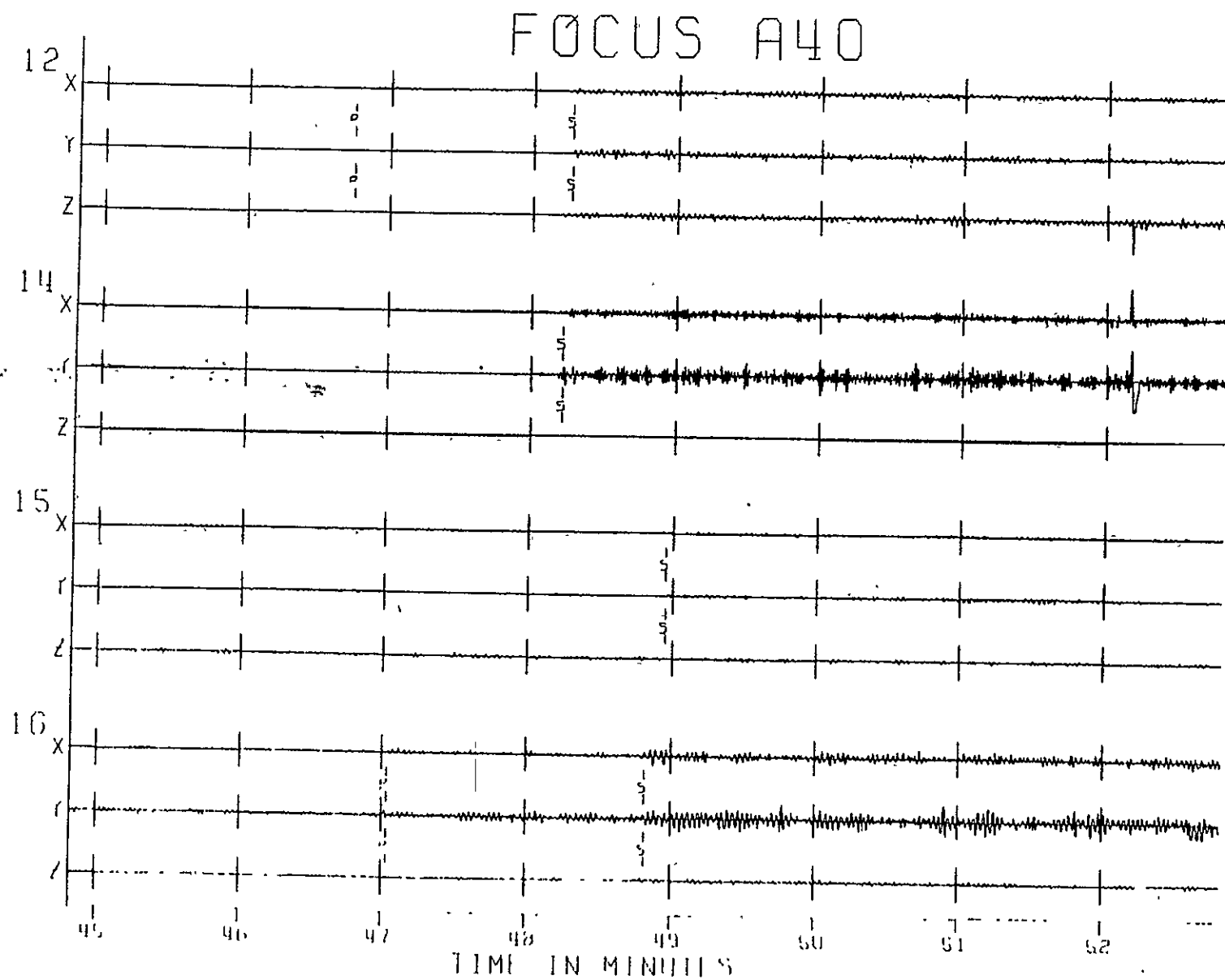
520

TIME IN MINUTES

FOCUS A34

Fig. A1-121

TIME IN MINUTES

521

FOCUS A36

Fig. A1-12m

TIME IN MINUTES

522

FOCUS A40

Fig. Al-12n

TIME IN MINUTES

523

FOCUS A4

Fig. A1-120

TIME IN MINUTES

524

FOCUS A42

Fig. A1-12P

TIME IN MINUTES

525

FOCUS A44

Fig. A1-12q

TIME IN MINUTES

FOCUS A45

Fig. A1-12r.

TIME IN MINUTES

527
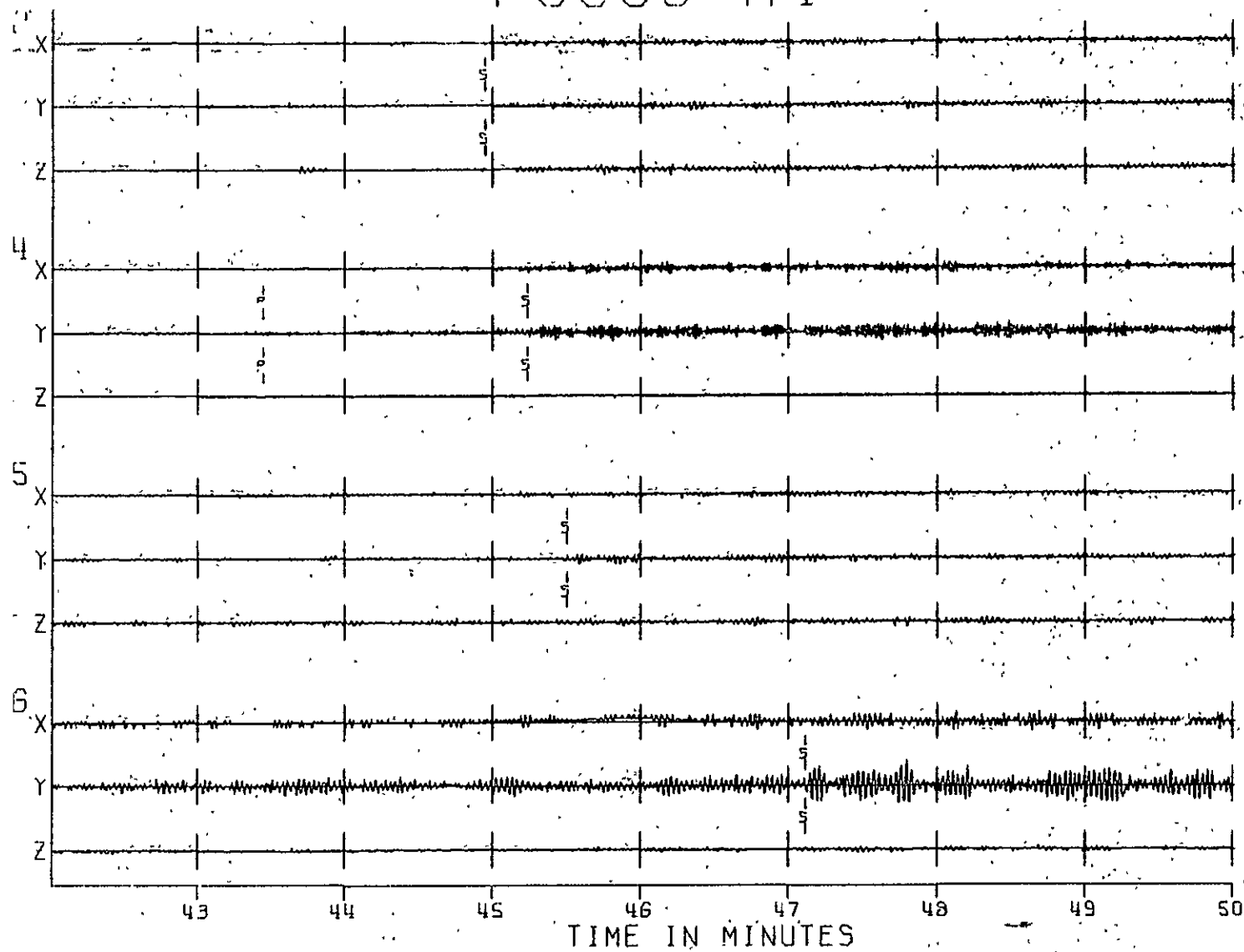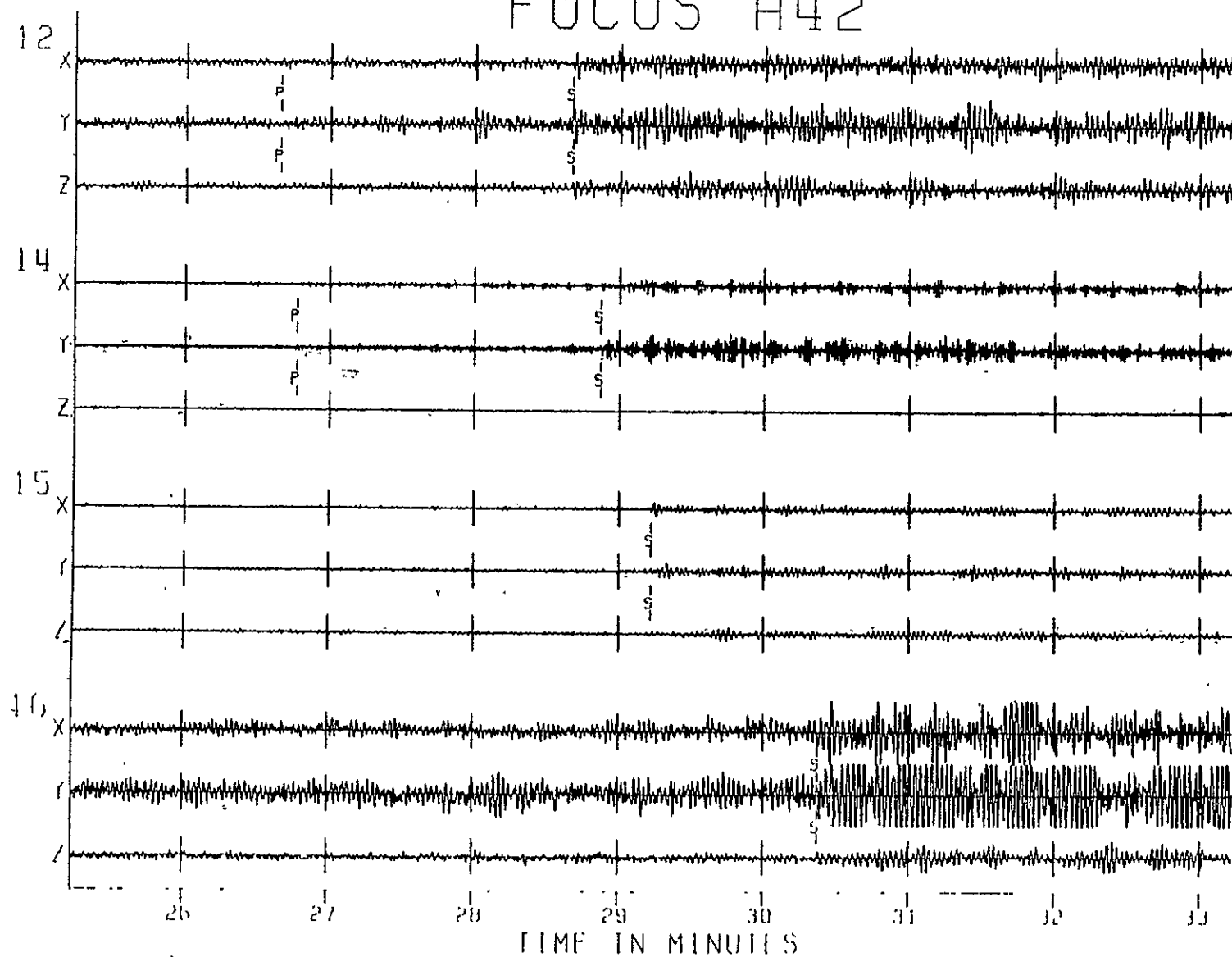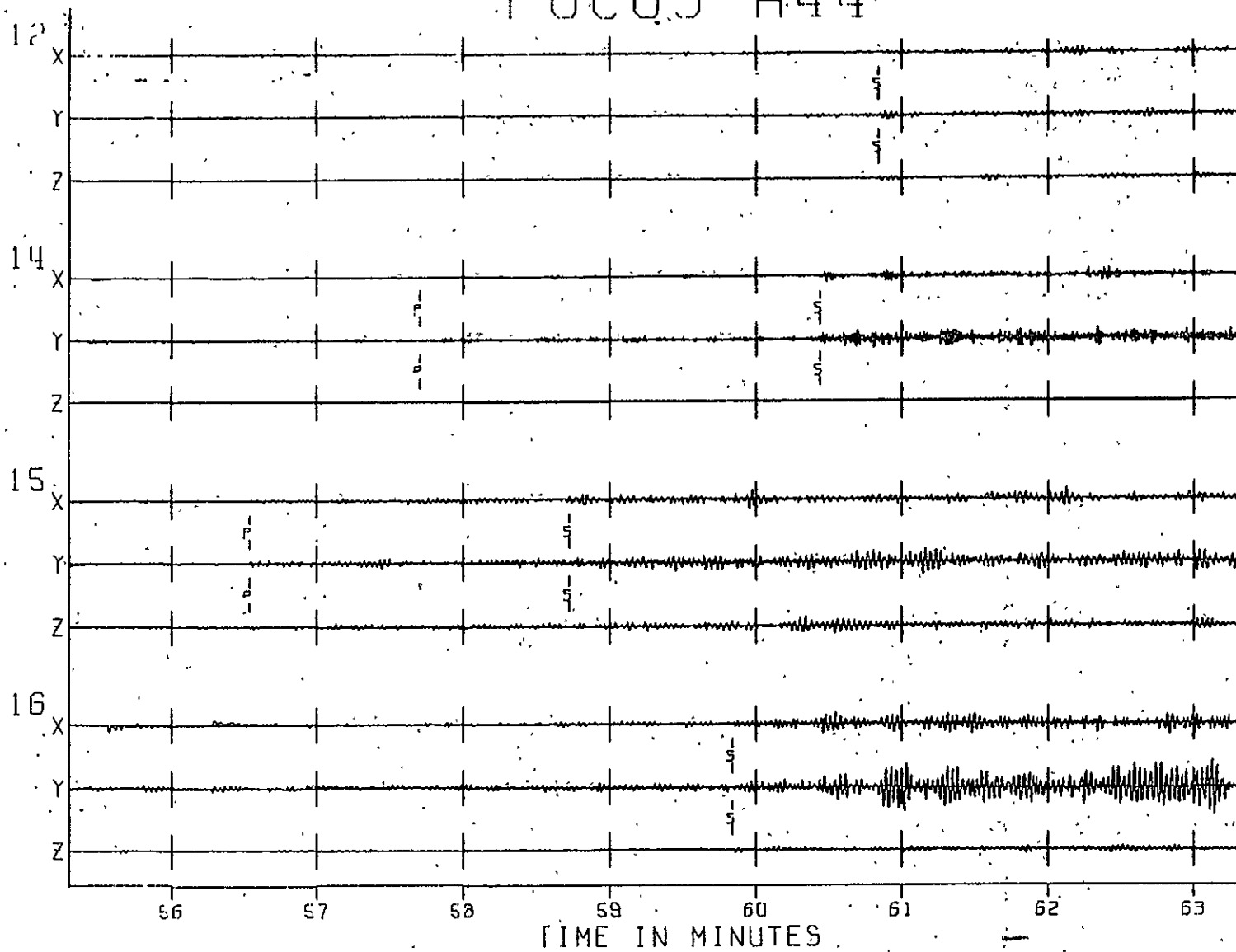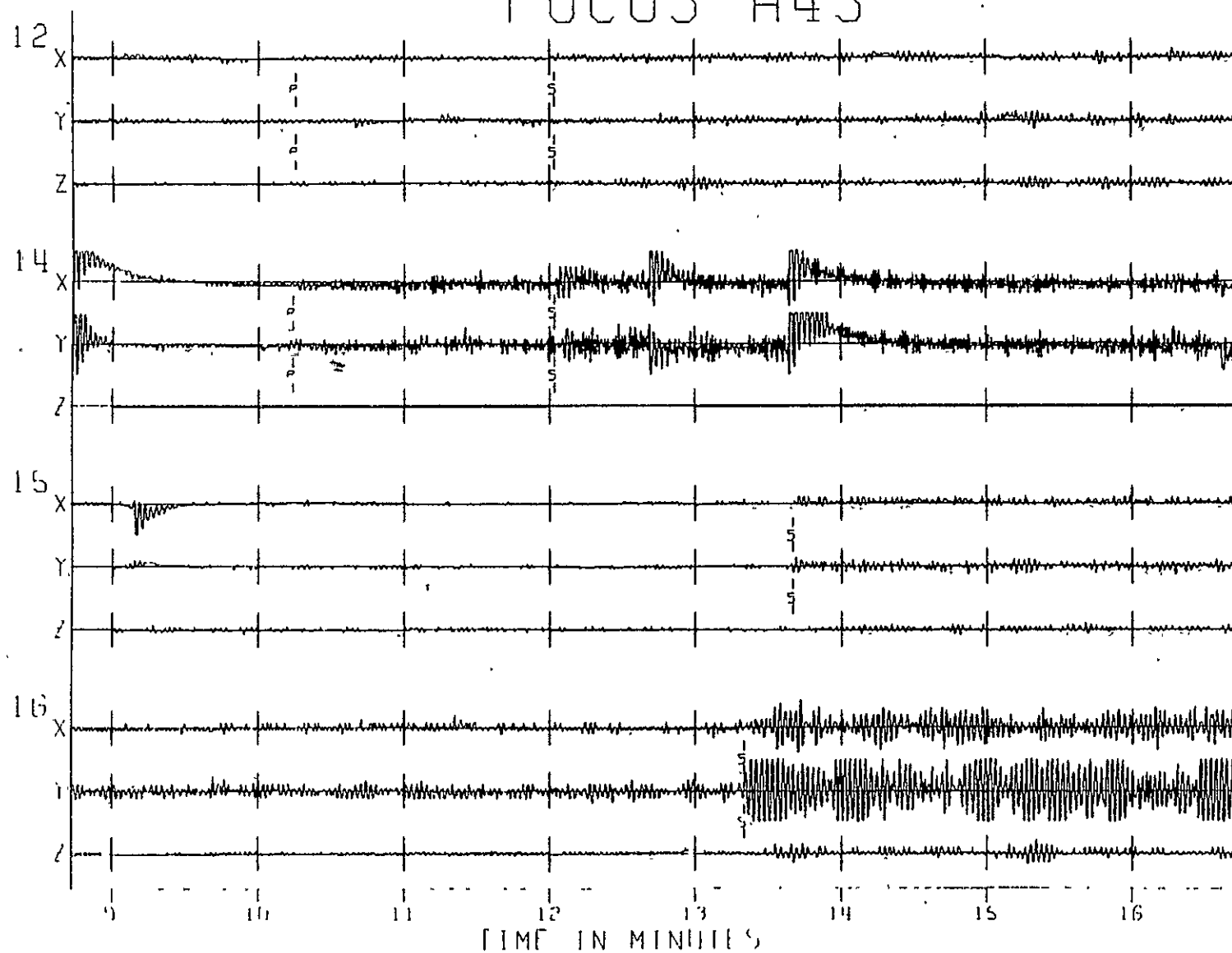
FOCUS A46

Fig. A1-12s

TIME IN MINUTES

FOCUS A50

Fig. A1-12t

TIME IN MINUTES

Fig. A1-12

FOCUS A5

TIME IN MINUTES

FOCUS A56

Fig. AL-127

TIME IN MINUTES

531

Fig. A1-12w

FOCUS H61

TIME IN MINUTES
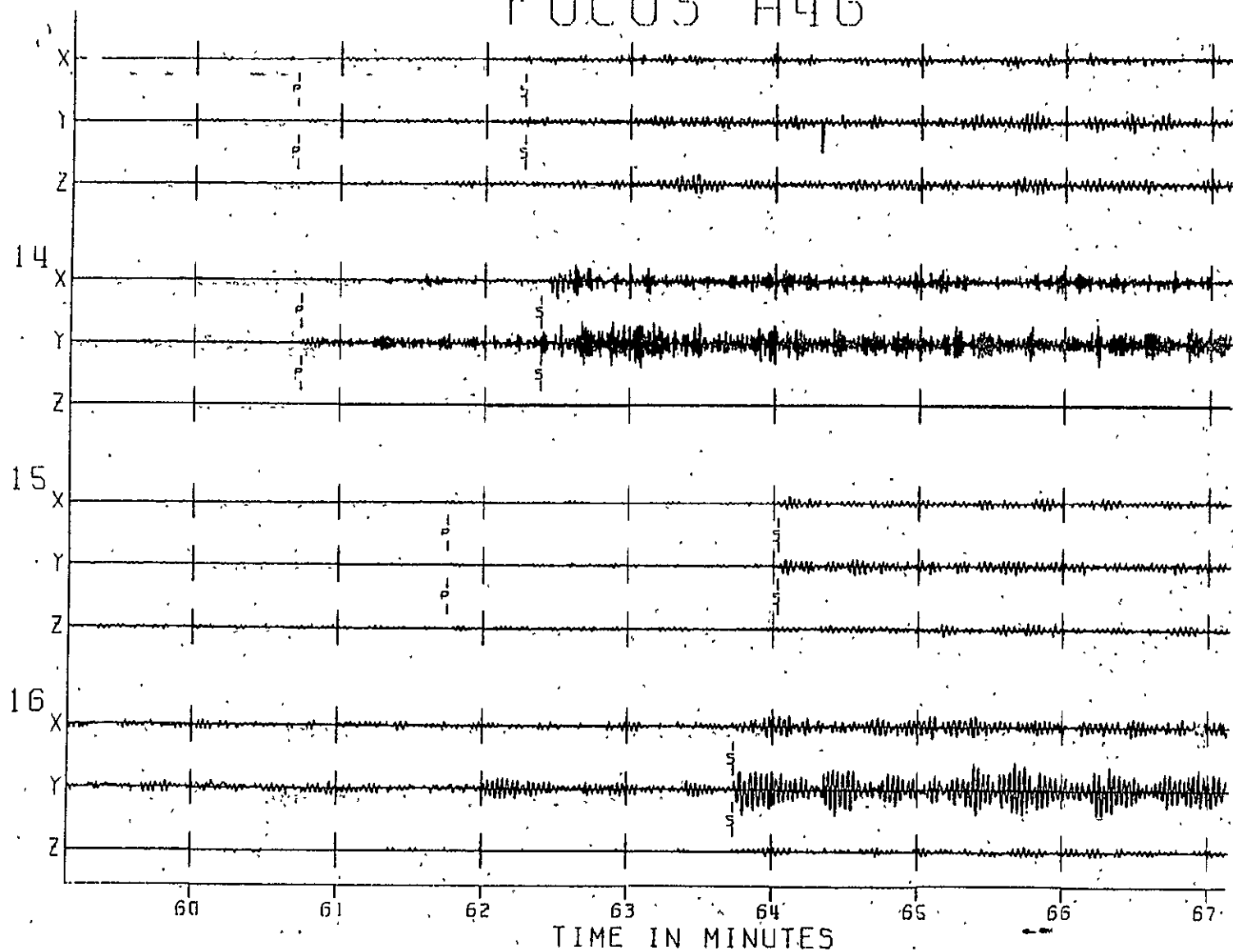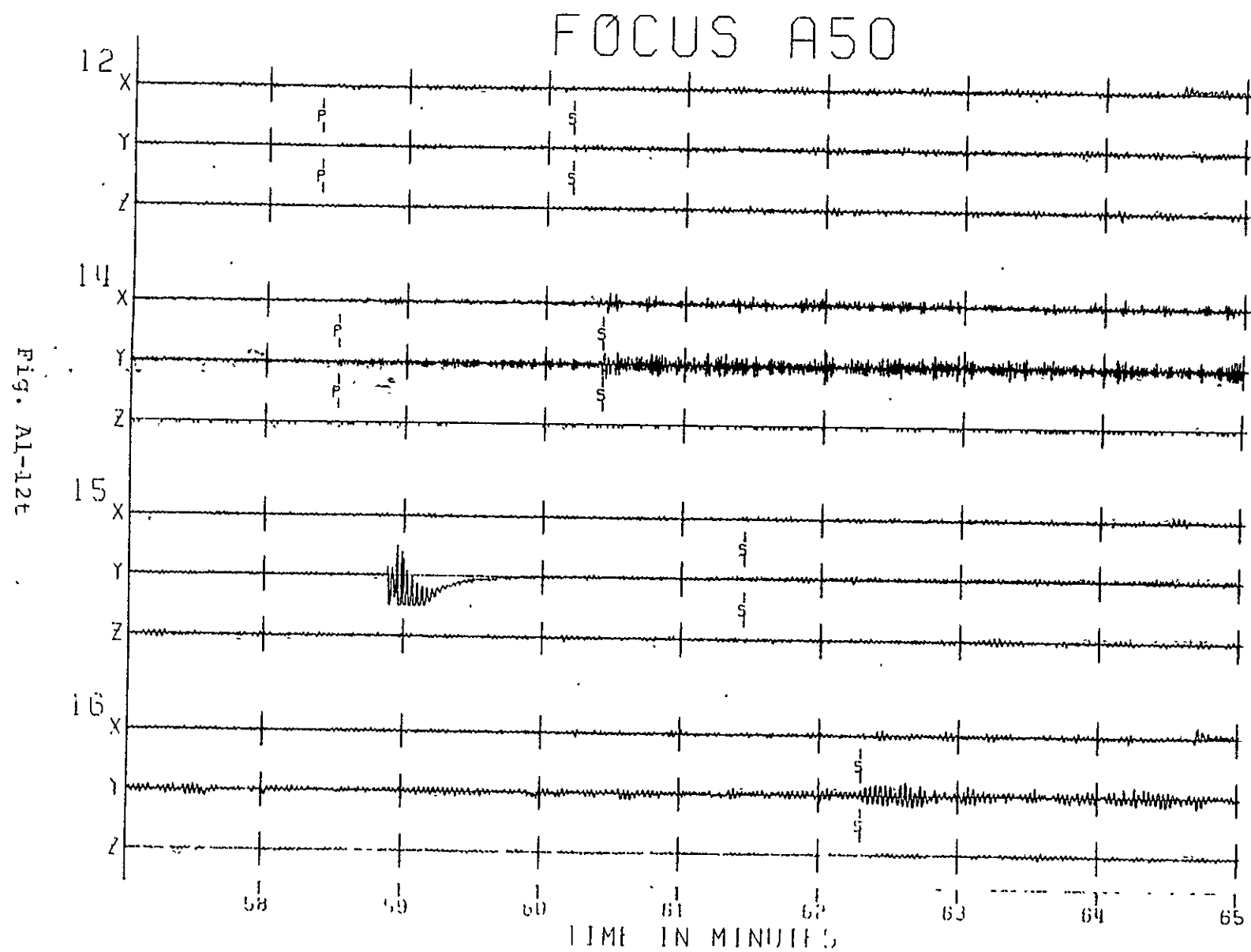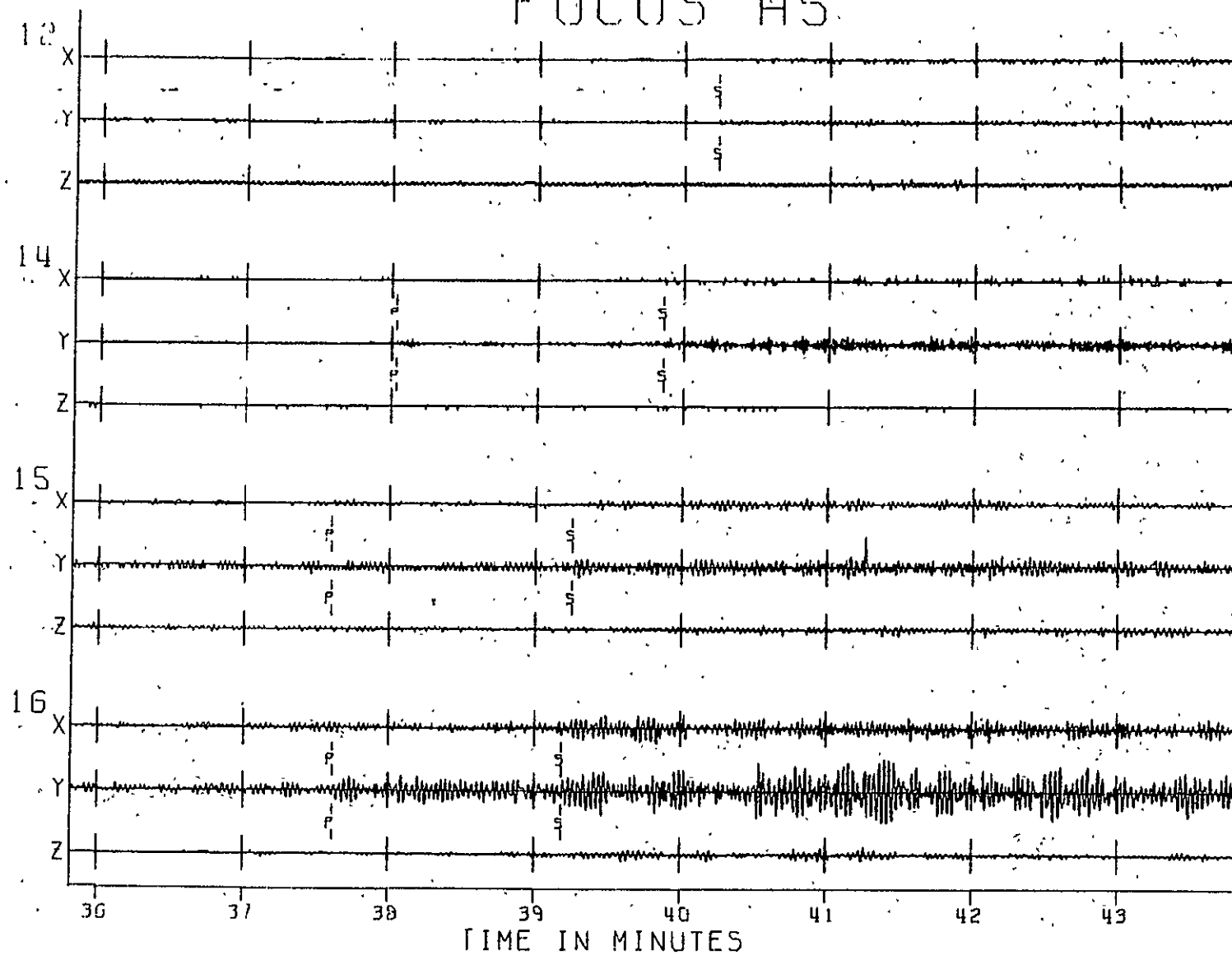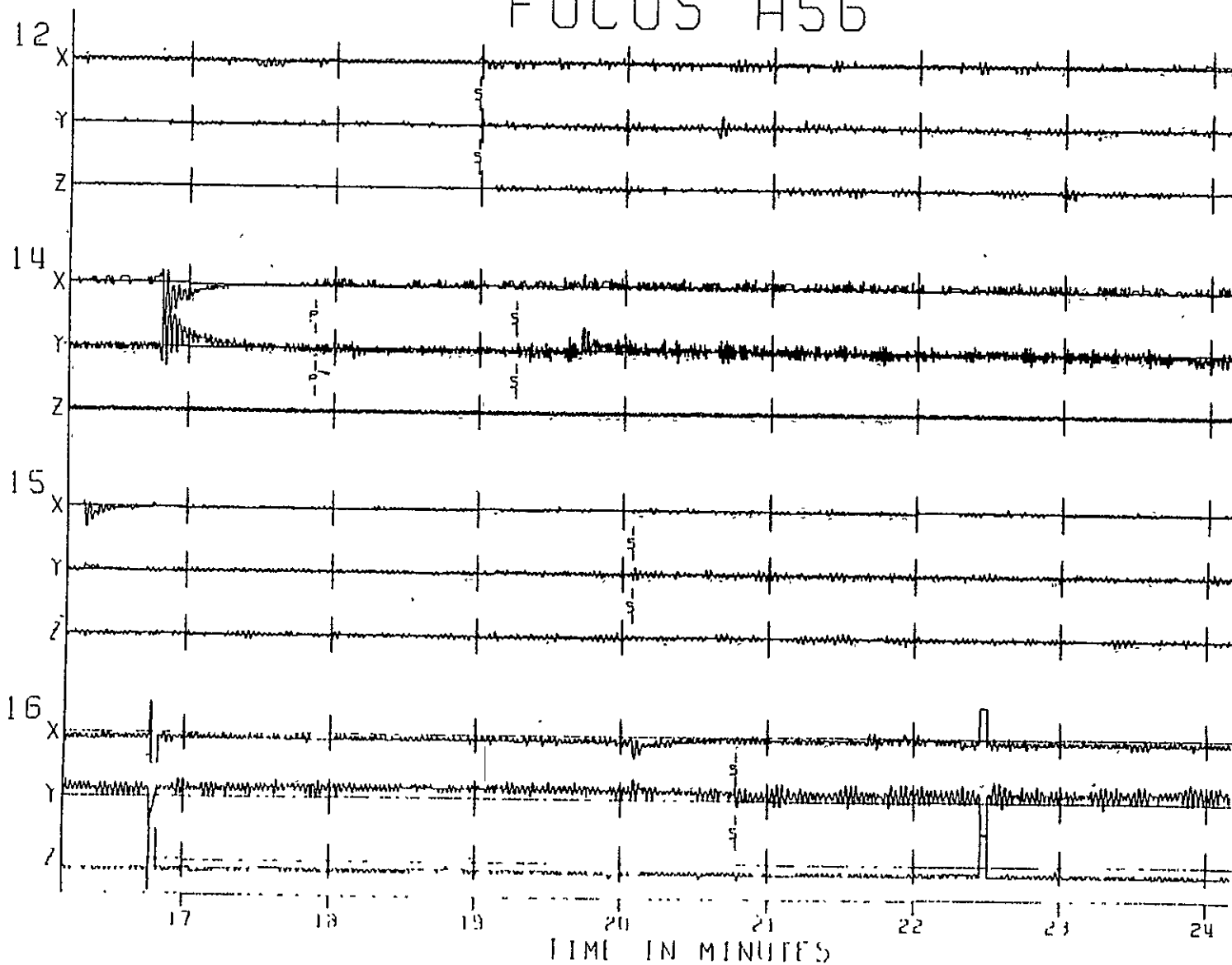
FOCUS A62

Fig. A1-12z

TIME IN MINUTES

FOCUS A1

TIME IN MINUTES

Fig. A1-13a

534

FOCUS A15

Fig. A1-13b

Fig. A1-13c

FOCUS A16

TIME IN MINUTES

536

FOCUS A17

Fig. A1-13a

537

FOCUS A18

Fig. A1-13e

FOCUS A20

TIME IN MINUTES

OCUS A27

Fig. A1-13g

TIME IN MINUTES

540

FØCUS A30

Fig. A1-13h

TIME IN MINUTES

541

FOCUS A31

Fig. A1-13i

TIME IN MINUTES

FOCUS A32

Fig. A1-13j

TIME IN MINUTES

543

Fig: A1-13k

FOCUS A34.

Fig. A1-131

TIME IN MINUTES

545

FOCUS H36

Fig. A1-13m

TIME IN MINUTES

FOCUS A40

Fig. A1-13n

TIME IN MINUTES

FOCUS A41

Fig. A1-130

TIME IN MINUTES

548

.FOCUS A42

Fig. A1-13p

TIME IN MINUTES

549

Fig. A1-13q

FOCUS A45

Fig. A1-13r

TIME IN MINUTES

551

FOCUS A46

TIME IN MINUTES

Fig. A1-13s

552

FOCUS A50

TIME IN MINUTES

Fig. A1-13t

553

FOCUS A51

TIME IN MINUTES

Fig. A1-13u

554

FOCUS A56

Fig. A1-13v

TIME IN MINUTES

555

Fig. A1-13w.

FOCUS: A61

TIME IN MINUTES

FOCUS A62

Fig. A1-14a

TIME IN MINUTES

FOCUS A15

Fig. A1-14b

Fig. A1-14

TIME IN MINUTES

560

FOCUS A17

Fig. A1-14d

TIME IN MINUTES

FOCUS A18

TIME IN MINUTES

Fig. A1-14e

562

FØCUS A20

Fig. A1-14f

TIME IN MINUTES

563

FOCUS H27

Fig. A1-14g

TIME IN MINUTES

564

FOCUS A30

Fig. A1-14h

TIME IN MINUTES

565

Fig. A1-141

LOCUS H31

TIME IN MINUTES

566

FOCUS A32

Fig. A1-14j

TIME IN MINUTES

567

FOCUS H33

Fig. A1-14k

TIME IN MINUTES

FØCUS A34

Fig. A1-141

TIME IN MINUTES

569
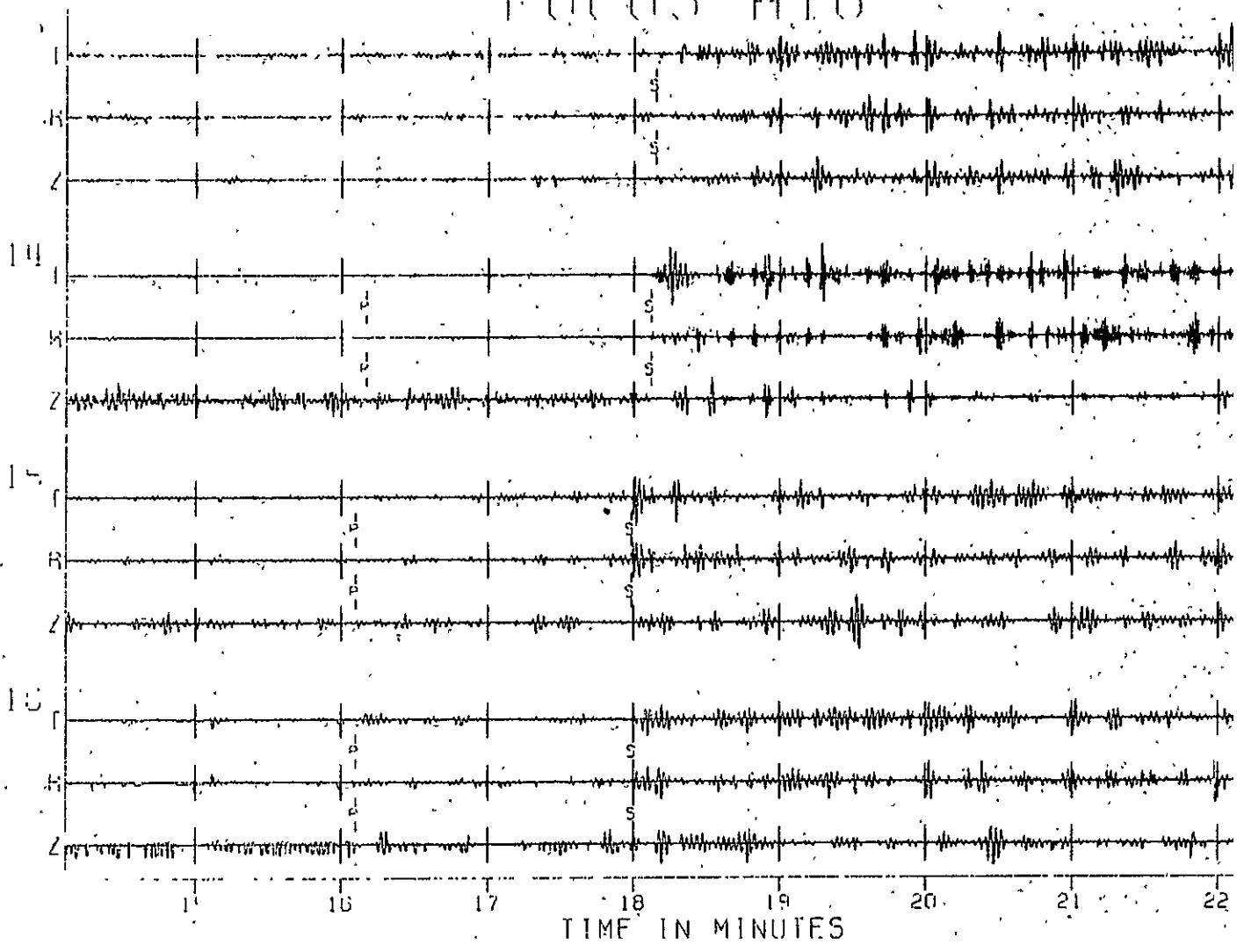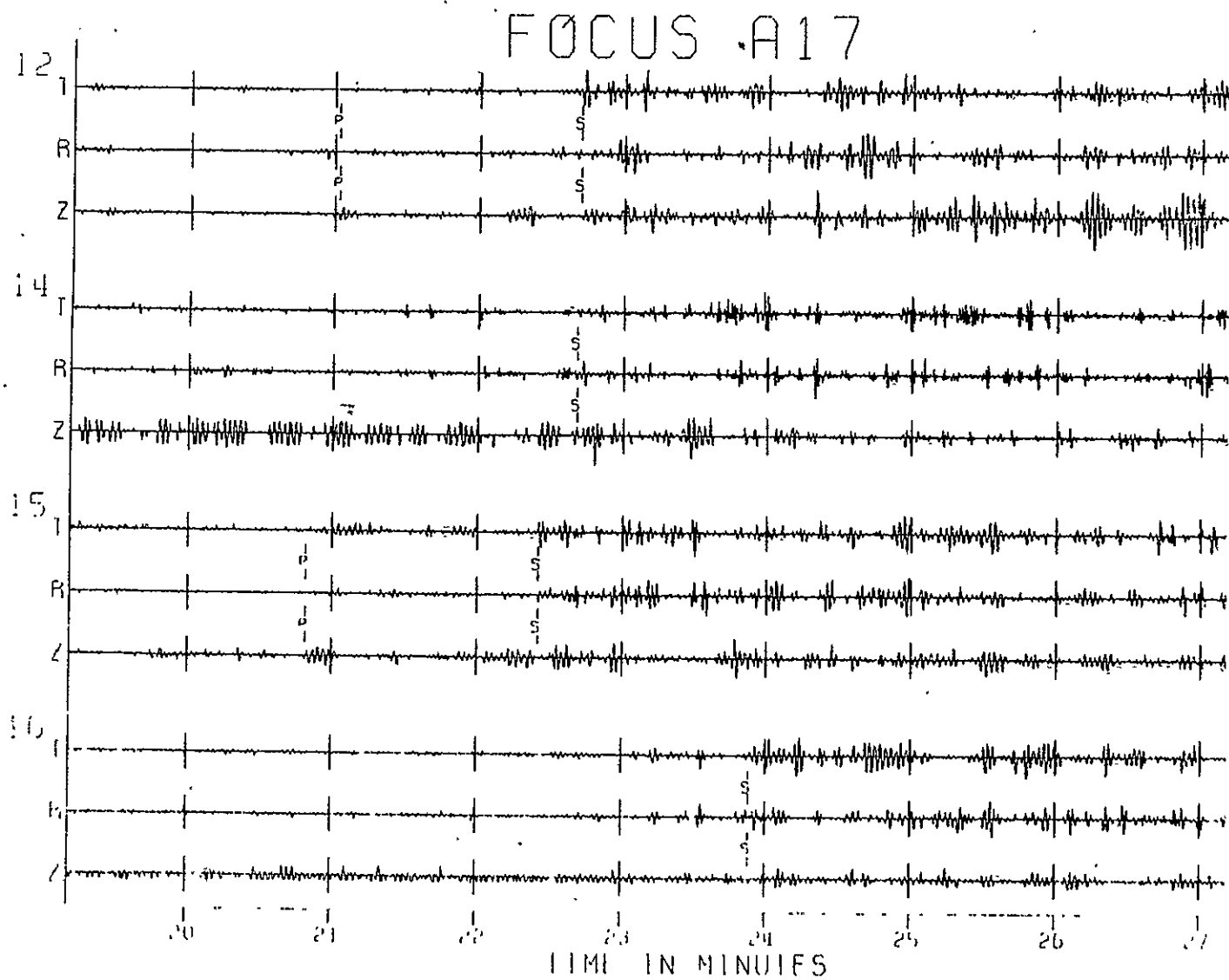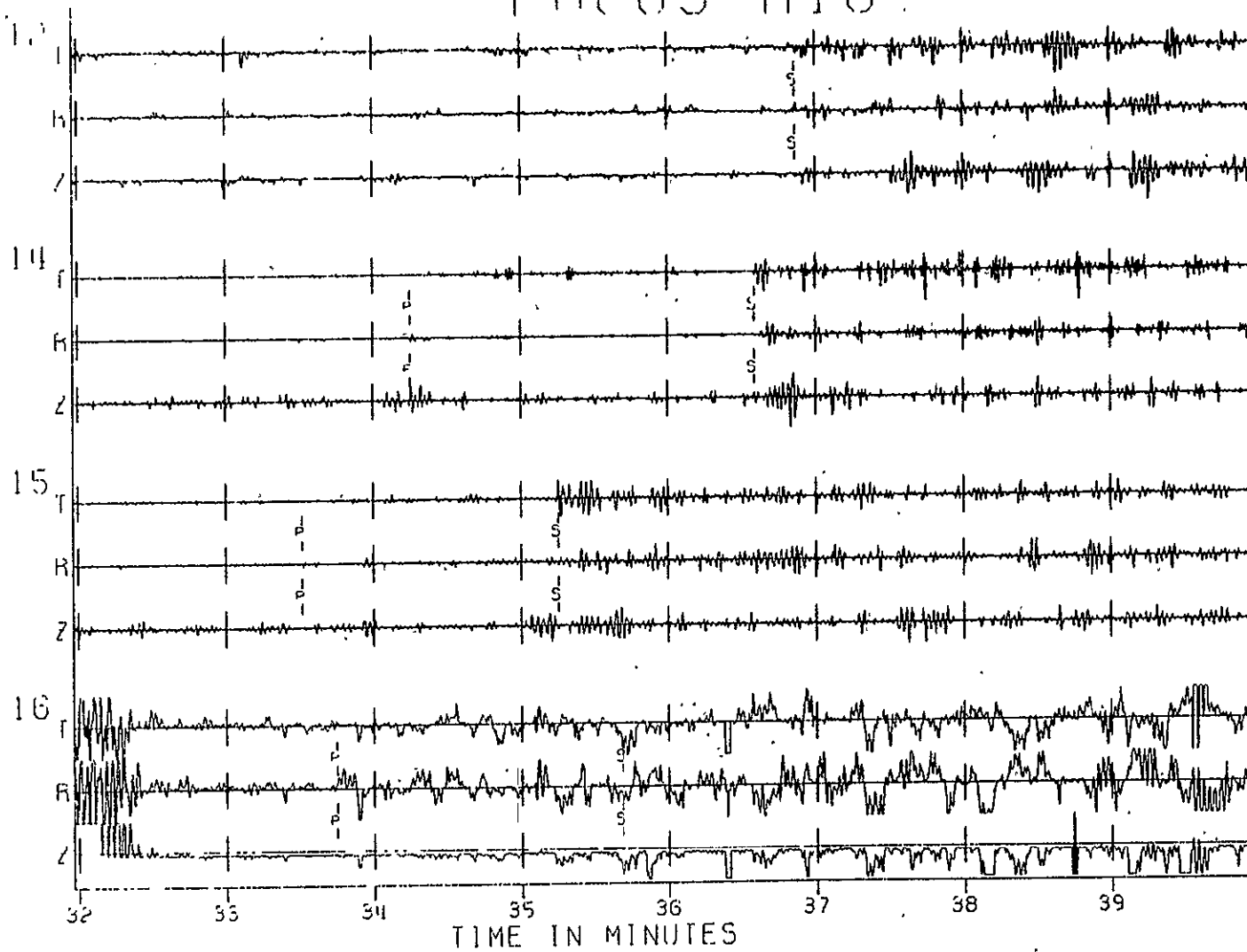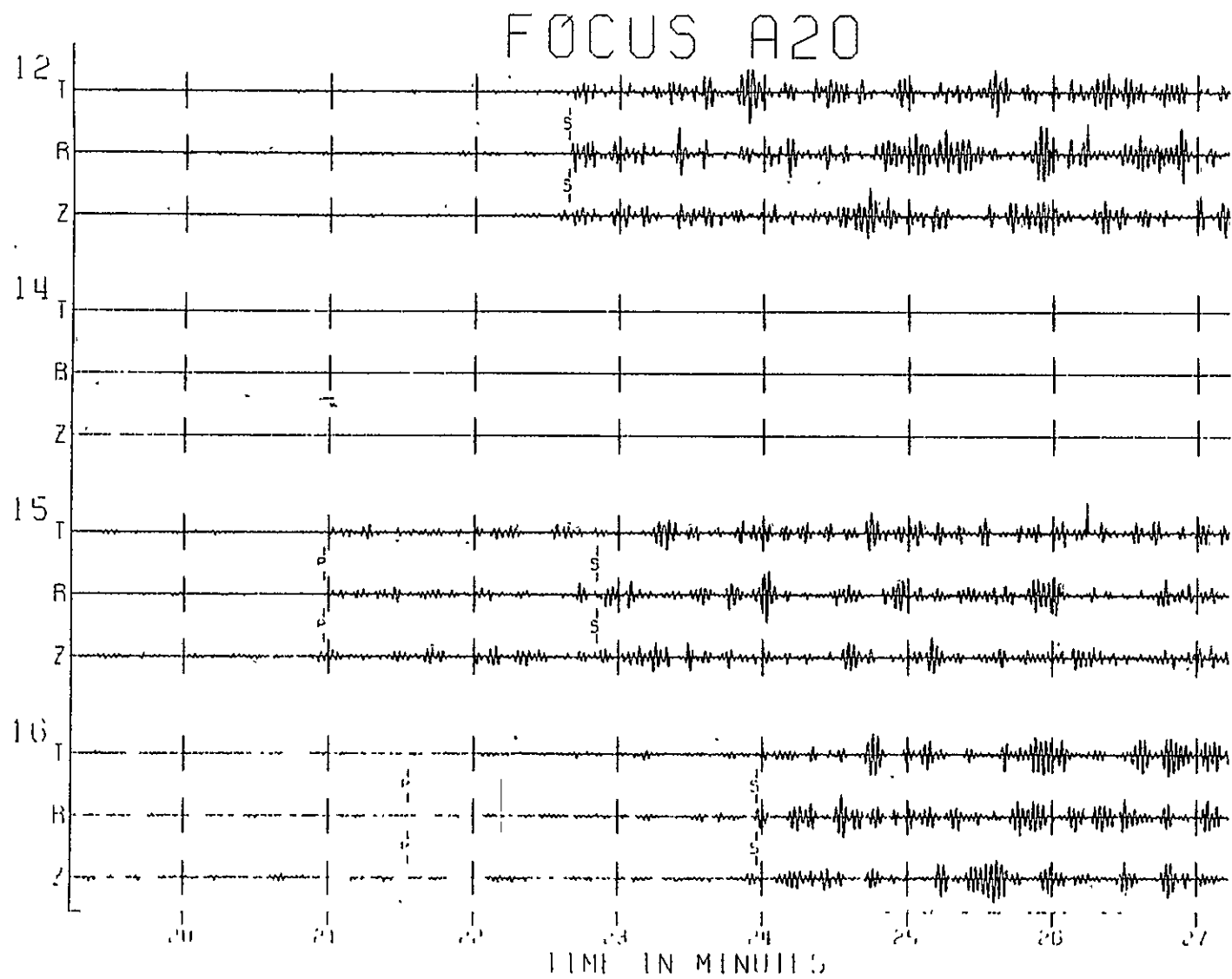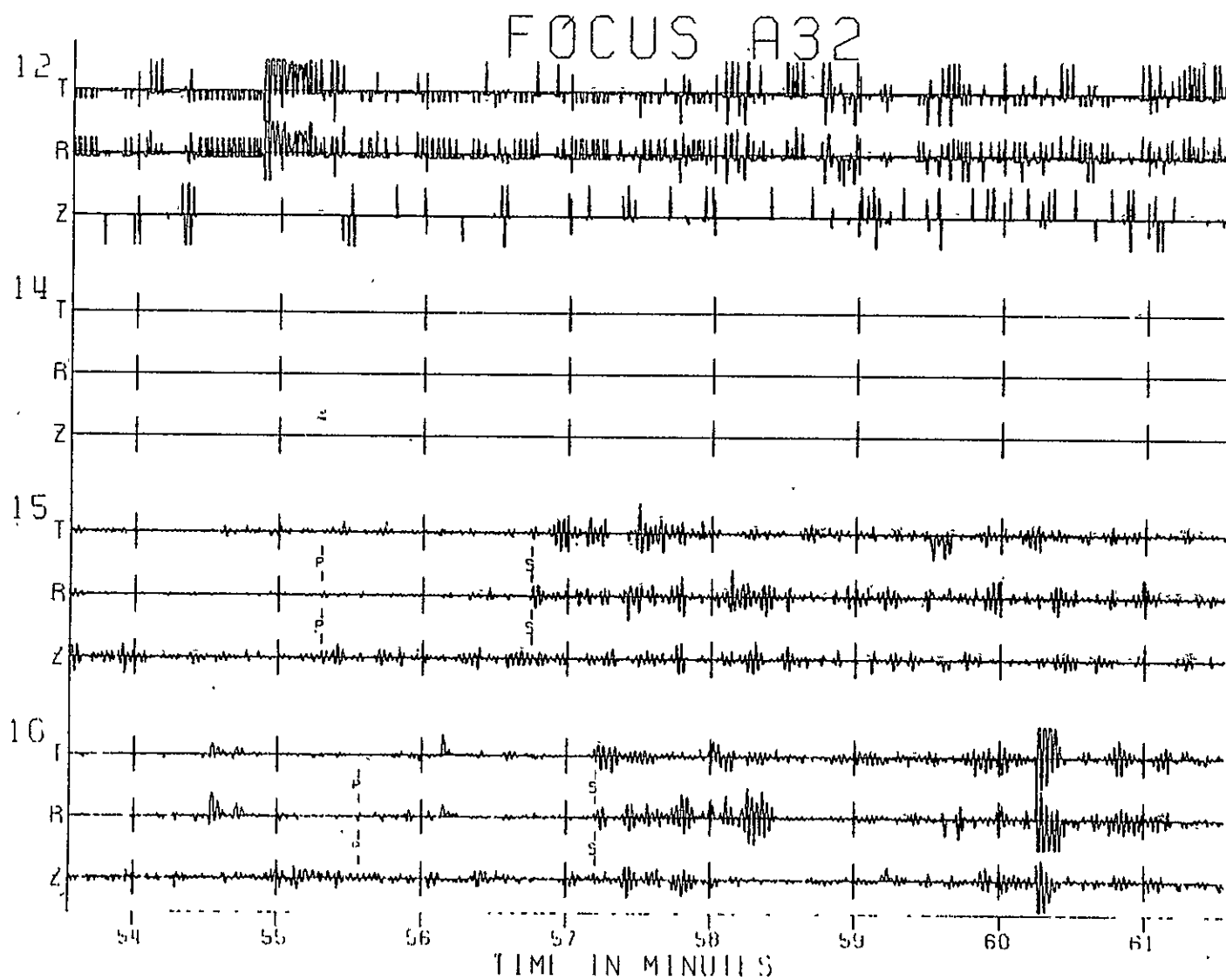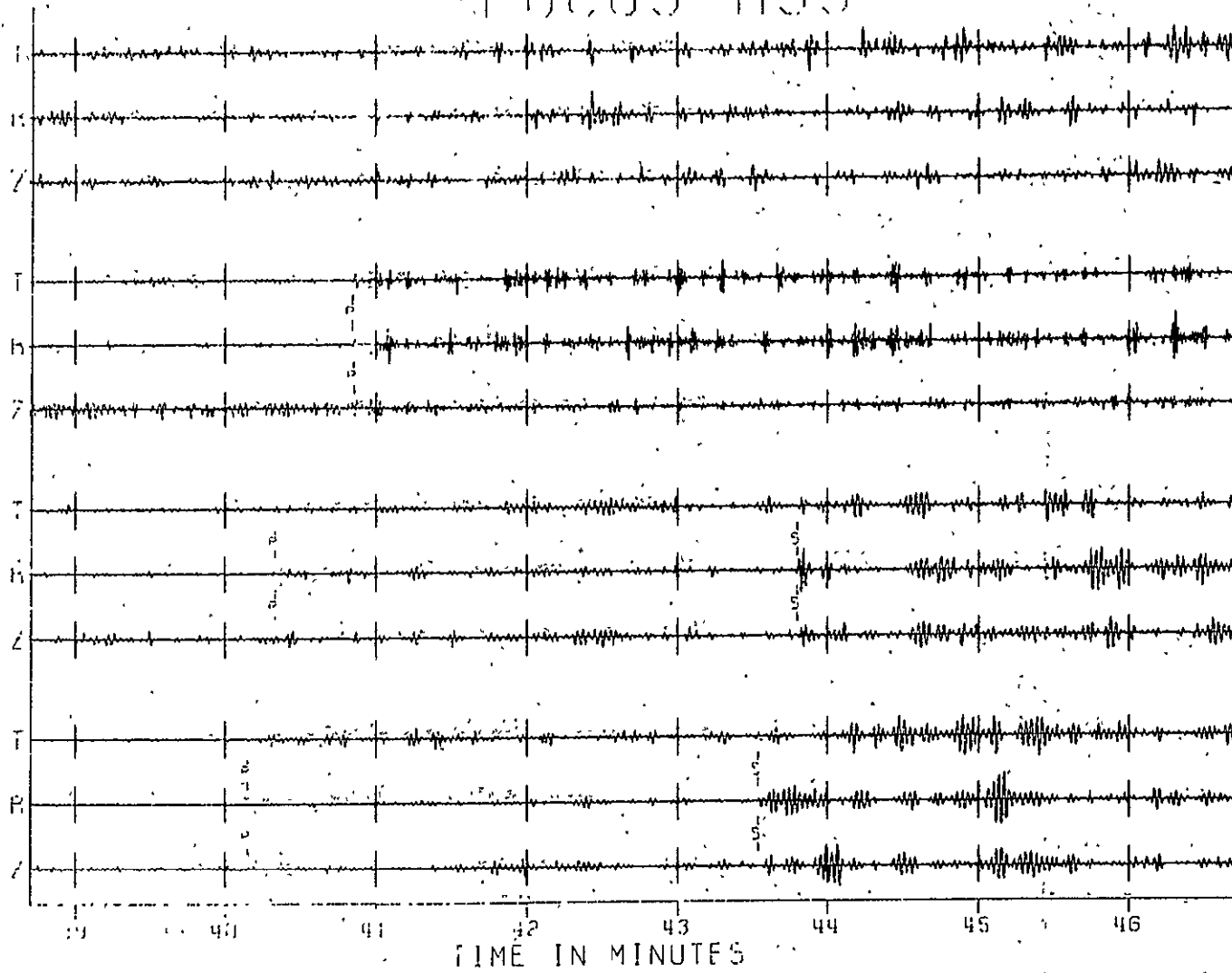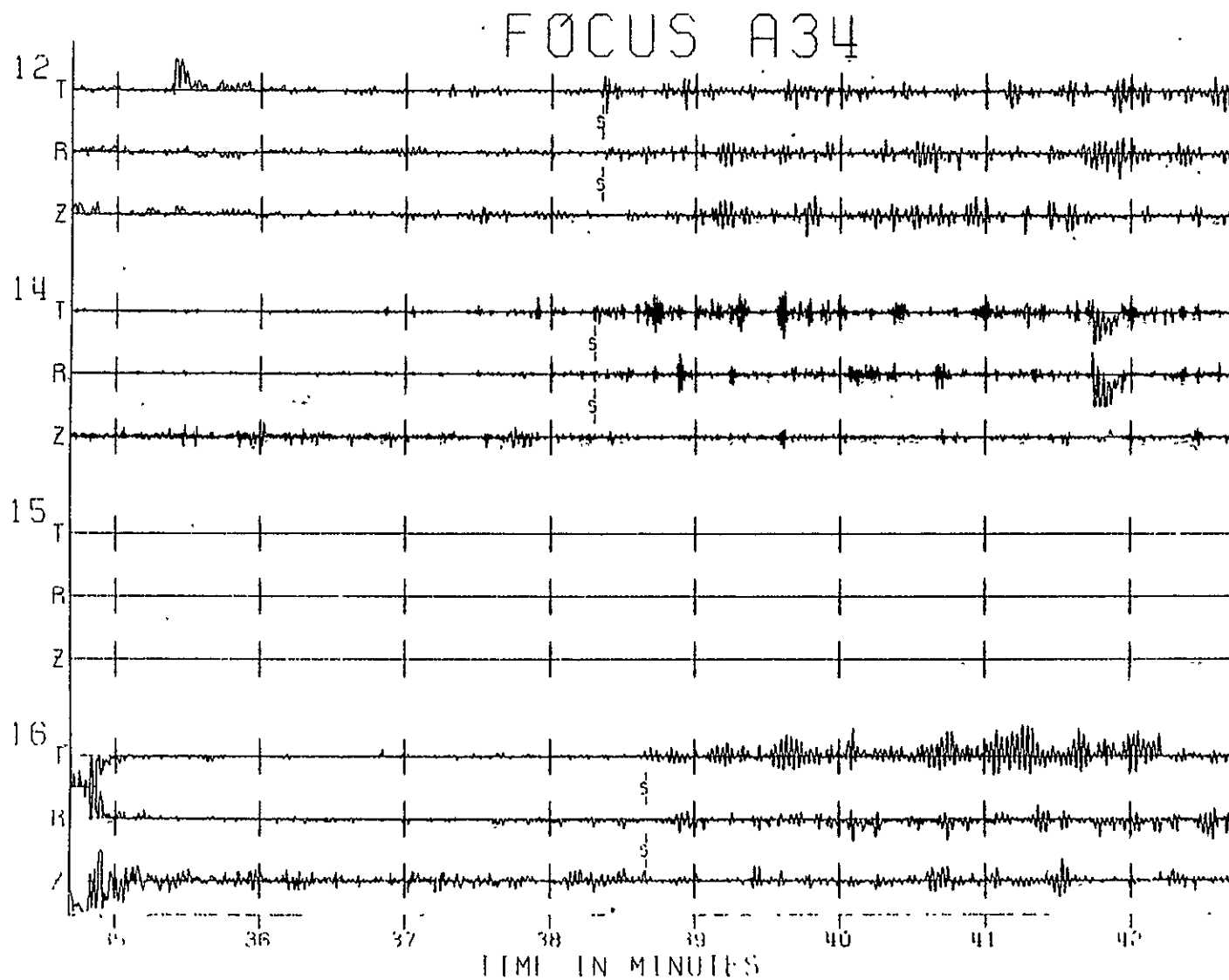
FOCUS A30

Fig. A1-14m

TIME IN MINUTES

FOCUS A40

TIME IN MINUTES
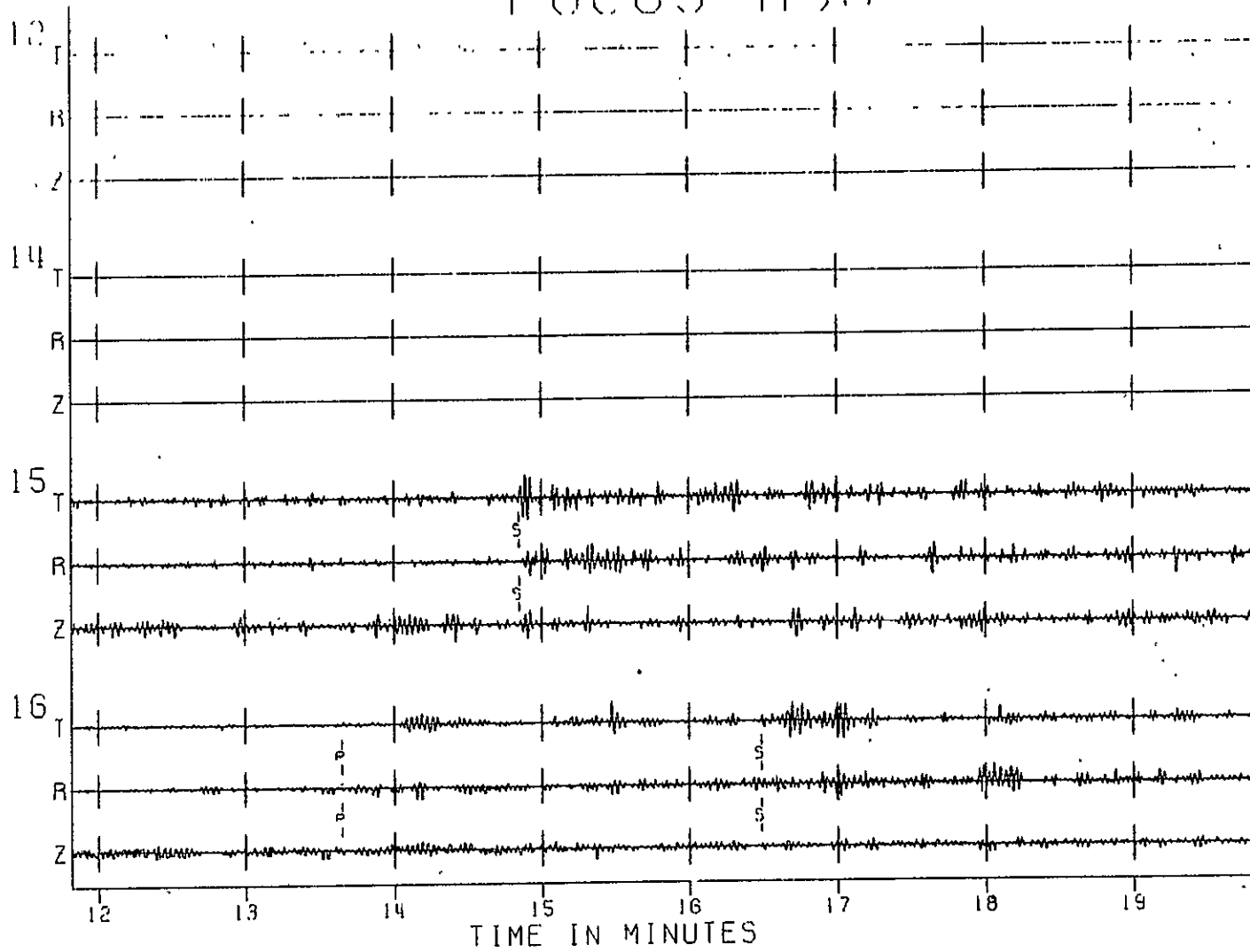
Fig. A1-14n

FOCUS A41

Fig. A1-140
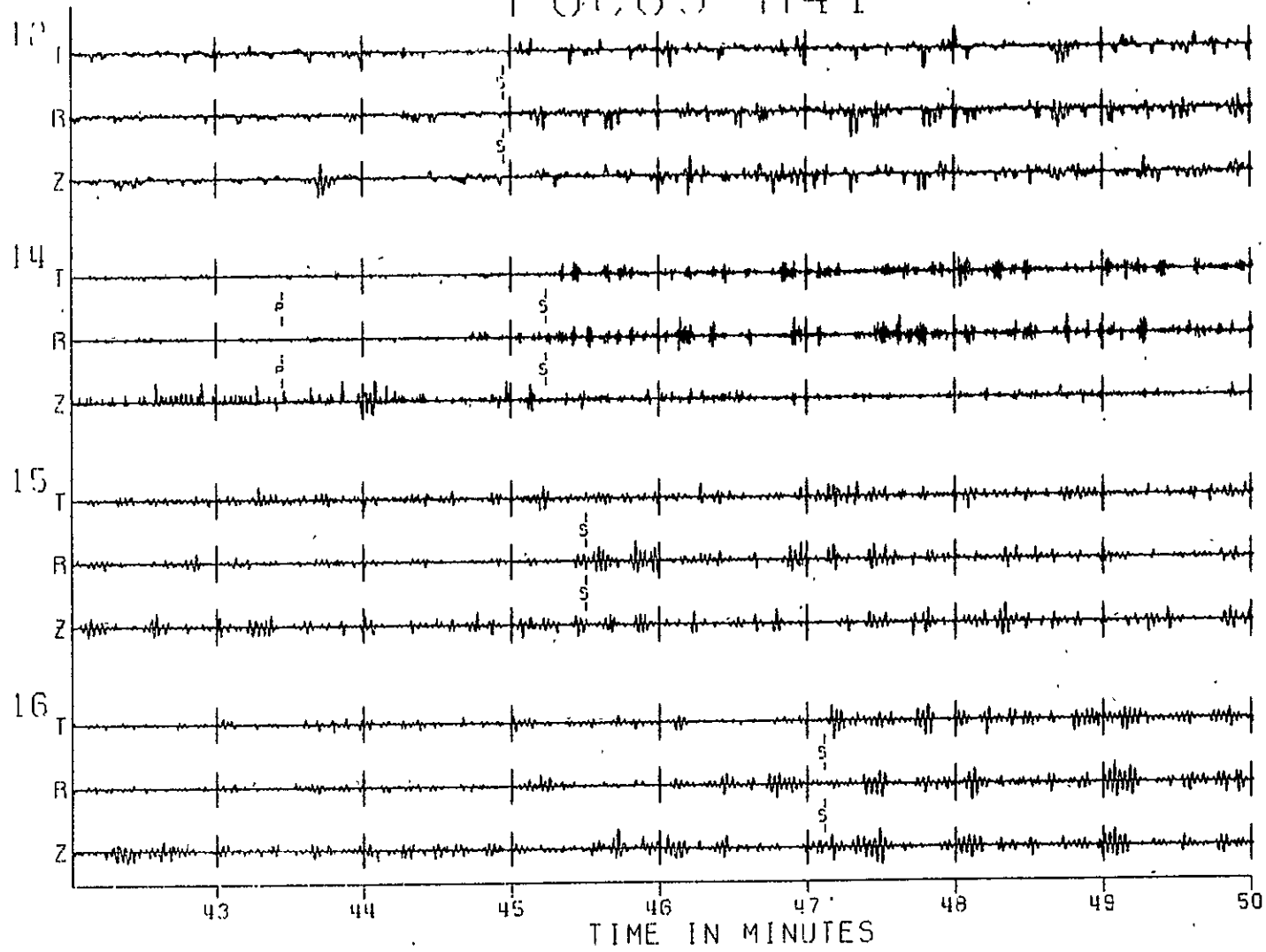
FOCUS A42

Fig. A1-14p

TIME IN MINUTES

573

Fig. A1-14q

574
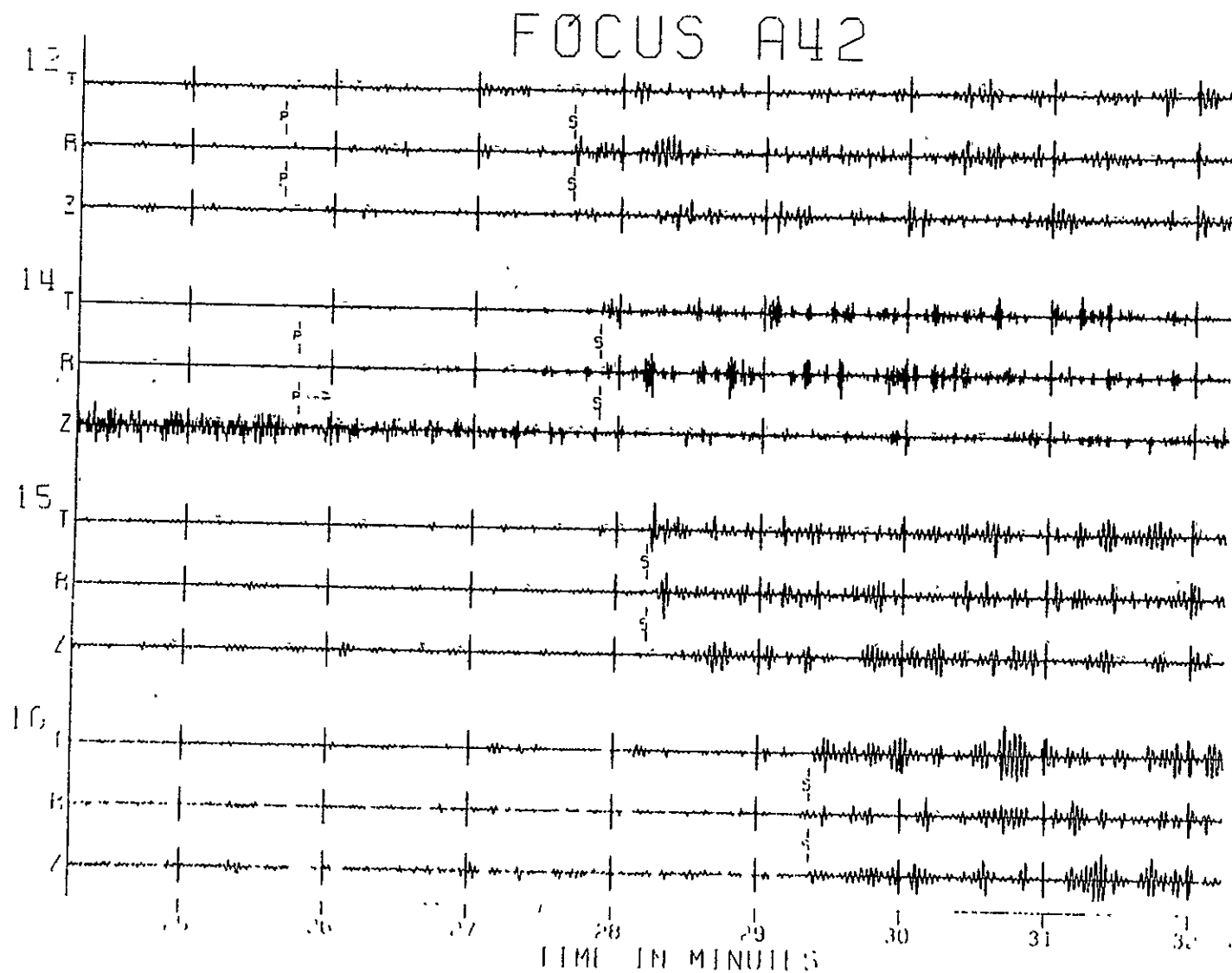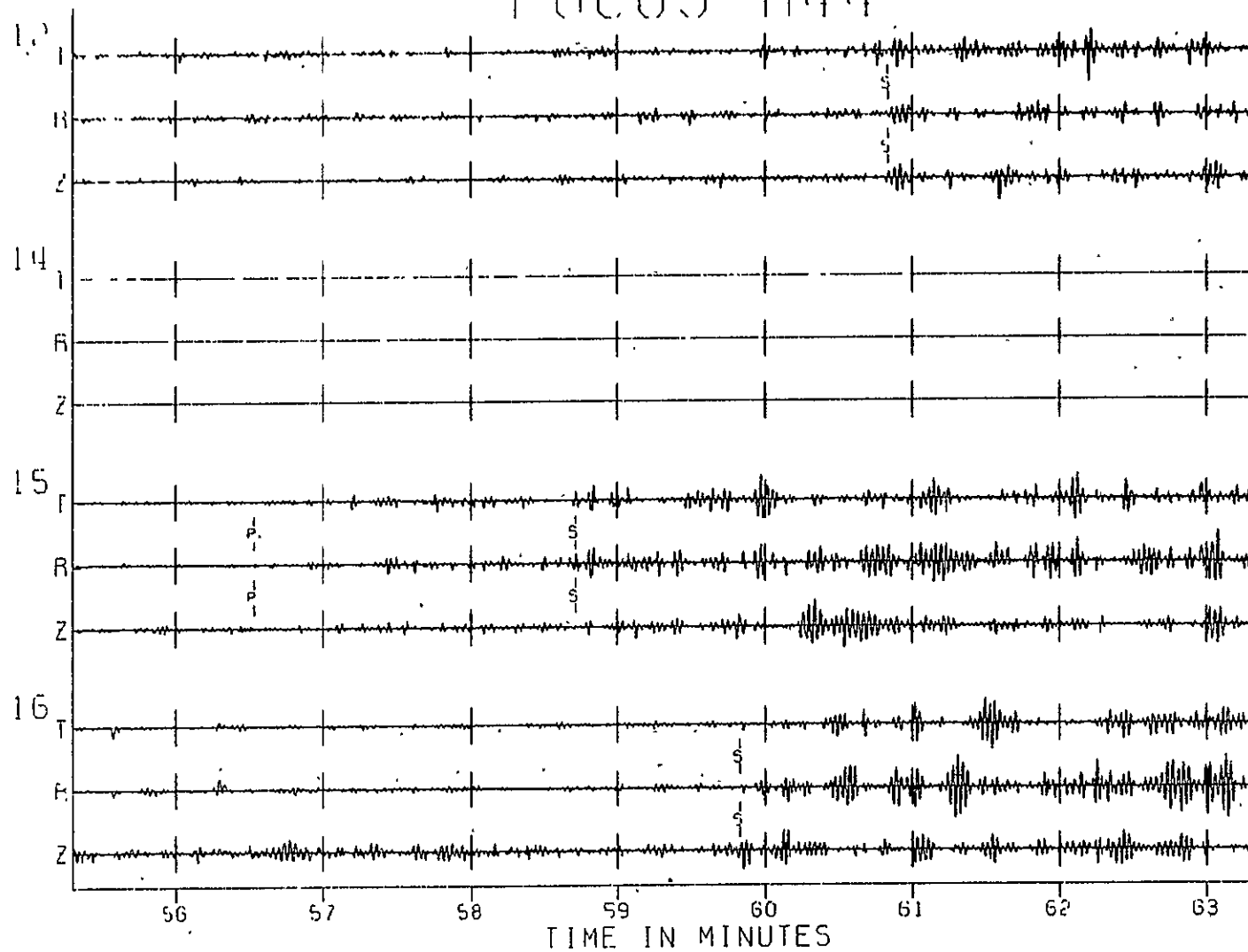
FOCUS A45

Fig. A1-14r

FOCUS H46

Fig. A1-14s

TIME IN MINUTES

FOCUS A50

Fig. A1-14t

TIME IN MINUTES

577

FOCUS A51

TIME IN MINUTES

FOCUS A56

TIME IN MINUTES

Fig. A1-147

579

FOCUS A61

Fig. A1-14w

TIME IN MINUTES

FOCUS A62

Fig. Al-14x

TIME IN MINUTES

581
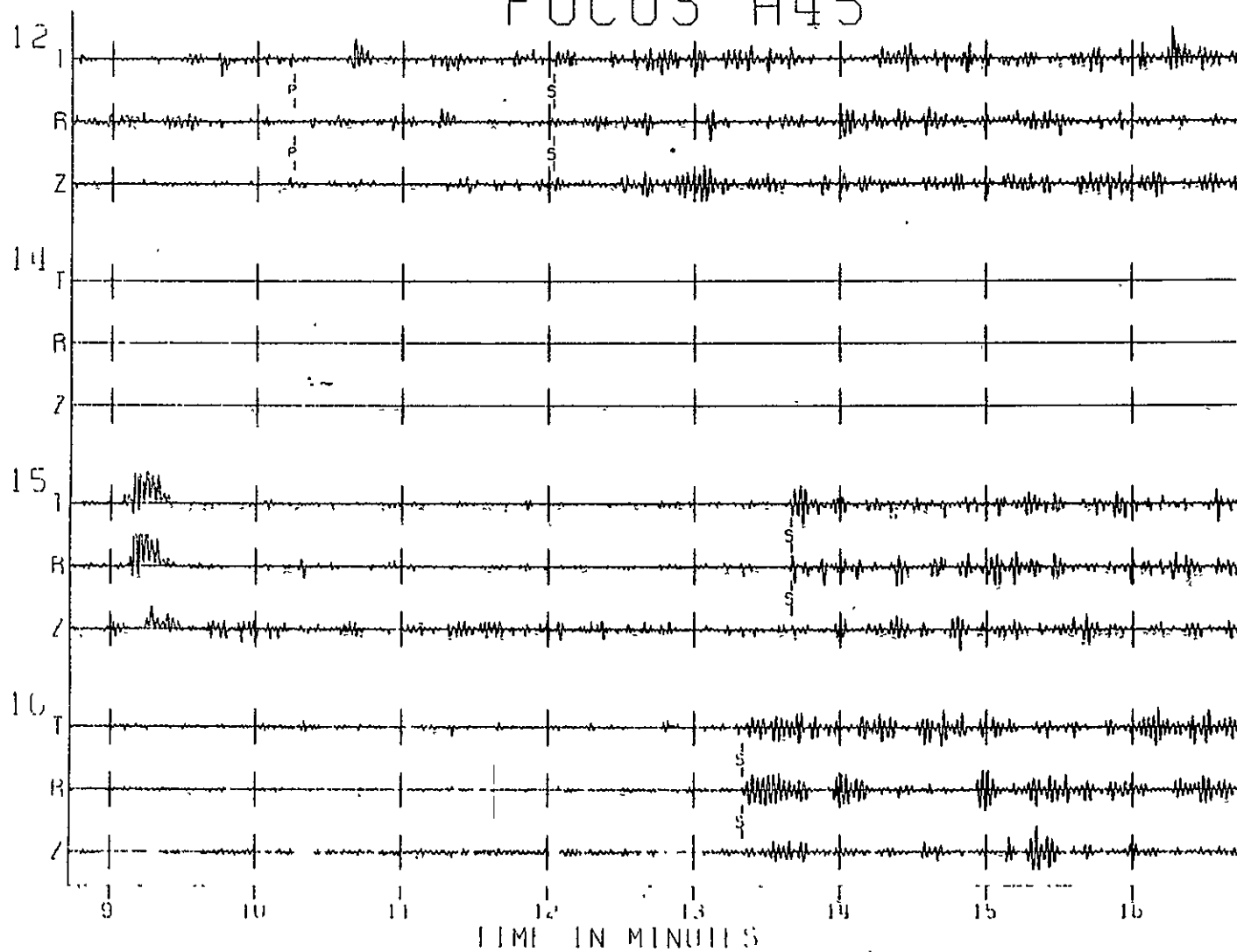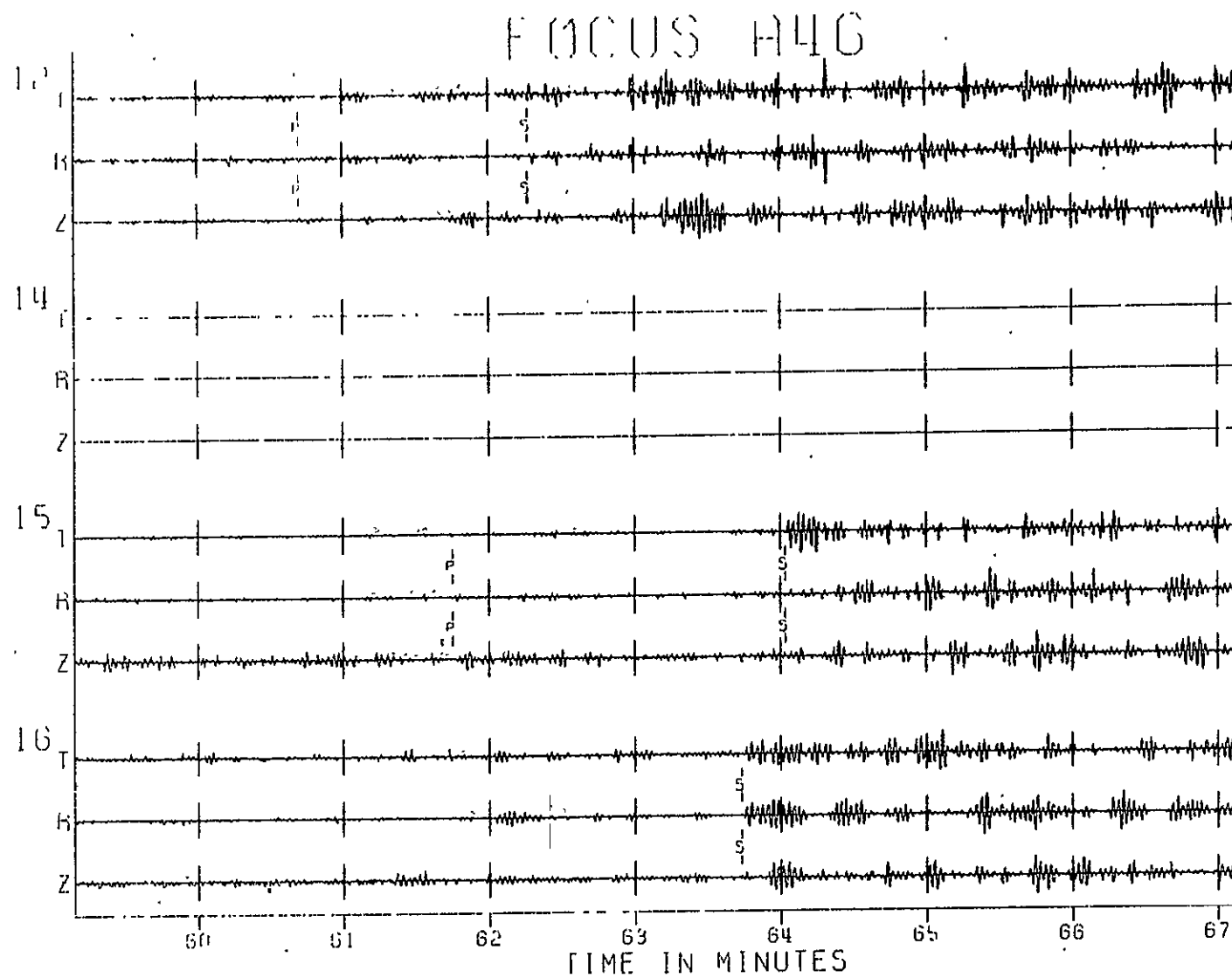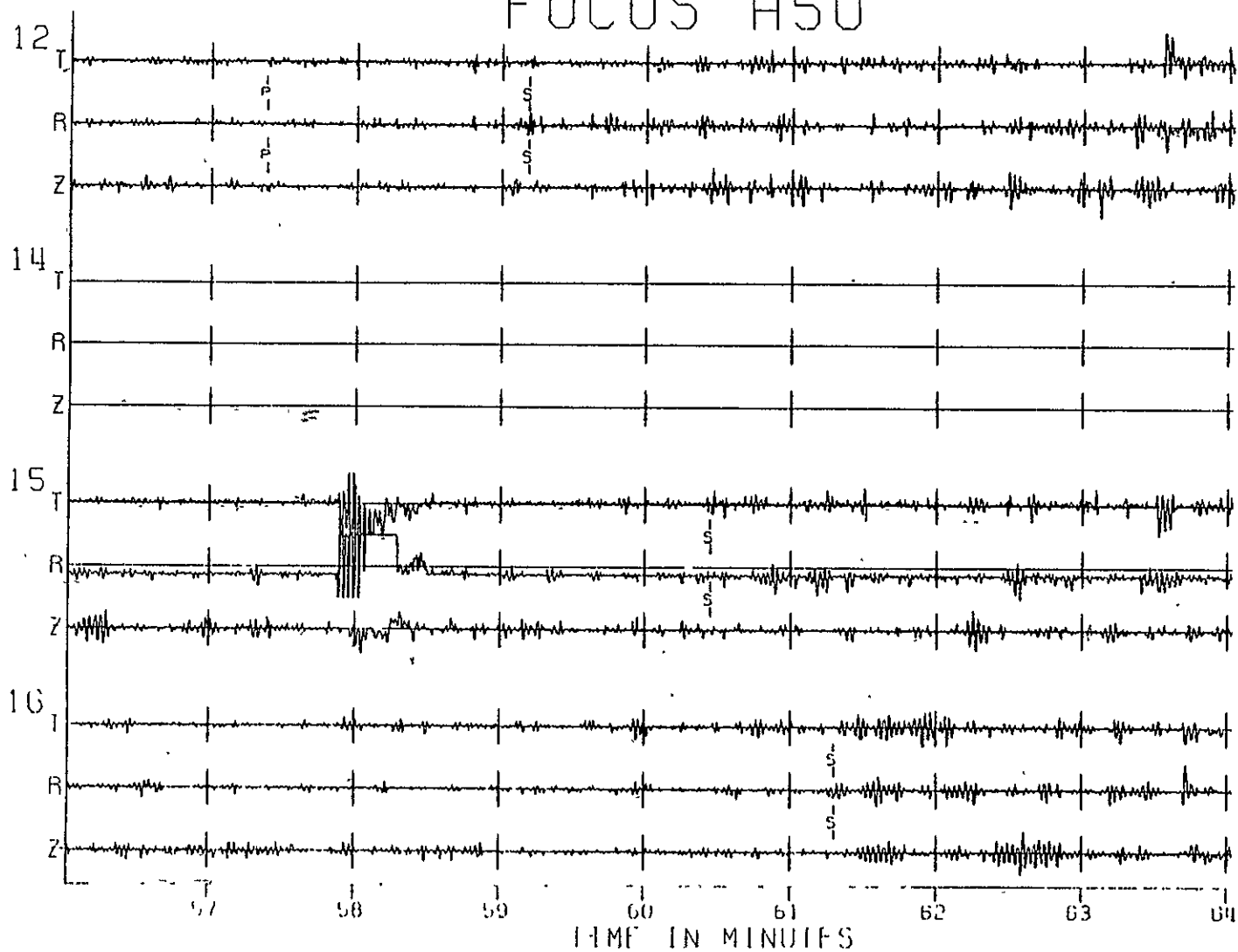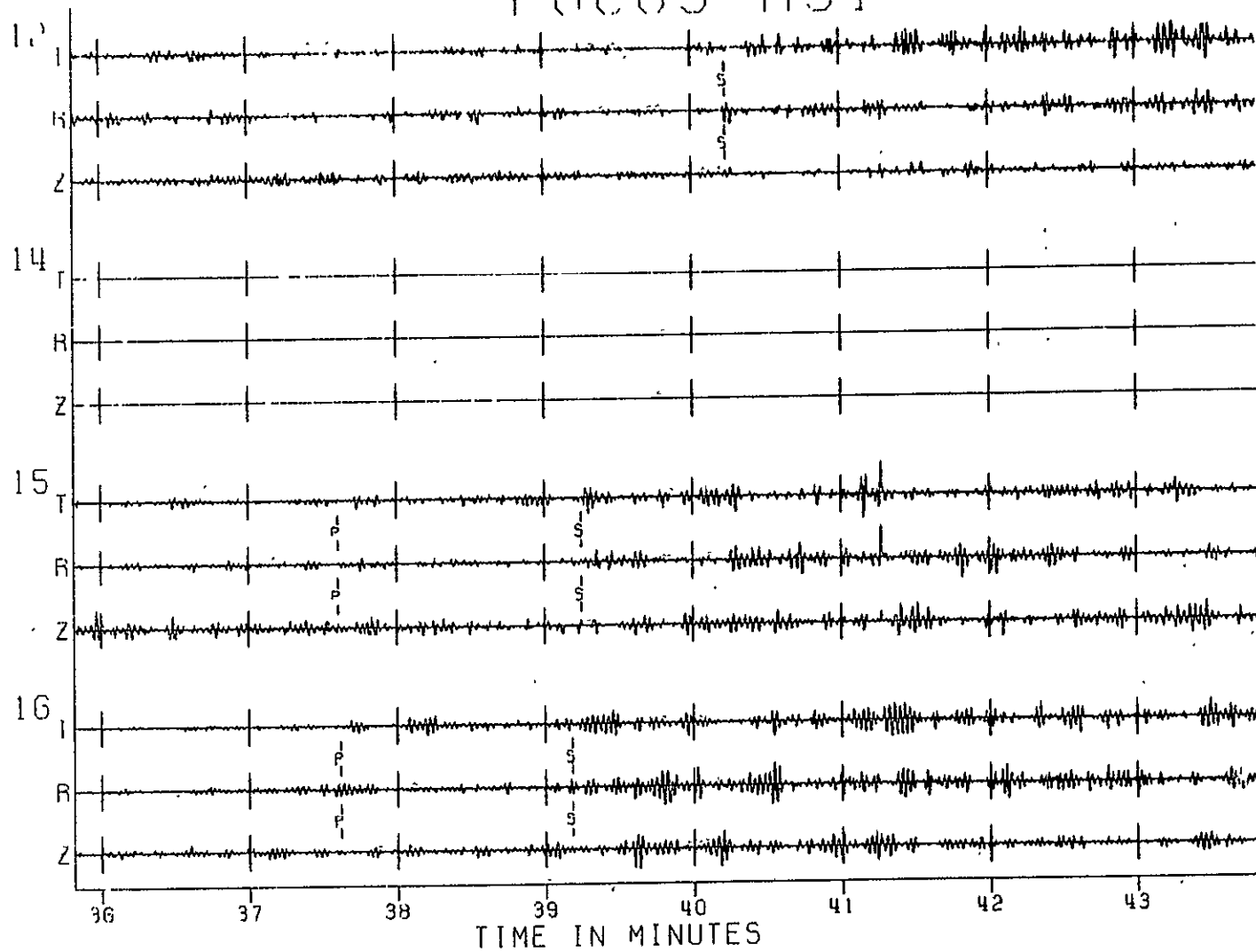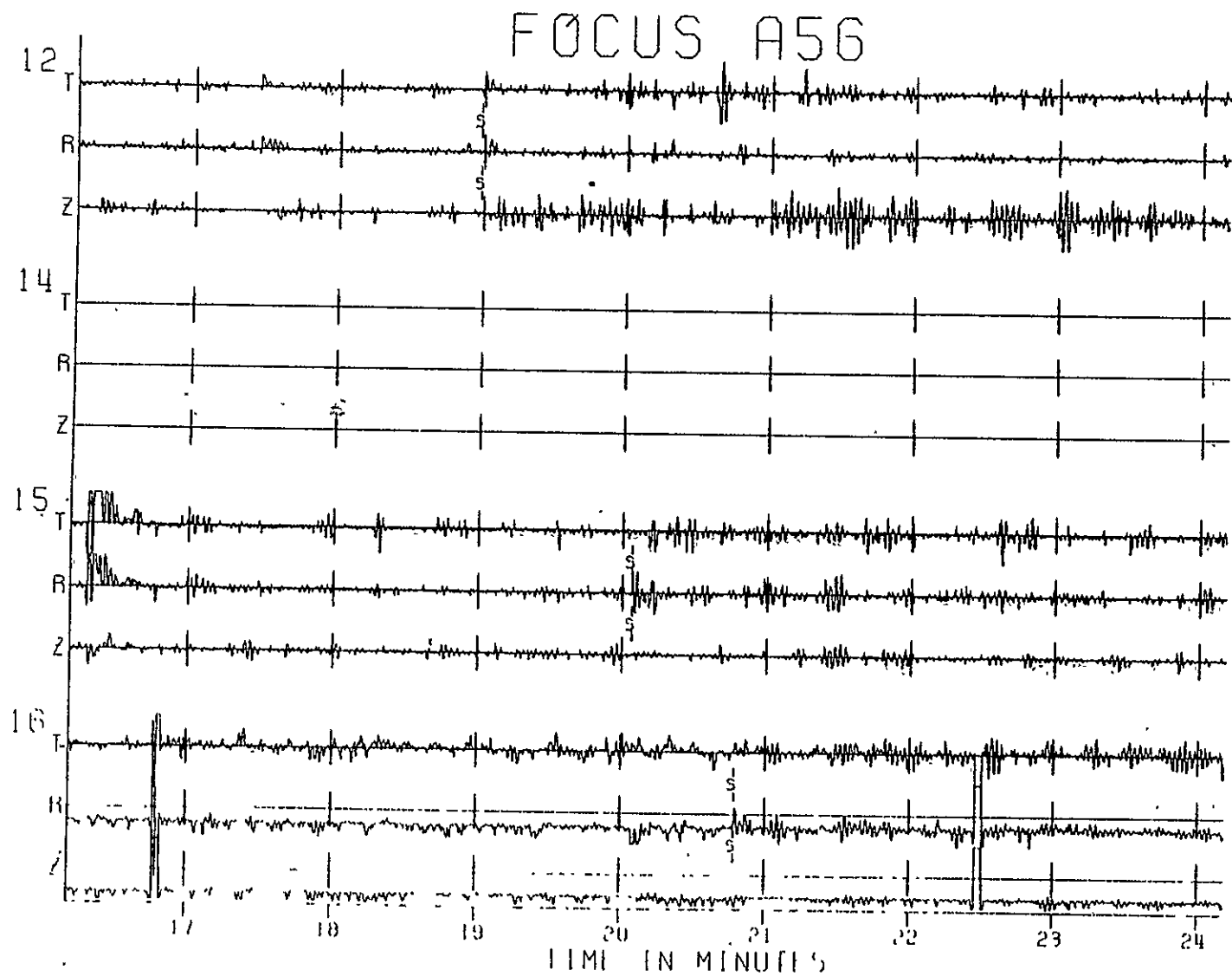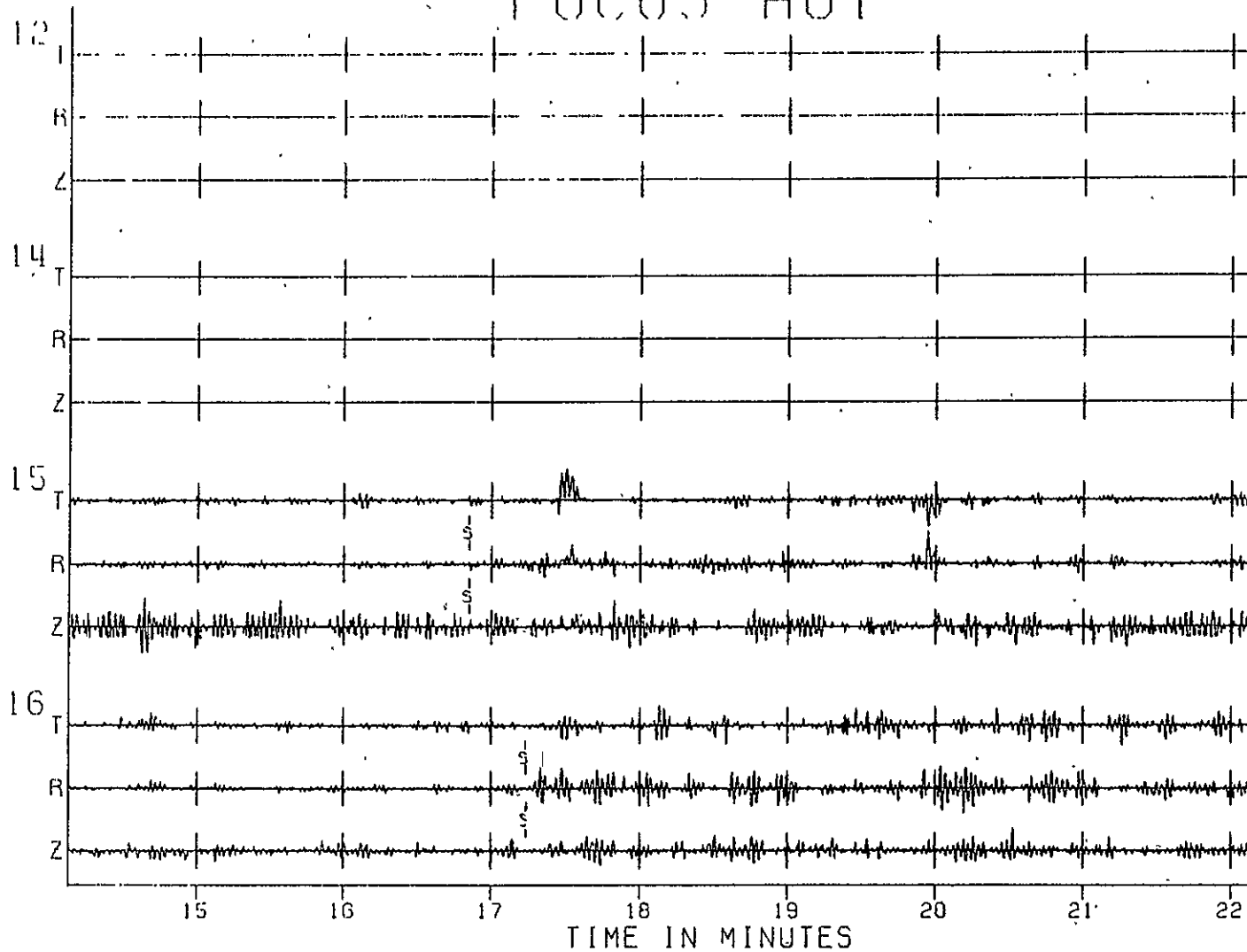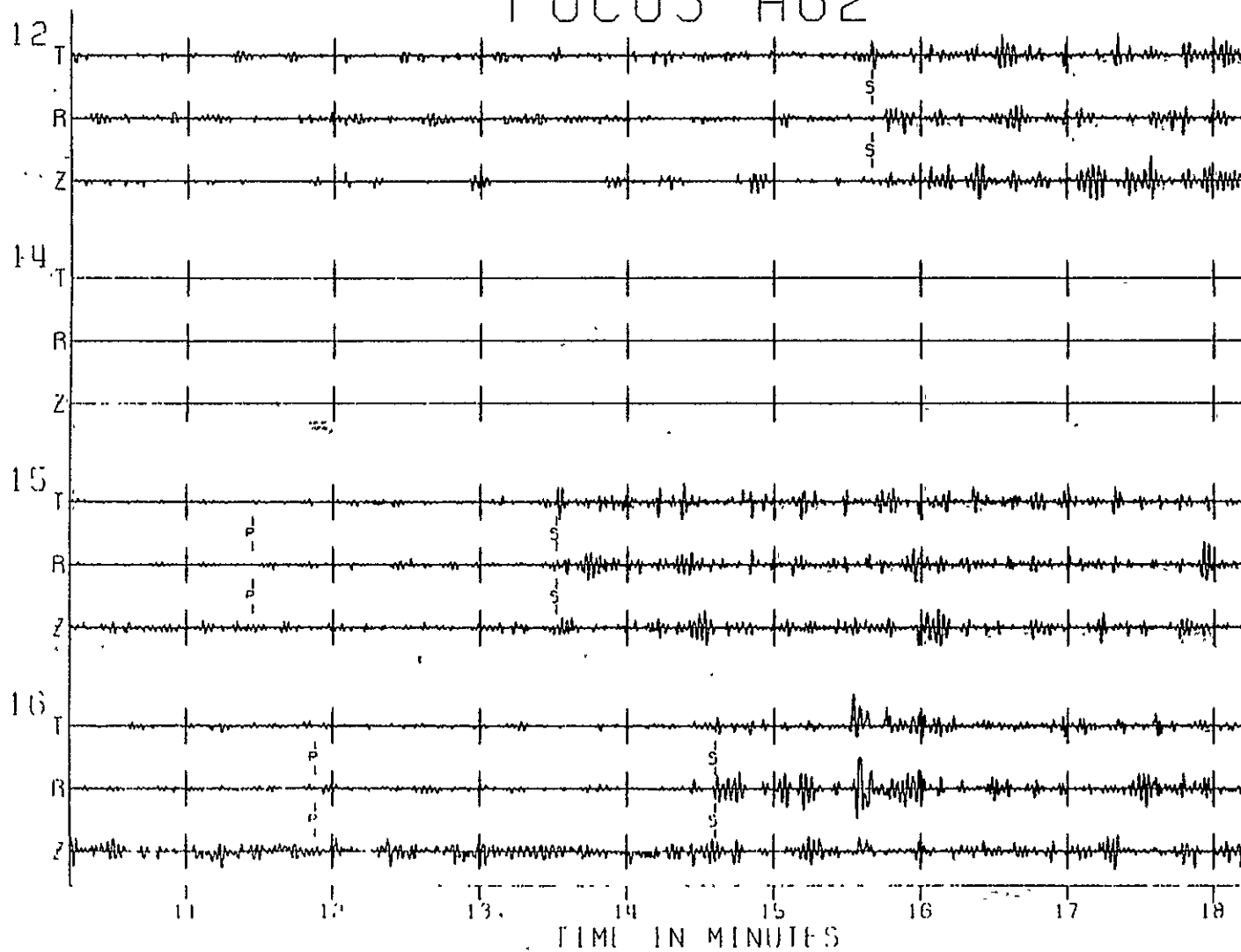
APPENDIX 2

RAY TRACING

A large number of ray tracing programs were written
for and used throughout this work. The first section deals
with ray tracers developed specifically to calculate the
direct P and S wave arrival times for the inversion
routines discussed in Appendix 4, while the second section
contains descriptions of programs used to plot travel
time curves and observe amplitude trends of secondary
seismic phases for use on record section plots as
described in Appendix 3. The final section discusses the
more sophisticated ray tracers used to compare observed
direct wave amplitude envelopes with theory.

A2.1 Travel Times for Direct P and S Waves

The inversion routines described in Appendix 4
require that theoretical P and S wave arrival times be
calculated for specific source locations and velocity
models for comparison with the observed values. This
entails doing the forward problem of computing the
travel time between two specified points on or in the
moon using a tentative velocity model; for a typical event

with six observed arrivals six such rays must be found.
In the matrix inversion program, the arrival time
derivatives with respect to the various unknown parameters,
e.g. source location and velocity values, must also be
calculated. This is done in some cases (e.g. velocity) by
varying the parameter under consideration incrementally in
either direction, recalculating all the travel times
affected by the parameter, and forming differences to
produce a centered finite-difference derivative estimate.
Clearly, it behooves us to perform the ray tracing in as
efficient a manner as possible.

With this in mind, it is necessary to choose the most
efficient method to calculate these arrival times so as to
keep the computation cost within reason. The task is made
easier by the fact that it is appropriate to model the
moon as a small series of constant-velocity layers, for
three reasons. First, with only four stations, seismic
events of limited size and unknown location, and the
complexities introduced by the strong scattering layer,
it is impossible to obtain detailed structural knowledge
of the lunar interior; the goal is to extract as much
average information about the various interior regions as
possible. Second, as long as the velocity gradients within
layers are moderate and the transition zones between layers

of limited extent, then the determination of average
velocities in constant velocity layers is a valid approach
(this is discussed in detail in Chapter 3 and Appendix 4).
Finally, even the lunar crust, where detailed information
is available as the result of the artificial impact data,
can be modeled accurately enough for the purposes of
calculating teleseismic travel times by two constant
velocity layers with a constant time addition to account
for the very-low-velocity surficial zone, as discussed
in Chapter 2. Thus typically in this work it is necessary
to trace rays through four constant velocity layers; two
crustal layers, an upper mantle, and a lower mantle. As
discussed in Chapter 3, other ray tracers were used to
test the effect of allowing velocity gradients; one such
ray tracer that assumes linear gradients (kindly supplied
by Dr. Anton Dainty) increased the cost of a matrix
inversion program by about a factor of three, which means
that the ray tracing was slower by even a larger factor
over the constant-velocity case since a significant part of
the computation time is used in the actual matrix inversion.
A comprehensive ray tracer, written by Bruce Julian, uses
ar^b velocity curves (where r is the radius) and is even
more costly.

There are three techniques available for tracing seismic waves between specified locations. (The problem of simply tracing a ray through a given velocity structure for some take-off angle is straightforward; to determine the particular ray that travels between two specified points is an inverse problem.) The first is the table look-up scheme, where travel time values are tabulated as a function of velocity structure, source-receiver separation, and focal depth. The spacing of values and therefore the table size is determined by the required accuracy of the interpolated values. Although this method was used in some preliminary investigations of this work, it rapidly proved infeasible as the data and number of varying parameters increased, due to the enormously large tables required. The second method is termed "shooting", where one or two initial rays are traced and a convergence scheme followed to find the required ray that connects the two specified locations (source and receiver). The advantage of this method is that it is easy to program and consequently rather foolproof; the disadvantage is that for detailed or laterally heterogeneous velocity model structures it rapidly becomes unwieldy and costly. The last technique is termed "bending" (c.f. Julian and

Gubbins, 1977). Briefly it involves using Fermat's principle to find the minimum delay, and thus physically real, ray between two points; the computation procedure involves numerically solving a set of 5 simultaneous differential equations. The major advantage of this method is that it is extremely efficient compared to the shooting process when complex velocity structures are involved; on the debit side it requires a larger investment in programming effort and start-up time to produce a working routine to implement the calculations. Packaged programs were not readily available when the routines used in this thesis were initially written.

Thus the ray tracing programs in this thesis use the shooting technique, for the following reasons. First, it is not clear whether the savings in computation time and cost, if any, would be significant for a four-layer constant-velocity model; the bulk of the cost of the location program is absorbed in doing the matrix inversion. A very rough estimate places the cost of doing say 3000 ray tracings discussed above is only between two and four dollars. Second, the additional complexity in programming does not appear justified in view of the above.

It remains then to choose the appropriate shooting technique for our problem. Basically this consists of selecting a suitable convergence scheme to determine the desired ray from one or two starting guesses. There are essentially three types available (Acton, 1970); a) Newton's method, requiring one starting guess and the derivative at that point (which could be calculated numerically), b) two-point first-order methods using two starting values and linear interpolation-extrapolation, and c) higher order methods requiring both more starting points and higher order derivative calculation. In this work option b is preferable, because Newton's method while quadratically convergent is often unstable, and the other higher-order methods are computationally more bulky, require more start-up values, and for modest accuracy requirements may not provide significantly faster convergence.

Two linear interpolation schemes were considered, the secant method and the false position method. The latter technique requires that the starting points and all future pairs of points straddle the desired value (in our case, the source-receiver separation), thus producing a linear convergence rate that is guaranteed. The secant method simply replaces the oldest point by the next oldest, and

the next oldest by the new, in order as the iteration

proceeds. As a result, the convergence rate is faster

(Acton (1970) gives an order of 1.6), but since both

interpolation and extrapolation is used, convergence is

not guaranteed. This latter difficulty however can be

obviated, and so the secant method is used herein,

providing nearly a second-order convergence rate. The

scheme is implemented by the formula

$$\phi_3 = (\Delta - \Delta_2) * \frac{(\phi_2 - \phi_1)}{(\Delta_2 - \Delta_1)} + \phi_2$$

where (ϕ_1, Δ_1) and (ϕ_2, Δ_2) are the two previous (or start-up)

values of take-off angle and resulting distance traveled

and Δ is the required distance (source-receiver separation).

ϕ_3 is the next estimate and Δ_3 will be the distance

achieved by that ray. The iteration is done by

$$\phi_1 = \phi_2 \quad , \quad \Delta_1 = \Delta_2 \quad , \quad \phi_2 = \phi_3 \quad , \quad \Delta_2 = \Delta_3$$

The next step is to choose starting take-off angles to

begin the iteration. It is important that the algorithm

to do this provide sufficiently accurate values so that

the above iteration will be generally convergent, in

order that the ray tracers can be used with confidence in

a location routine. This must be done differently for deep moonquakes and surface events. Several algorithms were tried for the deep events, and it was found that the following formulas were accurate enough to ensure convergence for all distances given the observed variation in source depths.

$$\phi_1 = \Delta + \sin^{-1}\left\{ \frac{(R-D)\sin\Delta}{[(R-D)^2 + R^2 - 2(R-D)R\cos\Delta]^{1/2}} \right\}$$

$$\phi_2 = \phi_1 - 1.3 * (\Delta_1 - \Delta)$$

where R is the planetary radius, D is the source depth, is the required source-receiver separation, and Δ_1 is the distance corresponding to ϕ_1. The first angle represents that which would be correct if the planet were homogeneous, and the second represents a bracketing corrected value based on the first. The factor 1.3 is appropriate to the average moonquake depth (900 km) and the rough velocity structures known a priori. (ϕ is measured from the radial, or vertical, direction.)

The surface events present a more complex problem. As seen in Fig. A2-1, the travel time curve for a surface

source consists of a number of branches equal to the number of homogeneous layers. The gap at 90° is caused by a velocity drop going from the third layer to the one below it. The surface event ray tracer initially calculates the take-off angles that correspond to the endpoints of the respective branches; this can be done easily because for each endpoint the bottoming depth (either immediately above or below the appropriate layer boundary) and the corresponding angle with respect to the vertical (90°) are known. Specifically,

$$\phi_{lim} = \sin^{-1} \left\{ \frac{V_s \, (R_b \pm \epsilon)}{R_s \, V_b} \right\}$$

where (R_s, V_s) are the radius and velocity at the surface and (R_b, V_b) are at the bottoming point; ϵ is an incremental distance above or below the exact boundary depth and V_b is then the velocity either above or below the boundary. For the branch beginning after the shadow zone it is necessary to do a short iteration along the retrograde spur in order to locate the onset of the prograde branch that represents the required first arrival. Using these eight limiting take-off angles, the corresponding distances are found simply by tracing the rays for those take-off angles. Assume now that the desired

source-receiver distance lies only in the range covered
by the third branch, say 60°. Then the two endpoints
of that branch are used as the start-up values for the
iteration. Furthermore, if any iteration step yields an
estimated take-off angle beyond one of the boundaries, the
boundary point is re-used. Thus the iteration is bound,
and absolutely convergent. This operation is repeated for
each branch containing the desired source-receiver
separation, and finally the shortest of the travel times
is chosen as the first arrival and theoretical travel time.
In addition, using this method it is trivial to ascertain
if a requested distance lies in a shadow zone.

The final distance accuracy required of the iteration
was 10^{-5} radians (or 5.7×10^{-4} degrees), giving a maximum
travel-time error of .01 seconds. Even with this strict
requirement typically only 6-8 iterations were required.
Thus the secant method provides an optimal mix of
reliability, speed, and computational simplicity; more
complex iteration schemes would probably loose as much
efficiency in extra calculations as they gain in a
reduced number of necessary iterations.

The final step of course is to actually trace the

rays for a specified take-off angle. For both classes of events this was done simply by calculating the ray parameter and applying the conservation principle to progress through the layers in the proper fashion. The travel time was calculated only for the final, desired ray in order to speed the computations.

One other ray tracing program was used in the inversion routines; it was desired to place the HFT events at shallow depths within the crustal layers to observe the effect on their epicentral locations and residual errors. The ray tracer used for shallow sources was the same as that for surface sources except for the following. 1) The distance range was divided into that reached by upgoing rays and that reached by downgoing rays, simply by tracing the ray leaving the source horizontally. 2) For distances requiring upgoing rays, the start-up rays for the iteration were the ray leaving horizontally and the ray leaving vertically upwards. 3) For farther distances, the travel time branch limits were used for all layers below the source; the layer containing the source was represented by the usual lower limit (the ray bottoming immediately above the lower boundary) and by the ray leaving horizontally. 4) The actual ray tracing was accomplished

by tracing a ray from a surface source and subtracting that part of the ray traveling from the actual source at depth and the surface along the same ray path. Thus, all take-off angles refer to the equivalent surface source ray, but the program returns the travel time and distance for the true source at depth.

Each of the ray tracers described above produced calculated travel times for specified source and station locations. These were then added to the origin times to produce arrival times which could be compared with the observed data.

A2.2   Travel Times and Amplitudes for Reflected, Refracted, and Converted Phases

As discussed in Chapters 2, 3 and 4, it is desirable to search for secondary seismic arrivals on lunar seismograms in the hopes of extracting additional structural information. In particular, the reflected and refracted converted waves from known or suspected interfaces (velocity discontinuities) are of interest. In order to do this theoretical travel time curves are needed to correlate with observed pulses on the record section plots, and amplitude curves are useful in estimating which phases

are likely to be visible given the direct P and S wave signal amplitudes. Accordingly, the following ray tracers were written.

Moonquakes: 1) Direct ray tracer - calculate the direct P and S waves for any source depth below the velocity drop (which is somewhere between 300 and 500 km depth) and any central angle. In addition refracted converted waves (e.g. SP) can be calculated for any depth of conversion. 2) Crustal peg-leg multiples - traces the reflected and converted phases from crustal boundaries as described in Chapter 2; there are nine such waves with four distinct arrival times. 3) Core reflections - this program traces rays that leave the moonquake source, travel downwards, reflect (either same type or conversion) at a deep boundary (e.g. a core) and then travel to the surface.

Surface events: 1) Direct ray tracer - calculate the direct P and S waves for any epicentral distance. No refracted waves are calculated because in general a) S-P conversions are not possible at the crustal interfaces, b) P-S conversions would not be seen because of the relatively low amplitudes of the direct P wave and c) few surface events are far enough away so that rays pass through deeper boundaries (e.g. 400-800 km depth) and the

signals that do exist are relatively weak. 2) Reflected
phases - the ray.tracer calculates travel paths for rays
that travel down from the surface source and reflect
(same type or convert) from a boundary at any depth.
3.) Crustal peg-leg multiples - as discussed in Chapter 2,
only two such waves are expected (with identical travel
times) since no conversions are possible due to the
shallow incident angles. The amplitudes should be
comparable to the equivalent phases from moonquake
events, and so no ray tracers were written especially
for these phases. The expected travel times were
calculated using a travel-time program kindly supplied by
Dr. Anton Dainty, which traces rays for a given take-off
angle.

The rationale behind the above selection of secondary
phases is given in the sections of the main body wherein
they are discussed. As in section A2.1, the above ray
tracers were designed to find the ray that connected two
given points in the moon. Commonly, rays were found for
every 5 or 10 degrees of epicentral distance, thus giving
a smooth picture of the travel times and amplitudes without
the user worrying about the proper ray parameter selection.
In all cases the secant interpolation-extrapolation method

was used and the candidate rays were traced with the appropriate application of ray parameter conservation. The only variations in each program were the methods used to obtain start-up values for the iteration; appropriate algorithms had to be found for each ray type. These will not be described explicitly herein because they are essentially heuristic, the only requirement being that they provide sufficiently accurate values to ensure convergence. In most cases they are similar to those formulas given above for direct waves.

In addition to travel times, these ray tracers were designed to calculate theoretical amplitudes. In determining whether a reflected or converted phase is likely to be visible on record section plots, the quantity of interest is the comparison between the theoretical secondary phase amplitude and the direct P and S wave amplitudes which are observed. For example, if peg-leg multiples arising from the incident shear wave at the base of the crust are expected to have about .1 of the amplitude of the corresponding direct shear wave, it is possible that such phases would be observable. These ratios are controlled primarily by the reflection and transmission coefficients

at the boundaries involved, and to a lesser extent by the
ray tube spreading factors. Again constant-velocity layers
are used, even though velocity gradients can strongly affect
amplitudes, for two reasons: a) when the ray tracers were
written, only limited knowledge of possible velocity
gradients in the moon was available, and b) since we are
interested in *relative* amplitudes the inclusion of velocity
gradients would not affect the comparisons to a significant
extent because both the secondary phases and the direct
phases to which they are compared traverse such gradients
in similar fashions. Further discussions of the possible
effect of velocity gradients on the relative amplitudes are
given in the appropriate section of the main body.

Naturally a complete calculation of theoretical
amplitudes would have to include source effects and
detailed path effects, such as the precise nature of the
velocity discontinuities and their relation to the seismic
wavelength. Ultimately, wave theory should be used and/or
theoretical seismograms calculated, as was done for the
direct P arrivals from artificial impacts. However, given
the fact that these secondary reflected and converted phases
are obscured by scattered energy, and the real lack of
detailed structural information, it is not feasible at this
point to make such precise calculations and comparisons.

The object of the amplitude calculations described herein is to determine, given a simple velocity structure, which reflected and refracted secondary phases might produce sufficient energy to be observable. For this purpose the following calculations, assuming infinitely sharp first-order discontinuities and constant velocity layers, are sufficient.

Four general subroutines are needed to calculate the amplitude factors for the above ray tracers. The first gives reflection (same type and converted) coefficients for incident P and SV waves at a free surface; the SH reflection coefficient is unity because no conversion can occur for flat (or spherical) surfaces. The second and third routines calculate the reflection and transmission coefficients at an interior boundary, i.e. an interface between two half-spaces; one routine assumes incident SH waves and the other does the calculation for incident P and SV waves. The last program calculates the ray-tube spreading factors.

The equations for reflection at a free surface are derived in Ewing et al. (1957), pp. 24-29. The ratio of reflected to incident energy flux per unit area is given therein by equations 2-19; substitution of equations 2-11 and 2-15 yields the complete solution. (Note that equations 2-11

and 2-15 contain factors of $(1 + 3 \tan^2 e)$ which result from assuming that Poisson's ratio is 0.25. We have used the more general expression, i.e. $(\tan^2 f - 1)$. The quantities e and f are the angles of emergence of the P and SV waves respectively). These equations are implemented in program ECSPHS, and require only the velocity values, incident angle and wave type, and reflected wave type as input. The energy ratio coefficients produced are similar to those in Figs. 2-3 and 2-4 of Ewing et al. (1957).

The second program calculates the reflection and transmission coefficients for SH waves incident on a welded boundary between two half-spaces. The appropriate equations for the amplitude ratios of the wave field potentials are given in Bullen (1965), p. 103, equation 8. In order to obtain the energy flux ratios, the appropriate expressions are

$$\frac{E'}{E} = \frac{\rho' \sin f' \cos f'}{\rho \sin f \cos f} \left(\frac{c'}{c}\right)^2$$

$$\frac{E_o}{E} = \left(\frac{c_o}{c}\right)^2$$

where C, C_o, and C' are the amplitudes of the incident, reflected, and transmitted SH potential wave fields, respectively; the ratios are given in the above Bullen

(1965) equation reference. The quantities ρ and f are the density and angle of emergence in each half-space. The implementing subroutine is ECSH, requiring similar input as the previous routine.

.The third routine calculates the equivalent reflection and transmission coefficients for P and SV waves incident at an interior interface. There are 16 such coefficients, and the equations are derived in Ewing et al. (1957), pp. 74 to 89. The final formulas used in this thesis are given at the bottom of p. 87 and the top of p. 89; substitution is required from equations 3-34 thru 3-37, 3-28 thru 3-31, and finally 3-10. Subroutine TRANS implements these relations, and produces the appropriate coefficients given incident wave type and direction, desired outgoing wave, and elastic parameters (Vp, Vs, ρ) for each medium. Graphs of the 16 energy ratios and the four calculated by ECSH are shown in Figs. 3-15 and 3-16 in Ewing et al. (1957).

The equations used in these last two subroutines are known as Knott's equations, and the relations used in the first routine are the analogous versions for a free surface. They are derived as follows. First the elastic wave fields are written in the form of potential solutions to the elastic wave equation. These are then differentiated with respect

to location to obtain displacement; the displacements are inserted into Hooke's Law to find stresses. The resulting expressions can then be inserted into the appropriate boundary condition equations which apply either at the free surface or welded contact. These equations are solved to find the ratios of the reflected and/or transmitted potential field amplitudes relative to the incident amplitude as a function of incident angle and elastic properties. Finally the energy density flux per unit area is calculated from the potentials (by differentiating with respect to location and time, squaring, and multiplying by density and the vertical component of the medium velocity) and the ratios of transmitted and reflected to incident energy related to the potential amplitude ratios. This completes the solution. Thus the derivation is straightforward but algebraically involved, and the resulting relations are lengthy. Therefore they are not repeated herein; standard treatments are to be found in the above references.

The last routine calculates the ray-tube spreading factor; for a homogeneous sphere it is

$$F = 1/R^2$$

where R is the travel path length. The formula used is

from Bullen (1965), p. 126, equation 1

$$E\left(\Delta\right) = \frac{1}{R_o^2} \left\{ \frac{\sin i_1}{\sin \Delta \cos i_o} \right\} * \left| \frac{d i_1}{d \Delta} \right|$$

where E is the energy observed at the receiver for unit source energy, R_O is the planetary radius, Δ is the central angle traveled, i_1 is the take-off angle relative to the vertical, and i_O is the incident angle at the station. The derivation of this is given on pp. 125-126 of Bullen (1965). In the ray-tracing programs described above the derivative in this formula was calculated numerically by tracing rays with take-off angle .1% larger and smaller than the desired value.

These subroutines are then included in the various ray tracers discussed in the text, and all the various energy ratio factors combined appropriately to give a single value. The numbers listed by the subroutines and shown in various tables herein are the square roots of the energy ratios, assuming a unit source energy, multiplied by 1000 to allow easier presentation. Note that these are just the square roots of the energy, no attempt has been made to convert them to actual amplitudes due to the complexity introduced by the scattering layer (Goins et al., 1978); in any case

the conversion is only a constant scaling factor. Also,
the free surface amplification effect (Bullen, 1965, pp. 128-
130) is not included due to the nearly vertical incidence
of all arriving waves on the moon.

A2.3 Amplitudes of Direct Waves in Continuously-Varying
      Velocity Structure

As discussed in Chapter 3, theoretical amplitude
calculations are needed to compare with measurements of the
direct shear wave amplitude as a function of distance. Of
particular interest is the relative values for rays that
bottom in the crust as opposed to rays that bottom in the
mantle. In order to do this calculation it is necessary to
use a continuous velocity structure so that the crustal
structure can be properly modeled; as discussed above, this
is not necessary for strictly teleseismic amplitude studies.
Furthermore, it is desirable to include the effects of Q
(anelastic attenuation).

These calculations have been done using programs kindly
supplied by their authors; TRAVEL (Dr. Anton Dainty) which
assumes linear velocities between given points, and TVT4
(Dr. Bruce Julian) which uses ar^b velocity curves. Once
the ray tracing is done in each of these cases, the actual

amplitude calculation is straightforward. Both programs use Bullen's ray tube spreading formula (TVT4 divides by an extra factor of 2π times the surficial velocity, a partial conversion factor from (energy)$^{1/2}$ to amplitude), and the anelastic attenuation is included as

$$\underline{E}' = \exp\left(-\omega \sum_i t_i/Q_i\right) E$$

where ω is the angular frequency and t_i, Q_i are the time the ray spends in layer i and the Q factor in that layer, respectively. (Q^{-1} is defined as $(2\pi)^{-1}$ times the fractional energy lost per cycle.)

These programs do not include the effects of transmission and reflection coefficients. However, this is a minor effect for the direct P and S waves which are nearly totally transmitted ($\sqrt{E_T/E_I} \geq 0.9$) through any interface as long as grazing incidence or post critical angles are avoided (see Figs. 3-15 in Ewing et al., 1957). In addition, neither program converts fully to amplitude or includes the surface amplification effect. The use of these programs is described in Chapter 3.

Figure Caption

Fig. A2-1. Trave-time curve for a surface event and a velocity model of four constant-velocity layers (velocity drop between the third and fourth).

Fig. A2-1

SURFACE EVENT
DIRECT P WAVE

TRAVEL TIME (SEC)

DISTANCE (DEGREES)
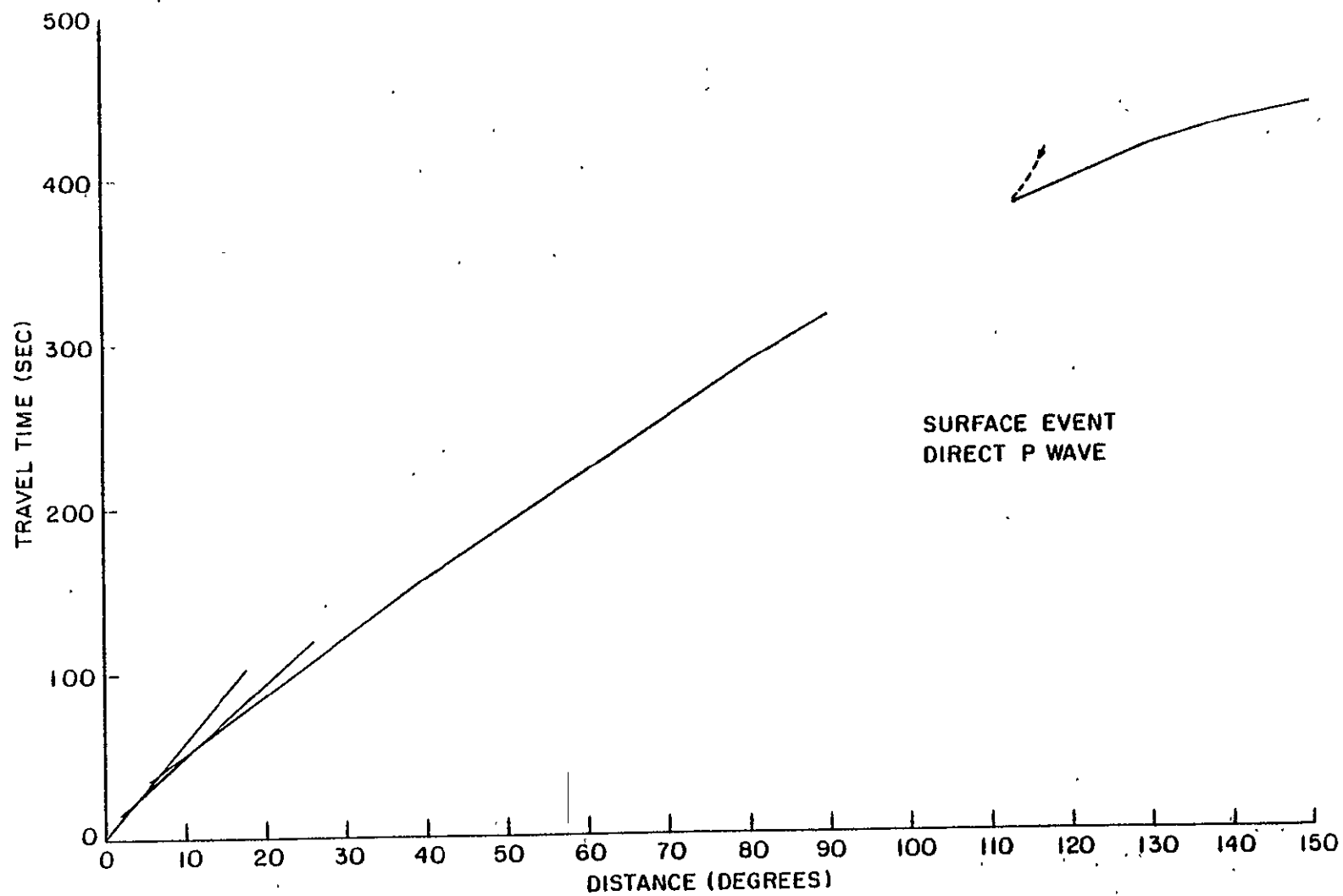
APPENDIX 3

POLARIZATION FILTERING

A3.1 Theoretical Background

As discussed in Chapter 2, the object of polarization filtering is to discriminate against one sort of particle motion and enhance another. This way, based on the knowledge of the expected particle motions, particular seismic phases can be searched for and enhanced on a seismogram relative to the ambient energy levels. An excellent review of the various filtering schemes that have been devised and their applications is given in Kanesewich (1973).

The filtering method used in this thesis is perhaps the most direct approach, originally proposed by Flinn (1965), discussed by Montalbetti and Kanasewich (1970), and described in Kanasewich (1973). The following derivation is similar to that in Kanasewich (1973). Initially it is assumed that three matched time series are available, with digital sampling at an interval of Δt seconds, representing the radial, transverse, and vertical components of ground motion of a surface point. The orthogonal directions are measured relative to the source epicenter (due to the very-low-velocity zone at

the lunar surface, the seismic waves arrival at the seismometers essentially vertically, and so these are the component directions of interest), and it is helpful if the signals are bandpass-filtered so that a narrow range of periods is dominant. For a signal of length T, the resulting traces are labeled R_i, T_i, Z_i, where $i = 1$, $T/.t$.

Now, for continuous sinusoidal time series, the particle motion in space will be an ellipsoid, or an ellipse in two dimensions. If the time series representing orthogonal components of particle motion are

$$q_x(t) = A_x \cos(\omega t + \phi_x)$$

$$q_y(t) = A_y \cos(\omega t + \phi_y)$$

the resulting ellipse will be of the form

$$\frac{q_x^2}{A_x^2} + \frac{q_y^2}{A_y^2} - 2\frac{q_x q_y}{A_x A_y}\cos(\phi_y - \phi_x) = \sin^2(\phi_y - \phi_x)$$

This is the standard equation for an ellipse centered at the origin. It can be recast in matrix form, giving

$$\begin{pmatrix} q_x & q_y \end{pmatrix} \begin{pmatrix} A_x^2 & -A_x A_y \cos(\phi_y - \phi_x) \\ -A_x A_y \cos(\phi_y - \phi_x) & A_y^2 \end{pmatrix} \begin{pmatrix} q_x \\ q_y \end{pmatrix} = A_x^2 A_y^2 \sin^2(\phi_y - \phi_x)$$

Now the center matrix (call it B) contains the squared
amplitude and cross-amplitude terms, and if it is
diagonalized to

$$\begin{pmatrix} A_{x'}^2 & 0 \\ 0 & A_{y'}^2 \end{pmatrix},$$

contains the squares of the semi-major axes of the particle
motion ellipse, since the ellipse equation then reads

$$\frac{\delta_{x'}^2}{A_{x'}^2} + \frac{\delta_{y'}^2}{A_{y'}^2} = 1$$

The coordinate system rotation angle represented by the
diagonalization is

$$\tan(2\varphi) = \frac{2 A_x A_y}{A_x^2 - A_y^2} \cos(\phi_y - \phi_x)$$

giving the direction of the major and minor axes vectors.
Thus the particle motion ellipse parameters are determined
by diagonalizing the matrix B.

Returning to three-dimensional digital data, we
consider enough points from each time series to complete at
least one cycle of the dominant period r, or at least
$r/\Delta t$ points. Then to obtain the matrix B we find the

expected squared amplitudes and cross-amplitudes of the three digital time series R, T, and Z_i these quantities are otherwise known as the variance and covariance, or the second moments and cross-moments of random variables. So

$$E\left[(R-m_r)^2\right] = E\left[R^2 - 2Rm_r - m_r^2\right] =$$

$$= E(R^2) - 2m_r E(R) + m_r^2 = E(R^2) - m_r^2 \equiv Var(R)$$

where $\quad m_r = E(R) = \frac{1}{n}\sum_{\lambda=1}^{n} R_\lambda$

and n is the number of points used from the time series R. E denotes expected value. Analogous equations hold for T and Z, and

$$E\left[(R-m_r)(T-m_t)\right] = E(RT) - m_r m_t = Cov(RT)$$

yield the covariance terms. Thus the matrix B for three-dimensional digital time series can be written as

$$B = \begin{pmatrix} Var(R) & Cov(RT) & Cov(RZ) \\ Cov(RT) & Var(T) & Cov(TZ) \\ Cov(RZ) & Cov(TZ) & Var(Z) \end{pmatrix}$$

where

$$Var\ (X) = \frac{1}{n} \sum_{\lambda=1}^{n} x_\lambda^2 - \left(\frac{1}{n} \sum_{\lambda=1}^{n} x_\lambda\right)^2$$

and

$$Cov\ (XY) = \frac{1}{n} \sum_{\lambda=1}^{n} x_\lambda y_\lambda - \frac{1}{n^2} \sum_{\lambda=1}^{n} x_\lambda \sum_{\lambda=1}^{n} y_\lambda$$

This matrix then represents the expected amplitudes of the components of ground motion, and describes the best-fitting ellipsoid in a least-squares sense to the particle motion described by the orthogonal time series.

To obtain the principal axes of this ellipsoid, we diagonalize the matrix B, as in the continuous case, or equivalently find the eigenvalues and eigenvectors. The eigenvectors represent the vectors which are only stretched, not rotated by the linear function described by the matrix, and so are equivalent to the principal axis vectors. The eigenvalue gives the stretching factor (the square of the axis length) determined by the component amplitudes. The eigenvalues are denoted λ_1, λ_2, λ_3 in decreasing order, and the longest eigenvector is e_r, e_t, e_z, or $\underline{e}$.

Having found the characteristic parameters of the particle motion ellipsoid from the data, it remains to devise a scheme to enhance the particular particle motion desired. As discussed in Chapter 2, we are attempting to observe body waves which will arrive initially with rectilinear particle motion, and wish to eliminate random

or ellipsoidal particle motion that represents primarily noise or scattered energy. (Note that if the angle of incidence of an S wave at the surface is greater than the critical angle, then the observed particle motion will not in fact be rectilinear (Nuttli, 1961). Due to the steep velocity gradient near the surface, however, all incident angles are less than 5°, so this situation is not encountered). The first discriminating criterion is thus for rectilinearity, or high aspect ratio of the particle motion ellipse. One way to measure this is by the quantity

$$F = 1 - \left(\lambda_2 / \lambda_1 \right)^{\alpha}$$

where λ_2 is the intermediate eigenvalue and λ_1 is the largest. λ_3 is considered to be the out-of-plane ellipsoidal component. This factor thus approaches zero when $\lambda_1 = \lambda_2$ and the motion is nearly circular, and goes to one as $\lambda_1 \gg \lambda_2$ indicating rectilinear motion. The exponent a can be varied to suit the particular application; as a increases F discriminates more slowly as a function of aspect ratio. In this work a = 1.2, so that $F = 1 - (A_2/A_1)$ where $A_{1,2}$ are the amplitudes of the axial ground motions or equivalently the linear measure of the particle motion ellipsoid dimensions, and the filter curves strongly discriminate against high aspect ratio particle motion.

Now this factor evaluates the rectilinearity of the particle motion ellipsoid, calculated for a string of n points representing at least one cycle of the dominant period. Herein one cycle will be used; the factor can then be applied to the center point vector, and the calculation rolled along one point at a time. In addition, it is desirable to include a factor measuring to what degree the vector at the center point lies along the dominant particle motion (largest eigenvector) direction. Accordingly, we take the projection of the center point position vector $\underline{D}$ on the largest eigenvector. So

$$P = (\underline{e} \cdot \underline{D})\underline{e} = (|\underline{e}||D|\cos\theta)\underline{e} = (|D|\cos\theta)\underline{e}$$

since $\underline{e}$ is a unit vector. Thus this factor passes only that part of the particle motion that lies along the dominant motion direction; the rest is considered to be noise. Finally, these two factors are combined, so that the output vector for the center point motion is

$$\underline{Y} = (F|D|\cos\theta)\underline{e} = \left([1-(\frac{\lambda_2}{\lambda_1})^{\frac{1}{2}}]|D|\cos\theta\right)\underline{e}$$

giving the expression for the polarization filter used in this work.

It should be noted here that Voss et al. (1976)
and Jarosch (1977) have used a different polarization
filtering technique than that described above in studying
lunar seismograms. Basically it consists of using a
running average of the product of the radial and vertical
components of ground motion as a filter to be applied to
those records. There are two disadvantages and one
advantage to this method. First, it does not use or
process the SH ground motion, where quite often the
largest amplitude secondary arrivals are expected. Second,
it is most sensitive to arrivals with an incident angle of
45°; phases seen only on either the vertical or radial
records will be filtered out. Unfortunately, due to the
surficial low-velocity zone as discussed above, most
teleseismic waves in the moon should approach the surface
at close to vertical incidence, implying that the above
filter will not optimally enhance the desired signals. As
a result, of course, noise pulses occurring on only one
trace will be surpressed whereas the method used herein
will pass them; on the whole, however, the particle
motion ellipsoid approach seems better as long as proper
care is taken in the presence of obvious noise pulses.

A3.2   Application to Lunar Seismograms

The operations described below are carried out in a Polarizer package developed during this work to polarization filter lunar seismograms using the theory given above. The first step is to read in each record and high-pass filter those traces that were received in the broad-band response mode, using a cut-off period of 10 seconds and a filter length of 5, as described in Appendix 1. This is only necessary for surface events; moonquake stacked records are pre-filtered during the stacking process.

Next, the individual component traces are normalized so that each has about the same average amplitude. This step requires some discussion. As described in Chapter 1, the amplitudes of each component of ground motion received at a particular station tend to have a constant relationship to each other that is relatively independent of the location or focal mechanism of the source (see for example any of the raw seismograms in Appendix 1). These scale factors seem to persist along all portions of the seismic records. This implies that the relative gain of each component seismometer is controlled by instrument effects (e.g. the y-axis cable acting as an additional spring or differences in the instrument sensitivities as discussed by Jarosch (1977)) or

near-station structural effects (e.g. the increased

horizontal vs. vertical Rayleigh wave particle motion

caused by the very-low-velocity regolith layer (Mark and

Sutton, 1975)) rather than by source or teleseismic travel

path effects. Thus the particle motion ellipsoids at each

station are consistently biased by these constant effects

that dominate the relative component amplitudes. In addition,

the polarization filter is less effective on such data since

the particle motion ellipsoids will tend to have similar

shapes when one component is much larger than the others.

Clearly it is desirable to remove those parts of the

relative amplitude gains which are constant for any

seismic-signal, in an attempt to retrieve the particle

motion that existed prior to the near-surface and station

effects that are specific to each ALSEP site.

In the absence of a priori knowledge of the mechanisms

producing the amplitude bias, an approximate procedure is

to simply normalize all the traces to a common average level.

In the lunar case this is a reasonable approach since, as

mentioned, the relative component amplitudes are remarkably

constant. The scaling was done automatically in the program

using a window length of four minutes (1200 points at the

0.2 sampling interval of the LP instruments) beginning about

1.5 minutes before S. This interval represents half of the

total signal length processed for each moonquake, and one quarter of that used for surface events, allowing a reasonably accurate average amplitude to be measured without excessive computing time. These parameters were varied occasionally to avoid noise spikes that would bias the scaling factors. An additional advantage that resulted from the amplitude normalization was that convenient plotting was facilitated.

The final scaling factors for each trace are given in Tables A3-1, along with the relative factors normalized to the vertical component at each station. (Note that ALSEP 14 is normalized to the Y component since the vertical instrument is usually not operational.) It is clear that over all 40 events there is a remarkable uniformity of relative component amplitudes, as asserted above. Table A3-1e gives the average relative scaling factor and standard deviation for each component at each station for moonquakes, surface events, and all events. Values from records dominated by noise or produced by improperly functioning instruments were omitted from the averages as indicated by the asterisks. It is interesting that the surface event horizontal records seem to be more enhanced relative to the vertical component than is the case for

moonquakes, possibly as the result of greater surface wave generation and subsequent horizontal motion amplification by the very low surficial velocities. The differences, however, are within one standard deviation. (Note that the relative <u>station</u> gains are not compared due to the small number of events which would result in biasing by event location).

The next step is to rotate the horizontal components to the transverse and negative radial directions relative to the source epicenters, using the equations

$$T = X \cos + Y \sin \theta$$
$$R = Y \cos - X \sin \theta$$

where θ is the angle measured <u>clockwise</u> (due to the left-handed coordinate system) from the Y direction to the negative radial vector, obtained from the station and source epicenter coordinates and the Y-axis azimuth using the standard equations in Bullen (1965), pp. 154-155. (Both equations 7 and 8 therein are used in order to determine the azimuth quadrant without ambiguity). It is not worthwhile to rotate the vertical axis to point at the focus, because even for surface events within 10°

of the a station the angle of emergence is only 3-5 degrees
from the vertical due to the steep near-surface velocity
gradient. As discussed in Chapter 2, the locations used are
preliminary ones, listed in Tables A3-2, but comparison
with the final locations given in Tables 3-8
shows that there are only small differences.

The resulting traces are then ready to be passed to the
polarization filter as described in section A3.1. The data
length used for the correlation matrix calculation was 11
points or 2 seconds, corresponding to one cycle of the
dominant period on the ALSEP 12, 15, and 16 seismograms and
two cycles on the ALSEP 14 records. The resulting filtered
traces, along with the scaled and rotated traces, were
plotted and stored on disc; the plots are presented and
described in Appendix 1. It is obvious from these plots
that the polarization filter is successful in removing a
great deal of energy. The direct P and S wave arrivals
are particularly well enhanced, suggesting that at least
some of the other pulses are also true enhanced body
waves, i.e. secondary phase arrivals. The fact that usually
the initial few cycles of the known direct body waves are
well-passed while the following amplitudes are decreased is
excellent confirmation of the hypothesis that the initial
body wave arrivals are relatively unscattered and have

rectilinear particle motion while the later scattered coda does not. Furthermore, the polarization filter used seems to effectively discriminate between the two types of seismic energy. The rectilinearity function, defined in section A3.1 as $F = 1 - (\frac{\lambda_2}{\lambda_1})^{1/2}$ was also stored on disc for each three component record, and occasionally plotted. However, it was usually of little use in measuring arrival times.

A few final points remain to be mentioned. First, on traces dominated by large noise pulses such as leveling movements or on records with little signal content the scaling routine did not always produce precisely scaled traces; this was allowed since polarization filtering was of little use in these cases. Second, the polarization filter was not applied in cases where little or no signal was available on one component of ground motion, as was usually the case at ALSEP 14. This produced blank records on the polarization filtered seismograms given in Appendix 1. Finally, in the calculation of the eigenvalue of the correlation matrix, 1% was added to the three diagonal terms to stabilize the computations. This is equivalent to a stochastic inverse as described in Appendix 4.

A3.3 Record Stations

The final step in the data processing is to plot the seismograms on record sections to allow the identification of true seismic arrivals, as opposed to random noise pulses. For surface events this is straightforward; the origin times (listed in Table A3-2a) are aligned and each record is plotted at the appropriate source-receiver separation one component at a time. The separations for surface events are given in Table A3-3a, as calculated from the equations in Bullen (1965), pp. 154-155. Travel time curves of suspected phases can then be plotted on the record section. (Note that these theoretical travel times should be calculated from the same model used to locate the events and determine the origin times. Within reasonable limits the model can be varied, relocating the events and recalculating travel times, and the correlation between the travel time curves and the seismograms will be essentially the same.)

The moonquake events must be corrected to a common source depth before a record section plot can be constructed. Since the required corrections are different for each seismic phase, it is difficult to examine a moonquake record section for seismic wave arrivals of different types. For a given moonquake focus, the correction for a particular

phase is obtained in the following way. First, the travel time of the phase to a seismic station is calculated. Then the source is moved vertically to the reference source depth and a new travel time computed.. The time difference is found, and applied to the origin time, thus obtaining the effective origin time as it would be if the focus had in fact been at the reference depth. This process of course assumes lateral homogeneity since the two ray paths are different. The calculation is repeated for each station-focus pair, since the necessary correction is a function of focal depth and source-receiver separation. Fortunately, the required corrections are very similar for phases of similar geometry, such as the nine peg-leg multiples, and so it is possible to search for several related phases on a single record section, greatly reducing the complexity of the process. In this thesis a variation of ±2 seconds in correction was allowed, although usually crucial correlations were rechecked by examining the true correction values. As for the original origin times, the data-theory correlations were not strongly dependent on the exact velocity values used in the seismic model as long as the same ones were used for calculating the corrections and the theoretical travel times.

Although the average moonquake depth is close to 900 km,
the reference source depth used is 1000 km, because moving a
focus up in depth requires greater incident angles at
velocity interfaces in order for the ray to reach an
equivalent distance. Since there is a velocity drop at
about 300-500 km, above all the moonquake foci, this means
that if deep foci at far distances from the ALSEP array are
moved up too much, the rays will encounter a geometric
shadow zone, and the correction will not be calculable. Even
if there weren't a velocity drop, the S-P phase converted at
the velocity discontinuity enters a shadow zone as the foci
move up in depth and approach the boundary. The 1000 km
depth reference source depth is sufficient to prevent this
from occurring except occasionally, and so significant data
is not lost. Of course, the opposite effect occurs if we
consider phases reflected from a boundary below the moon-
quakes, so that the reflected waves from deeper foci
cannot reach to large distances. Since the moonquake foci
nearly are all within 90° of the farthest ALSEP station, this
did not present a serious problem.

In sum, the moonquakes were corrected for the appropriate
appropriate phases as discussed in the main text, and care
was taken not to artificially eliminate data. Once the

origin time corrections were applied, then the record section plotting could proceed as for surface events. The moonquake locations, origin times, and source-receiver separations for the moonquake foci are given in Tables A3-2b and A3-3b.

Various origin time correcting programs were written; corrections were calculated for direct waves, peg-leg multiples, refracted converted phases, and core reflections. In each case various appropriate interface depths were used and layer velocities were varied to observe the effects on the corrections. The resulting record section plots for both surface events and moonquakes are shown throughout this thesis.

Table A3-1a

Scaling factors for ALSEP 12 seismograms

Moonquakes

Focus Number	Scaling Factors			Relative Scaling Factors		
	X	Y	Z	X	Y	Z
A1	2.092	1.750	1.812	1.15	0.97	1.0
A15	2.906	3.465	3.308	0.88	1.05	1.0
A16	3.351	2.839	2.936	1.14	0.97	1.0
A17	2.182	1.803	2.382	0.92	0.76	1.0
A18	2.632	2.364	2.877	0.91	0.82	1.0
A20	1.860	1.640	1.591	1.17	1.03	1.0
A27	3.137	3.477	3.266	0.96	1.06	1.0
A30	3.196	2.928	3.612	0.88	0.81	1.0
A31	--	--	--	--	--	--
A32	7.405	2.991	7.694	0.96	0.39	1.0
A33	4.765	4.743	4.083	1.17	1.16	1.0
A34	3.416	2.960	2.414	1.42	1.23	1.0
A36	--	--	--	--	--	--
A40	3.096	2.873	3.157	0.98	0.91	1.0
A41	3.211	2.903	3.003	1.07	0.97	1.0
A42	0.959	0.592	1.005	0.95	0.59	1.0
A44	3.136	2.923	3.918	0.80	0.75	1.0
A45	2.035	1.876	1.975	1.03	0.95	1.0

A46	2.090	1.642	1.776	1.18	0.92	1.0
A50	2.942	3.209	3.467	0.85	0.93	1.0
A51	3.332	2.596	1.615	2.06	1.61	1.0
A56	1.421	2.416	3.735	0.38	0.65	1.0
A61	--	--	--	--	--	--
A62	1.487	1.300	1.531	0.97	0.85	1.0

Surface Events

Event Yr Day	Scaling Factors X	Y	Z	Relative Scaling Factors X	Y	Z
72 134	0.009	0.010	0.010	0.90	1.0	1.0
72 199	0.192	0.160	0.150	1.28	1.07	1.0
72 213	0.506	0.443	0.520	0.97	0.85	1.0
72 324	0.578	0.547	0.643	0.90	0.85	1.0
72 102	0.166	0.141	0.155	1.07	0.91	1.0
72 124	0.067	0.065	0.056	1.20	1.16	1.0
72 25	0.071	0.079	0.086	0.83	0.92	1.0
77 107	0.166	0.159	--	--	--	--
73 72	0.085	0.082	0.089	0.96	0.92	1.0
73 171	0.274	0.269	0.290	0.94	0.93	1.0
74 192	0.513	0.481	0.590	0.87	0.82	1.0
75 3	0.064	0.066	0.067	0.96	0.99	1.0
75 44	1.760	1.290	1.869	0.94	0.69	1.0
76 4	1.213	0.794	1.708	0.71	0.46	1.0
76 66	0.413	0.386	0.382	1.08	1.01	1.0
76 68	0.943	0.797	1.085	0.87	0.73	1.0

Table A3-1b

Scaling factors for ALSEP 14 seismograms

Moonquakes

Focus Number	Scaling Factors			Relative Scaling Factors		
	X	Y	Z	X	Y	Z
A1	1.664	0.705	3.163	2.36	1.0	4.49
A15	2.184	1.403	--	1.56	1.0	--
A16	1.812	1.400	2.732	1.29	1.0	1.95
A17	1.231	0.907	2.225	1.36	1.0	2.45
A18	2.402	1.493	3.444	1.61	1.0	2.31
A20	2.206	1.375	--	1.60	1.0	--
A27	2.521	1.972	--	1.28	1.0	--
A30	1.583	1.024	--	1.55	1.0	--
A31	1.569	1.938	--	0.81	1.0	--
A32	2.336	1.868	--	1.25	1.0	--
A33	4.256	1.894	2.829	2.25	1.0	1.49
A34	2.009	1.751	4.202	1.15	1.0	2.40
A36	1.270	1.647	--	0.77	1.0	--
A40	2.264	1.292	--	1.75	1.0	--
A41	2.334	1.485	5.559	1.57	1.0	3.74
A42	1.746	0.958	8.255	1.82	1.0	*8.62
A44	2.952	1.523	--	1.94	1.0	--
A45	0.559	0.433	--	1.29	1.0	--
A46	1.225	0.656	--	1.87	1.0	--

	1.797	0.975	--	1.84	1.0	--
A50	1.797	0.975	--	1.84	1.0	--
A51	9.704	1.585	--	*6.12	1.0	--
A56	1.208	1.041	--	1.16	1.0	--
A61	0.514	0.067	--	*7.67	1.0	--
A62	1.102	0.882	--	1.25	1.0	--

Surface Events

Event Yr Day	Scaling Factors X	Y	Z	Relative Scaling Factors X	Y	Z
72 134	0.003	0.003	--	1.0	1.0	--
72 199	0.101	0.083	--	1.22	1.0	--
72 213	0.154	0.113	--	1.36	1.0	--
72 324	0.188	0.146	--	1.29	1.0	--
75 102	0.339	0.028	--	*12.11	1.0	--
75 124	0.136	0.027	--	*5.04	1.0	--
76 25	--	--	--	--	--	--
77 107	0.070	0.040	0.234	1.75	1.0	5.85
73 72	0.048	0.239	--	*0.20	1.0	--
73 171	0.162	0.078	--	2.08	1.0	--
74 192	0.183	0.057	--	*3.21	1.0	--
75 3	0.024	0.019	--	1.26	1.0	--
75 44	--	--	--	--	--	--
76 4	0.500	0.664	--	0.75	1.0	--
76 66	0.104	0.059	--	1.76	1.0	--
76 68	0.401	0.199	--	2.02	1.0	--

Table A3-1c

Scaling factors for ALSEP 15 seismograms.

Moonquakes

Focus Number	Scaling Factors			Relative Scaling Factors		
	X	Y	Z	X	Y	Z
A1	1.566	1.449	1.878	0.83	0.77	1.0
A15	3.693	2.253	3.633	1.02	0.62	1.0
A16	2.474	1.954	2.617	0.95	0.75	1.0
A17	1.305	0.958	1.362	0.96	0.70	1.0
A18	1.655	1.596	2.266	0.73	0.70	1.0
A20	2.151	1.490	2.018	1.07	0.74	1.0
A27	2.514	1.761	2.308	1.09	0.76	1.0
A30	3.798	3.176	3.726	1.02	0.85	1.0
A31	2.341	1.316	2.525	0.93	0.52	1.0
A32	2.146	1.704	2.200	0.98	0.77	1.0
A33	1.962	1.698	1.891	1.04	0.90	1.0
A34	2.457	1.356	--	--	--	--
A36	2.018	1.791	1.556	1.30	1.15	1.0
A40	5.331	4.808	4.242	1.26	1.13	1.0
A41	3.195	2.685	2.552	1.25	1.05	1.0
A42	2.422	1.977	2.311	1.05	0.86	1.0
A44	2.150	1.383	1.973	1.09	0.70	1.0
A45	2.151	1.681	2.192	0.98	0.77	1.0
A46	2.035	1.637	2.452	0.83	0.67	1.0

A50	3.865	3.727	3.399	1.14	1.10	1.0
A51	1.842	1.059	2.039	0.90	0.52	1.0
A56	5.012	1.922	1.983	*2.53	*0.97	1.0
A61	1.213	1.046	2..218	0.55	0.47	1.0
A62	1.491	1.080	1.945	0.77	0.56	1.0

Surface Events

Event Yr Day	Scaling Factors			Relative Scaling Factors		
	X	Y	Z	X	Y	Z
72 134	0.055	0.038	0.081	0.68	0.47	1.0
72 199	0.088	0.067	0.115	0.77	0.58	1.0
72 213	0.070	0.044	0.117	0.60	0.38	1.0
72 324	0.328	0.217	0.585	0.56	0.37	1.0
75 102	0.070	0.045	0.093	0.75	0.48	1.0
75 124	0.096	0.070	0.106	0.91	0.66	1.0
76 25	0.167	0.121	0.256	0.65	0.47	1.0
77 107	0.522	0.319	0.528	0.99	0.60	1.0
73 72	0.162	0.587	0.241	*0.67	*2.44	1.0
73 171	0.301	0.250	0.668.	*0.45	*0.37	1.0
74 192	0.217	0.210	0.419	0.52	0.50	1.0
75 3	0.013	0.024	0.058	0.22	0.41	1.0
75 44	1.211	1.427	1.183	1.02	1.21	1.0
76 4	1.394	1.168	1.835	0.76	0.64	1.0
76 66	0.593	0.444	0.934	0.63	0.48	1.0
76 68	1.040	0.882	1.887	0.55	0.47	1.0

Table A3-1d

Scaling factors for ALSEP 16 seismograms

Moonquakes

Focus Number	Scaling Factors			Relative Scaling Factors		
	X	Y	Z	X	Y	Z
A1	0.910	0.251	1.523	0.60	0.16	1.0
A15	1.887	1.046	3.444	0.55	0.30	1.0
A16	1.240	0.560	2.092	0.59	0.27	1.0
A17	1.145	0.505	2.958	0.39	0.17	1.0
A18	1.049	0.697	2.078	0.50	0.34	1.0
A20	1.028	0.457	2.048	0.50	0.22	1.0
A27	1.723	0.941	2.210	0.78	0.43	1.0
A30	3.005	1.460	4.394	0.68	0.33	1.0
A31	1.480	0.601	1.927	0.77	0.31	1.0
A32	1.042	0.527	2.131	0.49	0.25	1.0
A33	0.970	0.341	1.669	0.58	0.20	1.0
A34	2.348	1.019	4.486	0.52	0.23	1.0
A36	1.145	0.598	1.619	0.71	0.37	1.0
A40	1.859	0.938	3.720	0.50	0.25	1.0
A41	1.161	0.644	3.819	0.30	0.17	1.0
A42	0.379	0.204	0.963	0.39	0.21	1.0
A44	1.522	0.799	3.543	0.43	0.23	1.0
A45	0.609	0.268	1.257	0.48	0.21	1.0
A46	1.145	0.511	2.334	0.49	0.22	1.0

	X	Y	Z	X	Y	Z
A50	2.252	1.027	3.626	0.62	0.28	1.0
A51	0.992	0.431	1.872	0.53	0.23	1.0
A56	1.267	0.814	1.820	0.70	0.45	1.0
A61	0.554	0.346	1.712	0.32	0.20	1.0
A62	0.923	0.451	1.236	0.75	0.36	1.0

Surface Events

Event		Scaling Factors			Relative Scaling Factors	
Yr Day	X	Y	Z	X	Y	Z
72 134	0.017	0.009	0.052	0.33	0.17	1.0
72 199	0.043	0.021	0.114	0.38	0.18	1.0
72 213	0.050	0.073	0.595	*0.08	*0.12	1.0
72 324	0.392	0.193	1.082	0.36	0.18	1.0
75 102	0.057	0.026	0.147	0.39	0.18	1.0
75 124	--	--	--	--	--	--
76 25	0.082	0.059	0.252	0.32	0.23	1.0
77 107	0.119	0.077	0.324	0.37	0.24	1.0
73 72	0.049	0.026	0.144	0.34	0.18	1.0
73 171	0.151	0.085	0.565	0.27	0.15	1.0
74 192	0.130	0.062	0.317	0.41	0.20	1.0
75 3	0.021	0.013	0.071	0.30	0.18	1.0
75 44	0.981	0.610	2.833	0.35	0.22	1.0
76 4	1.387	1.011	1.507	*0.92	*0.67	1.0
76 66	0.422	0.246	0.855	0.49	0.29	1.0
76 68	0.231	0.212	1.002	0.23	0.21	1.0

Table A3-1e

Average relative scaling factors
by station

Station	Component	Moonquakes	Surface Events	All Events
12	X	1.04 ± 0.31	0.97 ± 0.15	1.01 ± 0.25
	Y	0.92 ± 0.25	0.89 ± 0.17	0.91 ± 0.22
	Z	1.0	1.0	1.0
14	X	1.39 ± 0.43	1.45 ± 0.44	1.41 ± 0.43
	Y	1.0	1.0	1.0
	Z	2.69 ± 1.05	5.85	3.09
15	X	1.06 ± 0.19	0.72 ± 0.21	0.93 ± 0.19
	Y	0.78 ± 0.19	0.56 ± 0.21	0.70 ± 0.19
	Z	1.0	1.0	1.0
16	X	0.55 ± 0.13	0.35 ± 0.06	0.48 ± 0.11
	Y	0.27 ± 0.08	0.20 ± 0.04	0.24 ± 0.07
	Z	1.0	1.0	1.0

Table A3-2a

Surface event locations used for horizontal component
rotation and record section plotting

Event Yr Day	Latitude	Longitude	Origin Time (sec)*
72 134	88.9	-16.3	-18.0
72 199	56.3	129.4	-367.0
72 213	54.2	5.6	-55.0
72 324	24.7	-43.8	-178.0
75 102	87.2	38.7	-128.0
75 124	123.6	-125.0	-344.0
76 25	96.5	-71.2	-201.0
77 107	104.5	-56.0	-140.0
73 72	163.4	-167.0	-315.0
73 171	84.2	-64.8	-172.0—
74 192	74.9	95.7	-313.0
75 3	62.8	-107.0	-273.0
75 44	104.9	-20.1	-57.0
76 4	45.0	28.9	-126.0
76 66	41.7	-23.5	-151.0
76 68	106.0	-11.8	-40.0

*relative to the reference times given in Tables
1-4 and 1-5.

Table A3-2b

Moonquake locations used for horizontal component
rotation and record section plotting

Focus	Colatitude	Longitude	Depth	Origin Time (sec)*
A1	103.2	-31.1	846.0	-112.0
A15	99.4	4.4	1014.0	-109.0
A16	83.5	2.2	1029.0	-140.0
A17	66.4	-19.2	794.0	-132.0
A18	68.9	26.0	919.0	-105.0
A20	69.4	-28.3	947.0	-153.0
A27	70.5	14.5	991.0	-101.0
A30	79.4	-28.5	889.0	-106.0
A31	76.7	7.4	1099.0	-154.0
A32	73.0	18.0	769.0	095.0
A33	83.6	108.6	1027.0	-248.0
A34	82.8	-6.8	936.0	-98.0
A36	33.4	-8.9	1058.0	-117.0
A40	90.9	-10.7	874.0	-78.0
A41	67.2	037.7	721.0	-112.0
A42	68.3	-44.9	983.0	-117.0
A44	45.8	43.4	956.0	-125.0
A45	105.7	-34.4	971.0	-124.0
A46	102.5	-30.4	879.0	-80.0

Table A3-2b (cont.)

A50	80.9	-47.3	886.0	-117.0
A51	80.9	14.0	837.0	-87.0
A56	81.6	-24.2	721.0	-55.0
A61	67.9	35.8	857.0	-199.0
A62	46.7	52.4	971.0	-150.0

*relative to the reference times given in Table 1-6.

Table A3-3a

Source-receiver separation for surface events
used in record section plotting

Event		Separation (central angle in radians)			
Yr	Day	12	14	15	16
72	134	0.144	0.085	0.550	0.580
72	199	2.447	2.390	1.764	2.003
72	213	0.827	0.785	0.172	0.799
72	324	1.221	1.249	0.859	1.502
75	102	1.088	0.986	0.713	0.452
75	124	1.709	1.787	2.361	2.152
76	25	0.833	0.935	1.386	1.497
77	107	0.595	0.689	1.235	1.221
73	72	1.751	1.757	2.311	1.704
73	171	0.738	0.841	1.189	1.421
74	192	2.074	1.977	1.487	1.448
75	3	1.496	1.592	1.652	2.145
75	44	0.215	0.201	0.821	0.616
76	4	1.166	1.113	0.484	0.966
76	66	0.897	0.912	0.536	1.166
76	68	0.302	0.237	0.780	0.481

Table A3-3b

Source-receiver separation for moonquakes used in record section plotting

Focus Number	Separation (central angle in radians)			
	12	14	15	16
A1	0.221	0.288	0.904	0.801
A15	0.495	0.392	0.620	0.192
A16	0.477	0.386	0.343	0.355
A17	0.471	0.477	0.365	0.821
A18	0.944	0.860	0.368	0.555
A20	0.421	0.462	0.519	0.911
A27	0.759	0.681	0.208	0.498
A30	0.255	0.315	0.594	0.837
A31	0.605	0.523	0.231	0.414
A32	0.795	0.710	0.282	0.455
A33	2.304	2.202	1.752	1.640
A34	0.341	0.267	0.371	0.480
A36	1.061	1.059	0.556	1.197
A40	0.225	0.128	0.529	0.477
A41	0.513	0.577	0.657	1.065
A42	0.566	0.644	0.775	1.164
A44	1.324	1.262	0.641	1.028
A45	0.290	0.358	0.974	0.857
A46	0.205	0.272	0.888	0.789

Table A3-3b (cont.)

A50	0.466	0.564	0.892	1.136
A51	0.684	0.591	0.341	0.317
A56	0.201	0.241	0.554	0.754
A61	1.100	1.013	0.514	0.644
A62	1.428	1.363	0.748	1.083

APPENDIX 4

INVERSION METHODS

Inverse problems arise frequently in geophysics, and there are many papers reporting the use of inverse techniques in geophysical analyses (c.f. Wiggins, 1972; Aki et al., 1977; Aki and Lee, 1976; Minster et al., 1974; and many others). The purpose of this appendix is to describe the inverse methods used in this thesis. Discussions on the choice of these methods, their advantages and disadvantages, and the results of applying them to the lunar seismic data set are given in Chapter 3.

In the following sections, the problem to be solved is the determination of seismic event locations and origin times, along with some parameters of the velocity model, from the direct P and S wave arrival times at the four ALSEP stations. Thus the unknowns (or parameters to be determined) are the latitude, longitude, depth and origin time for each event plus typically two to four velocity values (model parameters) of the velocity model. Note that depth need not be determined if the event is known or constrained to be on the surface. The knowns (or data values) are the P and S wave arrival times, a maximum

of eight per event. As discussed in Chapter 3, a minimum
of four (three for surface events) data points are required
for each event simply to be able to determine the location
parameters.

A4.1 Parameter Search Method

The essence of this technique is simply to search
through the parameter space to find a best fit, in some
sense, to the data. The discussion below is for a single
seismic event in the lunar interior (i.e. its depth must
be determined). Extension to surface sources and multiple
event data sets is described afterwards.

For one event, the following scheme is used. First,
the velocity model is fixed, including the model parameters
(e.g. the upper mantle P and S wave velocities) that we
wish to determine. Then a tentative location is chosen
for the event; as described below, it need not be near
the final best location so minimal a priori information is
required. Using this location, the P and S wave travel
times to the four ALSEP stations are calculated, and
subtracted from the observed arrival times to give up to
eight estimates of the event origin time. The variance of
these estimates is then formed (call it e^2) and serves as
the scalar parameter to be minimized. Therefore this

method essentially finds a least-squares fit to the arrival time data in the sense that the variance of the predicted origin time is minimized.

The original location is then used as the center point of a 3 x 3 x 3 grid of locations in latitude, longitude, and depth; the spacing between points is about 30 km. For each of these locations the P and S waves are again traced and e^2 formed at each grid point. The smallest e^2 in the grid is found, and the center of the grid shifted to be at that location.

A new grid of e^2 values is then formed (only a few new values need be calculated) and the grid center moved again. This continues until the minimum e^2 is at the center; this signifies that at least a local minimum, or best location, has been found. Finally, the best location is refined by doing as iterated linearized matrix inversion as described in the next section. In all cases this last step converged to a location within or just outside the area of the final grid.

The result of the above procedure is thus a best location for the event given the seismic velocity model. The value of e^2 for this location is a measure of how well the velocity model and location can explain this observed

data. In practice, no local minima were found for the event locations; the grid would move quickly to the same area independent of where it was started. This is of course partially a result of the data selection process (Chapter 1) which only selected events which had a good (triangular) distribution of observed arrival times (i.e. at least one arrival was required at each corner of the ALSEP array). The fact that the matrix inversion routine did not exit the final grid shows that the wavelengths of the e^2 variation in the parameter space are larger than the grid spacing and therefore the grid is fine enough to follow the structure of the parameter space.

The last step of this method is to systematically vary the velocity model parameters that are to be determined. For each combination, the best event location is again found, and the corresponding value of e^2 calculated. Finally, the e^2 values are printed in an array of the model parameter combinations and the "best" velocity parameter values will correspond to the smallest e^2 and can be found by inspection.

In order to apply this method to surface events, the grid is simply modified to a 3 x 3 configuration on the surface, and the procedure is then the same as above.

However, there is no clear-cut way to apply the technique to many events simultaneously. In the early phases of this work several schemes were tried, including simply stacking the final e^2 arrays for each event, summing the e^2 values for each velocity model considered. The smallest value in the stacked array will then point to an optimal velocity model (in some sense) for the suite of events. Of course, this procedure is somewhat _ad hoc_ and is subject to biasing by events with overly large e^2 value variations. Therefore this multiple event analysis was only used in preliminary studies, mostly to study the characteristics of the parameter space. All seismic velocity results reported in this thesis were obtained by the matrix inversion method discussed in the next section.

As mentioned in Chapter 3, this method (for single events) is inefficient in terms of computation time; many methods with faster convergence rates are available (c.f. Acton, 1970, p. 458). However, the search method is very stable and allows the user to proceed with a minimum of _a priori_ knowledge. In addition, the parameter space can be systematically studied to determine its characteristics. Also, the actual cost of computation is not excessive if reasonable initial location estimates are used based on

relative arrival times.

Accordingly, this technique was used primarily in two ways. First, the parameter space was systematically studied in preliminary investigations; an example is shown in Fig. A4-1. In this case the velocity model parameters varied were the P wave velocity and the Vp/Vs ratio in the whole lunar mantle. A total of 299 models were considered, and the array shows the stacked e^2 values for 8 deep moonquake events. (The dashed lines are iso-Vs curves.) The contours of e^2 are as shown, and a minimum is seen at Vp = 7.9 km/sec and Vp/Vs = 1.88 (Vs = 4.20). The shape of the minimum valley clearly indicates that Vs is more closely constrained than Vp, and no local minima are seen.

The second application of the parameter search method was to obtain preliminary locations for the seismic events used in this thesis and evaluate the internal consistency of various arrival time sets for each event. This is described in more detail in Appendix 1. An example of a residual error (e^2) array used for this purpose is shown in Table A4-1 for a surface event of arrival times. The velocity values refer to the upper mantle velocities. As can be seen, the residuals are of reasonable size given the

accuracy of the arrival time measurements, and the best

velocity model for this data appears to be within the

range considered. It is not possible to identify the

true location of the minimum with such a sparse grid,

but for the purposes of comparing arrival time sets

such an array is sufficient and requires a minimum of

computation time. (Initially, finer arrays were used

until it became obvious that for one event the variations

in e^2 were reasonably gradual over the velocity ranges

considered and it was therefore not necessary to use a

small array spacing.)

A4.2 Linearized Matrix Inversion

This method is far more efficient and more powerful

than the parameter search technique described above. Since

most of its use in this work has been on data sets from

many events, the following discussion (following Aki, 1975)

is for this general case. Naturally, it can also be used

for only one event, as done in the final step of the

previous technique. The purpose of this section is to

briefly outline the theory and describe the main features

of the matrix inverse method, and then discuss its

application to the lunar problem. Further details on

non-linear and linear inverse theory and function

minimization are given in Aki (1975), Aki and Lee (1976),
Aki et al. (1977), Lanczos (1961), Marquardt (1963),
Franklin (1970), Wiggins (1972), Backus and Gilbert
(1967, 1968, 1970), Minster et al. (1974) and many others.

The first step in implementing this method is to
linearize the problem. We define

$$d_i \ , \ i = 1, \ n; \quad \text{vector } \underline{d}$$

to be the P and S wave arrival time data points observed
from N events. Thus $n \leq 8N$. The unknowns are denoted as

$$b_i, \ i = 1, \ m; \quad \text{vector } \underline{b}$$

where $m = 3I + 4J + K$ and $N = I + J$.

Thus m is the number of parameters to be determined,
consisting of 3 values (latitude, longitude, and origin
time) for each of I surface seismic events, 4 values (the
above plus depth) for J interior events, and K velocity
model values. (Note that for the full data set inversion
described in Chapter 3, $K = 4$, $I = 16$, $J = 24$, $N = 40$,
$n = 228$, $m = 148$.) Initial values are now chosen for the

unknowns, and the forward problem done so that

$$\underline{d}' = F(\underline{b}')$$

where $\underline{b}$ are the first-guess values, F is the (non-linear) functional relationship between the knowns and unknowns, and $\underline{d}'$ are the predicted data values. We form

$$\underline{\Delta d} = \underline{d} - \underline{d}'$$

and then linearize the problem by writing

$$\underline{\Delta} d = A \underline{\Delta b}$$

where $\underline{\Delta b}$ are the corrections to the first-guess model values and

$$A = \begin{pmatrix} \dfrac{\partial d_1}{\partial b_1} & \cdots & \dfrac{\partial d_1}{\partial b_m} \\ \vdots & & \vdots \\ \dfrac{\partial d_n}{\partial b_1} & \cdots & \dfrac{\partial d_n}{\partial b_m} \end{pmatrix}$$

Thus the misfit between the predicted and observed data values are written as a linear combination of the corrections to the first-guess model parameters (unknowns), and the problem is reduced to inverting equation 1, which represents a set of simultaneous equations. Unfortunately, in the general case this system can be both over-constrained (i.e. two or more contradictory data misfit values for the same linear combination of model corrections) and under-determined (i.e. the data misfit is totally or nearly independent of one or more of the model parameter corrections). This latter problem manifests itself as zero or near-zero eigenvalues in the matrix A.

Various schemes have been designed to deal with these difficulties as discussed in Aki (1975), Aki et al. (1977), and Aki and Lee (1976). Other references are given therein. In all of the calculations done in this work, the system of equations has been only over-constrained, meaning that there is no exact solution to equation 1. Thus equation 1 should read

$$\underline{\Delta d} = A \underline{\Delta b} + \underline{e}$$

where e is noise contained in the data resulting in the
inconsistencies in the system of equations. Now this
noise can basically have four components. One is random
variations, assumed to have a Gaussian distribution,
caused by measurement error. The second component is
systematic measurement error which for example could result
from consistently missing the true first arrival. Third,
systematic errors could result from discrepancies between
the form of the assumed velocity model and true lunar
structure for example, a plug of anomalous velocity
material beneath one station would consistently bias the
"noise" seen in arrival time measurements at the station.
Finally, higher order terms introduce discrepancies. In
the absence of a priori information we assume that all
data noise is Gaussian distributed. In partial defense of
this, it should be noted that thre was little correlation
between station and arrival time residual.

The standard approach then is to find the solution to
1 that minimizes

$$| \underline{\Delta d} - A \underline{\Delta b} |^{2}$$

thus finding in a least-squares sense the model corrections

that will best account for the observed minus predicted data
residuals. The particular solution that does this is given
by the normal equation

$$A^T \underline{\Delta d} = (A^T A) \underline{\Delta b}$$

or $\qquad (A^T A)^{-1} A^T \underline{\Delta d} = \underline{\Delta b} = G^{-1} \underline{\Delta d}$

where $\underline{\Delta b}$ is now the standard least-squares solution to
the over-constrained problem.

Before proceeding, it should be noted here that it
was not always obvious beforehand during this work that the
matrix $A^T A$ would have a stable inverse, i.e. that all the
Δb's would be well-constrained by the Δd's. If this were
not true, then $A^T A$ would have small eigenvalues that would
cause the inversion to fail. As mentioned above, there
are several ways of dealing with this; we chose to
initially use a form of the stochastic inverse (Aki and
Lee, 1976; Marquardt, 1963; Franklin, 1970), given by

$$\underline{\Delta b} = (A^T A + \theta) A^T \underline{\Delta d}$$

where θ can be written as $(\sigma_d^2 / \sigma_x^2) I$ and σ_a^2 is the variance

of the data and r_i^2 is the variance of the ith model point.
This solution minimizes

$$\left| \underline{\Delta d} - A \, \underline{\Delta b} \right|^2 + \Delta b^T \theta \Delta b$$

which includes the size of the Δb values as well as the
least-squares term. Thus σ_i^2 can be viewed as the amount by
which one will allow the ith model parameter to vary.

This option was built in to the inversion routines
used in this work and tested in various ways. However,
since it was not necessary to use it to obtain the results
in Chapter 3, it will not be discussed further.

Returning to the least-squares solution in
equation 2, the next step is to add the corrections Δb to
the initial guess values $\underline{b}$. If the problem were truly
linear (i.e. if the function F were linear) then the result
would be the final least-squares solution fitting the
data points with the model parameters. However, the
arrival time problem is definitely non-linear, and so
when the model corrections are applied the new model has
different partial derivative values in the matrix A.
Thus we must iterate a few times to hopefully converge to

a stable solution where the data misfit cannot be reduced further and the final model corrections are near zero.

This completes linearized matrix inversion method. In addition to those discussed above, there are two potential difficulties that may arise. First, the convergence of the above iteration to a minimum least-squares fit to the data is contingent on the assumption that the linearization of the function F is a valid approximation and that the resulting correction to the model parameters will in fact improve the fit to the data. If the function is very non-linear and/or the initial guess is for away from a minimum region, the iterations may fail to converge. As discussed in Marquardt (1963), this problem can also be obviated by judicious use of the stochastic inverse operator; again this was not necessary in this work since the parameter search method allowed us to obtain a reasonably accurate starting model. Second, since the fit to the data is a non-linear function of the model parameters, it is possible that local minima exist, and so any stable solution must be considered to be non-unique. As discussed in Chapter 3, the solutions obtained in this work were found to have a wide radius of convergence and no local minima were found within the range of

parameters and models considered reasonable.

There are three matrices that can be calculated with this method that provide valuable information (Aki, 1975). First, the parameter resolution matrix is given by

$$P = G^{-1}A = (A^T A)^{-1}A^T A = I$$

since the matrix $A^T A$ is invertible. This matrix relates the model parameters that were included in the inversion with the actual parameters that could be determined by the data. In this case since all parameters could be determined by the data (there were no zero eigenvalues in $A^T A$), the matrix becomes the identity matrix.

Second, the data resolution matrix (also known as the information density matrix) can be calculated by

$$D = AG^{-1} = A(A^T A)^{-1}A^T$$

and relates the observed data with the predicted values from the final model. If the data were all completely consistent (no noise) and the system of equations were exactly soluble, this matrix would equal I. Since the solution is a least-squares fit to the data, the

predicted values are weighted averages of the observed
data and the rows of D give the weight coefficients. Thus
large off-diagonal elements point to observed data points
that were inconsistent with the datum represented by the
diagonal term and give the averaging scheme produced by
the least-squares solution. The diagonal elements give
the "importances" of each datum to the final solution, and
Trace (D) = m, the number of parameters that were
determined.

Finally, perhaps the most interesting matrix is
the parameter covariance matrix, given by

$$C = \langle \Delta b \, \Delta b^T \rangle = \langle G^{-1} \, \Delta d \, \Delta d^T \, G^{-T} \rangle$$

$$= G^{-1} \langle \Delta d \, \Delta d^T \rangle \, G^{-T} = (A^T A)^{-1} A^T \langle \Delta d \, \Delta d^T \rangle A (A^T A)^{-1}$$

where $\langle \Delta d \, \Delta d^T \rangle$ is the data covariance matrix. We now
suppose that $\langle \Delta d \, \Delta d^T \rangle$ can be written as $\sigma_d^2 I$ where σ_d^2
is the variance of each data point. This assumes that the
errors in the data (arrival times) are uncorrelated, which
will not be true if, as discussed above, the errors are
due to structural anomalies not included in the velocity

model, such as a plug of high velocity material under one station. Since no evidence of such an effect has been observed the assumption that the off-diagonal terms of $\Delta d \, \Delta d^T$ are zero is probably at least approximately valid. Furthermore, the expression $\sigma_d^2 \, I$ implies that the variances in each datum are the same, i.e. σ_d^2 . This is reasonable given the quality of the lunar data, but this assumption is re-examined below.

The parameter covariance matrix then becomes

$$C = \sigma_d^2 \, (A^T A)^{-1} \, A^T A \, (A^T A)^{-1} = \sigma_d^2 \, (A^T A)^{-1}$$

Now the diagonal terms of this matrix are the variance in the model parameters, and the square root gives the standard deviations as quoted in Chapter 3. These values include the effects of uncertainties in the data, inconsistencies in the data, and the uncertainties due to the extent to which the data can uniquely constrain the solution. The off-diagonal terms are the cross-covariance values which, when divided by the square root of the associated row and column diagonal terms, represent the correlation coefficients between the parameters. Thus these quantities indicate which of the determined parameters

can be most effectively traded off without damaging the fit
to the solution.

In addition to these matrices, we can calculate an a
posteriori estimate of σ_d^2 by

$$\sigma_d^2 = \frac{\sum_i \Delta d_i^2}{n-m}$$

where n-m is the number of degrees of freedom. This number
is a measure of the final fit to the data, and is quoted in
Chapter 3 for the various solutions obtained. Furthermore,
it is used in the calculation of the matrix C. As
mentioned in Chapter 3, this a posteriori estimate is
generally in good agreement with the a priori estimate of
indicating that the velocity model is sufficiently
appropriate to fit the data to within the accuracy with
which it can be measured.

The next step is to apply the linearized matrix
inversion method to the lunar problem. First, the forward
problem is done using the initial guess values for the
event locations, origin times, and velocity model
parameters; the necessary ray tracers are described in
Appendix 2. The resulting predicted data values are used
to form the data misfit vector Δd. Then the partial

derivative matrix is calculated, using a combination of analytic expressions and centered finite-difference calculations. The terms of the matrix are the partial derivatives of all the arrival times with respect to all the model parameters; thus many of them are zero since an arrival time from any event is only dependent on the source parameters of that event and the velocity model parameters. Now the model parameters are not scaled by their range, so that the partial derivatives have the following magnitudes:

$$\frac{\partial T}{\partial \theta} \, , \frac{\partial T}{\partial \phi} \quad \sim \quad 10^1 - 10^2 \quad (\pm)$$

$$\frac{\partial T}{\partial D} \quad \sim \quad 10^{-1} \quad (+)$$

$$\frac{\partial T}{\partial V} \quad \sim \quad 10^1 - 10^2 \quad (-)$$

$$\frac{\partial T}{\partial \, \text{OT}} \quad = \quad 1$$

where θ, ϕ, D, OT, and V are latitude, longitude, depth, origin time, and seismic wave velocity respectively. As a result, the matrix $A^T A$ has entire rows (and columns) of values which are much smaller (say by a factor of 10^4) than other rows. In order to partially

compensate for this, the appropriate rows and the corresponding columns can be multiplied by scaling factors to roughly normalize the matrix. After inversion, the operation is repeated to remove the scaling. This scaling allows the necessary computations to be done within the precision of the computer. A straightforward scaling of all input model parameters is perhaps more straightforward, but this method was somewhat easier to implement in the context of our routines.

The matrix manipulations, including the matrix inversion, were carried out using standard programs included in the IMSL subroutine package. (In the early phases of this work, an equivalent routine in the SSP package was used.) In particular, the routine LINV2P was used to invert the matrix $A^T A$. Iterative improvement of the inverse matrix is invoked, so that the inverse is refined until machine accuracy is reached. This also tests the inverse for stability. Descriptions of these routines and references for the algorithms they implement are given in the IMSL reference manual, Library 1.

After the inversion is performed, the model corrections are calculated and added to the initial model parameter values, and the process repeated. Usually, with the starting models used herein, convergence occurs within

three iterations (i.e. the third set of model corrections are less than a few percent of the initial correction values).

In the course of the work reported in this thesis, many tests of the linearized matrix inversion routines were performed, in addition to the basic de-bugging process. Many sets of artificial data were generated (using the ray tracers of Appendix 2), with and without random noise, and inverted to observe the results which were in all cases consistent with expectations. A few of the more pertinent tests are discussed in the following paragraphs.

The first test was of course just to use artificial exact data for a given velocity model and set of event locations; the routine converged quickly to the proper answer for a variety of starting models. Then computer-generated random noise (again using an IMSL routine) with a variance of 4 $\sec^2$ was added to the arrival times of each event to simulate real data; the results of the inversion changed only slightly.

Next, artificial data was calculated for interior events (depth ~ 900 km) using velocity models with a) increasing velocities and b) decreasing velocities with

depth in the mantle. The arrival times were then inverted assuming that the mantle velocities were constant. The results were slightly biased from the true average velocities (averaged along a vertical path); case b produced higher velocities (+.1), shallower depths (-50 km) and late origin times (+10 sec) relative to the true values. Case a produced the opposite biases; both sets can be explained by the program's attempt to straighten the ray path by modifying the depth. Similar tests using surface events produced much smaller biases. In the actual inversion a two-layer mantle is used, allowing the program to simulate either increasing or decreasing velocity profiles, so the potential biases are small and well within the quoted uncertainties. This is also seen in the test discussed in Chapter 3 where the average shear wave velocity in the upper mantle changed by only .01 km/sec when the gradient was changed from 0 to -6 km/sec/km.

Turning to the observed data, eigenvalues were calculated for several of the matrix inversions. A typical condition number for the matrix was 10^7 before normalization and 10^4 after. Also, experiments were done with weighting the data. For example, in the moonquake

inversion the shear wave arrival times are generally better constrained than the P wave data, and so the variance of the S wave times was arbitrarily assumed to be $1/2$ that of the P times. This is implemented simply by multiplying the data residuals and the rows of the matrix A by the appropriate values either σ_s^{-1} or σ_p^{-1} where $\tau_p^2 = 2 \sigma_s^2$. (Note also that the calculation of the parameter covariance matrix must be modified to use the proper data covariance matrix.) In all cases the weighted data produced results similar to those obtained from unweighted data; since a good deal of arbitrary decision is involved in postulating weighting factors, all results reported in Chapter 3 are from unweighted data.

Finally, preliminary data sets that had been examined using the first method and stacked arrays were inverted. The agreement of the matrix inversion results with the parameter values determined by the location of the minimum e^2 was excellent.

In sum, the linearized matrix inversion method is a powerful but sensitive technique. In this work it has been invaluable in extracting the mantle seismic velocity values required by the arrival time data.

Table A4-1

Residual location error grid for Day 134, 1972 surface
event; values in sec^2.

Vs (km/sec	Vp (km/sec) 7.5	8.0	8.5
4.1	4.7	25.8	68.9
4.6	25.9	4.2	6.0
4.9	80.6	34.2	12.5

Figure Captions

Fig. A4-1. Residual errors of best event locations as

function of mantle Vp and Vp/Vs. Minimum as shown.

Fig. 14-1

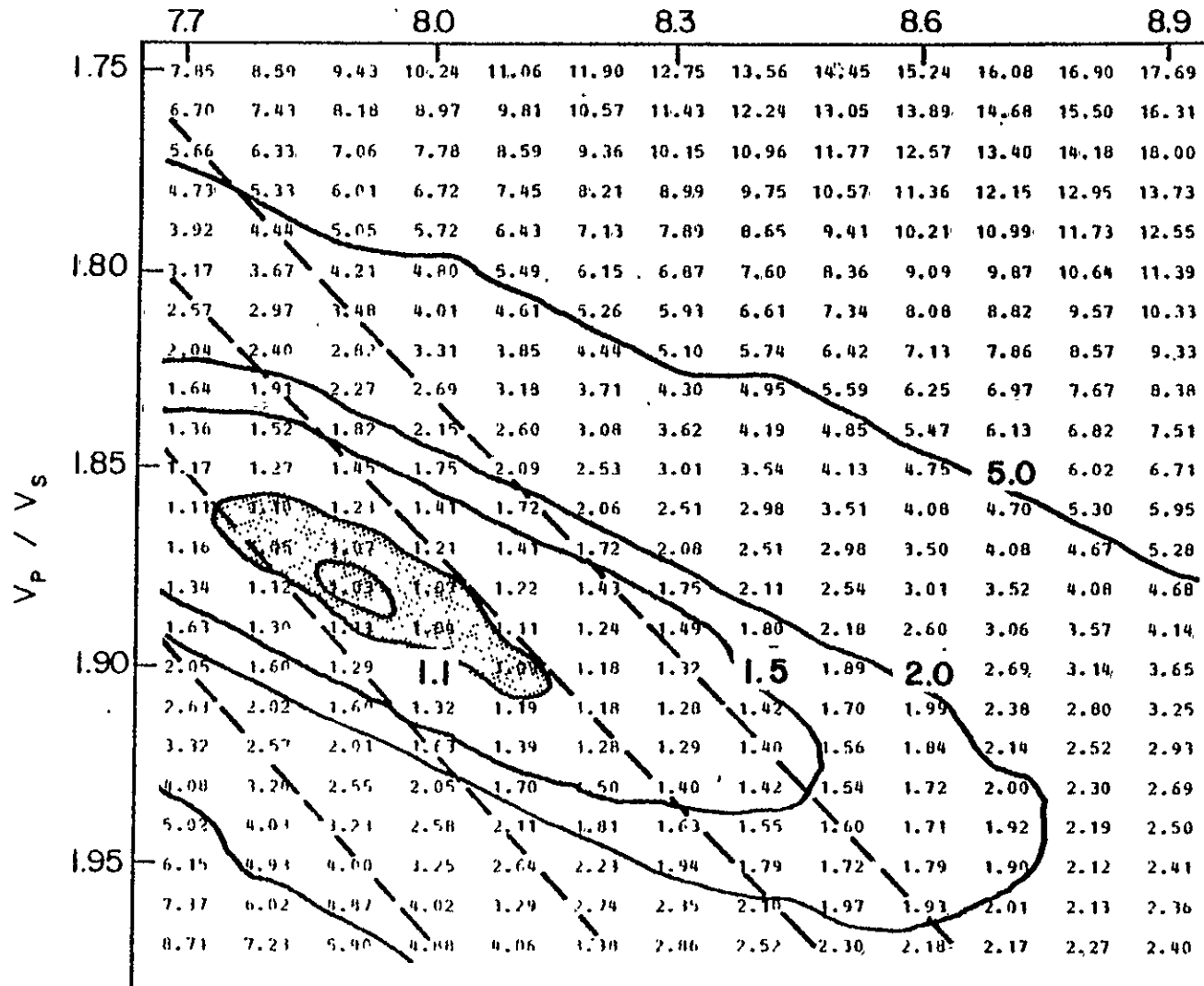## P VEL. (KM/SEC.)

V_P / V_S

	7.7			8.0			8.3			8.6			8.9
1.75	7.85	8.59	9.43	10.24	11.06	11.90	12.75	13.56	14.45	15.24	16.08	16.90	17.69
	6.70	7.43	8.18	8.97	9.81	10.57	11.43	12.24	13.05	13.89	14.68	15.50	16.31
	5.66	6.33	7.06	7.78	8.59	9.36	10.15	10.96	11.77	12.57	13.40	14.18	18.00
	4.73	5.33	6.01	6.72	7.45	8.21	8.99	9.75	10.57	11.36	12.15	12.95	13.73
	3.92	4.44	5.05	5.72	6.43	7.13	7.89	8.65	9.41	10.21	10.99	11.73	12.55
1.80	3.17	3.67	4.21	4.80	5.49	6.15	6.87	7.60	8.36	9.09	9.87	10.64	11.39
	2.57	2.97	3.48	4.01	4.61	5.26	5.93	6.61	7.34	8.08	8.82	9.57	10.33
	2.04	2.40	2.87	3.31	3.85	4.44	5.10	5.74	6.42	7.13	7.86	8.57	9.33
	1.64	1.91	2.27	2.69	3.18	3.71	4.30	4.95	5.59	6.25	6.97	7.67	8.38
	1.36	1.52	1.82	2.15	2.60	3.08	3.62	4.19	4.85	5.47	6.13	6.82	7.51
1.85	1.17	1.27	1.45	1.75	2.09	2.53	3.01	3.54	4.13	4.75	5.0	6.02	6.71
	1.11	1.10	1.21	1.41	1.72	2.06	2.51	2.98	3.51	4.08	4.70	5.30	5.95
	1.16	1.05	1.07	1.21	1.41	1.72	2.08	2.51	2.98	3.50	4.08	4.67	5.28
	1.34	1.12	1.03	1.07	1.22	1.43	1.75	2.11	2.54	3.01	3.52	4.08	4.68
	1.63	1.30	1.11	1.09	1.11	1.24	1.49	1.80	2.18	2.60	3.06	3.57	4.14
1.90	2.05	1.60	1.29	1.1	1.09	1.18	1.32	1.5	1.89	2.0	2.69	3.14	3.65
	2.61	2.02	1.60	1.32	1.19	1.18	1.20	1.42	1.70	1.99	2.38	2.80	3.25
	3.32	2.57	2.01	1.61	1.39	1.28	1.29	1.40	1.56	1.84	2.14	2.52	2.93
	4.08	3.20	2.55	2.05	1.70	1.50	1.40	1.42	1.54	1.72	2.00	2.30	2.69
	5.02	4.01	3.21	2.58	2.11	1.81	1.63	1.55	1.60	1.71	1.92	2.19	2.50
1.95	6.15	4.93	4.00	3.25	2.64	2.23	1.94	1.79	1.72	1.79	1.90	2.12	2.41
	7.37	6.02	4.87	4.02	3.29	2.74	2.35	2.10	1.97	1.93	2.01	2.13	2.36
	8.71	7.23	5.90	4.88	4.06	3.38	2.86	2.52	2.30	2.18	2.17	2.27	2.40

BIOGRAPHICAL NOTE

·Neal R. Goins was born in ██████, ██, on ████████████. His childhood was spent there, in Central and South America, and in Norfolk, Virginia. At age 14 he entered the Phillips Exeter Academy and graduated in three years cum laude. He then went to Princeton University and obtained an A.B. degree in Physics with honors. Having decided that geophysics had a great deal to offer, he went to graduate school at M.I.T. and, after five years of diverse activities, managed to complete a large research project and produce this thesis.

During the course of his educational career, various detours were taken to sample other activities. A good deal of time was spent on other aspects of science besides research, such as paper presentation, committees, and participation in various project efforts (e.g., the Viking Seismology Team). Numerous hobbies such as singing, bicycling and other sports, and traveling occasionally threatened to exceed the time allotted for them. During his stay at M.I.T., consistent weekend visits to Amherst provided companionship and a relief from the urban environment.

In all, he considers the educational phase of his existence to have been quite an experience.